X-RAY POPULATION
OF THE GALACTIC CENTER REGION

Masaaki Sakano

Department of Physics. Graduated School of Science,
Kyoto University, Sakyo-ku, Kyoto 606-8502, Japan

`Submitted to the Department of Physics,`
`Kyoto University on January 5, 2000,`

Abstract

We present the results of the systematic and intensive study of the central region of our Milky Way Galaxy (the Galactic Center) with hard X-rays. We analyzed all the available data around the Galactic Center 5×5 degree^2 taken with the X-ray satellite *ASCA* since 1993 until 1999, including the data with the *ASCA* Galactic Center survey as well as with pointing observations.

We developed the image convolution technique and made the fine images with several energy bands with the angular resolution of about $1'$. In particular, the images with above 3 keV band have the best angular resolution and are accordingly the finest image. We could clearly resolve the point sources and the diffuse structures.

We developed the point source finding method, and consequently found 46 point sources, combining the search results with 0.7–3 keV and 3–10 keV bands. We then performed spectral fitting with power law function for all the detected sources. We also performed the intensive study on the bright sources with the flux larger than 10^{-11} erg cm^{-2} s^{-1} with 3–10 keV band, *i.e.,* 1E 1740.7$-$2942, A 1742$-$294, 1E 1743.1$-$2843, SLX 1737$-$282, GRS 1734$-$292, AX J1749.2$-$2725, SLX 1744$-$299, SLX 1744$-$300, GX 3+1, GRS 1737$-$31, KS 1741$-$293, GRS 1741.9$-$2853, and XTE J1739$-$302, except for the several sources of which the *ASCA* data were already published. In particular, we detected X-ray bursts from A 1742$-$294 and SLX 1744$-$300, X-ray pulsation from AX J1749.2$-$2725, or X-ray flare from XTE J1739$-$302. The power law slopes of the spectra for the sources were found to be significantly different according to the class of objects. On the other hand, we analyzed some selected extended structures: the radio supernova remnants and two newly discovered X-ray structures, designated as AX J1751$-$29.6 and AX J1747.0$-$2828. Significant line emission from both of AX J1751$-$29.6 and AX J1747.0$-$2828 was found.

We found the column density of each bright source to be well expressed with a function with the galactic coordinates, especially the galactic latitude, and established the observational formula of the column densities for the Galactic Center sources for the first time. From the column density distribution, we succeeded in constraining the cold interstellar mass distribution in the Galactic Center region, subtracting the interstellar matter (ISM) component on the Galactic disk; we derived the Gaussian widths of the distribution for parallel and perpendicular directions to the Galactic plane to be ~170 and ~20 pc, respectively, for the assumed distance to the Galactic Center of 8.5 kpc. The total mass of the ISM in

the Galactic Center region is estimated to be less than 6×10^7 $M_\odot$.

Based on the derived function for the column density, we established the method to estimate the distance of the sources in the direction toward the Galactic Center. Among the detected faint sources toward this region, at least two sources were estimated to be actually located near or farther than the Galactic Center. We also discovered a significant pulsation with the period of 725±12 seconds from one of the two sources, designated as AX J1740.2−2848.

Although the density of the X-ray sources in the Galactic Center region was found to be larger than that of the sources on the Galactic plane, the distribution of the X-ray point sources in the Galactic Center region is still consistent with that of stars. However, the deficit of high mass X-ray binaries in the Galactic Center region is apparent. It may suggest no violent starburst activity $\sim 10^7$ years ago in the Galactic Center region.

Contents

1 **Introduction** **13**

2 **Review** **17**

2.1 Quick look at the Galactic Center region 17

2.1.1 With radio to infrared band 17

2.1.2 High energy activity 20

2.2 Each X-ray source 23

2.2.1 Sgr A* & AX J1745.6−2901 23

2.2.2 1E 1740.7−2942 25

2.2.3 A1742−294 28

2.2.4 1E 1743.1−2843 29

2.2.5 SLX 1737−282 31

2.2.6 GRS 1734−292 31

2.2.7 SLX 1744−299/300 32

2.2.8 GX 3+1 33

2.2.9 SLX 1735−269 34

2.2.10 GRS 1737−31 35

2.2.11 KS 1741−293 35

2.2.12 GRS 1741.9−2853 35

2.2.13 XTE J1739−302 36

2.2.14 GRO J1744−28 37

2.2.15 XTE J1748−288 39

2.2.16 GRO J1750−27 41

2.2.17 Sgr B2 — X-ray reflection nebula 41

2.2.18 SNR G359.0−0.9 44

2.2.19 SNR G359.1−0.5 46

3 Instrumentation **49**
3.1 The ASCA satellite 49
3.1.1 Overview 49
3.1.2 Attitude control system 49
3.1.3 Data transfer 50
3.2 XRT (X-Ray Telescope) 50
3.3 GIS (Gas Imaging Spectrometer) 53
3.4 SIS (Solid-state Imaging Spectrometer) 56

4 Observations **59**
4.1 Pointing observations & the Galactic Center Survey 59
4.2 Data screening 60
4.2.1 Data screening criteria 60
4.2.2 Telemetry saturation & bit-rate selection 61
4.2.3 GIS gain, rejection of NXB & arrival time correction 61

5 Results I. — Image & Source Finding **67**
5.1 X-ray images 67
5.1.1 Method for constructing image 67
5.1.2 Global *ASCA* X-ray images for several energy bands 74
5.2 Source finding & extraction of spectra 80
5.2.1 Method of source detection & spectrum accumulation 80
5.2.2 Spectral fitting & source list 81

6 Results II. — Nature of Bright Sources **93**
6.1 Persistent point sources 93
6.1.1 1E 1740.7−2942 94
6.1.2 A 1742−294 106
6.1.3 1E 1743.1−2843 112
6.1.4 SLX 1737−282 117
6.1.5 GRS 1734−292 122
6.1.6 AX J1749.2−2725 124
6.1.7 SLX 1744−299/300 127
6.1.8 GX 3+1 133
6.1.9 Other sources 134
6.2 Transient point sources 136
6.2.1 GRS 1737−31 136

6.2.2 KS 1741−293 139
6.2.3 GRS 1741.9−2853 141
6.2.4 XTE J1739−302 144
6.3 Extended sources 149
6.3.1 Radio supernova remnants 149
6.3.2 Other extended sources 153
6.4 Population of bright sources 158
6.4.1 Summary of bright sources 158
6.4.2 Population of bright sources in the Galactic Center region . 158

7 Results III. — Column Density Distribution 161
7.1 What determines the source $N_{\rm H}$? 161
7.1.1 The most dominant factor for $N_{\rm H}$? 161
7.1.2 The observational formulation to express $N_{\rm H}$ (1) 164
7.1.3 The observational formulation to express $N_{\rm H}$ (2) 165
7.2 The Galactic Center cold ISM distribution 172
7.2.1 Fitting of the $N_{\rm H}$ profile with the Galactic Center ISM model 172
7.2.2 The cold ISM distribution in the Galactic Center region . . 175
7.2.3 Total mass of the Galactic Center cold ISM 176
7.3 Comparison with other wavelengths results 177
7.3.1 Scale lengths of the Galactic Center ISM distribution 177
7.3.2 Total mass of the Galactic Center cold ISM 178

8 Results IV. — Nature of Faint Sources 179
8.1 Application of the $N_{\rm H}$-$|b'|$ relation to faint sources 179
8.2 Nature of faint X-ray sources probably near the G.C. 181
8.2.1 AX J1754.5−2928 181
8.2.2 AX J1754.2−2755 183
8.2.3 AX J1742.6−2901 183
8.2.4 AX J1740.2−2848 183
8.3 Population of faint X-ray sources 185

9 Discussion 187
9.1 Number and density of the Galactic Center bright sources 188
9.1.1 Observation biases 188
9.1.2 Comparison with the population on the Galactic plane . . . 189
9.1.3 Comparison with star distribution 191

9.2 Population of X-ray sources in the Galactic Center region 193
  9.2.1 X-ray population obtained with *ASCA* in the Galactic Center region 193
  9.2.2 Comments on the nature of black hole candidates 193
  9.2.3 Comparison with LMC/SMC population 194

10 Concluding Remarks 197

A The Galactic Disk ISM Distirubion Model 199

B Terminology 201

Bibliography 205

acknowledgments 225

List of Figures

2.1 Past 511 keV-line detection from 1E 1740.7−2942 26
2.2 Correlation of variability between radio and X-ray emission of 1E 1740.7−2942 27
2.3 Radio jet of 1E 1740.7−2942 27
2.4 Molecular cloud around 1E 1740.7−2942 28
2.5 One day averaged *XTE*/ASM light curve of A 1742−294 29
2.6 *ASCA* example of the light curve of GRO J1744−28 38
2.7 (GRO J1744−28) Correlation between the total burst counts and the flux deficiency in the subsequent dip 38
2.8 (GRO J1744−28) Energy spectrum in the first observation with the best fit model 39
2.9 (XTE J1748−288) Long term light curve. 40
2.10 (Sgr B2) Spectrum with the best-fit model. 42
2.11 (Sgr B2) Observed and simulated iron line images. 42
2.12 (Sgr B2) Allowed region for the abundances and the mass. 43
2.13 (G359.0−0.9) 0.7–1.5 keV contour map superposed on the radio image 45
2.14 (G359.0−0.9) GIS2+3 spectrum with the best-fit model. 45
2.15 (G359.1−0.5) 1.6–2.1 keV contour map superposed on the radio image 46
2.16 (G359.1−0.5) GIS spectrum with the model 47

3.1 Configuration of XRTs and the detectors aboard *ASCA*. 50
3.2 Energy and position dependence of XRT effective area. 51
3.3 *ASCA* PSFs of XRT/GIS. 52
3.4 Schematic views for incorrect light paths with the stray light photons 52
3.5 Observed stray light structures due to Crab 53
3.6 Schematic diagram of the principle of GIS. 54
3.7 GIS spectra of day earth, blank sky and night earth. 55
3.8 Change of GIS NXB since the launch 56
3.9 SIS Grade definition. 57

4.1 The GIS fields of views of all the *ASCA* pointings in the GC region 62
4.2 Exposure map of all the *ASCA* observations in the GC region . . . 63

5.1 Flow charts for constructing wide-area images 71
5.1 (continued) 72
5.1 (continued) 73
5.2 *ASCA* X-ray images in the Galactic Center 5° × 5° region 76
5.2 (continued) 77
5.2 (continued) 78
5.2 (continued) 79

6.1 (1E 1740.7−2942) Light curves 97
6.2 (1E 1740.7−2942) Power spectrum density (Obs-ID=1). 98
6.3 (1E 1740.7−2942) The spectra with the best-fit model 99
6.4 (1E 1740.7−2942) Long term variability of Γ, $N_{\rm H}$, $N_{\rm Fe}$ and $F_{\rm X}$ . . . 100
6.5 (1E 1740.7−2942) Diffuse cold iron line distribution near 1E 1740.7−2942102
6.6 (1E 1740.7−2942) *M*-*v*-*n* diagram to explain the observed luminosity of 1E 1740.7−2942 105
6.7 (A 1742−294) Light curves with 16 sec bin. 107
6.8 (A 1742−294) Typical burst profile with hardness ratio 108
6.9 (A 1742−294) Light curve with 256 sec bin for Obs-ID=41. 108
6.10 (A 1742−294) Power spectrum density (Obs-ID=41). 108
6.11 (A 1742−294) GIS2+3 spectra with Obs-ID=41 when an absorbed power-law is applied. 109
6.12 (A 1742−294) The GIS2+3 spectra with the best-fit model (Absorbed power-law by iron-abundant ISM). 110
6.13 (1E 1743.1−2843) GIS2+3 light curves with 2–10 keV bands 113
6.14 (1E 1743.1−2843) Power spectrum density (Obs-ID=21). 114
6.15 (1E 1743.1−2843) GIS2+3 spectra when an absorbed power-law is applied. 115
6.16 (1E 1743.1−2843) Long term variability. 116
6.17 (SLX 1737−282) GIS2+3 light curves with 2–10 keV bands 118
6.18 (SLX 1737−282) Power spectrum density (Obs-ID=30). 119
6.19 (SLX 1737−282) GIS2+3 spectra when an absorbed power-law is applied. 120
6.20 (GRS 1734−292) GIS2+3 light curves with 2–10 keV bands 122

6.21 (GRS 1734−292) GIS2+3 spectra when an absorbed power-law is applied. 123
6.22 (AX J1749.2−2725) Power spectrum density (Obs-ID=19). 125
6.23 (AX J1749.2−2725) Folded light curves (Obs-ID=19). 125
6.24 (AX J1749.2−2725) GIS2+3 spectrum in Obs-ID=46 with the best-fit model. 127
6.25 (SLX 1744−299/300) The 3–10 keV image with the photon extracting region 128
6.26 (SLX 1744−299/300) GIS2+3 light curves with 2–10 keV bands . . 130
6.27 (SLX 1744−300) A burst profile with hardness ratio 131
6.28 (SLX 1744−299) GIS2+3 spectrum with the best-fit bremsstrahlung model. 131
6.29 (SLX 1744−300) GIS2+3 spectrum with the best-fit power-law function. 131
6.30 (SLX 1744−299) GIS2+3 spectra with the best-fit power-law model. 132
6.31 (SLX 1744−300) GIS2+3 spectra with the best-fit bremsstrahlung model. 133
6.32 (GX 3+1) GIS3 spectra with the best-fit model. 135
6.33 (GRS 1737−31) GIS2+3 light curves with 2–10 keV bands 137
6.34 (GRS 1737−31) Power spectrum density (Obs-ID=42). 137
6.35 (GRS 1737−31) GIS2+3 spectrum with the best-fit model. 138
6.36 (KS 1741−293) GIS2+3 light curve with 2–10 keV bands 139
6.37 (KS 1741−293) Power spectrum density (Obs-ID=72). 140
6.38 (KS 1741−293) GIS2+3 spectrum with the best-fit model. 140
6.39 (GRS 1741.9−2853) GIS2+3 light curves with 2–10 keV bands . . . 142
6.40 (GRS 1741.9−2853) GIS2+3 spectrum with the best-fit model. . . . 143
6.41 (XTE J1739−302) GIS2+3 light curves 145
6.42 (XTE J1739−302) X-ray images before and during flare (Obs-ID=76).145
6.43 (XTE J1739−302) Power spectrum density (Obs-ID=76). 146
6.44 (XTE J1739−302) GIS2+3 spectrum with the best-fit model. 147
6.45 (AX J1739.6−2911 (G359.1+0.9)) The 0.7–3.0 keV GIS contour map 150
6.46 (AX J1739.6−2911 (G359.1+0.9)) The radial profile 151
6.47 (AX J1739.6−2911 (G359.1+0.9)) The radial profile 151
6.48 (G0.9+0.1) The 3–10 keV GIS contour map 152
6.49 (G0.9+0.1) The GIS spectrum with the best-fit model 153
6.50 (G0.0−1.3: AX J1751−29.6) The 0.7–3 keV GIS contour map . . . 154

6.51 (G0.0−1.3: AX J1751−29.6) The GIS spectrum with the best-fit model . . . 154
6.52 (G0.56−0.01: AX J1747.0−2828) The 6.0–7.0 keV GIS contour map 155
6.53 (G0.56−0.01: AX J1747.0−2828) The GIS spectrum with the best-fit model . . . 156
6.54 Flux-Γ relation for bright sources . . . 160

7.1 $N_{\rm H}$-Γ relation for bright sources . . . 162
7.2 $|l_{\rm II}|$-$N_{\rm H}$ relation for bright sources . . . 162
7.3 $|b'|$-$N_{\rm H}$ relation for bright sources . . . 163
7.4 Best-fit $N_{\rm H}$-$|b'|$ profiles . . . 166
7.5 $N_{\rm H}$-$l_{\rm II}$-$b_{\rm II}$ relation for bright sources . . . 167
7.6 Fitting results for $N_{\rm H}$-$l_{\rm II}$-$b_{\rm II}$ relation . . . 169
7.7 Best-fit $N_{\rm H}$-$|b'|$ and $N_{\rm H}$-$|l'|$ profiles . . . 170
7.8 Fitting results of $N_{\rm H}$-$l_{\rm II}$-$b_{\rm II}$ with the G.C. ISM model . . . 173
7.9 Best-fit $N_{\rm H}$-$|b'|$ profiles in the Galactic Center ISM model . . . 174

8.1 Application of the $N_{\rm H}$-$|b'|$ relation to faint sources . . . 180
8.2 The spectra of the Galactic Center faint sources with best-fit model 182
8.3 (AX J1740.2−2848) FFT results . . . 184
8.4 (AX J1740.2−2848) Epoch folding search . . . 184
8.5 (AX J1740.2−2848) Folded light curve with P =725.4 seconds . . . 184

9.1 Log$N$-Log$S$ ($N > S$) relation with 2–10 keV band . . . 191
9.2 Comparison with the star distribution . . . 192

A.1 Face-on surface ISM density distribution of the Galaxy . . . 200

List of Tables

2.1 Past observations 30

4.1 Observational log 64
4.1 Observational log (Continued from the previous page.) 65
4.1 Observational log (Continued from the previous page.) 66
4.2 Comments on each observation 66

5.1 Detected X-ray source list 82
5.1 Source list (Continued from the previous page.) 83
5.1 Source list (Continued from the previous page.) 84
5.1 Source list (Continued from the previous page.) 85
5.1 Source list (Continued from the previous page.) 86
5.1 Source list (Continued from the previous page.) 87
5.1 Source list (Continued from the previous page.) 88
5.2 Identification of the detected X-ray sources 89
5.2 Identification table (Continued from the previous page.) 90
5.2 Identification table (Continued from the previous page.) 91

6.1 (1E 1740.7−2942) Observational log for SISs 95
6.2 (1E 1740.7−2942)Best-fit parameters in the fitting with a power-law function 101
6.3 (A 1742−294) Best-fit parameters in the fitting with a power-law function 111
6.4 (1E 1743.1−2843) Best-fit parameters in the fitting with a power-law function 116
6.5 (SLX 1737−282) Best-fit parameters in the fitting with a power-law function 119
6.6 (GRS 1734−292) Best-fit parameters in the fitting with a power-law function 123

6.7 (AX J1749.2−2725) Best-fit parameters in the fitting with a power-law function . . . 126
6.8 (SLX 1744−299/300) Best-fit parameters in the fitting . . . 132
6.9 (GX 3+1) Best-fit parameters in the fitting . . . 134
6.10 Summary of *ASCA* results on bright sources . . . 159

7.1 Best-fit parameters for $N_{\rm H}$-$|b'|$ profile . . . 165
7.2 Best-fit parameters for $N_{\rm H}$-$|l'|$-$|b'|$ relation . . . 171
7.3 Best-fit parameters for $N_{\rm H}$-$|l'|$-$|b'|$ profile with the G.C. ISM mass model . . . 173

8.1 Flux-Γ relation of newly selected four sources . . . 181
8.2 Summary of population of faint X-ray sources . . . 185

9.1 Summary of positions & fluxes of bright sources . . . 190
9.2 X-ray population in the Galactic Center region . . . 193

Chapter 1

Introduction

The center of our Milky Way galaxy, the Galactic Center, is one of centers of our interests in cosmic objects. Stars as well as hot or cold gas are intensively distributed there. Such dense distribution may cause some activity which is not seen in other places. In fact, many galaxies show central activities, such as, active galactic nuclei or starburst. We thus expect such interesting phenomena also in the Galactic Center region; if so, we can perform by far the most detailed study on such activity because of by far the nearest distance, and then we could open a new sight for this issue.

However, the study of the Galactic Center region with the optical or ultraviolet band is impossible due to strong interstellar absorption. Although one can observe the Galactic Center region with radio and infrared (IR) wavelengths, the high background (with radio) and the large extinction (with IR) make the detailed study of the Galactic Center region difficult. On the other hand, hard X-ray band is the most suitable for the study of the activity of the Galactic Center region, because hard X-rays are basically the tracer of the high energy activity, and are almost not absorbed with interstellar matter to the Galactic Center region. Past X-ray satellites, however, have been either not sensitive for hard X-rays or not equipped with mirrors, accordingly not able to resolve each X-ray source in the Galactic Center region which are crowded with many sources.

The astronomical X-ray satellite, *ASCA*, is first equipped with X-ray mirrors and detectors with high sensitivity as well as with the good spectral resolution in the hard X-ray band above 3 keV. Thus we expect to obtain a fine picture of the Galactic Center region and to perform the detailed spectroscopy of the resolved sources. From this motivation, we began the observations of the Galactic Center region with *ASCA*, and the analysis.

The most distinct component in the Galactic Center region is the X-ray point source, which may be an X-ray binary, an active galactic nucleus, a star, or something. The population of those X-ray sources carries unique information on some kinds of star distribution in the Galactic Center region according to the class of the X-ray sources, and further, on the past star formation activity. Some of the point sources, such as, GRO J1744−28 or 1E 1740.7−2942, are already known to show peculiar natures. However, due to lack of sensitivity of the past satellites, systematic study of the population except for several brightest sources has not been made. In this thesis, we reveal the population of the X-ray sources located in the Galactic Center region for the first time. We note that we can probably estimate each source distance from the X-ray absorption in the spectrum, hence we can separate the sources actually located in the Galactic Center region from foreground sources and possibly from background sources.

On the other hand, X-ray spectra of the Galactic Center sources include the important information on the interstellar material along the line of sight. The nature on the interstellar matter in the Galactic Center region or the Galactic disk has been studied with various wavelengths. In particular, the molecular line observations in radio wavelength has been intensively made for the Galactic Center region, which is full of dense molecular clouds. Although radio observations are powerful method to investigate the detailed nature on the cloud in the Galactic Center region, the measurement has sometimes large uncertainties in the derived absolute physical quantities because of large uncertainties of the conversion factor from molecular line fluxes to the amount of hydrogen. It strongly depends on the conditions of the matter: temperature, density, chemical state (gas or dust) or the composition of the molecular. The X-ray absorption, mainly due to the K-shell photo-electric absorption of oxygen and heavier nuclei, is virtually independent of such conditions of the matter; it only depends on the total amount of the cold interstellar matter of oxygen and heavier atoms in the line of sight. Therefore the X-ray absorption measurement would give pure information on the distribution of the cold matter. At least, it gives the result, completely independent of other methods, hence important.

The goals of our study are the followings; (1) obtaining the fine hard X-ray image of the Galactic Center region, and revealing the overall nature, (2) resolving the X-ray sources there, and performing the detailed study on each source to understand each source nature, (3) estimating the source distance, as well as deriving the cold matter distribution in the Galactic Center region, from the X-ray absorption, (4) revealing the X-ray population in the Galactic Center region and giving some restriction for past starburst activity.

The outline of this thesis is as follows. We give a brief review on the present understanding of the Galactic Center region, in particular, on the nature of each X-ray source that we investigated, in the next chapter (Chapter 2). In Chapter 3, the instrumentation about the *ASCA* satellite, of which the data we have analyzed, is briefly explained. Chapter 4 is for the detail of the observations of the Galactic Center region with *ASCA*. Then, we describe the analyses and the results: the overall image, point source detection and the source list in Chapter 5, the detailed results on selected bright sources in Chapter 6, the statistical analysis of column density distribution derived from each source spectrum in Chapter 7[1], and estimation of the distances of the faint sources based on the relation derived in Chapter 7 and detailed study on the selected candidate sources located actually in the Galactic Center region in Chapter 8. Next Chapter 9 is devoted for discussion on X-ray population in the Galactic Center region. Finally, we summarize all the results in Chapter 10.

Through this paper, we adopt 8.5 kpc for the distance[2] to the Galactic Center, unless otherwise mentioned. For the spectral analysis, we define the photon index Γ according to $E^{-\Gamma}$, where E is photon energy. We summarize, in Appendix B, main abbreviations that we use in this thesis. Note that for the characteristics of past X-ray satellites, Bradt *et al.* (1992) gave a good review.

---

[1] The formulation for the interstellar mass distribution in the Galaxy that is used in this Chapter 7 is given in Appendix A.

[2] Reid (1992) performed the detailed study on the distance to the Galactic Center, and concluded the distance to be 8.0±0.5 kpc. This value is slightly smaller than 8.5 kpc, but still consistent with it. Therefore, we adopt 8.5 kpc, which is the IAU recommended value.

Chapter 2

Review

Several good reviews for the general nature observed in the Galactic Center region have been already presented (e.g., Morris & Serabyn 1996; Mezger *et al.* 1996; Maeda 1998). In particular, the review of reviews about the Galactic Center region summarized by Mezger *et al.* (1996) may be useful. Therefore we give here only brief summary for the overall nature (Section 2.1.1 and 2.1.2), and concentrate on the review about the X-ray sources closely related to our work (Section 2.2).

2.1 Quick look at the Galactic Center region

2.1.1 With radio to infrared band

Due to the heavy absorption (or extinction) with $N_{\rm H} \gtrsim$ several$\times 10^{22}$ H cm^{-2}, optical or ultraviolet light from the sources in the Galactic Center region is completely absorbed. Therefore, the observations of the Galactic Center region are limited with the wavelengths of radio, infrared (IR), X-ray and γ-ray.

Infrared stars

The most massive population in the Galactic Center region (within several hundred parsecs) is the star. Being different from the other places in the Galaxy, there is little dark matter. Although the most of the stars in the bulge are old, many known massive stars are also distributed near the plane, as represented by the Quintuplet cluster and G 0.121+0.017, both of which are located with the distance of larger than a few tens pc from Sgr A*. It suggests the past violent starburst activity as well as the strange initial mass function.

Molecular clouds

The Galactic Center region with radius of a few hundred parsecs is known to be full of molecular clouds. In the Galactic Center region, most of the interstellar matter (ISM) exist not as HI, but as molecules. Various complex molecular lines are also detected, which suggests the high density. Whereas most of the molecular clouds are observed along the simple nuclear rotation curve, which suggests the (rotating) molecular ring, some of clouds show more complicated velocity distribution. In addition, there is a probable expanding structure from the Galactic Center center, so-called the expanding molecular ring (e.g., see review by Combes (1991)). The average velocity dispersion of the clouds are rather high, several tens km s^{-1}, whereas the temperature is also high as several tens Kelvin.

Non-thermal radio structure

The centimeter observations reveal a complex non-thermal structure in the Galactic Center region. There are many filamentary structures, most of which are perpendicular to the Galactic plane, as represented by the Radio Arc (e.g., Morris 1994; Morris 1996). Some other unusual (relatively compact) structures, such as, the Mouse or the Pistol, are also seen. In addition, there are about ten of known supernova remnants (e.g., Green 1998). Two remarkable structures in the Galactic Center region is the Galactic Center lobe and the jet-like structure. The former is the bridge-like structure with a scale of over 100 pc, whereas the latter is extending over kpc scale from the Galactic Center to the upper plane (Sofue *et al.* 1989).

Magnetic field

The direction and the strength of the magnetic field is known to be quite peculiar in the Galactic Center region. The radio polarization measurement of the non-thermal filaments show the magnetic field to be parallel to the filaments, namely perpendicular to the Galactic plane. This phenomenon is contrary to that on the Galactic disk, where the magnetic field direction is parallel to the plane. The strength of the magnetic field is estimated to be about 1 mG almost everywhere in the Galactic Center region where the magnetic field was measured, which is much higher the averaged interstellar magnetic field strength on the Galactic disk, μG order. However, it is not understood whether such strong magnetic field is extended all over the Galactic Center region, or localized at some points. On the other hand, the mid- and far-infrared polarization measurements of the dust in the clouds which may be apparently along radio filaments shows the magnetic field direction to be rather parallel to the filaments, namely parallel to the Galactic plane. This fact make this issue complex.

Abundance

The abundance of the Galactic Center region is still not well understood due to the difficulty of the observation. The observations of the Galactic disk region show the apparent abundance gradient to the Galactic Center from the outer region of the Galaxy to a point of a few kpc distant from the Galactic Center (e.g., Majewski 1993). If we extrapolate the abundance gradient to the Galactic Center, the abundance in the Galactic Center region may be about 3 times of the solar or possibly much larger. There are some other measurements for the abundance; some of them favors higher abundance in the Galactic Center region (for ISM: $\sim$2 solar by Mezger *et al.* (1979); $\gtrsim$3 solar by Murakami *et al.* 2000a), whereas recent infrared star observations give inconsistent results (Sellgren, Carr, & Balachandran 1997; Ramírez *et al.* 1998; Carr *et al.* 1999).

Starburst activity?

Some suggestions for the past starburst activity in the Galactic Center region have been reported: (1)the abundance is probably higher than the solar (see the above paragraph), although it is not completely confirmed, yet. (2) There is the eccentric star population; some star clusters have unusually large number of massive stars, although such clusters are localized. (3) Many shell-like cloud structures were found (Hasegawa *et al.* 1998; Tsuboi *et al.* 1997), which may be originated in many supernova remnants born 10^6–10^7 years ago. (4) the distribution of expansion velocities of the circumstellar shells of OH/IR stars shows an unexpectedly narrow peak, suggesting the enhanced star formation at least one Gyr ago (Sjouwerman *et al.* 1999). (5) the intense 1.8 MeV emission from ^{26}Al suggests the existence of many massive stars and further the past star formation (e.g., Prantzos 1998; Naya *et al.* 1996), although there are also another regions with stronger ^{26}Al emission along the disk. On the other hand, present Galactic Center region is quiet. Anyway, when, where, and with how much largely the starburst occurs, even if the starburst really occurs, is still a question. We note that there is a serious problem for the theoretical approach for the star formation in this region if it really occurs; the strong magnetic field with 1 mG which is possibly extended all over the Galactic Center region may prevent the star formation in this region.

2.1.2 High energy activity

X-ray observations (Point sources)

The X-ray observations of the Galactic Center region began with *Uhuru* (Kellogg *et al.* 1971). The results with early X-ray observations in 1970's were summarized in Proctor *et al.* (1978). Since 1980, many satellites including *Einstein* (e.g., Watson *et al.* 1981), *Spacelab-2* (e.g., Skinner *et al.* 1987), *Spartan-1* (Kawai *et al.* 1988), *ROSAT* (Predehl & Trümper 1994), *Ginga* (e.g., Yamauchi *et al.* 1991), *Mir-Kvant* (e.g., Sunyaev *et al.* 1991d), *Granat* (e.g., Sunyaev *et al.* 1991d; Pavlinsky *et al.* 1994; Churazov *et al.* 1994), *XTE*, *SAX* (Sidoli *et al.* 1999), and *ASCA*, have observed the Galactic Center region.

The most distinct structures in X-ray band are point sources. Although many transient sources are detected in the Galactic Center region, the number of X-ray pulsars are relatively small: GRO J1744−28, GRO J1750−27 (see Section 2.2), and two pulsars, which were found with *ASCA*, reported in this thesis. Details for the point sources that was, in particular, detected with *ASCA*, are reviewed in the next Section (Section 2.2).

X-ray diffuse emission

Some excess emission along the Galactic plane had been suggested since the early stage of the X-ray observations. Koyama *et al.* (1986) discovered the diffuse thermal emission along the Galactic plane with strong emission line at 6.7 keV from highly ionized iron, which implies the plasma with the temperature of around 10 keV. Koyama *et al.* (1989) then discovered the intense distribution of the 6.7-keV line centered at the Galactic Center with *Ginga*. Note that such high temperature plasma cannot be confined with the gravity of the Galactic Center region. With the detailed analysis of the *Ginga* survey data, Yamauchi *et al.* (1990) concluded that the surface brightness distribution of the plasma is elliptical with a major axis of $1.^\circ8$ (FWHM) and an axial ratio of about 0.5, and that the major axis is tilted about 20° with respect to the Galactic plane.

The existence of the line from highly ionized iron is confirmed with *ASCA* with better energy resolution (Koyama *et al.* 1996; Maeda 1998; Sakano *et al.* 1999c); they found three iron lines at 6.97, 6.7, and 6.4 keV, each of which corresponds to the Kα line from hydrogen-like, helium-like and neutral iron. The total energy of the plasma is quite high as about 10^{54} erg. In addition, the 6.7 and 6.97 keV lines were found to be slightly broad with the sigma of $\sim$75 eV. It suggests that the plasma is far from thermal equilibrium. Whereas the plasma surface brightness is varied from position to position, the temperature was found to be unexpectedly uniform (Koyama *et al.* 1996; Maeda 1998). Although the origin of the plasma is still an enigma, Koyama *et al.* (1996) proposed that the origin of the wide-spread plasma may be the past activity of Sgr A* about 5×10^4 years ago, from all these facts as well as some other indirect evidence.

On the other hand, the spatial distribution of the 6.4-keV line is quite clumpy. The distribution is in good agreement with that of radio molecular clouds (Maeda *et al.* 1996). Hence it is thought to be the fluorescent K-line from molecular clouds which are illuminated by strong X-ray sources. However, there is a serious problem; the total flux is too high to explain it with known persistent sources. The detailed result for the largest peak, located at Sgr B2 cloud, is reviews in Section 2.2.17.

Koyama *et al.* (1996) and Maeda (1998) also found strong Kα lines from highly ionized silicon, sulfur and argon, which implies the temperature of about 1 keV. Therefore, the plasma seen in the direction for the Galactic Center region has multi temperature structure. It has at least two components of 1 keV and 10 keV.

Maeda (1998) and Sakano *et al.* (2000) found that the 6.7-keV line is extended to at least $b_{\rm II} = -7^\circ$. They derived the typical temperature of the plasma, independently from the absorption effect, and concluded that the typical temperature decreases as a function of the (angular) distance from the Galactic plane (galactic latitude). The origin for the iron line in the bulge region is also an enigma.

High energy γ-ray view

Positron-electron annihilation line at 511 keV from the Galactic Center region as well as the possible Compton back-scattered feature at 170 keV was repeatedly observed. Some reports show the long term flux variation (see the summary by Leventhal (1991) and Purcell *et al.* (1997)). If it is true, some portion of 511 keV line should be originated in point-like component. However, due to the difficulty of the calibration, it is still uncertain whether the variation is real or not (e.g., Purcell *et al.* 1997).

One remarkable discovery is three components of the 511 keV line: a central bulge, emission in the Galactic plane, and an enhancement or extension of emission at positive latitudes above the Galactic center. Large amount of positrons must be required to reproduce the observed 511 keV nature. However, the mechanism to produce them is still an enigma.

The nuclear line (^{26}Al) and the γ-ray emission above 30 MeV were also observed from the Galactic Center region (see the previous section and Section rev:SgrA).

Cosmic ray

One other remarkable topic in the Galactic Center is the excess of the high energy cosmic ray. The cosmic ray with the energy above 10^{15} eV, so-called "knee", has been generally thought to be extragalactic origin. However, the AGASA team recently found that the the distribution of the cosmic ray with the energy above 10^{17} eV has significant anisotropy, 4% at 10^{18} eV, of which the excess coincides with the Galactic Center and the Cygnus regions (Hayashida *et al.* 1998). The origin and the mechanism to accelerate particles up to such high energy are still an enigma.

2.2 Each X-ray source

In this section, we review the past observational results on each X-ray source in the Galactic Center region.

2.2.1 Sgr A* & AX J1745.6$-$2901

The gravitational center of our Milky Way galaxy, Sagittarius A* (Sgr A*), is the most interesting object in this region. It has been extensively studied in all the wavelengths. The recent results on Sgr A*, especially with radio to infrared bands, are found in the proceeding book, "The central parsecs of the Galaxy" (eds. Falcke *et al.* 1999). In this sub-section, we quickly summarize the nature on Sgr A* from radio to infrared bands at first, then mention the high energy nature in more detail.

The Sgr A* is a quite bright source at GHz bands, and sometimes shows the variability (e.g., Tsuboi *et al.* 1999a). The mass of the close vicinity of Sgr A* has been accurately measured to be 2.6×10^6M$_\odot$ with proper motion observations of stars around Sgr A* in near infrared bands (Eckart & Genzel 1996, 1997; Ghez *et al.* 1998). Reid *et al.* (1999) measured the lower limit of the peculiar motion of Sgr A* with VLBA observations, and estimated the lower limit of the mass to be 10^3M$_\odot$; it is consistent with the near infrared measurements.

However, there is a serious problem; Sgr A* is too dim, less than the Eddington limit by at least an order of 7 for the mass of 10^6M$_\odot$, being different from other AGNs. In fact, Sgr A* is found to be quite dim in X-ray band.

Above 35 keV, Goldwurm *et al.* (1994) found no significant X-ray source associated at the position of Sgr A* in the intermittent monitoring observations of Sgr A* since 1990 until 1993 with the hard X-ray coded-mask telescope *Granat*/SIGMA. They could determine the source position with the accuracy of less than $5'$ for a point source with SIGMA, if it exists.

In the highest energy above 30 MeV, *CGRO*/EGRET has detected a γ-ray excess at the Galactic Center between 30 MeV–10 GeV (designated as 2EG J1746$-$2852) with an error circle of $0.\!\!'2^\circ$ for photons with $E_\gamma > 1$ GeV (Mayer-Hasselwander *et al.* 1998). Due to positional uncertainty, it is still unclear whether this γ-ray source is actually associated with Sgr A* or other sources, such as, Sgr A East diffuse structure.

Below 2–3 keV, a faint soft X-ray point source, of which the position is consistent with that of Sgr A*, was found with *Einstein* and *ROSAT*, designated as 1E 1742.5$-$2859 (Watson *et al.* 1991) and RX J1745.6$-$2900 (Predehl & Trümper

1994). The error radius for RX J1745.6−2900 is less than 10″. The absorption-corrected luminosity was estimated to be $\sim 7 \times 10^{35}$ erg s^{-1} in 0.8–2.5 keV for the assumed column density of 1.5×10^{23} H cm^{-2} (Predehl & Trümper 1994). However, it is still unclear whether this soft X-ray source is the real counter part of Sgr A^* because the large column density to Sgr A^*, probably $> 10^{23}$ H cm^{-2}, may prevent such soft X-ray detectors from detecting it.

In 3–10 keV, some X-ray observations have suggested a weak X-ray counter part of Sgr A^*, which may have been variable (see the references in Predehl & Trümper (1994) and in Maeda *et al.* (1996)). However, recent *ASCA* observations with by far the best spatial resolution above 3 keV band revealed that it might be merely due to the contamination from a nearby source (Koyama *et al.* 1996; Maeda *et al.* 1996). They found two X-ray sources in the close vicinity of Sgr A^*; one is diffuse source with a thermal spectrum, located at the position consistent with that of Sgr A^*, and the other is found to be a burster, designated as AX J1745.6−2901. Maeda *et al.* (1996, 2000) found that AX J1745.6−2901 was variable by a factor of 6 in three *ASCA* observations in 1993, 1994 and 1997. Previous observations with other satellites could not resolve these two sources because the angular distance between Sgr A^* and AX J1745.6−2901 is only $1\overset{\prime}{.}5$. Therefore this *ASCA* discovery of the two sources gives serious suspect for the past reported variable X-ray fluxes from Sgr A^*, which should be contaminated with the emission from an variable source AX J1745.6−2901 (Maeda *et al.* 1996).

The discovery of the diffuse source at Sgr A^* (Sgr A diffuse, hereafter) indicates that the emission originated in the black hole should be quite weak. In fact, Maeda (1998) and Maeda *et al.* (1996, 2000) found that Sgr A diffuse has not shown the time variability in three *ASCA* observations in 1993, 1994 and 1997. They estimated the upper limit of the luminosity originated in a point-like source to be 3×10^{35} erg s^{-1} in 2–10 keV band. Sidoli & Mereghetti (1999) confirmed this result with recent *SAX* observations. The spectrum was found to be characterized with strong iron lines from highly ionized iron, hence it is thin thermal plasma with the temperature of about 10 keV. The density and the thermal energy of electrons were estimated to be 6 electron cm^{-3} and 3×10^{50} erg, respectively (Koyama *et al.* 1996; Maeda 1998). The origin of Sgr A diffuse plasma is unknown, but may possibly be the same as that of the wide-spread (wider than $1^\circ \times 1^\circ$) Galactic Center hot plasma because the spectral shape is quite similar to that of the Galactic Center hot plasma except for the surface brightness (Koyama *et al.* 1996; Maeda 1998).

From AX J1745.6−2901, Maeda *et al.* (1996) discovered a type-I burst, as well as periodic dips with the period 8.4 hr; thus, this source is very likely to be a LMXB with eclipse. Note that although they first identified the eclipsing source as the same source as an old transient A 1742−289 (Branduardi *et al.* 1976; Eyles *et al.* 1976)[1], Kennea & Skinner (1996) found it not to be A 1742−289 and designated it as a new source AX J1745.6−2901, reanalyzing the old archival data and finding no eclipse from A 1742−289.

Maeda *et al.* (1996, 2000) found the spectrum of AX J1745.6−2901 to be well represented with an absorbed power law. The best-fit hydrogen column density was quite high, $N_{\rm H}= 25^{+2}_{-1} \times 10^{22}$ H cm^{-2}. The photon index in high state was ∼2.2, whereas it was ∼1.8 in low state where the column density was fixed to the same value in high state. The phenomenon has been generally observed in other low mass X-ray binaries in rather faint states (e.g., Mitsuda *et al.* 1989).

They also found the significant X-ray emission even in eclipse. The ratio of the eclipse spectrum to that in persistent phase was found to be energy dependent with a power law index of 2–3; *i.e.*, the spectrum in eclipse was much softer than that in persistent phase. It implies that the X-ray emission in eclipse is mainly due to dust-scattering because the dust-scattering cross section is also energy dependent with power law index of ∼2.

2.2.2 1E 1740.7−2942

Among X-ray sources in the Galactic Center region, 1E 1740.7−2942 has been found to be quite unusual. This source was discovered with the *Einstein*/IPC in the soft X-ray band below 3.5 keV (Hertz *et al.* 1984). Higher energy observations revealed an unusually hard spectrum (Skinner *et al.* 1987, 1991; Kawai *et al.* 1988; Cook *et al.* 1991; Bazzano *et al.* 1992; Cordier *et al.* 1993a, 1993b; Heindl *et al.* 1993; Goldwurm *et al.* 1994). In fact, this is by far the brightest source within a few degree of the Galactic Center in the high energy band above 20 keV with a power-law spectrum extending up to 100 keV or higher. It showed flux variability in the time scale from a day to a few years (Bouchet *et al.* 1991; Sunyaev *et al.* 1991b; Churazov *et al.* 1993a, 1993b; Paciesas *et al.* 1993; Pavlinsky, Grebenev, & Sunyaev 1994; Zhang, Harmon, & Liang 1997). Variability of time scale shorter than a day has been detected by Smith *et al.* (1997a). The spectral shape has been almost stable in time, regardless of the flux variations. These spectra and time variabilities generally resemble those of Cygnus X-1 (e.g., Kuznetsov *et al.* 1997), the prototype of the galactic black hole candidate. Unlike Cygnus X-1, however, optical and IR observations have failed to find any companion stars (Prince *et al.* 1991; Mereghetti *et al.* 1992; Djorgovski *et al.* 1992; Bignami *et al.* 1993), probably due to strong extinction to the direction of the Galactic Center.

---

[1] They first designated it as A 1742−28.

The electron-positron annihilation line at 511-keV from this source was reported with the *Granat*/SIGMA observations, hence 1E 1740.7−2942 has been referred to as the "Great Annihilator" (Bouchet *et al.* 1991; Sunyaev *et al.* 1991c; Churazov *et al.* 1993b; Cordier *et al.* 1993a). Jung *et al.* (1995), Harris, Share, & Leising (1994a, 1994b), Malet *et al.* (1995), Smith *et al.* (1996), Cheng *et al.* (1998), on the other hand, reported no evidence for the annihilation line, making this issue debatable. The VLA radio observations revealed that 1E 1740.7−2942 has a radio counterpart with variable flux correlated to the X-ray variation (Mirabel *et al.* 1992, 1993; Heindl *et al.* 1994). They also found non-thermal double jet-like structures emanating from the source, which resemble those of the galactic superluminal jet sources (e.g., Fender, Burnell, & Waltman 1997). Hence this source is also referred to as a "micro quasar". These facts altogether place 1E 1740.7−2942 to be one of the best candidates of stellar mass black holes.

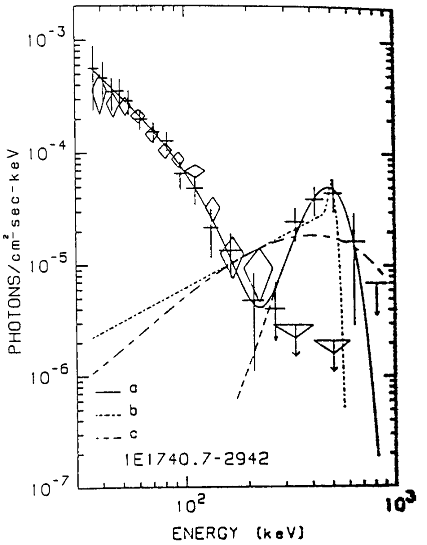

Figure 2.1: The *Granat*/SIGMA spectrum of 1E 1740.7−2942 in high state. This figure is adopted from Bouchet *et al.* (1991).

The CO observations found a giant molecular cloud whose density peak is in agreement with the position of 1E 1740.7−2942 (Bally *et al.* 1991; Mirabel *et al.* 1991). They proposed that 1E 1740.7−2942 is an isolated or a binary black hole, powered directly from a surrounding molecular cloud such as by the Bondi-Hoyle

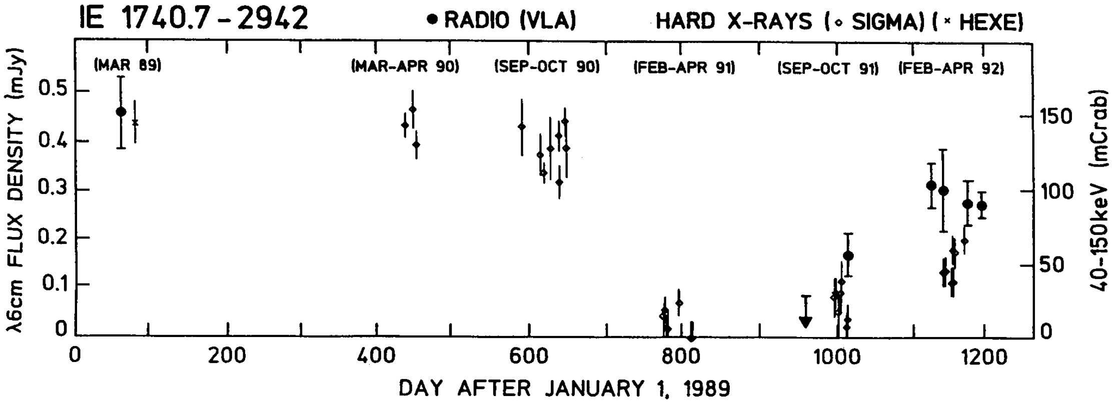

Figure 2.2: Time variability of 1E 1740.7−2942 in radio and X-ray bands. This figure is adopted from Mirabel *et al.* (1992).

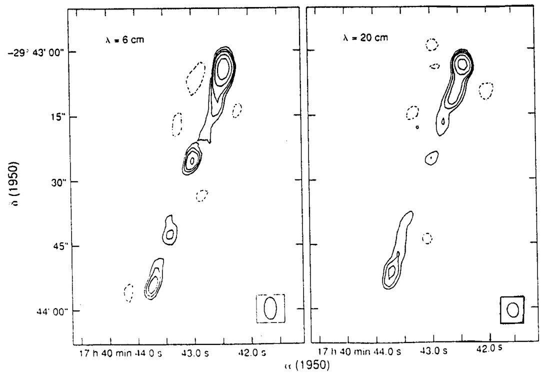

Figure 2.3: Image of bipolar jet-like structure of 1E 1740.7−2942 observed with cm-wave (Mirabel *et al.* 1992).

accretion (Bondi & Hoyle 1944), although the conventional binary scenario with mass accretion from a companion star cannot be excluded.

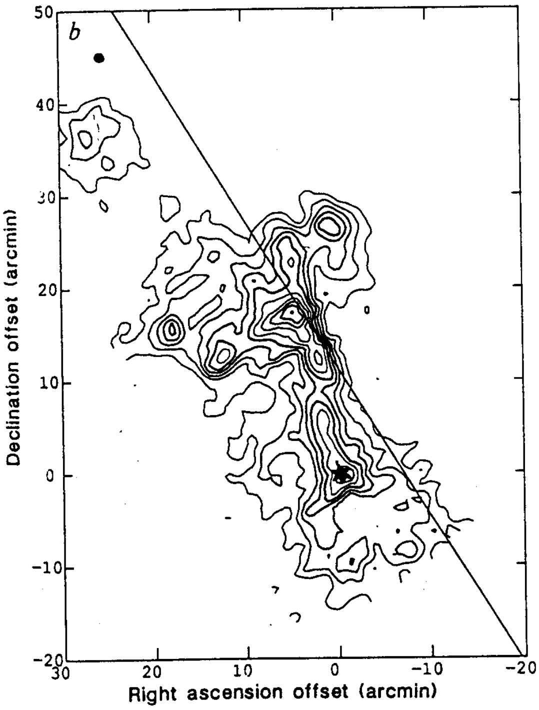

Figure 2.4: The CO-line image around 1E 1740.7−2942 by Bally *et al.* (1991).

2.2.3 A1742−294

A1742−294 was discovered with *Ariel-5* in 1976 (Ariel 5 Group 1976)[2]. Lewin *et al.* (1976) detected several bursts from this source[3] with *SAS-3*. Some of the detected bursts were found to be type-I bursts. Hence this source was identified as a low mass X-ray binary (LMXB). The burst peak luminosities were about $\sim 10^{39}$erg s^{-1} (3–19 keV) for the assumed distance of 10 kpc.

Since then, it has been almost always detected in 2–10 keV band when the Galactic Center region was observed with detectors with sufficient sensitivity (see 2.1). In fact, *XTE*/ASM light curve of A 1742−294 (Fig. 2.5) shows that it has been almost luminous with flux of a few tens mCrab with several occasional exception since 1996. Type-I burst activity of this source was also confirmed with several observations in 1990's (Sunyaev *et al.* 1991a; Pavlinsky *et al.* 1994; Sidoli *et al.* 1999). Thus A 1742−294 is definitely a persistent LMXB source.

---

[2] Ariel 5 Group (1976) first named it A 1743−29.

[3] Lewin *et al.* (1976) named it MXB 1743−29. Due to the positional coincidence and bursting activity, it is probably the identical source as A 1742−294.

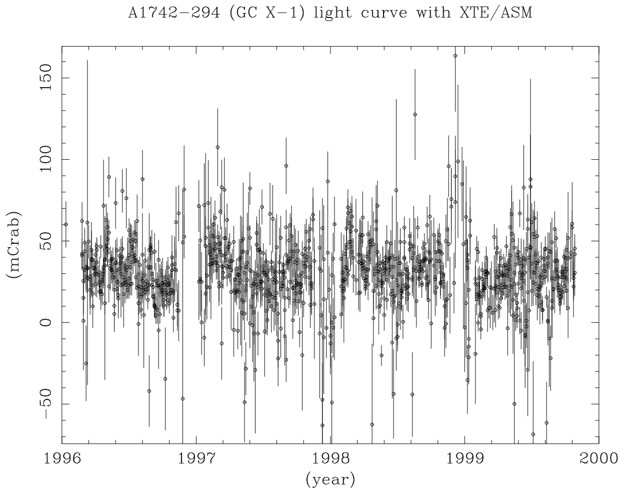

Figure 2.5: One day averaged *XTE*/ASM light curve of A 1742−294 adopted from the *XTE*/ASM team (1999). Note that they refer the name to as GC X-1.

Although searches for the optical counter part were made, no one has found the probable counter part (e.g., Jernigan *et al.* 1978). Therefore, the accurate distance to the source or the neutron star mass is not determined, yet.

The X-ray spectrum of LMXBs is known to have generally a cut-off above about 20 keV. However, Churazov *et al.* (1995) have found the significant X-ray emission above 35 keV from A 1742−294 in 1992 fall with SIGMA on board *Granat*, whereas they noted that such hard emission had been not significant in most of their other observation time. The spectrum above 35 keV then can be fitted with a power law of photon index of 3.1 or with bremsstrahlung of temperature of about 40 keV. The normalization at 100 keV was 9×10^{-6}photons cm^{-2} s^{-1} keV^{-1}. No firm conclusion for the origin was given, although they discussed some mechanisms. Similar hard X-ray emission from LMXBs are reviewed in later section (Section 2.2.9).

One of other interesting natures for A 1742−294 is the detection of milli-second oscillations during type I X-ray bursts. Strohmayer *et al.* (1997) discovered 589 Hz oscillations for the hard energy band above 8 keV with the amplitude of 18 %, but no such signal for lower energy band. They discussed that those oscillations may originate from the spin of a neutron star. However, the detailed theory has not been confirmed, yet.

2.2.4 1E 1743.1−2843

1E 1743.1−2843 was discovered with the *Einstein* satellite in 1979 (Watson *et al.* 1981). Since then, it has been almost always detected in 2–10 keV band when

Table 2.1: Past observations of bright sources

Satellite/Detector	Reference	Other names
	(for **A 1742−294**)	
Ariel-5	Ariel-5 Group 1976	A 1743−29
SAS-3-3	Lewin *et al.* 1976	MXB 1743−29.
SL1501	Proctor *et al.* 1978	
a rocket	Cruddace *et al.* 1978	
Einstein	Watson *et al.* 1981	1E 1742.9−2928.
a balloon-borne detector	Knight *et al.* 1985	
Spacelab-2	Skinner *et al.* 1987, 1990	
Spartan 1	Kawai *et al.* 1988	
Granat/ART-P	(e.g.) Pavlinsky *et al.* 1994	
Granat/SIGMA	Churazov *et al.* 1995	
EXOSAT	Lu *et al.* 1996	
ROSAT	Voges *et al.* 1999	1RXS J174605.0−293042
SAX	Sidoli *et al.* 1999	
XTE/ASM	*XTE*/ASM team 1999	
	(for **1E 1743.1−2843**)	
Einstein	Watson *et al.* 1981	
Spacelab-2	Skinner *et al.* 1987, 1990	
Spartan 1	Kawai *et al.* 1988	
Granat/ART-P	(e.g.) Pavlinsky *et al.* 1994	
EXOSAT	Lu *et al.* 1996	
SAX	Cremonesi *et al.* 1999	

the Galactic Center region was observed with detectors with sufficient sensitivity (see 2.1). The observed flux was usually fainter by several factors than that of A 1742−294.

However, *ROSAT* did not detect this source, possibly because of the heavy absorption for this source; *ROSAT* has no sensitivity above 3 keV. In fact, Kawai *et al.* (1988) suggested the heavy absorption of $N_{\rm H}\sim 2\times10^{23}$H cm^{-2}. Neither bursting activity nor pulsation has been found in the past observations. There is no successful report for the optical or infrared identification, either.

Thus 1E 1743.1−2843 is a persistent, moderately bright X-ray source, however, the detailed nature is not understood.

2.2.5 SLX 1737−282

SLX 1737−282 was discovered with Spacelab-2 in 1985 by Skinner *et al.* (1987) with the 3–30 keV flux of 0.9×10^{36}erg s^{-1} on the assumption of 10 kpc distance, They also reanalyzed the *Einstein* archival data taken in 1979, and again detected this source. With later observations with *Granat*/ART-P in 1990, Pavlinsky *et al.* (1994) gave 3σ upper limit of the luminosity for this source to be 0.74×10^{36}erg s^{-1}, assuming the Crab-like spectrum and the distance of 8.5 kpc.

No other report for the detection of this source can be found in the SIMBAD database.

2.2.6 GRS 1734−292

GRS 1734−292 was discovered with *Granat*/ART-P in 1990 by Sunyaev (1990b). Pavlinsky *et al.* (1994) derived the 4–20 keV X-ray spectrum with *Granat*/ART-P data and found it to be well represented with a power law function of photon index of 2 and hydrogen column density of $\sim 6\times10^{22}$ H cm^{-2}. With a later observation by *Granat*/SIGMA, Churazov *et al.* (1992) detected a big hard X-ray outburst of which the spectrum extended up to 400 keV.

Barret & Grindlay (1996) detected the counter part in the soft X-ray band with *ROSAT*. Then, thanks to the accurate position measured with *ROSAT*, Martí *et al.* (1998) found a radio source, NVSS J173728−290802, with strong flux (at the 48 mJy level) in the *ROSAT* position error circle from NRAO VLA sky survey catalogue (Condon *et al.* 1993). NVSS J173728−290802 shows a jet-like morphology. The radio spectrum is represented with a power law function (Martí *et al.* 1998). The estimated chance probability that such a strong radio source within the *ROSAT* error circle was only 2×10^{-5}.

Martí *et al.* (1998) made V, R, I, J, K-bands optical/infrared photometric observations and an optical spectroscopic observation of GRS 1734−292. Then they found the optical and infrared counter part of NVSS J173728−290802, and identified it to be a Seyfert 1 galaxy with redshift $z = 0.0214 \pm 0.0005$. Combining the radio/optical/infrared/X-ray results, they concluded that GRS 1734−292 is a Seyfert 1 galaxy with $z = 0.0214$, identical with NVSS J173728−290802.

One problem in the identification by Martí *et al.* (1998) is a discrepancy of hydrogen column density. Adding to the optical/infrared observations, Martí *et al.* (1998) carried out H I absorption experiment at 21 cm for this source. Combining H I absorption, Na D interstellar absorption at 5890 Å and the optical extinction estimated with Hα/Hβ, they adopted the optical extinction of $A_V = 6 \pm 1$ mag, or hydrogen column density of $N_{\rm H}$= $(1.0 \pm 0.2) \times 10^{22}$ H cm^{-2}. This value is, however, inconsistent with the X-ray absorption column density of $N_{\rm H}\sim$ 6×10^{22} H cm^{-2} estimated with ART-P (Pavlinsky *et al.* 1994).

2.2.7 SLX 1744−299/300

SLX 1744−299/300 were two sources with closely located with each other (offset $\sim 3'$) at ($l_{\rm II}$, $b_{\rm II}$)$\simeq$($-0.^\circ7$, $-0.^\circ9$). It was first discovered with Spartan 1 in 1985 by Kawai *et al.* (1988)[4]. Skinner *et al.* (1987) confirmed it with a Spacelab-2 observation, which was made six weeks after the Spartan 1 observation, and designated it SLX 1744−299. Both of Kawai *et al.* (1988) and Skinner *et al.* (1987) could not resolve two sources and regarded it as only one source.

Skinner *et al.* (1990) reanalyzed the Spacelab-2 data in detail, and found that the source consists of two sources, SLX 1744−299 and SLX 1744−300. The averaged persistent fluxes of the both sources were comparable of about 14 and 10 $\times 10^{-11}$ erg cm^{-2} s^{-1} in 2–10 keV band, respectively. They also found a burst from SLX 1744−300 with the peak flux of about 1.2×10^{8} erg cm^{-2} s^{-1} in 2–10 keV band. Pavlinsky *et al.* (1994) detected five type-I bursts from SLX 1744−299/300 complex with *Granat*/ART-P observations. One of the bursts was quite big with the 4–17 keV luminosity of 1.9×10^{38} erg s^{-1} for 8.5 kpc distance. Then that burst location was well determined and identified to be SLX 1744−299 origin. They also noted that this burst was characterized with unusually long exponential decay time of 43 sec.

---

[4] They designated it SP 1744.2−2959.

Predehl & Kulkarni (1995) with *ROSAT* and Sidoli *et al.* (1999) with *SAX* resolved two sources with imaging detectors, hence confirmed the existence of two sources, *i.e.*, confirmed that both of them are probably persistent sources. Sidoli *et al.* (1999) also found that the (unabsorbed) fluxes of SLX 1744−299 and SLX 1744−300 to be 2 and 1.2×10^{-10} erg cm^{-2} s^{-1} in 2–10 keV band, and that SLX 1744−299 was significantly brighter than SLX 1744−300.

The reported column densities of SLX 1744−299 and SLX 1744−300 are somewhat different. Skinner *et al.* (1990) reported that $N_{\rm H}\gtrsim 10^{22}$ H cm^{-2} are required for both sources. Predehl & Kulkarni (1995) reported $N_{\rm H}$ to be 4.2 ± 0.3 and $6.8 \pm 0.3\ \times10^{22}$ H cm^{-2} for SLX 1744−299 and SLX 1744−300, respectively. On the other hand, Sidoli *et al.* (1999) reported $N_{\rm H}$ of each source to be nearly the same, $(4\text{–}5.5)\times10^{22}$ H cm^{-2}. The difference might mean the column density variability. However, we should be conservative because the estimation of spectral parameters for these sources might have large systematic uncertainty due to, for example, lack of imaging capability for Spacelab-2 observation, or lack of broad band spectroscopy for *ROSAT* observation.

2.2.8 GX 3+1

GX 3+1 (4U 1744−26) was discovered in the early X-ray observations with rockets (e.g., Bradt *et al.* 1968). It is one of the LMXBs with the brightest persistent emission, located in the Galactic Center region. The average X-ray flux has been 0.2–0.5 Crab (see Asai *et al.* (1993) and references therein), which is converted to the luminosity of $\sim 10^{38}$erg s^{-1} on the assumption of the distance of 8.5 kpc.

It shows frequent type-I bursts (first detected with *Hakucho* by Makishima *et al.* (1983)), hence has been regarded as a LMXB. With comprehensive analysis of *EXOSAT* and *Ginga* data, it is classified as an atoll source (Lewin *et al.* 1987; Schulz *et al.* 1989; Makishima *et al.* 1989). The burst peak luminosity reaches $L_{\rm X}\sim (3\text{–}6)\times10^{38}$erg s^{-1}, *i.e.*, larger than Eddington limit, for the assumed distance of 8 kpc (Asai *et al.* 1993). The column density toward this source is estimated at $(1\text{–}2)\times10^{22}$ H cm^{-2} with the *Ginga* data (Makishima *et al.* 1989), which is consistent with the fact that no optical counter part was found. All these facts imply that this source is near or slightly in front of the Galactic Center.

2.2.9 SLX 1735−269

SLX 1735−269 was discovered with Spacelab-2 in 1985 by Skinner *et al.* (1987). Later observations with *Granat*/ART-P (Pavlinsky *et al.* 1992, 1994) and with *Mir-Kvant*/TTM (In't Zand 1992) confirmed the 2–10 keV emission from this source. The accurate position is given from *Einstein* source, 1ES 1735−26.9 (Elvis *et al.* 1992), as well as the *ROSAT* source.

A peculiar signature for this source is the persistent hard X-ray emission, extending up to above 100 keV, reported by Goldwurm *et al.* (1994, 1996) with *Granat*/SIGMA observations. Although such strong X-ray emission in the hard X-ray band above 35 keV is unusual for a LMXB, they noted that the spectrum is still softer than that of galactic black hole candidates.

David *et al.* (1997) analyzed the *ASCA* data taken in 1995, and found that the spectrum is well represented with an absorbed power law function, photon index Γ of 2.12–2.18 and hydrogen column density $N_{\rm H}$ of 1.40–1.55. No other spectral feature, such as a line, was found. They noted that the index is flatter than that of usual galactic black hole candidates. Although they tried pulsation searches with good statistics data with *ASCA*, they found no periodicity from this source.

Bazzano *et al.* (1997a, 1997b) and Cocchi *et al.* (1999a) found a large burst from this source with the peak flux of about 0.9 Crab in *SAX*/WFC observation for 1.8–30 keV energy range. It strongly suggests that this source is a LMXB. The power law tail extending up to 100 keV has been believed to be the strong criterion for black hole candidates. However, hard X-ray emission was recently detected from about 10 of neutron star binaries (or bursts have been detected from X-ray sources with hard X-ray emission above 35 keV) (see Barret *et al.* 1996 and references therein)[5]. The *SAX*/WFC discovery placed this source on another LMXB with hard X-ray emission.

Wijnands & van der Klis (1999) recently reported the *XTE* observational result. They found the power spectrum to be very similar to that of other LMXBs and black hole candidates. However, they found an unusual nature; the break frequency increases when the inferred mass accretion rate decreases. They noted that the same behavior is only observed in the accretion-powered millisecond X-ray pulsar SAX J1808.4−3658, although no periodicity from this SLX 1735−269 was found.

---

[5] We briefly mention on the hard X-ray emission from a burster A 1742−294 in Section 2.2.3.

2.2.10 GRS 1737−31

GRS 1737−31 was discovered with *Granat*/SIGMA as a hard X-ray transient on 1997 March 14 (Sunyaev *et al.* 1997). It was also detected with the follow-up observations with *SAX*/WFC (Heise 1997) and with *ASCA* (Ueda *et al.* 1997), then the position was refined. Marshall & Smith (1997) reanalyzed the *XTE*/PCA scan data on 1997 February 17–20, and found that the source was already detected in the data. The X-ray luminosity for 2–150 keV in the bright phase was 1.9×10^{37} erg s^{-1} for the assumed distance of 8.5 kpc.

Cui *et al.* (1997) found that GRS 1737−31 showed violent variability on time scales down to a few seconds, using the*XTE*/PCA data taken on 1997 March 21 and 28, and April 2. The detected rapid flares in the light curves and the power-density spectrum of GRS 1737−31 were found to resemble the nature of black hole candidates in the hard (or low) state. The spectrum was found to be characterized by a simple power law with a photon index of about 1.7 over a broad energy range 2–200 keV (Cui *et al.* 1997), which is also similar to that of Cyg X-1 in the hard state. Thus, Cui *et al.* (1997) concluded that GRS 1737−31 is a likely black hole candidate. However, GRS 1737−31 showed no soft component, hence it was not in the soft state even during the outburst, unlike most transient black hole candidates (Cui *et al.* 1997).

2.2.11 KS 1741−293

KS 1741−293 was discovered with *Mir/Kvant* as an X-ray transient in 1989 (in't Zand *et al.* 1991). In't Zand *et al.* (1991) also detected two type-I X-ray bursts; hence it is probably a LMXB. The calculated distance from the burst peaks are consistent with that of the Galactic Center. Since then, it has been never detected with other satellites (e.g., Pavlinsky *et al.* 1994, Lu *et al.* 1996), until *SAX*/WFC detection with 31 mCrab in 2–25 keV band on 1998 March 10–12 (in't Zand *et al.* 1998).

Optical/infrared/radio identification has not been succeeded, yet, although some sources are located in the X-ray positional error circle (Cherepashchuk *et al.* 1994).

2.2.12 GRS 1741.9−2853

GRS 1741.9−2853 was discovered with *Granat*/ART-P as an X-ray transient in 1990 spring (Mandrou 1990; Sunyaev 1990; Sunyaev *et al.* 1991b), with the flux of

9.6±0.7 mCrab for 4–20 keV, corresponding to about 1.6×10^{36} erg cm^{-2} s^{-1} for the assumed distance to the Galactic Center. During the *Granat* observations, it was also marginally detected ($>3.5\sigma$) with SIGMA in the 40–100 keV band (Churazov *et al.* 1993c, Vargas *et al.* 1997). However, in ART-P and SIGMA observations 4 months later, it was not detected, with 3σ upper limit of 1.2 mCrab for 4–20 keV band (Pavlinsky *et al.* 1994). Since then, it has not been detected with *Granat* and other satellites until the observation with *SAX*/WFC.

Cocchi *et al.* (1999b) detected three type-I bursts from this source with *SAX*/WFC in 1996 August and fall. Hence this source is very likely to be a low mass X-ray binary containing a neutron star. The burst peak (bolometric, unabsorbed) flux was $(3.26 \pm 0.26) \times 10^{-8}$ erg cm^{-2} s^{-1}; the distance was accordingly calculated to be 7.2±0.6 kpc. Cocchi *et al.* (1999b) also found that the column density was significantly different between the first or the third burst and the second burst. The former had a column density of $(10 \pm 10) \times 10^{22}$ H cm^{-2}, whereas the latter, $(36^{+21}_{-13}) \times 10^{22}$ H cm^{-2}. Note that the column density in the persistent phase was not reported.

2.2.13 XTE J1739−302

XTE J1739−302 was discovered with *XTE* as a transient at (17^{h} 39^{m} 00^{s}, -30° $16'.2$ (J2000)) on 1997 August 12 (Smith *et al.* 1997b, 1998a). Although it was the brightest source in the Galactic Center region while active ($\sim 3.0 \times 10^{-9}$ erg cm^{-2} s^{-1} from 2 to 25 keV), it was only observed on that day; it was not detected 9 days earlier or 2 days later. The 3 σ upper limit of the flux with *XTE* on August 3 and August 14 were 14% and 4% of the peak flux, respectively (Smith *et al.* 1998a). It also showed shorter time-scale variability; the flux, 2.55 hr before the flux peak on August 12, was only 56% of the peak flux (Smith *et al.* 1998a). On the other hand, no pulsation was found. Smith *et al.* (1998a) also noted that the *SAX*/WFC data on 1997 September 6 showed no detection.

The spectrum was found to be well described with a bremsstrahlung model with $kT = 12.4 \pm 0.3$ keV from 2 to 25 keV, whereas a power law function was rejected. The hydrogen column density was $N_{\mathrm{H}}=(4.9\text{–}6.4)\times10^{22}$ H cm^{-2} (Smith *et al.* 1998a).

These natures may possibly suggest that this source is a Be/NS binary; however, there is some counter evidence, the quite short duration (less than 11 days) and no detection of pulsation.

2.2.14 GRO J1744−28

GRO J1744−28 is one of the most peculiar X-ray objects, sometimes referred to as "the bursting X-ray pulsar". It was first detected with *CGRO*/BATSE as a bright hard X-ray transient (Fishman *et al.* 1995; Kouveliotou *et al.* 1996). Many bursts as well as the pulsation with frequency of 2.14 Hz were found (e.g., Finger *et al.* 1996), hence this is the first compact X-ray object showing both of bursts and pulsation. Lewin *et al.* (1996) remarked that the observed bursts were probably due to spasmodic release of gravitational potential energy (type II), just like those observed for the Rapid Burster, whereas other mechanism for the bursts were also proposed (Kouveliotou *et al.* 1996; Bildsten & Brown 1997).

Augusteijn *et al.* (1997) and Cole *et al.* (1997) found a variable counterpart from optical and near-infrared observations within *ROSAT* error circle; accordingly GRO J1744−28 may be a kind of LMXB. However, Hurley *et al.* (2000) gave a suspect for this identification from the recent precise position measurement with *Ulysses* and *CGRO*/BATSE.

Since then, GRO J1744−28 has been extensively studied with many instruments for wide energy range, radio to γ-ray. Detailed review for this source is beyond this thesis; they are found in, for example, Nishiuchi *et al.* (1999), Woods *et al.* (1999) and references therein. We here mention only the *ASCA* results on GRO J1744−28, reported by Nishiuchi *et al.* (1999).

With *ASCA*, Nishiuchi *et al.* (1999) observed the region around GRO J1744−28 three times: on 1995 September 19, 1996 February 26 and 1997 March 16. The 2–10 keV flux was found to be less than 10^{-12} erg cm^{-2} s^{-1}, 2.0 and 0.50 $\times 10^{-8}$ erg cm^{-2} s^{-1} in the three observations, respectively. They detected totally 29 type II bursts. Fig. 2.6 shows an example of the light curve that contains two bursts.

They found the burst fluence and the integrated flux deficiency in the subsequent dip show a good correlation; the burst fluence was approximately 1/2 to 1/4 of the flux deficiency. They interpreted the correlation to be because of the compensation of the burst luminosity by the following dip luminosity. It may suggest that the burst activity is not due to global increase of the mass supply from the companion, but to sudden increase of the infall matter that has been accumulated in a reservoir near the neutron star.

The spectrum was found to be approximated by an absorbed power law function with additional structure around 6–7 keV: the photon index $\Gamma \sim 1.2$ (in the first observation) or ~ 1.0 (in the second observation), hydrogen column density

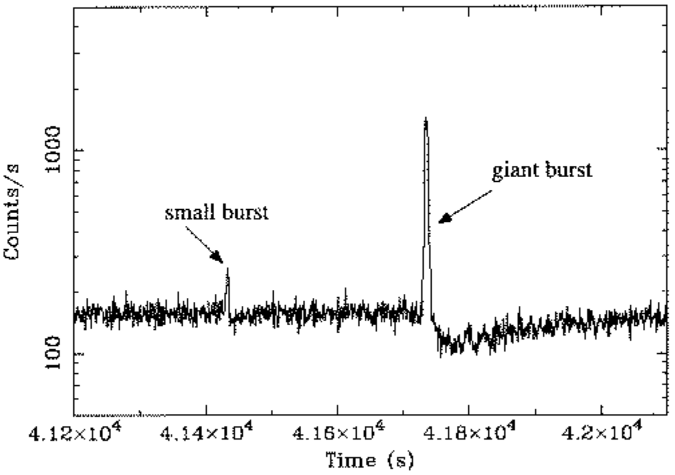

Figure 2.6: *ASCA* example of the light curve of GRO J1744−28 that contains both a giant and a small burst followed by an intensity dip in 1996 February observation. This figure is adopted from Nishiuchi *et al.* (1999).

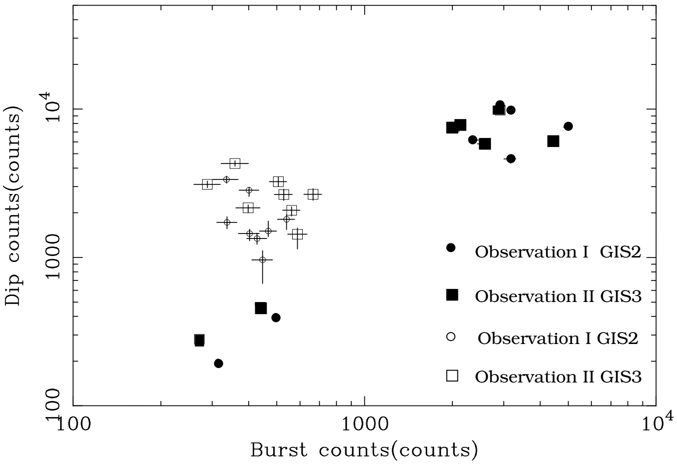

Figure 2.7: Correlation between the total burst counts and the flux deficiency in the subsequent dip from the *ASCA* GRO J1744−28 observations. This figure is adopted from Nishiuchi *et al.* (1999).

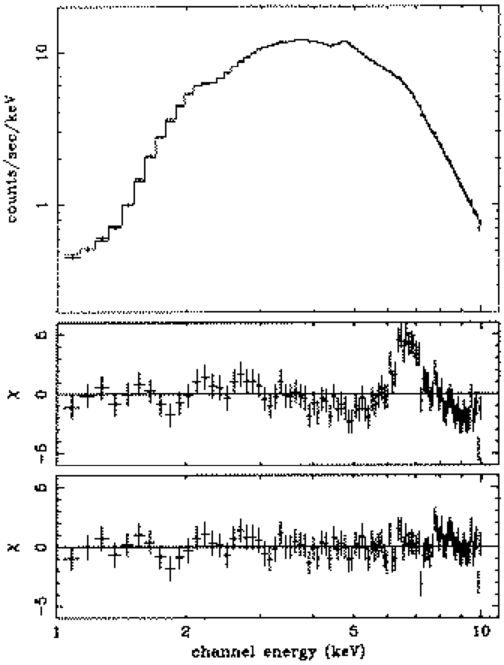

Figure 2.8: Energy spectrum of GRO J1744−28 in the first observation with the best fit model, adopted from Nishiuchi *et al.* (1999). The middle and the lower panels show the fit residuals with the model of an absorbed power law and of an absorbed power law plus a broad Gaussian line around 6.7 keV, respectively.

$N_{\rm H}$=(5–6)×10^{22} H $\rm cm^{-2}$, and a broad line (σ =600–800 eV) centered at 6.6–6.8 keV with equivalent width of 200–400 eV (Fig. 2.8). The absorption column density was constant, regardless of the observation date and the source status (persistent, burst, and dip). This fact implies that the observed column density corresponds to the interstellar absorption in front of the Galactic Center. Nishiuchi *et al.* (1999) also found that the spectrum of the pulsed component was harder than that of the non-pulsed component, which suggests the different emission region for the both of the components.

2.2.15 XTE J1748−288

XTE J1748−288 is one of the three galactic jet sources from which the motion near the speed of light ($> 0.9c$) was detected[6]. It was discovered with *XTE*/ASM and *CGRO*/BATSE on 1998 June 3 (Smith *et al.* 1998b; Harmon *et al.* 1998). The peak X-ray flux was about 600 mCrab (Strohmayer *et al.* 1998), then decayed with an e-folding time of ~20 days (The *XTE*/ASM team 1999).

---

[6] Other two are GRS 1915+105 and GRO J1655−40. CI Cam also showed the jet motion with a slower speed. For the galactic jet sources, see Fender *et al.* (1997).

The radio counter part was also detected with the VLA (Strohmayer *et al.* 1998). Rupen *et al.* (1998) discovered a one-sided radio jet moving with 20 mas day^{-1}, which corresponds to a velocity of $0.93c$ for the assumed distance of 8 kpc. The radio activity lasted 200 days. Around 1998 April 9, the expansion of the leading edge was found to slow to a rate of $\sim$5 mas day^{-1}, corresponding to $0.23c$ (Hjellming *et al.* 1998). They also found that the leading edge brightened dramatically.

With *ASCA*, the region around XTE J1748$-$288 was observed twice after the outburst, on 1998 September 6 and 26. Kotani *et al.* (2000) reported the preliminary result. We briefly summarize their results below.

The 2–6 keV flux in the two observations was 46 and 2.2 $\times 10^{-12}$ erg cm^{-2} s^{-1}, respectively. The flux of the first observation was found to be consistent with the extrapolation of the exponential decay with an e-folding time of 12–16 days since the outburst peak (Fig. 2.9). On the other hand the flux of the second observation was below the extrapolation by an order of magnitude. There might be a phase transition from the exponential decay phase to another phase, such as off state, in the period between the two *ASCA* observations.

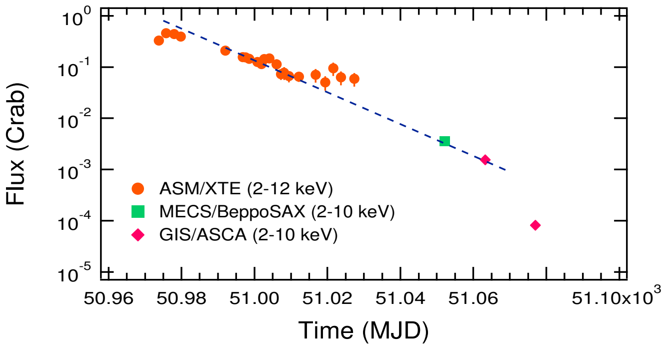

Figure 2.9: Long term light curve of XTE J1748$-$288. The data of *XTE*/ASM (The *XTE*/ASM team 1999), *SAX*/MECS (Sidoli *et al.* 1999) and *ASCA* are compiled. This figure is adopted from Kotani *et al.* (2000).

They found that the spectrum in each observation was well represented with an absorbed power law function of photon index $\Gamma \sim 2.6$–2.7, and hydrogen column density of 9×10^{22} and 6.1×10^{22} H cm^{-2} for the first and the second observation data, respectively. They also found the presence of two lines at 5.85 and 6.76 keV with uncertainty of about 0.15 keV. These features are possibly originated from a jet or jets.

2.2.16 GRO J1750−27

GRO J1750−27 was discovered as a transient X-ray pulsar with the period of 4.45 seconds on 1995 July 29 with *CGRO*/BATSE (Scott *et al.* 1997). A relatively faint outburst (<30 mCrab at peak) lasting at least 60 days was observed during which the spin-up rate peaked at 38 pHz s^{-1} and was correlated with the pulsed intensity. They also measured the orbit period of 29.8 days from the pulse arrival time analysis. On the other hand, no optical/infrared counterpart has not been reported, yet, probably due to large extinction toward this source. From all the X-ray natures of GRO J1750−27, Scott *et al.* (1997) concluded that this source is likely to be a Be/X-ray binary system.

Dotani *et al.* (1995) reported the preliminary results with the *ASCA* follow-up observation; they determined the precise position with the accuracy of $2'$ and confirmed the pulse period. The spectrum was found to be approximated by a power law with photon index of 0.8 and the column density of 2×10^{22} H cm^{-2}.

2.2.17 Sgr B2 — X-ray reflection nebula

One of the most remarkable results with *ASCA* on the Galactic Center region is the discovery of a new category source which emits almost only 6.4 keV line, corresponding to Kα line from neutral iron (Koyama *et al.* 1996; Maeda 1998; Murakami *et al.* 1999, 2000a, 2000b). This 6.4 keV line is emitted with photo-electric process from the cold objects that are illuminated from external (or internal) strong X-ray sources. The good coincidence of the X-ray brightest position with radio giant molecular cloud, Sgr B2, strongly supports the hypothesis. Hence Murakami *et al.* (2000a) named it an "X-ray reflection nebula".

Murakami *et al.* (2000a) tried the quantitative study for this scenario. Fig. 2.10 shows the X-ray spectrum of Sgr B2 cloud. The strong 6.4 keV line as well as the 7.1 keV edge structure are clearly seen. The detection of the deep edge again strongly supports the X-ray reflection scenario; the hypothesis that this 6.4 keV line is emitted from the clouds excited by high energy particles, is excluded.

The X-ray image of 6.4-keV line (Fig. 2.11(a)) was found to be extended; and moreover, it shows the significant shift by $1\overset{'}{.}2$ of the X-ray peak from the molecular cloud peak toward the Galactic Center direction (Koyama *et al.* 1996; Murakami *et al.* 2000a). Since Sgr B2 cloud is so dense, the central region of Sgr B2 cloud may be optically thick even in the hard X-ray band. Therefore the apparent positional shift can be naturally explained if the illuminating source is located out of Sgr B2

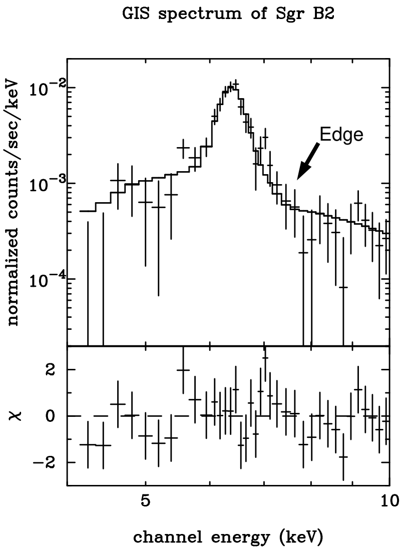

Figure 2.10: Spectrum of Sgr B2 with the best-fit model. See text for the description of the model. This figure is adopted from Murakami *et al.* (2000a).

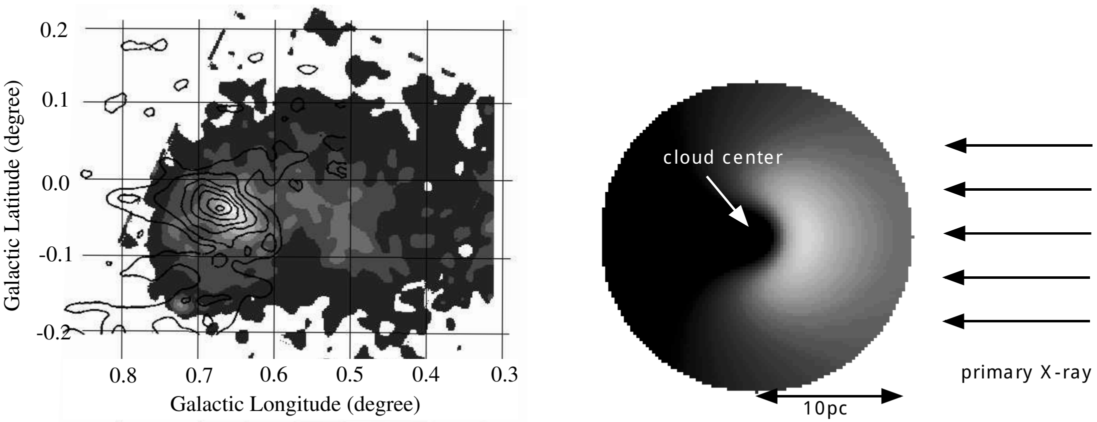

(a) Observed iron line image.

(b) Simulated iron line image.

Figure 2.11: (a) Observed iron line image of Sgr B2 cloud taken with *ASCA*. The radio CH_3CN line contours (Bally et al. 1988) are superposed. Note that 0.1 degree corresponds to 15 pc for 8.5 kpc distance. (b) Simulated iron line image of Sgr B2 cloud, based on the "X-ray reflection nebula" scenario. See text for the description of the model. These figures are adopted from Murakami *et al.* (2000a).

cloud in the direction of the Galactic Center (Koyama *et al.* 1996; Murakami *et al.* 2000a).

Then, using the radio molecular cloud profile, Murakami *et al.* (1999, 2000a, 2000b) conducted the numerical simulation to reproduce the X-ray image and the spectrum, based on the above hypothesis (the X-ray reflection nebula model), and fitted the observed data with the simulated ones. Consequently they found that the model well reproduces the observed image and spectrum (Image — Fig. 2.11(b); Spectrum — Fig. 2.10). The model requires the higher abundances by at least a few factors than the solar abundances for both of iron and oxygen (or light elements), and in addition, smaller total mass of Sgr B2 than the original radio estimation by Lis & Goldsmith (1989). Fig. 2.12 shows the confidence contours to reproduce the observed data. They discussed that these results are not so unusual, taking the Galactic Center environment into account (Murakami *et al.* 1999, 2000a, 2000b).

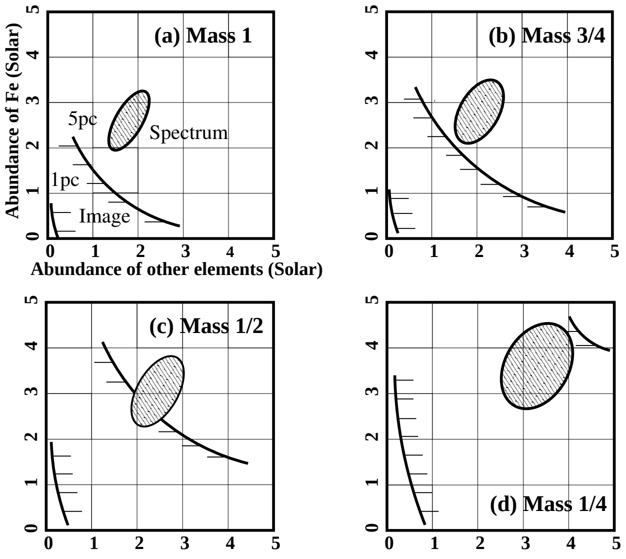

Figure 2.12: Allowed region for the abundances and the mass of Sgr B2 to reproduce the observed data with the simulated image, based on the "X-ray reflection nebula scenario". See text for the description of the model. This figure is adopted from Murakami *et al.* (2000a).

One serious problem unsolved for this X-ray reflection nebula is lack of illuminating sources, which are sufficiently bright to account for the luminosity of 6.4 keV line from Sgr B2 cloud. Even the total luminosity of known persistent X-ray sources is much smaller than the required luminosity by an order. Hence Koyama *et al.* (1996) and Murakami *et al.* (2000a) proposed that the illuminating source is past activity of the Galactic Center Sgr A*, based on the direction of the illuminating source and some other indirect evidence. Their suggestion is that Sgr A* was luminous as 10^{39} erg s^{-1} about 300 years ago, which is the light traveling time between Sgr B2 cloud and Sgr A*. Extending this conjecture, Sunyaev & Churazov (1998) further discussed future possibility to study the history of the past activity of Sgr A* by detailed imaging of the X-ray reflection nebula Sgr B2.

2.2.18 SNR G359.0−0.9

Supernova remnant (SNR) G359.0−0.9 was discovered with a 10 GHz radio observation by Sofue *et al.* (1984), and then confirmed with a 2.7 GHz observation by Reich *et al.* (1990) and with a 848 MHz observation (Gray 1994). It shows an incomplete shell structure. X-ray emission from this source was also detected with *Einstein*, where no spectral information was given (Leahy 1989). The X-ray emission is possibly associated with the radio shell, although the detailed study has not been made; the *Einstein* observation covered only the part of the SNR.

Bamba *et al.* (2000) performed detailed analysis for this source with *ASCA*. We briefly summarize the result, below. Fig. 2.13 shows the *ASCA* X-ray contour map superposed on the radio image (Gray 1994). We detected the diffuse X-ray emission below 3 keV that is apparently associated with the radio shell. The X-ray emitting region is consistent with the *Einstein* result by Leahy (1989).

The spectrum exhibits two clear lines around 1.36 keV and 1.86 keV (Fig. 2.14), which corresponds to K-α lines from helium-like magnesium (He-like Mg) and He-like silicon (Si), respectively. Hence the spectrum is definitely a thin thermal origin. However, a thin thermal plasma model with the solar abundance materials is rejected; they found the plasma has abundance anomaly, iron or magnesium abundance to the corresponding solar ratio of 1.3–2.2 or less than 0.5, respectively[7]. The flux is 2.4×10^{-12} erg cm^{-2} s^{-1} in 0.7–10 keV band[8]. The best-fit temperature and column density are kT =0.3–0.5 keV, $N_{\rm H}$=(1.1–2.0)$\times10^{22}$ H cm^{-2}, respectively.

From the column density to G359.0−0.9, Bamba *et al.* (2000) estimated the distance to be 6 kpc, hence this SNR is probably not located in the Galactic Center region, but merely a foreground SNR. This derived distance is consistent with the distance estimated with Σ-D relation (4.8 kpc: Sofue *et al.* 1984).

Solving the Sedov equation, they then derived the total explosion energy, the

---

[7] Due to the limited statistics, we cannot well determine the abundances of Mg and Fe at the same time.

[8] Most of the flux is limited below 3 keV (Fig. 2.14).

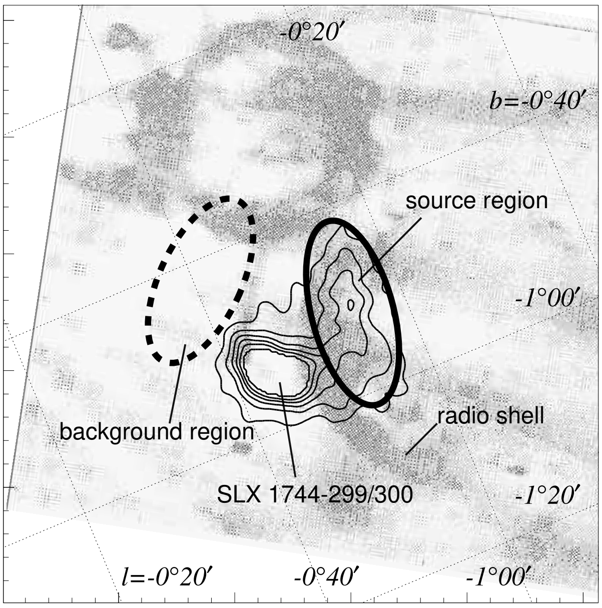
-0°20′
b=-0°40′
source region
-1°00′
radio shell
background region
SLX 1744-299/300
-1°20′
l=-0°20′
-0°40′
-1°00′

Figure 2.13: GIS contour map with 0.7–1.5 keV band superposed on the 848 MHz radio image (Gray 1994). Contour levels are linearly spaced and are saturated for SLX 1744−299/300. Source and background regions for spectral analyses are shown with solid and dotted lines, respectively. This figure is adopted from Bamba *et al.* (2000).

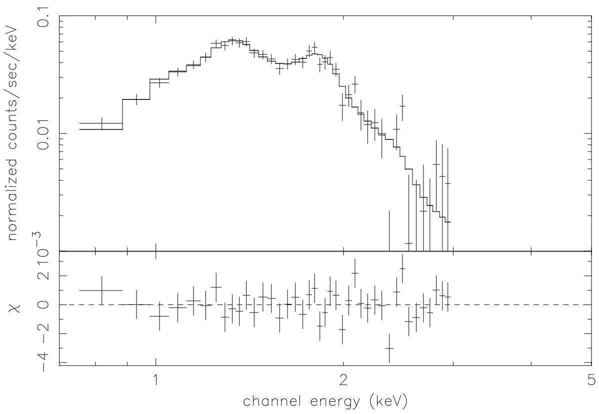

Figure 2.14: The GIS2+3 spectrum of G359.0−0.9 with the best-fit model. The fitting model is a thin thermal plasma, of which the abundances are fixed to be the same as the solar ratios except for that of magnesium. This figure is adopted from Bamba *et al.* (2000).

density of the interstellar matter (ISM), and the age to be 1.2×10^{51}erg, 0.5 cm^{-3}, and $1.8{\times}10^4$ years, respectively. The total mass of the X-ray emitting shell is about 40 $\mathrm{M}_\odot$; most of them are attributable to the interstellar matter. Hence the suggested abundance anomaly is probably that of the interstellar matter near G359.0−0.9, *i.e.*, the ISM near G359.0−0.9 is either over abundant in Mg or under abundant in Fe.

2.2.19 SNR G359.1−0.5

Supernova remnant (SNR) G359.1−0.5 was discovered with a 10 GHz radio observation by Sofue *et al.* (1984), and then confirmed with a 848 MHz observation (Gray 1994). It shows apparent shell structure. X-ray emission from this source was also detected with *ROSAT* (Egger & Sun 1998).. Yokogawa *et al.* (1999) and Bamba *et al.* (2000) performed detailed analysis for this source with *ASCA*. We briefly summarize the results, below.

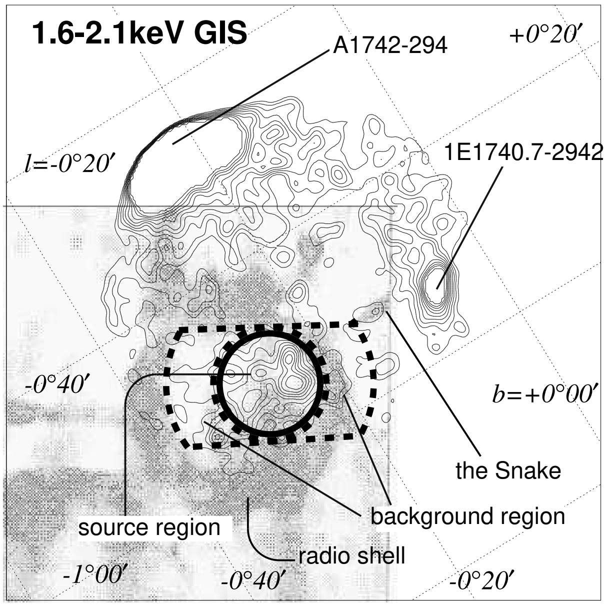

Figure 2.15: GIS contour map with 1.6–2.1 keV band superposed on the 848 MHz radio image (Gray 1994). Contour levels are linearly spaced and are saturated for A 1742−294 and 1E 1740.7−2942. Source and background regions for spectral analyses are shown with solid and dotted lines, respectively. This figure is adopted from Bamba *et al.* (2000).

Fig. 2.15 shows the *ASCA* GIS image of G359.1−0.5 with 1.6–2.1 keV band. They detected center-filled X-rays from this source, whereas the radio image shows a clear shell-like structure (e.g., Uchida *et al.* 1992).

The spectrum is found to have emission lines from highly ionized ion (Fig. 2.16),

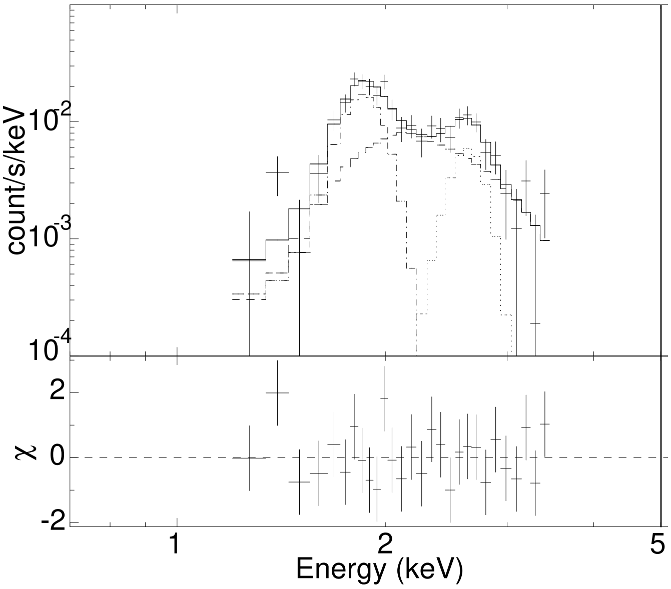

Figure 2.16: The background-subtracted GIS spectrum. We also show the best-fit model where we fit the spectrum with the model of the thermal bremsstrahlung and two narrow Gaussians with interstellar absorption. This figure is adopted from Yokogawa *et al.* (1999).

hence the X-rays come from thin thermal plasma. The most distinct two lines are Kα lines from helium-like silicon and hydrogen-like sulfur. They imply that the plasma has multi-temperature structure, where one component should be extremely sulfur rich: the abundance of larger than ~40 of solar. The absorption column density is estimated at $N_{\rm H}\sim 8\times 10^{22}$H cm^{-2}. It suggests that G359.1−0.5 is located at near or farther than the Galactic Center, which is consistent with the radio observations (Uchida *et al.* 1992)[9].

---

[9] Note that it may be slightly larger than the distance estimated with $\Sigma - D$ relation (6.2 kpc: Sofue *et al.* 1984).

Chapter 3

Instrumentation

The data that we analyze in this thesis were taken with the *ASCA* satellite. In this chapter, we give the brief overview of *ASCA* and the onboard detectors.

3.1 The ASCA satellite

3.1.1 Overview

ASCA is the fourth japanese astronomical X-ray satellite, which was launched into orbit on 1993 February 20 (Tanaka *et al.* 1994). The orbital heights at perigee and apogee are about 520 km and 620 km, respectively, whereas the inclination is $31.^\circ1$. The orbital period is approximately 96 minutes.

ASCA is equipped with two sets of the Gas Imaging Spectrometers (GISs) and the Solid-state Imaging Spectrometers (SISs) at the foci of four identical thin-foil X-ray telescopes (XRTs). All the XRTs are mounted in the same direction of the sky. Fig. 3.1 shows the configuration of XRTs and the detectors aboard *ASCA*. With these instruments, *ASCA* opened the X-ray sky image above 2 keV for the first time, and covers a wide energy range from 0.5 to 10 keV.

3.1.2 Attitude control system

The satellite attitude is controlled with four reaction wheels (RW) and three-axis magnetic torquers (MTQ). As an attitude sensor, *ASCA* has five inertial reference units (IRUs), two star trackers (STTs; optical CCD camera), one non-spinning solar aspect sensor (NSAS), one spinning solar aspect sensor (SSAS), and 3-axis geomagnetic aspect sensors (GAS). IRUs monitor the relative change of the attitude, whereas STTs are used to determine the absolute attitude of the satellite.

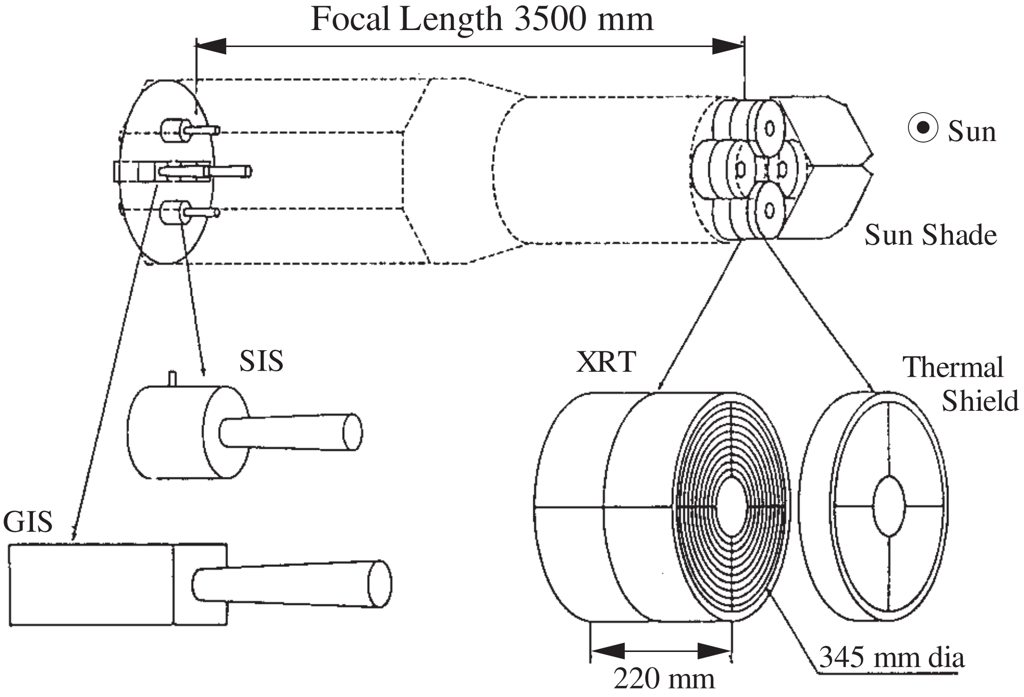

Figure 3.1: Configuration of XRTs and the detectors aboard *ASCA*.

The stability of the attitude is normally better than $10''$, whereas the absolute pointing accuracy is $\simeq 40''$ (Gotthelf 1996), except just after maneuver.

3.1.3 Data transfer

The telemetry data with *ASCA* are stored in the on board Bubble Data Recorder (BDR), except when the satellite can directly contact the ground station. The data acquisition rate is 32, 4, 1 kbit/sec for the three data bit-rates: high, medium, and low bit-rates, respectively. Since the total capacity of BDR is limited, we choose the best bit-rate according to the observation condition and the scientific objective. The stored data are transmitted to several grand stations about ten times a day; the main ground station is Kagoshima Space Center (KSC).

3.2 XRT (X-Ray Telescope)

The *ASCA* telescopes are configured according to the Wolter type-1 system. The four X-ray telescopes aboard *ASCA* are identical. The diameter and a focal length are 345 mm and 3.5 m, respectively. On the focal plane, 1 mm corresponds to 0.9822 arcmin. Each of XRTs consists of four identical quarter mirrors, called quadrants.

A number of thin-foils (120 foils) are nested for each quadrant to achieve large effective area in the hard X-ray band.

The effective area of mirrors is dependent on photon energy and incident angle[1] (Fig. 3.2). Because the XRTs consists of 4 parts (quadrants), a point source image (Point Spread Function: PSF) makes a so-called 4-leaves pattern, as given in Fig. 3.3. Although the PSF has large outskirts, we can nevertheless determine the relative source position accurately by less than 20″ at best, using the sharp peak of the PSF.

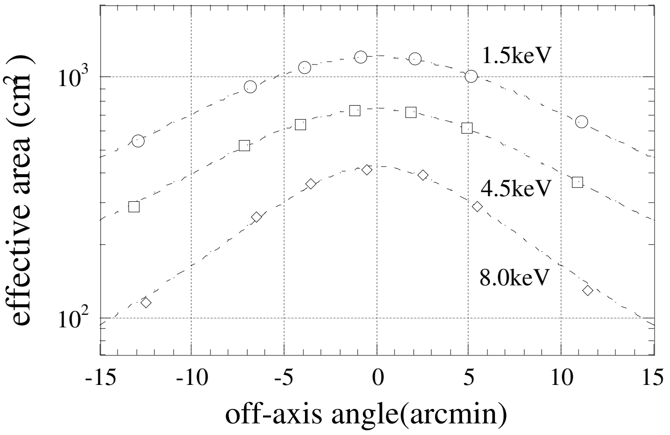

Figure 3.2: Energy and position dependence of *ASCA* XRT effective area.

Some of X-ray photons from out of the field of view (FOV) reach the focal plane through incorrect paths (Fig. 3.4). Those photons are called stray light. The intensity of stray light depends on the spectral shape of the source, as well as the source intensity and structure, because softer photons are more easily reflected with large angle than harder photons.

The stray light does not focus on the focal plane as the usual image, but produces a diffuse image; for example, the stray light from a point source out of FOV makes a shell-like structure depending on the source offset distance and the angle. Fig. 3.5 shows the observed stray light structures on the GIS detector, where the stray light source is Crab. The stray light from largely extended sources like the cosmic X-ray background, on the other hand, produces no distinct structure, but smooth extended structure over the focal plane, because of the large solid angles.

The influence of the stray light is sometimes not negligible. For the cosmic X-ray background, about the half of the detected photons at the focal plane are originated from the stray light, because they are integrated over large solid angles.

---

[1] This dependence of effective area on incident angle is called vignetting.

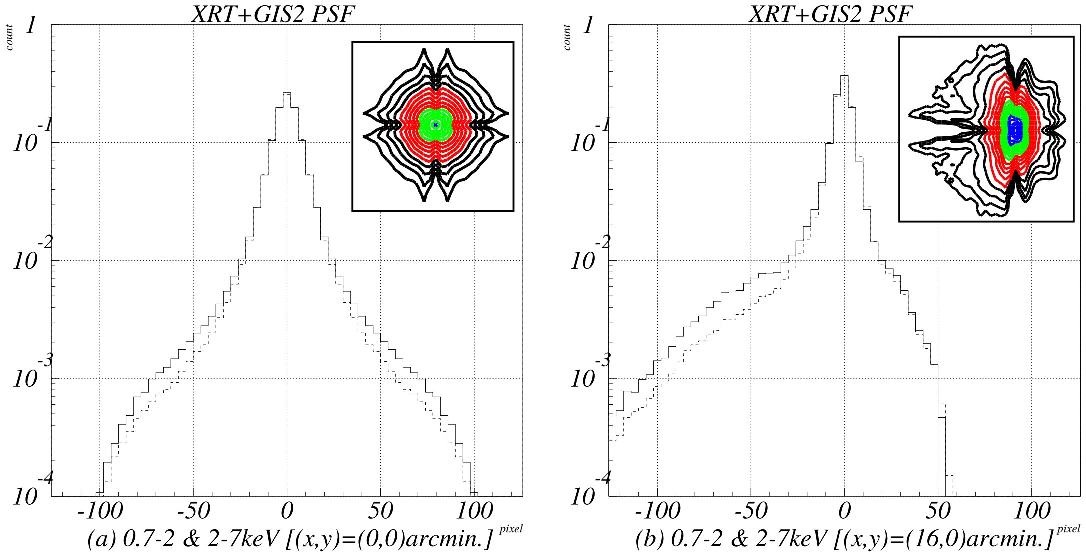

(a) 0.7-2 & 2-7keV [(x,y)=(0,0)arcmin.]

(b) 0.7-2 & 2-7keV [(x,y)=(16,0)arcmin.]

Figure 3.3: Images and the projected profiles of Point Spread Function (PSF) with XRT+GIS. The unit of horizontal axis is GIS channel (1 ch = 0.25 mm $\sim$ $0'\!.25$). Scattered and solid lines represent that with 0.7–2 keV and 2–7 keV, respectively. (a) PSF at the optical axis, (b) PSF with offset by $16'$ from the optical axis.

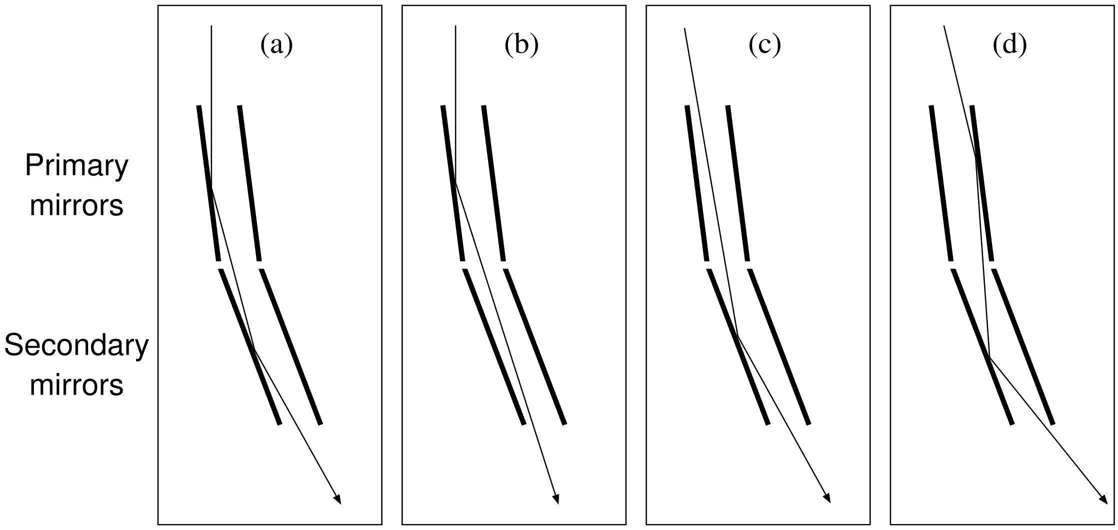

Figure 3.4: Schematic views for incorrect light paths with the stray light photons. This figure is adopted from Ishisaki (1996).

If there is an extremely bright point source by offset of 0.°5–2° from the center of FOV, the stray light from the source dominates the image at the focal plane. The *ASCA*/XRT team has developed the ray tracing method to reproduce the stray light structure and compared them with the observation. Consequently, the shape of the stray light is understood with the accuracy of about 20% except some cases[2] (Kunieda *et al.* 1995). However, it is quite difficult to guess where and what the source that makes the stray light is, from only observed focal plane image; accordingly it is quite difficult to subtract the stray light structure if we do not know the nature of stray light sources.

Details for XRTs are found in Serlemitsos *et al.* (1995).

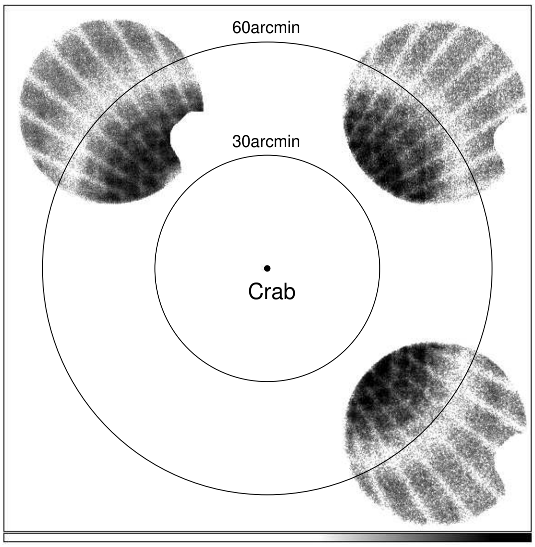

Figure 3.5: Observed stray light structures due to Crab taken with GIS. This figure is adopted from Ishisaki (1996).

3.3 GIS (Gas Imaging Spectrometer)

The Gas Imaging Spectrometer (GIS) is an imaging gas scintillation proportional counter (Ohashi *et al.* 1996; Makishima *et al.* 1996; Ishisaki 1996). *ASCA* has two GISs called GIS2 and GIS3, which are operated in parallel. Fig. 3.6 shows the schematic diagram of the principle of photon detection with GIS. The strong points of GIS, when we compare it with SIS, are a wide field of view with radius of ∼25 mm ($\sim 25'$), good time resolution, high detection efficiency in high energy band, and a little degradation for years in orbit.

---

[2] In some conditions with a certain azimuthal angle and offset, the simulation still cannot

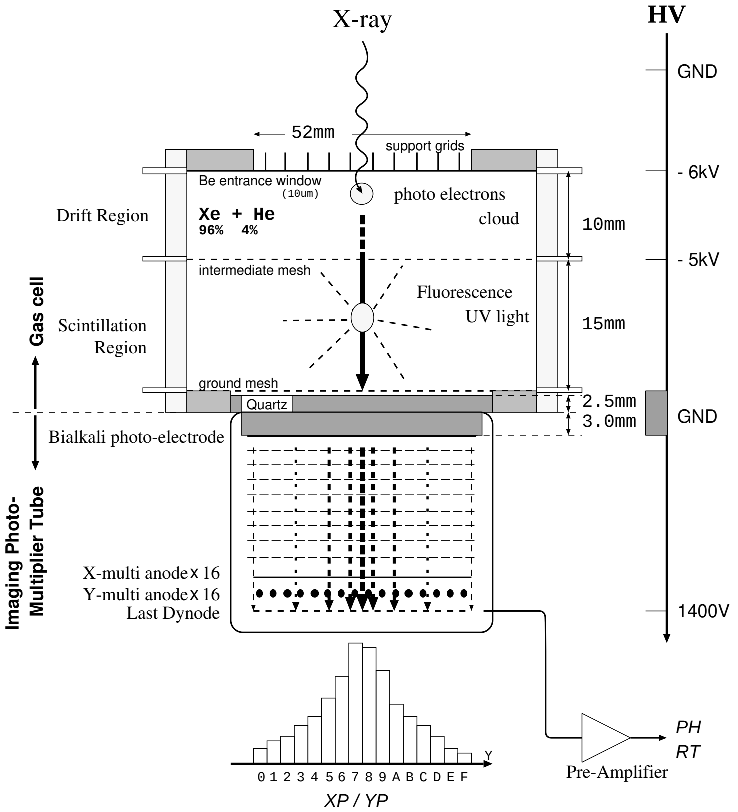
X-ray
HV
GND
52mm
support grids
Be entrance window
(10um)
photo electrons
cloud
Drift Region
Xe + He
96% 4%
10mm
- 6kV
- 5kV
intermediate mesh
Fluorescence
UV light
Gas cell
Scintillation
Region
15mm
ground mesh
Quartz
2.5mm
3.0mm
GND
Bialkali photo-electrode
Imaging Photo-
Multiplier Tube
X-multi anode x 16
Y-multi anode x 16
Last Dynode
1400V
PH
RT
Pre-Amplifier
Y
0 1 2 3 4 5 6 7 8 9 A B C D E F
XP / YP

Figure 3.6: Schematic diagram of the principle of the GIS detector.

GIS has sensitivity from 0.7 to 15 keV, whereas the nominal energy range is actually limited below 10 keV, due to lack of sensitivity with XRT above 10 keV. Although GIS has three observational modes: PH, PCAL and MPC modes, we here concentrate on the performance in only the PH mode because all of the observations that we use in this thesis were operated with PH mode.

GIS achieves low background count rate with effective discriminations of non-X-ray events with pulse height, rise time, spread of light, and the position information. Most of non-X-ray events are rejected in orbit, whereas some of them are rejected in the data analysis at ground[3]. Fig. 3.7 shows the GIS spectra of day earth[4], blank sky[5] and night earth[6]. The night earth data (image and spectrum) are thought to represent the non-X-ray events.

---

reproduce a part of the actual stray light structure.

[3] Sometimes the important data (especially, rise time information) to reject the non-X-ray events are not included in the telemetry data, depending of the selected GIS bit assignment; in that case, the rejection of non-X-ray events at ground is not so effective.

[4] The earth surface which is illuminated by the sun (at day).

[5] The high galactic latitude fields where no bright X-ray sources are seen.

[6] The same as day earth, but at night.

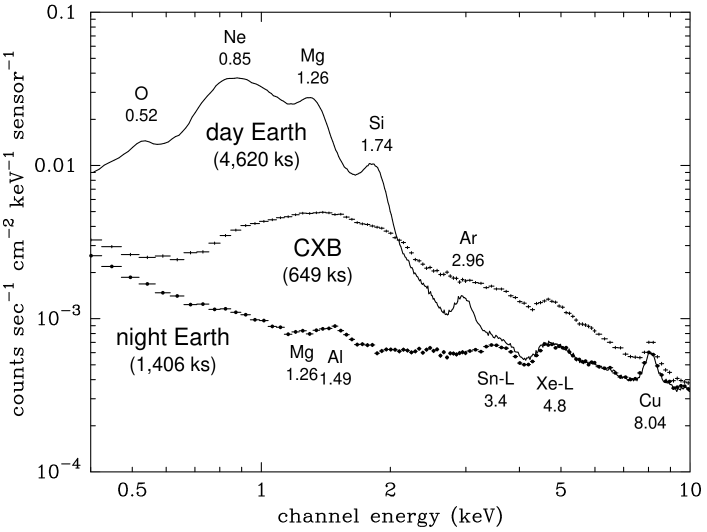

Figure 3.7: GIS spectra of day earth, blank sky and night earth. This figure is adopted from Ishisaki (1996).

The long-term monitoring of the night earth data shows that the GIS non-X-ray background (NXB) has been gradually increasing since the launch, whereas the spectral shape has not changed significantly (Ishisaki 1996; Ishisaki *et al.* 1997; see also Fig. 3.8). The reason is still not clear, although it is generally thought to be caused by a gradual build-up of long-term decay radioisotopes.

The bit assignment for the GIS telemetry data represents the quantity of information on (sensor-ID), pulse height, X-ray detected position for X- and Y-axes, rise time information, spread of light, and time stamp for each event. The standard bit assignment, with which most of the observations are done, are (1-)10-8-8-5-0-0 for the above items, respectively; it means that pulse height information is expressed with 10 bits, namely 1024ch, and the X-axis information is expressed with 8 bits, namely 256ch, for example. For the standard bit assignment, 1 ch for X- or Y-axis corresponds to 0.250 mm, and 1 ch for pulse height corresponds to ~0.012 keV.

The time resolution of GIS depends on bit-rate and GIS bit assignment that the observer selects. In high bit-rate, the best time resolution is achieved, whereas in medium and low bit-rates, the resolution is worse by a factor of 8 and 32, respectively, than that in high bit-rate. For standard bit assignment, the time resolution in high bit-rate is 65 msec. We can increase the time resolution by changing the bit assignment, sacrificing other information, such as, rise time information.

The energy gain of GIS is the function of the temperature, the detected position, and the time from launch, etc. Each of GIS sensor (GIS2 and GIS3) is equipped with the isotope ^{55}Fe at the edge of the sensor; we can refer the peak of the spectrum

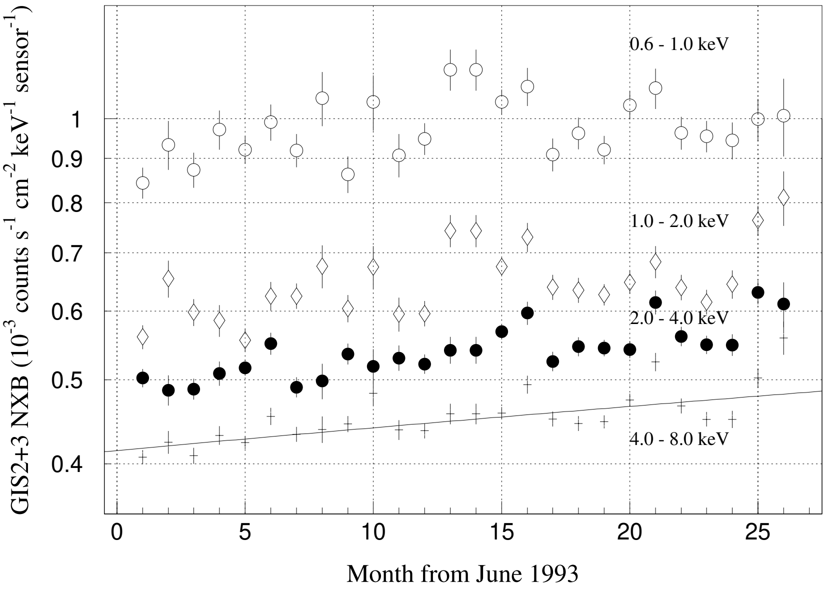

Figure 3.8: Change of GIS NXB fluxes with several energy bands since the launch. NXB shows gradual increase since the launch. This figure is adopted from Ishisaki (1996).

of the calibration isotope to correct the gain. Thus we correct the raw gain to the linear scale one.

Details for GIS are found in Ohashi *et al.* (1996), Makishima *et al.* (1996) and Ishisaki (1996).

3.4 SIS (Solid-state Imaging Spectrometer)

The Solid-state Imaging Spectrometer (SIS) is an X-ray CCD camera (Burke *et al.* 1991, 1994; Yamashita *et al.* 1997; Yamashita 1998). *ASCA* has two SISs called SIS0 and SIS1, which are operated in parallel. The strong points of SIS, when we compare it with GIS, are good energy resolution (130 keV at 5.9 keV, at launch), high detection efficiency in low energy band, high rejection rate of the particle events, and good spatial resolution[7].

Each of SISs has 4 chips, each of which has 420×422 pixel with a pixel size of 27 μm. Geometrical area of each chip is 11 mm×11 mm, corresponding to about $11' \times 11'$. All of the SIS chips can be operated in parallel, although only the selected chips are used in most of the observations to avoid telemetry saturation. The energy range of SIS is from 0.4 to 10 keV. Although many kinds of operation modes for SIS are available, we used only the Faint and the Bright modes in the observations of the Galactic Center region (see Burke *et al.* 1991, 1994). Hence we here concentrate on these two modes.

---

[7] The pixel size of SIS, 27μm, corresponding to $0'.027$, is the angular resolution of SIS, whereas the half power diameter of XRTs is $3'$.

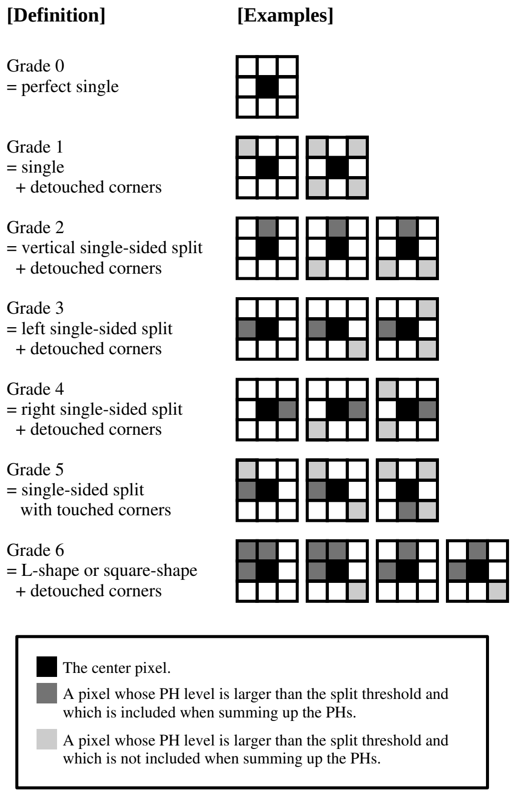
[Definition]
[Examples]
Grade 0
= perfect single
Grade 1
= single
+ detouched corners
Grade 2
= vertical single-sided split
+ detouched corners
Grade 3
= left single-sided split
+ detouched corners
Grade 4
= right single-sided split
+ detouched corners
Grade 5
= single-sided split
with touched corners
Grade 6
= L-shape or square-shape
+ detouched corners
■ The center pixel.
▩ A pixel whose PH level is larger than the split threshold and which is included when summing up the PHs.
□ A pixel whose PH level is larger than the split threshold and which is not included when summing up the PHs.

Figure 3.9: Grade definition and the rule to add pulse heights. The events out of these criteria are defined as Grade 7.

The time resolution of SIS is 4, 8, or 16 seconds, depending on how many chips are used for the observation. The events detected with SIS are often extended for two or more than two pixels. We classify the shape of extension into eight categories (Grade 0–7: Fig. 3.9). Nominally we regard Grade 0, 2, 3 and 4 events as X-ray events, whereas we regard others as non-X-ray events.

The SISs are known to have the serious degradation since the launch due to the accumulated radiation damage (Dotani *et al.* 1997; Yamashita *et al.* 1997; Yamashita 1998). It makes the large calibration uncertainty as well as the degradation of energy resolution, the detection efficiency, and the increase of the hot/flickering pixels.

Chapter 4

Observations

4.1 Pointing observations & the Galactic Center Survey

With *ASCA*, the Galactic Center $5^\circ \times 5^\circ$ region was observed 107 times in total as shown in Fig. 4.1 and Table 4.1. In 1993 of *ASCA* PV phase, 9 pointing observations were made; 8 of them are the mapping of the central $1.^\circ5 \times 1.^\circ5$ around the Galactic Center, whereas the rest one pointing is for 1E 1740.7−2942. After them, many pointing observations, including several TOO (Target Of Opportunity) observations for transient sources (see Table 4.2), were made for various purposes in AO 1–7 phases. Such pointing observations were mainly concentrated around the Galactic plane.

In addition, the Galactic Center survey project was started in 1997 fall, and mapped the places, which had not been observed with pointing observations. Until 1999 fall, the survey has almost completely mapped the central $4^\circ \times 4^\circ$ region, except a part of the region around $(l_{\rm II}, b_{\rm II}) = (-1.^\circ5, -1.^\circ5)$, which was not observed due to unexpected accidents in the operation.

The exposure time of each pointing for the pointing observations after data filtering (see the next section) is distributed from 10 ksec to 100 ksec, whereas that for the survey is from 5 ksec to 15 ksec. Some places, where some interesting objects exist, were observed several times; the total exposure of such places is occasionally over 200 ksec. Consequently, the exposure time for each place is highly different from place to place, about 5 ksec to 200 ksec. (see the exposure map of Fig. 4.2). The grand total exposure time for the Galactic Center $5^\circ \times 5^\circ$ region is about 1600 ksec until 1999 December.

The GIS modes of those observations are generally the PH mode with the standard bit-assignment (10-8-8-5-0-0; see the previous chapter) except for some pointings (Table 4.2). On the other hand, SIS modes were different from pointing to pointing. The ability of the SISs is crucially affected with the radiation damage by charged particles. In fact, the detection efficiency of the SISs with 4-CCD mode in 1999 January, for example, was degraded to only 30%–40% of that with 1-CCD mode in 1993 December before RDD correction (Dotani 1999). The main results with SIS data in 1993 fall, when the degradation of SIS was not serious, have been already published by Koyama *et al.* (1996) and Maeda (1998), except for the results on 1E 1740.7−2942, which is analyzed in this thesis (see Chapter 6). In addition, the field of view of SIS is much smaller than that of GIS even when all the four chips are used in an observation (4-CCD mode). Thus, we mainly concentrate on GIS data in this thesis. We do not use the SIS data unless otherwise mentioned.

Table 4.1 shows the summary of the *ASCA* observations of the Galactic Center $5^\circ \times 5^\circ$ region. We used all these data sets.

4.2 Data screening

Data screening was performed basically according to the standard method as described in Day *et al.* (1995). We briefly describe the data selection criteria in the followings.

4.2.1 Data screening criteria

We regarded the events which satisfy all the following criteria[1] as the X-ray events: `ELV`$> 5^\circ$, `COR`> 4 (GV), and the criterion given by Ishisaki *et al.* (1996) to avoid special region with high background (see Ishisaki *et al.* (1996)). We also rejected the data in SAA (the South Atlantic Anomaly) and the data when the attitude of the satellite was shifted from the mean pointing attitude in each observation by more than $30''$[2]. When the `L1` monitor count rate of one of GISs was 0 or less than 0, the sensor was regarded not to be operated normally, hence the data of the sensor at that time were also rejected. Due to the last criterion, the exposure time for GIS2 and GIS3 was sometimes different from each other, although the difference is less than 2% of exposure time for each observation.

---

[1] For the meanings of terminology, see Appendix B and Day *et al.* (1995).

[2] The purpose of this criterion is to use only the data when the attitude of the satellite was stable. Therefore, the mean pointing attitude was calculated not with data of whole observation duration of each pointing as the default processing, but with the data in the stable attitude with the attitude fluctuation of smaller than $30''$.

4.2.2 Telemetry saturation & bit-rate selection

The telemetry limits for one GIS sensor are 4 c/s, 16 c/s, 128 c/s for low, medium, high bit-rate data, respectively. We used the data of which the telemetry was not saturated with the significance of 2 σ; we used all the high bit-rate data, but did not use the data of which the averaged total count rate including that with the calibration isotope and non-X-ray background (NXB) exceeds 2 c/s and 8 c/s for low and medium bit-rate, respectively[3]. Note that for only the data of observation ID=27 (see Table 4.1) with the apparent count rate of 97 c/s, the telemetry was severely saturated.

4.2.3 GIS gain, rejection of NXB & arrival time correction

The energy gain for each GIS is changed with the temperature, the observation period, the position, and so on (see the previous chapter for detail). We corrected the gain into the standard energy-channel relation, using `temp2gain` package with the gain history file released on 1999 May. Therefore the extrapolation from known gain history was applied for the data taken after 1999 April, which correspond to our observation IDs of 93 to 107 (Table 4.1).

Using rise-time information, we applied the rejection of non-X-ray background (NXB) for all the GIS data after the selection described in the previous sections, except for the data of observation ID=27, which had no rise-time information (see Table 4.2). We also corrected arrival time of each event to barycentric dynamical time.

---

[3] Since the GIS telemetry limit in the unit time is 8 counts, the condition that the telemetry saturation do not occur with 2σ confidence is expressed as, on the assumption that all the events follow the Poisson statistics,

$$\frac{(8-x)[\mathrm{counts}]}{\sqrt{x}[\mathrm{counts}]} = 2[\mathrm{sigma}]$$

where the count in the unit time is x counts. Then x is solved as $x = 4$ counts per unit-time. The unit-times for low, medium, high bit-rate are 2, 0.5, 0.0625 seconds, respectively. The maximum count rates without the telemetry saturation with 2σ confidence are accordingly calculated to be 2, 8, 64 c/s for respective bit-rate data.

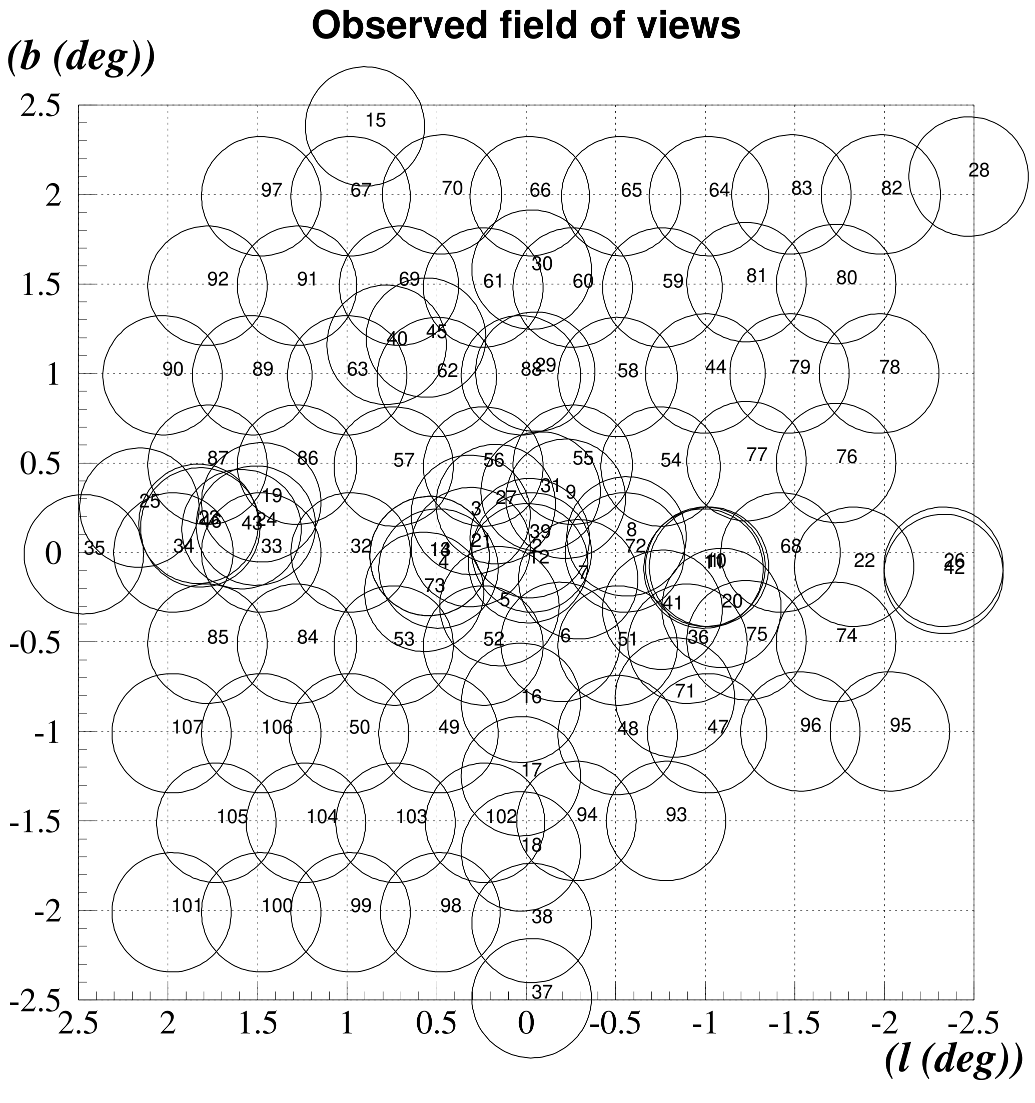

Figure 4.1: The GIS fields of views of all the *ASCA* pointings in the Galactic Center 5° × 5° region with the galactic coordinates. Each circle has 20′ radius. See Table 4.1 for the field IDs.

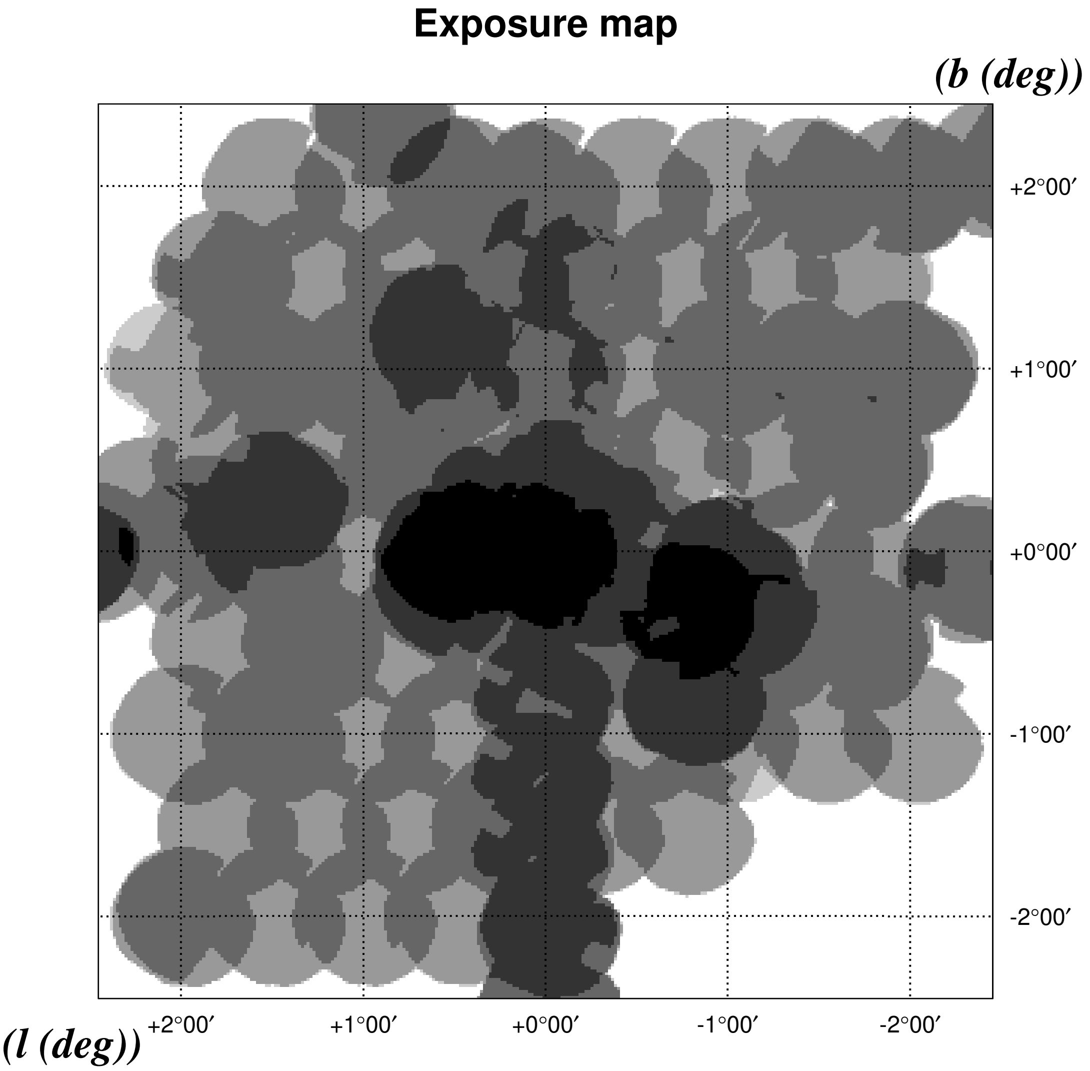
Exposure map
(b (deg))
+2°00′
+1°00′
+0°00′
-1°00′
-2°00′
(l (deg))
+2°00′
+1°00′
+0°00′
-1°00′
-2°00′

Figure 4.2: Exposure map of all the *ASCA* observations in the Galactic Center $5^\circ \times 5^\circ$ region with the galactic coordinates. The color levels are log(EXP[sec]) of 3.0, 3.5, 4.0, 4.5, 5.0, 5.5. The position of the calibration source for GISs is removed from each pointing.

Table 4.1: Observational log

ID	Date		Coordinates		Exp.[†]	Name	Rem.[§]
	Start	End	l_{II}	b_{II}			
	(UT)[‡]	(UT)[‡]	(deg.)	(deg.)	(ksec)		
1	1993/09/26-00:12	1993/09/27-05:08	358.98	−0.08	30.5	1E1740.7−294	
2	1993/09/30-17:35	1993/10/01-07:27	359.97	0.00	17.3	GC(0,0)	
3	1993/10/01-07:06	1993/10/01-21:06	0.31	0.21	17.7	GC(0,−0.37)	
4	1993/10/01-21:18	1993/10/02-10:14	0.49	−0.09	17.2	GC(0.37,−0.37)	
5	1993/10/02-10:06	1993/10/03-00:58	0.15	−0.30	19.9	GC(0.37,0)	
6	1993/10/03-00:30	1993/10/03-13:10	359.81	−0.50	14.7	GC(0.37,0.37)	
7	1993/10/03-13:34	1993/10/04-02:58	359.71	−0.15	20.3	GC(0,0.37)	
8	1993/10/04-02:54	1993/10/04-16:34	359.44	0.09	19.8	GC(−0.37,0.37)	
9	1993/10/04-16:29	1993/10/05-03:21	359.78	0.30	17.9	GC(−0.37,0)	
10	1994/09/08-19:40	1994/09/09-04:36	359.00	−0.08	13.5	1E1740.7−2942 N1	
11	1994/09/12-18:58	1994/09/13-01:06	359.01	−0.09	11.8	1E1740.7−2942 N2	
12	1994/09/15-22:46	1994/09/17-14:42	359.99	−0.06	81.9	SGR A	
13	1994/09/22-03:08	1994/09/23-12:48	0.54	−0.02	58.1	SGR B N1	
14	1994/09/24-02:51	1994/09/24-14:11	0.54	−0.02	19.7	SGR B N2	
15	1995/03/15-08:22	1995/03/15-22:06	0.90	2.38	18.6	SLX 1735−269	
16	1995/03/21-03:44	1995/03/22-00:04	0.03	−0.84	25.1	GC(0min,−50min)	
17	1995/03/22-00:00	1995/03/22-22:48	0.03	−1.25	27.0	GC(0min,−75min)	
18	1995/03/22-22:44	1995/03/23-20:36	0.03	−1.67	25.3	GC(0min,−100min)	
19	1995/03/26-03:31	1995/03/27-12:55	1.48	0.28	35.6	THE 200−PC RING N1	
20	1995/03/27-12:50	1995/03/28-17:54	358.91	−0.31	32.7	THE 200−PC RING N2	
21	1995/09/19-08:54	1995/09/21-21:38	0.31	0.03	63.0	THE 6.4KEV ISLAND	
22	1995/09/25-01:52	1995/09/25-08:36	358.17	−0.08	8.6	GALACTIC RIDGE N1	
23	1995/09/25-08:04	1995/09/25-14:08	1.83	0.16	5.0	GRO J1750−27 N1	Yes
24	1995/09/25-14:00	1995/09/25-17:20	1.51	0.15	2.5	GRO J1750−27 N2	Yes
25	1995/09/25-17:28	1995/09/26-00:44	2.16	0.25	8.9	GRO J1750−27 N3	Yes
26	1995/09/26-00:44	1995/09/26-09:00	357.67	−0.08	12.7	GALACTIC RIDGE N2	
27	1996/02/26-10:55	1996/02/27-02:47	0.17	0.27	14.0	GRO J1744−28	Yes
28	1996/03/08-17:19	1996/03/09-10:03	357.53	2.10	19.2	HP 1	
29	1996/09/10-03:56	1996/09/10-19:52	359.95	1.01	13.4	LB=0 75	
30	1996/09/10-19:20	1996/09/11-07:52	359.97	1.58	18.8	LB=0 100	
31	1996/09/11-07:47	1996/09/11-21:27	359.92	0.34	16.8	LB=0 50	Yes
32	1996/09/19-15:21	1996/09/19-22:33	0.98	0.00	8.2	GAL RIDGE2 N1	
33	1996/09/19-21:29	1996/09/20-04:33	1.48	0.00	10.7	GAL RIDGE2 N2	
34	1996/09/20-04:29	1996/09/20-09:21	1.97	0.00	7.7	GAL RIDGE2 N3	
35	1996/09/20-08:45	1996/09/20-13:25	2.47	−0.01	8.8	GAL RIDGE2 N4	
36	1996/09/23-14:36	1996/09/24-02:32	359.10	−0.51	14.8	G359.1−0.9	
37	1996/09/28-05:19	1996/09/28-21:55	359.97	−2.49	29.6	GC 0−150	
38	1996/09/29-13:26	1996/09/30-17:46	359.97	−2.07	36.8	GC 0−125	
39	1997/03/16-15:57	1997/03/18-07:09	359.98	0.08	28.5	SGRA N1	Yes
40	1997/03/18-07:45	1997/03/18-17:41	0.78	1.16	9.3	SGRA N2	
41	1997/03/20-21:36	1997/03/23-04:56	359.24	−0.32	76.0	G359.1−0.2	
42	1997/04/02-06:21	1997/04/02-22:53	357.67	−0.12	14.4	GRS 1737−31	Yes
43	1997/09/15-11:57	1997/09/16-20:09	1.59	0.13	6.0	AGPS267.3−27.4	
44	1997/09/19-05:28	1997/09/19-23:08	359.00	1.00	16.7	G359.1+0.9	Yes
45	1997/09/29-07:13	1997/09/30-12:49	0.56	1.20	32.3	GRS 1739−278	
46	1998/03/13-21:05	1998/03/16-09:09	1.82	0.14	8.8	AGPS267.3 S1	
47	1998/09/03-04:24	1998/09/03-10:00	358.99	−1.01	6.1	GC REG 1 N1	
48	1998/09/03-10:56	1998/09/03-20:44	359.49	−1.02	9.7	GC REG 1 N2	
49	1998/09/03-20:08	1998/09/04-03:16	0.49	−1.01	9.1	GC REG 1 N3	

(Continuing to the next page.)

Table 4.1: Observational log (Continued from the previous page.)

ID	Date Start (UT)[‡]	End (UT)[‡]	Coordinates l_{II} (deg.)	b_{II} (deg.)	Exp.[†] (ksec)	Name	Rem.[§]
50	1998/09/04-03:48	1998/09/04-09:44	0.99	−1.01	8.3	GC REG 1 N4	
51	1998/09/04-08:40	1998/09/04-16:08	359.49	−0.52	8.4	GC REG 1 N5	
52	1998/09/04-16:04	1998/09/05-00:40	0.24	−0.52	8.4	GC REG 1 N6	
53	1998/09/06-09:44	1998/09/06-18:44	0.74	−0.52	5.7	GC REG 1 N7	
54	1998/09/06-18:39	1998/09/06-21:07	359.25	0.48	3.3	GC REG 1 N8	
55	1998/09/07-01:51	1998/09/07-07:35	359.74	0.49	7.4	GC REG 1 N9	
56	1998/09/07-07:51	1998/09/07-15:27	0.24	0.48	9.3	GC REG 1 N10	
57	1998/09/07-15:43	1998/09/07-23:07	0.74	0.48	10.0	GC REG 1 N11	
58	1998/09/07-23:03	1998/09/08-05:59	359.49	0.98	10.0	GC REG 2 N1	
59	1998/09/08-05:55	1998/09/08-11:43	359.24	1.48	7.9	GC REG 2 N2	
60	1998/09/08-11:43	1998/09/08-21:51	359.74	1.48	9.5	GC REG 2 N3	
61	1998/09/08-21:19	1998/09/09-03:43	0.24	1.48	10.0	GC REG 2 N4	
62	1998/09/09-03:47	1998/09/09-18:59	0.50	0.98	14.5	UN SNR.5+1.0 N1	
63	1998/09/09-18:27	1998/09/10-06:35	1.00	0.99	10.9	UN SNR.5+1.0 N2	
64	1998/09/10-06:18	1998/09/10-14:06	358.98	1.99	8.1	GC REG 2 N5	
65	1998/09/10-14:54	1998/09/10-22:58	359.47	1.99	9.7	GC REG 2 N6	
66	1998/09/10-22:54	1998/09/11-05:42	359.98	1.99	10.0	GC REG 2 N7	
67	1998/09/11-04:38	1998/09/11-11:58	0.98	1.99	8.2	GC REG 2 N8	
68	1998/09/11-11:26	1998/09/11-19:58	358.58	0.00	7.2	GC REG 2 N9	
69	1998/09/12-18:26	1998/09/12-23:34	0.71	1.49	7.4	UN SNR.75+1.5 1 N1	
70	1998/09/12-23:18	1998/09/13-09:06	0.47	2.00	14.1	UN SNR.75+1.5 1 N2	
71	1998/09/13-09:42	1998/09/15-02:50	359.17	−0.81	60.3	THE MOUSE	
72	1998/09/15-02:17	1998/09/15-09:57	359.45	0.00	10.1	THE MOUSE off	Yes
73	1998/09/26-03:26	1998/09/26-16:26	0.57	−0.22	26.2	XTE J1748−288	Yes
74	1999/03/10-16:09	1999/03/10-22:37	358.27	−0.50	12.4	GC REG3 N1	
75	1999/03/10-22:36	1999/03/11-03:56	358.77	−0.49	10.3	GC REG3 N2	
76	1999/03/11-03:45	1999/03/11-08:13	358.27	0.50	11.6	GC REG3 N3	
77	1999/03/11-08:36	1999/03/11-14:04	358.77	0.51	8.8	GC REG3 N4	
78	1999/03/11-14:32	1999/03/11-20:00	358.03	1.00	12.5	GC REG3 N5	
79	1999/03/11-20:56	1999/03/12-01:32	358.53	1.00	10.3	GC REG3 N6	
80	1999/03/12-01:56	1999/03/12-06:48	358.27	1.50	5.2	GC REG3 N7	
81	1999/03/12-06:44	1999/03/12-12:48	358.77	1.51	6.1	GC REG3 N8	
82	1999/03/12-12:16	1999/03/12-19:32	358.02	2.00	12.1	GC REG3 N9	
83	1999/03/12-19:00	1999/03/13-00:40	358.52	2.00	10.8	GC REG3 N10	
84	1999/03/14-15:48	1999/03/14-22:32	1.28	−0.51	11.9	GC REG 4 N01	
85	1999/03/14-22:35	1999/03/15-02:19	1.78	−0.51	8.5	GC REG 4 N02	
86	1999/03/15-02:03	1999/03/15-09:03	1.28	0.49	6.8	GC REG 4 N03	
87	1999/03/15-09:27	1999/03/15-17:55	1.78	0.49	7.3	GC REG 4 N04	
88	1999/03/15-16:47	1999/03/15-22:11	0.03	0.99	9.8	GC REG 4 N05	
89	1999/03/15-21:35	1999/03/16-02:19	1.53	0.99	10.8	GC REG 4 N06	
90	1999/03/16-02:43	1999/03/16-09:55	2.03	0.99	5.0	GC REG 4 N07	
91	1999/03/16-08:47	1999/03/16-18:11	1.28	1.49	7.5	GC REG 4 N08	
92	1999/03/16-18:35	1999/03/16-23:43	1.78	1.49	10.1	GC REG 4 N09	
93	1999/09/25-03:02	1999/09/25-09:26	359.22	−1.50	9.1	GC REG 5 N7	
94	1999/09/25-09:22	1999/09/25-19:10	359.72	−1.50	9.1	GC REG 5 N8	
95	1999/09/25-19:06	1999/09/26-03:02	357.97	−1.00	8.1	GC REG 5 N9	
96	1999/09/26-02:26	1999/09/26-09:02	358.47	−1.00	8.8	GC REG 5 N10	
97	1999/09/29-13:04	1999/09/29-22:48	1.48	1.99	9.3	GC REG 4 N10	
98	1999/09/29-22:56	1999/09/30-05:00	0.48	−2.01	8.1	GC REG 6 N1	

(Continuing to the next page.)

Table 4.1: Observational log (Continued from the previous page.)

ID	Date		Coordinates		Exp.†	Name	Rem.§
	Start	End	$l_{\rm II}$	$b_{\rm II}$			
	(UT)‡	(UT)‡	(deg.)	(deg.)	(ksec)		
99	1999/09/30-05:16	1999/09/30-12:32	0.98	−2.01	9.8	GC REG 6 N2	
100	1999/09/30-12:44	1999/09/30-22:24	1.48	−2.01	9.5	GC REG 6 N3	
101	1999/09/30-22:20	1999/10/01-03:24	1.98	−2.01	10.6	GC REG 6 N4	
102	1999/10/01-09:24	1999/10/01-20:32	0.23	−1.51	10.2	GC REG 6 N5	
103	1999/10/01-21:32	1999/10/02-01:00	0.73	−1.51	7.6	GC REG 6 N6	
104	1999/10/02-01:28	1999/10/02-06:56	1.23	−1.51	6.6	GC REG 6 N7	
105	1999/10/02-07:28	1999/10/02-15:16	1.73	−1.51	9.0	GC REG 6 N8	
106	1999/10/02-15:36	1999/10/02-23:00	1.48	−1.01	10.4	GC REG 6 N9	
107	1999/10/02-23:56	1999/10/03-05:32	1.98	−1.01	8.6	GC REG 6 N10	

†: The average of the exposures with GIS2 and GIS3 after the screening.

‡: (Year/Month/Date-Hour:Minute).

§: Remarks; if "yes", some comments are described in Table 4.2.

Table 4.2: Comments on each observation

ID	Notes
23–25	TOO observations for GRO J1750−27.
27	TOO observation for GRO J1744−28. GIS bit assignment of 10-8-8-0-0-5.
31	GIS bit assignment of 8-8-8-5-0-2 for high and low bit-rate data, and 8-6-6-5-0-6 for medium bit-rate data.
39	GIS bit assignment of 10-8-8-0-0-5.
42	TOO observation for GRS 1737−31.
44	GIS bit assignment of 8-8-8-5-0-2.
72	Observation of the transient KS1741−293.
73	TOO observation for XTE J1748−288.

Chapter 5

Results I.
— Image & Source Finding

5.1 X-ray images

5.1.1 Method for constructing image

First of all, we constructed the GIS image in several energy bands. It is not trivial to construct a wide-area mosaic image into which many pointing images are superposed because the response of the detectors is highly dependent on the position on the detectors. Thus, we developed the following method to make a good image with GIS. We first mention the overall flow to construct image, then describe details on the items used. The flow charts are also given in Fig. 5.1.

Flow for constructing a mosaic image

We separately treat an X-ray image and an exposure time image, which contains all the efficiency of a detector; at last, we divide the X-ray image by the exposure time image to obtain the image in which the efficiency of the detector is corrected. The detailed flow is as followings.

1. We make an X-ray image (I) for a selected energy band with the usual method.
2. We make a mask image (II) to cut some regions undesirable, such as, the region near the calibration source, from the X-ray image. The mask must have the same size as that of the original X-ray image. Each pixel of the mask image must have a value of 1 or 0 for the selected or not selected region, respectively.

Then we multiply the X-ray image by the mask image to cut the regions undesirable. The generated image is hereafter called the masked X-ray image (III).

3. We make a NXB image (IV) with the same size as that of the original X-ray image. A mask image is also applied for this NXB image (IV).
4. We make a raw exposure time image (V), simply by scaling up the mask image by the exposure time.
5. We make an efficiency map image (VI) with the same size as that of the original X-ray image. This image expresses the position dependence of the effective area of mirror and the detection efficiency on a detector. Then we multiply the raw exposure time image (V) by this image (VI) to make the corrected-exposure image (VII).
6. We convolute the masked X-ray image (III), the NXB image (IV) and the corrected-exposure image (VII). The generated images are hereafter called the convoluted X-ray image (VIII), the convoluted NXB image (IX) and the convoluted-corrected-exposure image (X), respectively.
7. We subtract the convoluted NXB image (IX) from the convoluted X-ray image (VIII) to make the NXB-subtracted convoluted X-ray image (XI).
8. With the above convoluting procedure, some pixels out of the masked region in the convoluted-corrected-exposure image (X) may have the quite small exposure value, which may cause zooming of the small count fluctuation of the X-ray data image when the data image is divided by this exposure image to construct a flux map. Thus we cut such regions in the convoluted-corrected-exposure image (X) itself and in the NXB-subtracted convoluted X-ray image (XI), according to a certain criterion.
9. After making the both kinds of image ((X) & (XI)) for each pointing and for each detector (GIS2 and GIS3), we sum up all the NXB-subtracted convoluted X-ray image (XI) and the convoluted-corrected-exposure image (X) in the galactic coordinates, separately. The generated images are called the mosaic X-ray image (XII) and the mosaic exposure image (XIII), respectively.
10. We divide the mosaic X-ray image (XII) by the mosaic exposure image (XIII), and obtain the final convoluted mosaic image (XIV).

The adopted items for constructing a mosaic image

Mask image (II) We adopt the so-called GIS good mask supplied by the GIS team (e.g., Ueda 1996) as the mask image (II) at first.

Although *ASCA* GISs have 25′ diameter geometrically, the calibration uncertainty is rather large in the outer part of the detector, which is apart from the detector center by larger than about 20′. In addition, NXB much increases at near the rim of the detector. With this mask, the region with high NXB as well as the region near the calibration isotope can be cut.

NXB image (IV) NASA GSFC supplies the night-earth GIS image for several cut off rigidity level. This image is a good template for the NXB image. Ishisaki et al. (1996) indicated that NXB of GIS has continuously increased as time passes since the launch. Then we make a NXB image (IV) from the above mentioned night-earth image, taking account of the increasing rate of NXB according to Ishisaki et al. (1996). Cut of the outer region from the obtained NXB image with the mask image (II) is also made.

Efficiency map (VI) The effective area of XRT decreases as the distance from the detector center increases, whereas the detection efficiency generally decreases. In addition, GISs have a supporting grid structure on which the detection efficiency is quite low. Thus we make the efficiency map (VI) with the method described in the following.

First we prepare a GIS image of blank skies for the correspondent energy band, which Dr. Ishisaki kindly supplied. This image is what is constructed from many blank sky fields mentioned in Ishisaki (1996); bright sources have been already subtracted. Then we subtract the NXB image (IV) from this image. We adopt the obtained image as the efficiency map (VI).

This image (VI) should be identical with the GIS raw image of the cosmic X-ray background (CXB); accordingly it includes the effects of vignetting by XRT and of the efficiency of GIS which also includes the grid structure. Therefore, we can perfectly reproduce the original image structure using this efficiency map (VI) if the original structure has the same spatial distribution and the same spectrum as the CXB, *i.e.*, uniform distribution and a relatively flat spectrum (photon index of about 1.4)[1].

---

[1] The reason why the shape of the spectrum is a parameter for this deconvolution is that the *ASCA* point spread function (PSF) is a function of energy. Since the PSF dependence on energy

The Galactic Center region is known to be full of the wide-spread hot plasma, then the above approximation is rather good in our case.

Convolution in the 6th procedure We adopt simply the smoothing with a Gaussian filter with $\sigma = 3$ pixel ($0\farcm75$) for the convoluting method.

Criterion for the cut in the 8th procedure For the cut described in the 8th procedure in the explanation of the flow, we adopt the following one; we reject the pixels of which the value is less than 17% of the maximum pixel value of the convoluted-corrected-exposure image (X) from the convoluted-corrected-exposure image (X) itself and the NXB-subtracted convoluted X-ray image (XI).

---

is not sharp (see Chapter 3), the difference of the spectral shape between the object image and the CXB may be not a dominant parameter for the deconvolution in most cases. In particular, if a narrow energy band is selected, the influence originated in the difference of the spectral shapes is negligible.

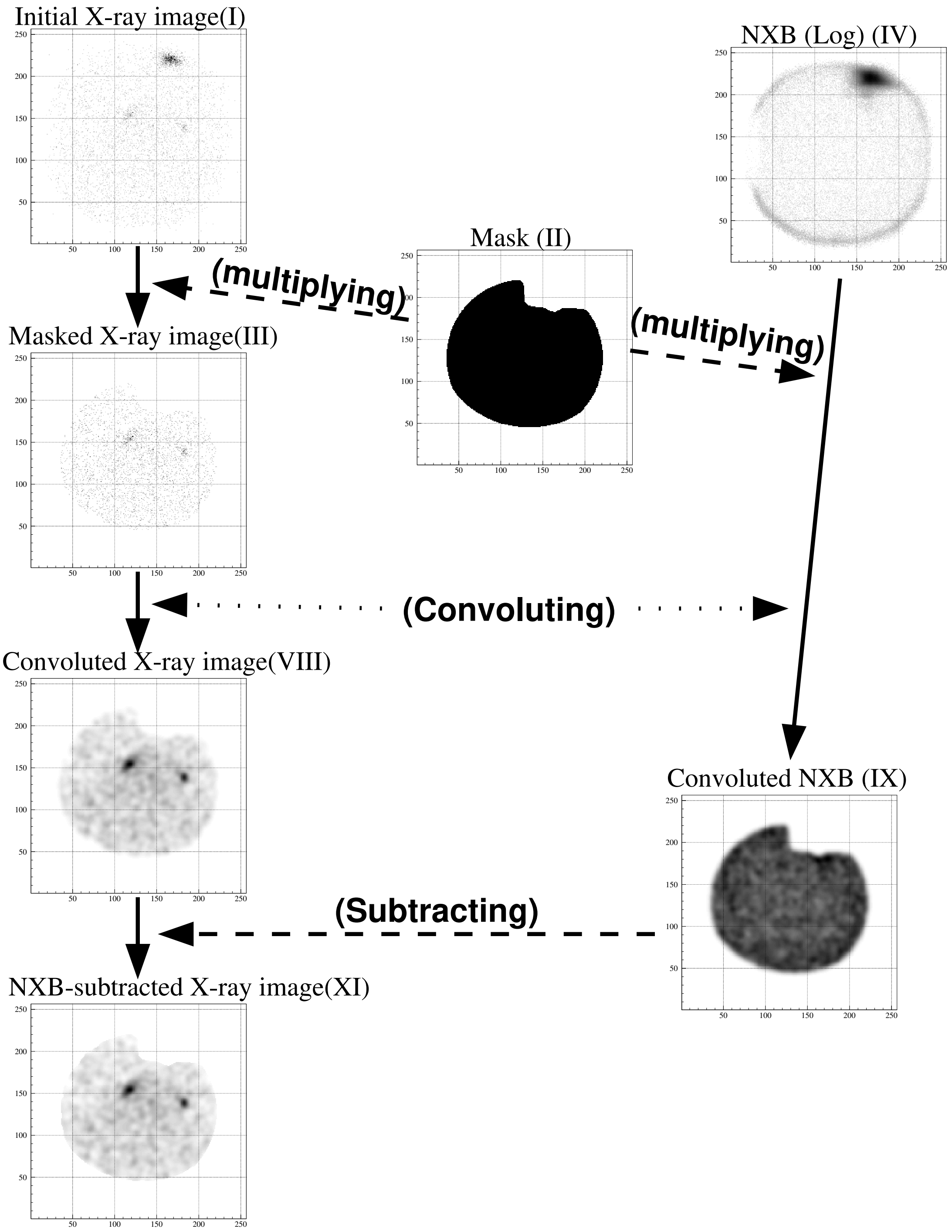
Initial X-ray image(I)
NXB (Log) (IV)
Mask (II)
(multiplying)
(multiplying)
Masked X-ray image(III)
(Convoluting)
Convoluted X-ray image(VIII)
Convoluted NXB (IX)
(Subtracting)
NXB-subtracted X-ray image(XI)
50
100
150
200
250

(a) For an X-ray data image

Figure 5.1: Flow charts for constructing wide-area images. Details on the flow are described in Section 5.1.1. The units of the both axes are GIS channel (1 (ch) $\cong 0'.25$).

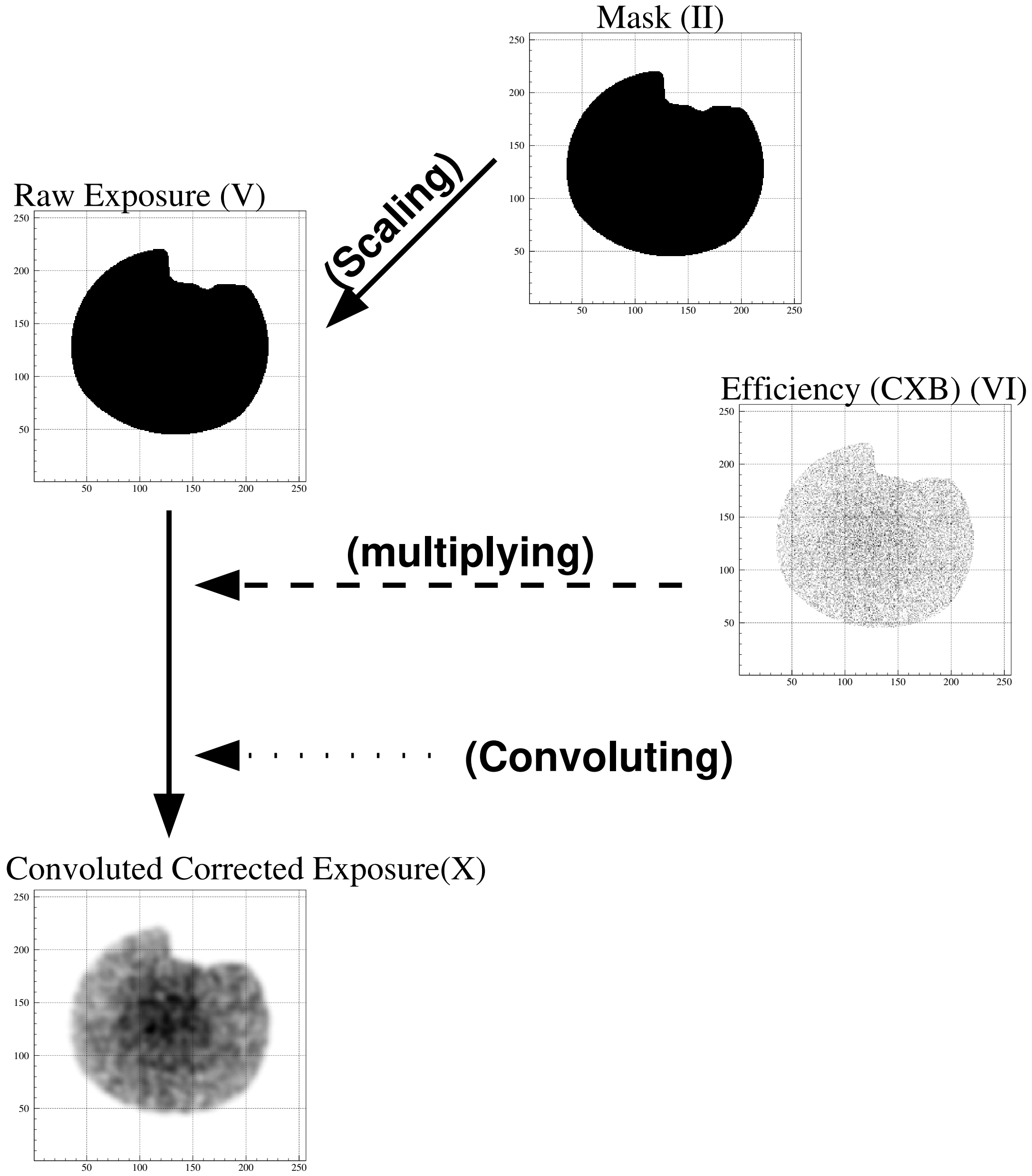
Mask (II)
(Scaling)
Raw Exposure (V)
Efficiency (CXB) (VI)
(multiplying)
(Convoluting)
Convoluted Corrected Exposure(X)
250
200
150
100
50
50
100
150
200
250

(b) For an exposure image

Figure 5.1: (↘) Flow chart (continued from the previous page and further to the next page (↗)).

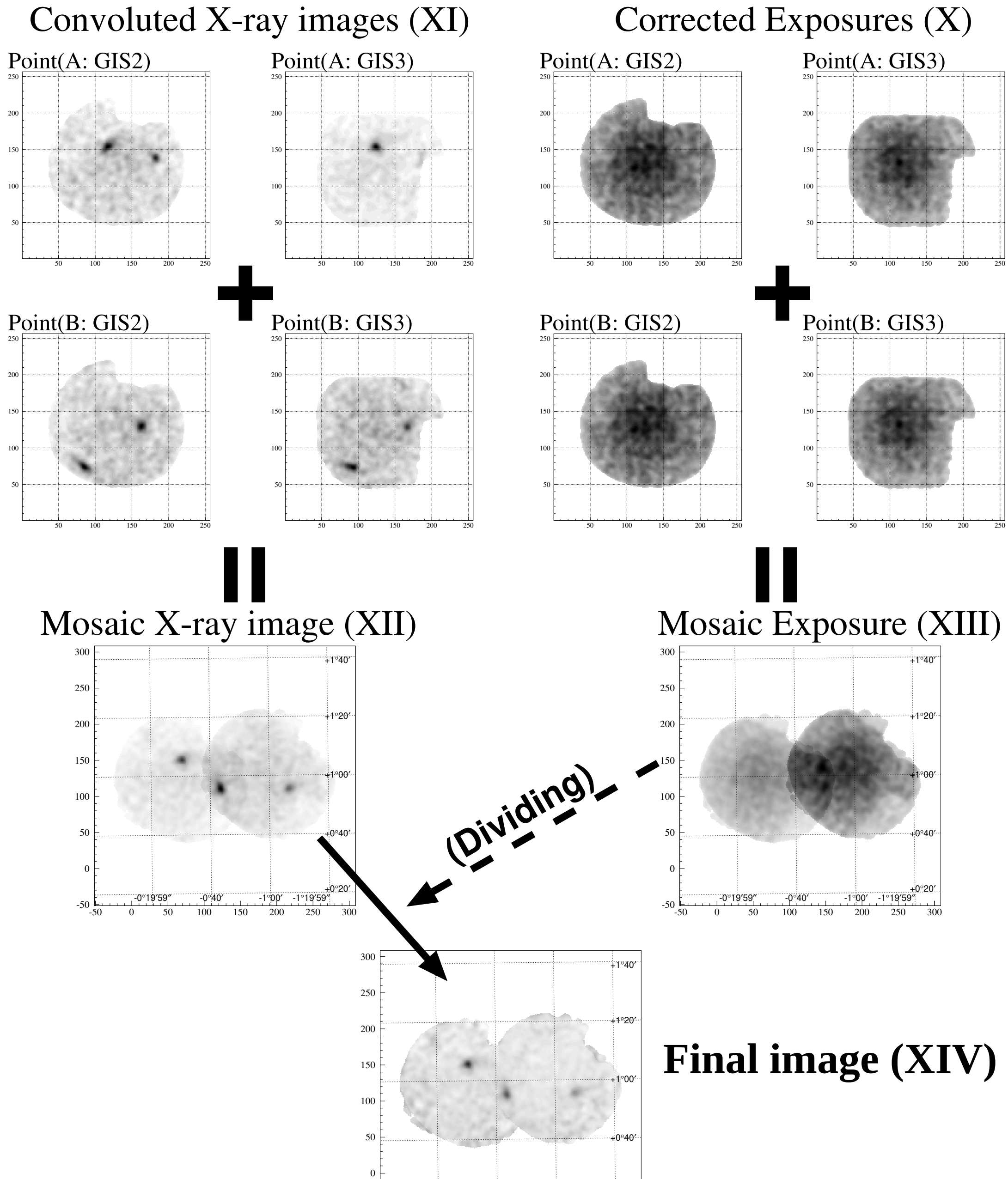
Convoluted X-ray images (XI)
Corrected Exposures (X)
Point(A: GIS2)
Point(A: GIS3)
Point(B: GIS2)
Point(B: GIS3)
+
=
Mosaic X-ray image (XII)
Mosaic Exposure (XIII)
(Dividing)
Final image (XIV)
+1°40′
+1°20′
+1°00′
+0°40′
+0°20′
-0°19′59″
-0°40′
-1°00′
-1°19′59″

(c) For superposition of images

Figure 5.1: (↘) Flow chart (continued from the previous page).

5.1.2 Global *ASCA* X-ray images for several energy bands

Fig. 5.2 (a)–(d) show the X-ray images in the Galactic Center $5^\circ \times 5^\circ$ region with energy bands of 3.0–10.0, 0.7–3.0, 7.1–10.0, 0.7–1.5 keV, respectively.

The hard band image (3.0–10 keV)

In the hard energy band of 3–10 keV (Fig. 5.2(a)), the brightest structures are X-ray point sources. On the other hand, some bright radiative structures are seen, which are due to the stray light from bright point sources out of field of view. For example, structures around $(l_{\rm II},\ b_{\rm II}) = (2^\circ,\ 0\overset{\circ}{.}5)$, $(l_{\rm II},\ b_{\rm II}) = (-0\overset{\circ}{.}2,\ -0\overset{\circ}{.}8)$ or $(l_{\rm II},\ b_{\rm II}) = (0\overset{\circ}{.}6,\ 1\overset{\circ}{.}0)$ are due to the stray light. Those stray light structures are generally time variable according to the variability of the original sources. They make the image discontinuous (see Chapter 3), and hence, quite difficult to analyze. In fact, the calibration for stray light structures are not so good; and moreover, the statistical fluctuation with the photons from stray light overwhelms the intrinsic structure in some places, which implies that the study of some intrinsic structures hidden by bright stray light is nearly impossible in such places.

Although there are many bright point sources and stray light structures, some diffuse structures, in particular near on plane, are nevertheless seen in the image. They were found to be the combination of hot plasma and possible X-ray reflection nebulae (Koyama *et al.* 1996; Maeda 1998; Murakami *et al.* 1999, 2000a, 2000b; Sakano *et al.* 1999c, 2000).

The hardest band image (7.1–10 keV)

In the hardest energy band of 7.1–10 keV (Fig. 5.2(c)), the X-ray structures are basically similar to that in 3–10 keV band; however the stray light structures are much fainter. This is partly because the stray light with softer energy photons is more effective than with harder energy photons (see Chapter 3), and partly because the bright point sources may not be so bright in such high energy band.

The sources with hard spectra may be more clearly detected in this energy band than in softer energy band. In fact, the source located at $(l_{\rm II},\ b_{\rm II}) \simeq (1\overset{\circ}{.}7,\ 0\overset{\circ}{.}1)$ is much brighter in this band than in 3–10 keV band. The source is found to have a quite hard spectrum, and identified as an X-ray pulsar, AX J1749.2−2725 (see Chapter 6.1.6).

The soft band image (0.7–3.0 keV)

On the other hand, in the soft energy band of 0.7–3 keV (Fig. 5.2(b)), the X-ray structures are much different from those in harder energy band. First, the point sources located at near the Galactic plane, which are quite bright in the hard energy band, are much fainter. This fact probably implies that the spectra of those sources are heavily absorbed, which is quantitatively discussed in later Chapter. Second, the stray light structures other than that around $(l_{\rm II},\, b_{\rm II}) = (2^\circ,\, 0\overset{\circ}{.}5)$ are quite dim, definitely because the point sources which cause stray light structures in the hard energy band are not so bright in this energy band. Third, some diffuse structures are detected. The distribution of those structures are found to be clumpy, which is different from that in the hard energy band. The nature of some of those diffuse structures are discussed in Chapter 6.3.

The softest band image (0.7–1.5 keV)

In the softest energy band of 0.7–1.5 keV (Fig. 5.2(d)), the differences of the X-ray structures between in the 0.7–3.0 keV band and in the 3.0–10.0 keV band are found to be much enhanced. Almost no diffuse structure can be seen on plane. On the other hand, there are bright diffuse structures especially in the lower galactic latitude region.

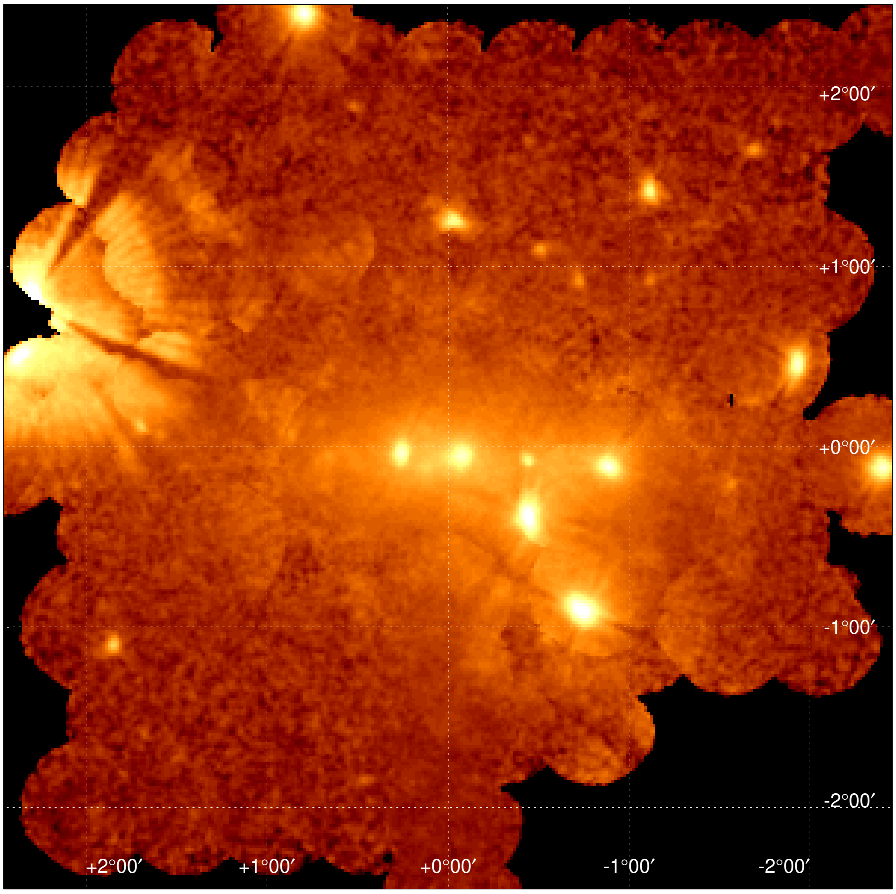

(a) 3.0–10.0 keV band.

Figure 5.2: *ASCA* X-ray images in the Galactic Center $5^\circ \times 5^\circ$ region for the energy band of 3.0–10.0 keV with the galactic coordinates. The color levels are logarithmic. Almost all the data are superposed in this image except for several pointings which includes too bright structures due to transient sources. The images are corrected for exposure, vignetting of mirrors and GIS efficiency including the grid structure after subtraction of non-X-ray background, according to the method described in Section 5.1.1.

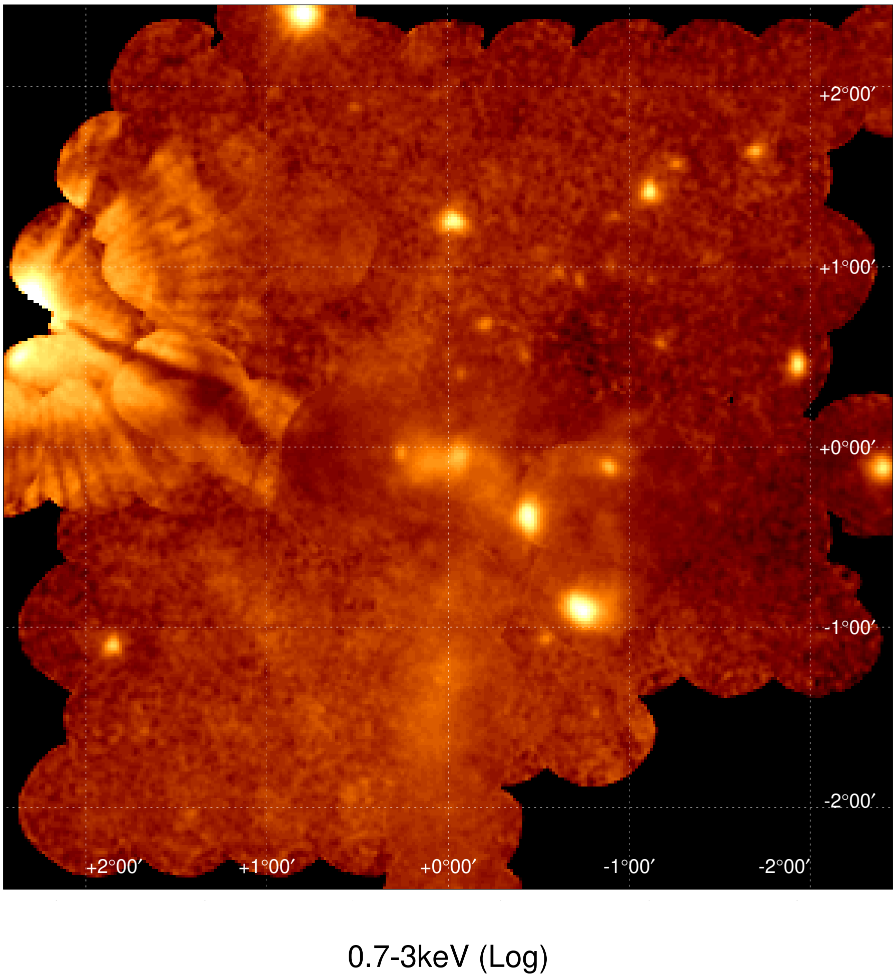

(b) 0.7–3.0 keV band.

Figure 5.2: ($\searrow$) *ASCA* X-ray image (continued from the previous page and further to the next page ($\nearrow$)).

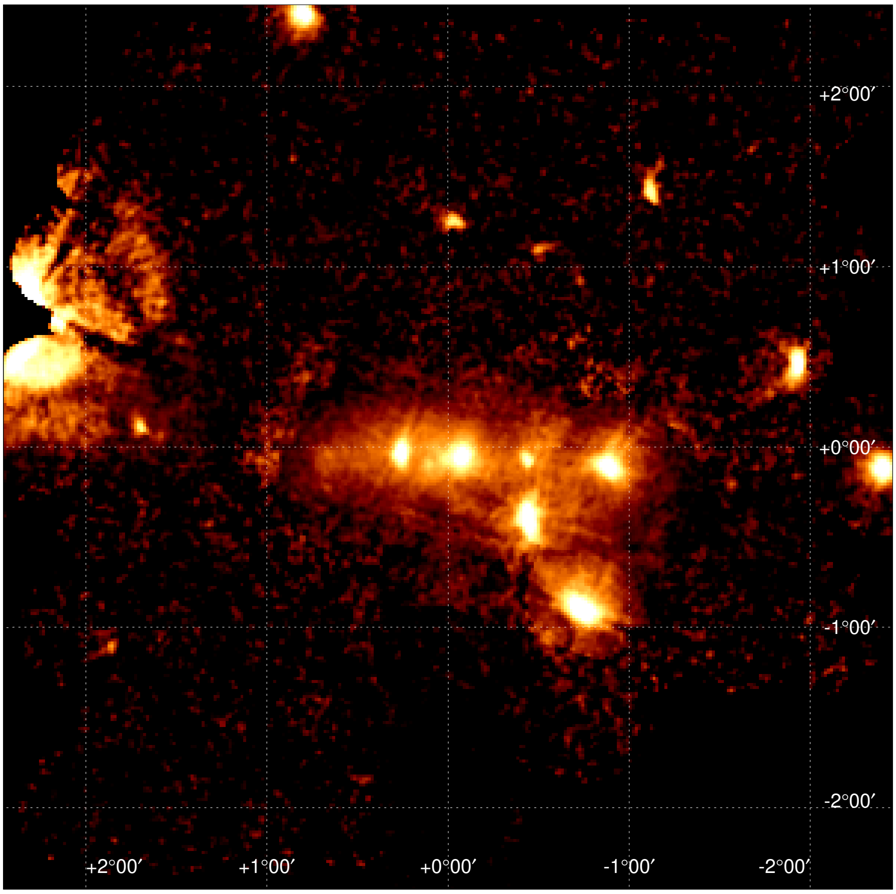

7.1-10keV (Log)

(c) 7.1–10.0 keV band.

Figure 5.2: (↘) *ASCA* X-ray image (continued from the previous page and further to the next page (↗)).

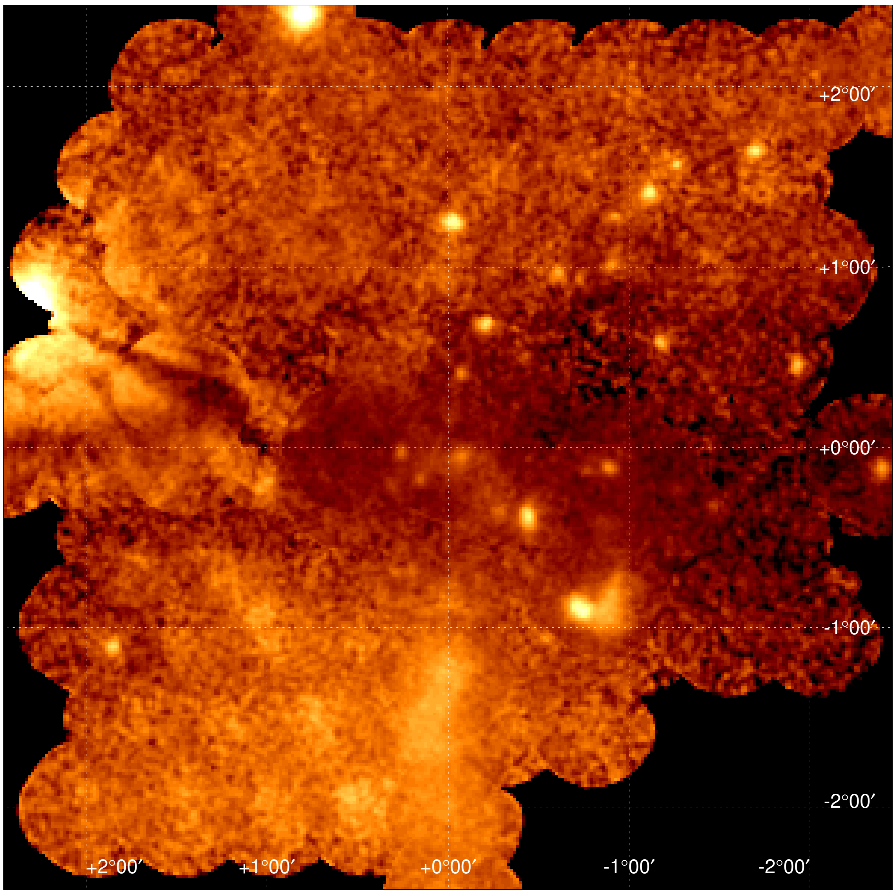

0.7-1.5keV (Log)

(d) 0.7–1.5 keV band.

Figure 5.2: (↘) *ASCA* X-ray image (continued from the previous page).

5.2 Source finding & extraction of spectra

We tried finding point sources in all the observed area.

5.2.1 Method of source detection & spectrum accumulation

Due to the complicated background by diffuse emission and stray light structures, we cannot simply apply the usual source detection method in this region. Thus, we developed the method as described below.

First of all, we pick up source candidates from each pointing image according to the method described in Ueda *et al.* (1998b). In this procedure, we can resolve neighboring sources of which angular separation is as small as 1 arcmin.

Then we determine the accurate source positions by 2-dimensional image fitting of the raw GIS2+3 image with the correspondent PSF and the background (blanksky image) according to the method described in Ueda *et al.* (1998b) and Ueda *et al.* (1999). In this fitting, we used narrow region with $10' \times 10'$ centered at the source to minimize the fluctuation of the background; and the positions of other source candidates were fixed.

The nominal positional error with *ASCA*/SIS is $40''$ (Gotthelf 1996; see also Chapter 3). The positional uncertainty with GIS may be slightly larger than that with SIS due to the positional sensitivity with GIS itself. However, we found the statistical uncertainties for the detected sources to be less than several arcseconds in most cases. Then we adopt the positional uncertainty to be $1'$, taking account of the systematic effect: such as, the background fluctuation, or the calibration uncertainty for the outer part of GIS, which is known to cause the relative positional uncertainty.

For each of the candidate sources, we accumulated the spectrum from circular region with radius of $3'$. At the same time we collected the background spectrum from annular region with radius of $3'$–$5'$ centered at the source position. In the above accumulations, we rejected the pixels, which are located near to the nearby source candidates or to the diffuse enhancement by less than $2'$. We regarded the diffuse enhancement as the place, which have larger pixel values than that of source peak, in the convoluted images. We also rejected the pixels which are out of the mask (see the Section 5.1.1), *i.e.*, near the detector edge or the calibration isotope.

We define the significance of the source as follows, according to the usual manner;

$$\text{Significance} \equiv \frac{(\text{Counts}_{\text{source}-\text{region}} - \text{Counts}_{\text{BGD}-\text{region}})}{\sqrt{\text{Counts}_{\text{BGD}-\text{region}}}}. \tag{5.1}$$

We regarded the source candidates with significance of more than 5σ as the true sources.

After filtering with the above criterion, some of the bright diffuse structures, which may be real diffuse structures or just due to stray light, are still left as point source candidates, or superposition of the candidates. Therefore, we reviewed all the source images and the spectrum accumulating regions, and rejected the candidates, which are suspected as diffuse structures.

5.2.2 Spectral fitting & source list

We applied the source finding method above mentioned on the 0.7–3.0 keV and the 3.0–10.0 keV band images in each observation. Then we compiled the soft and the hard band source lists. Many of the sources are significant in both of the source lists. Thus, we regard the sources of which the positions in the both source lists are close by less than $1\overset{\prime}{.}5$ as the identical source. Table 5.1 shows the resultant *ASCA* source list in the Galactic Center $5^\circ \times 5^\circ$ region.

Then we fitted each source spectrum after subtraction of the corresponding background spectrum with an absorbed power-law function. The best-fit parameters are also given in Table 5.1.

The identification of the sources with X-ray sources observed by past X-ray satellites are also included in Table 5.1. We also present the identification with multi-wavelengths data, where we use the SIMBAD database, in Table 5.2; we listed the sources located within $80'$ radius from the *ASCA* center position.

Table 5.1: X-ray source list in the Galactic Center region detected with *ASCA*

No	Name		$l_{\rm II}$	$b_{\rm II}$					ID
	(Obs-ID)	$\sigma^{0.7-10}$	$\sigma^{0.7-3}$	σ^{3-10}		Γ	$N_{\rm H}$	χ^2	(refs.)
		$F_{\rm X}^{0.7-10}$	$F_{\rm X}^{0.7-3}$	$F_{\rm X}^{3-10}$	$L_{\rm X}^{2-10}$	Error	Error	d.o.f.	
1	AX J1755.2−3017		−0.088	−2.484					
	(37)	5.5	1.1	8.7		1.42	10.2	30.90	
		4.3	0.1	4.1	6.0	$^{+4.63}_{-2.37}$	$^{+36.5}_{-<10.2}$	23	
2	AX J1758.0−2818		1.939	−2.020					
	(101)	2.8	-0.0	6.5		2.07	16.7	4.599	
		4.9	0.1	4.8	10.3	$^{+>8}_{-2.60}$	$^{+133.1}_{-<16.7}$	5	
3	AX J1754.5−2928		0.544	−1.937					
	(98)	4.4	5.5	-0.0		7.58	3.7	2.385	
		2.2	2.1	0.2	2.0	$^{+>2}_{-3.83}$	$^{+4.4}_{-2.8}$	5	
4	AX J1754.0−2930		0.463	−1.858					
	(98)	7.8	4.5	8.0		1.16	0.4	12.37	
		11.5	2.6	8.8	9.0	$^{+4.88}_{-1.06}$	$^{+9.2}_{-<0.4}$	6	
5	AX J1755.7−2818		1.681	−1.584					
	(105)	5.8	3.4	5.5		0.31	< 10.5	2.670	
		10.1	1.2	8.9	8.2	$^{+3.29}_{-<2}$		4	
6	AX J1754.2−2755		1.849	−1.100					
	(106)	24.7	17.8	17.6		3.69	4.5	2.941	
		78.3	29.2	49.0	119.0	$^{+1.45}_{-1.25}$	$^{+2.8}_{-2.3}$	2	
	(107)	>50	42.1	41.8		2.54	2.1	8.968	
		88.7	29.9	58.7	85.1	$^{+0.34}_{-0.31}$	$^{+0.6}_{-0.5}$	13	
7	AX J1748.5−2957		−0.545	−1.068					
	(48)	12.7	9.8	8.1		1.77	0.9	11.24	
		13.5	4.0	9.5	10.9	$^{+1.02}_{-0.90}$	$^{+1.4}_{-<0.9}$	14	
8	AX J1750.4−2900		0.484	−0.934					SAX J1750.8−2900
	(49)	4.9	1.9	5.3		0.39	< 74.8	6.850	
		7.5	1.0	6.5	6.1	$^{+>10}_{-1.24}$		7	
9	AX J1747.4−3003		−0.749	−0.914					SLX1744−300
	(47)	>50	>50	>50		2.08	5.3	87.61	[155]
		2044.5	244.2	1800.3	2639.7	$^{+0.14}_{-0.13}$	$^{+0.4}_{-0.4}$	82	
	(48)	>50	>50	>50		1.98	5.5	73.22	
		2402.4	258.1	2144.3	3070.6	$^{+0.10}_{-0.10}$	$^{+0.3}_{-0.3}$	62	
	(71)	>50	>50	>50		2.14	5.9	412.9	
		2920.5	325.0	2595.5	3939.2	$^{+0.02}_{-0.02}$	$^{+0.1}_{-0.1}$	198	
10	AX J1753.6−2745		1.914	−0.890					
	(107)	2.0	-0.0	5.1		0.51	21.1	1.752	
		8.4	0.0	8.4	13.2	$^{+>9}_{-<3}$	$^{+>100}_{-<100}$	1	
11	AX J1747.4−3000		−0.707	−0.885					SLX1744−299
	(47)	18.1	13.1	12.7		2.33	3.2	23.90	[155]
		204.2	46.8	157.4	225.3	$^{+0.94}_{-0.76}$	$^{+2.1}_{-1.6}$	24	
	(48)	>50	>50	>50		1.79	3.7	49.76	
		891.4	122.1	769.3	985.3	$^{+0.17}_{-0.16}$	$^{+0.4}_{-0.4}$	61	
	(71)	>50	>50	>50		1.86	4.3	180.1	
		1445.6	183.5	1262.1	1677.8	$^{+0.03}_{-0.03}$	$^{+0.1}_{-0.1}$	183	
12	AX J1748.3−2854		0.329	−0.475					
	(52)	9.5	8.8	4.9		4.58	5.4	12.19	
		6.1	2.8	3.2	11.9	$^{+>5}_{-2.77}$	$^{+8.8}_{-3.9}$	9	
13	AX J1751.1−2749		1.585	−0.453					
	(84)	2.1	1.8	1.1		—	—	—	
		0.0	—	—	0.0			—	

(Continuing to the next page.)

Table 5.1: Source list (Continued from the previous page.)

No	Name		$l_{\rm II}$	$b_{\rm II}$					ID
	(Obs-ID)	$\sigma^{0.7-10}$	$\sigma^{0.7-3}$	σ^{3-10}		Γ	$N_{\rm H}$	χ^2	(refs.)
		$F_{\rm X}^{0.7-10}$	$F_{\rm X}^{0.7-3}$	$F_{\rm X}^{3-10}$	$L_{\rm X}^{2-10}$	Error	Error	d.o.f.	
	(85)	5.2	5.6	1.2		2.69	0.3	5.195	
		6.6	4.4	2.2	3.1	$^{+>7}_{-1.36}$	$^{+7.5}_{-<0.3}$	3	
14	AX J1746.1−2931		−0.444	−0.391					A1742−294
	(6)	>50	>50	>50		1.4	5.9	104.3	
		2658.0	162.8	2495.2	3177.0	$^{+0.10}_{-0.10}$	$^{+0.4}_{-0.4}$	75	
	(7)	>50	>50	>50		1.64	6.5	67.31	
		2256.3	151.2	2105.1	2880.1	$^{+0.10}_{-0.09}$	$^{+0.4}_{-0.4}$	66	
	(41)	>50	>50	>50		1.84	6.6	292.4	
		5297.9	402.6	4895.3	7052.9	$^{+0.03}_{-0.03}$	$^{+0.1}_{-0.1}$	229	
	(51)	>50	>50	>50		1.82	5.8	125.6	
		2141.8	188.4	1953.4	2728.8	$^{+0.07}_{-0.06}$	$^{+0.2}_{-0.2}$	128	
15	AX J1748.1−2829		0.670	−0.220					XTE J1748−288
	(4)	5.1	3.3	3.9		—	—	—	
		0.0	—	—	0.0			—	
	(13)	5.5	1.0	6.3		5.93	59.1	38.41	
		7.7	0.0	7.6	687.1	$^{+0.00x}_{-0.00x}$	$^{+62.4}_{-35.5}$	31	
	(14)	3.4	1.1	3.5		—	—	—	
		0.0	—	—	0.0			—	
	(32)	—	—	—		—	—	—	
		0.0	—	—	0.0			—	
	(53)	40.7	14.5	39.6		1.81	7.3	2.017	
		548.4	35.8	512.6	750.5	$^{+0.86}_{-0.79}$	$^{+3.8}_{-3.3}$	6	
	(73)	12.9	6.3	11.3		2.26	5.9	34.74	
		12.2	1.5	10.8	17.0	$^{+1.37}_{-1.07}$	$^{+4.3}_{-3.1}$	26	
16	AX J1742.7−3022		−1.562	−0.203					
	(22)	5.7	2.3	5.4		0.17	2.6	3.684	
		26.1	1.1	24.9	24.5	$^{+3.71}_{-<2}$	$^{+48.5}_{-<2.6}$	3	
	(68)	5.9	1.9	6.2		7.76	22.5	0.1648	
		12.2	2.2	10.0	608.9	$^{+0.00x}_{-0.00x}$	$^{+18.8}_{-16.2}$	1	
	(74)	4.7	-0.0	6.9		1.44	14.9	2.623	
		40.3	0.5	39.8	66.5	$^{+6.87}_{-<3}$	$^{+61.7}_{-<14.9}$	1	
17	AX J1744.3−2941		−0.784	−0.146					
	(1)	2.5	3.2	1.0		—	—	—	
		0.0	—	—	0.0			—	
	(8)	—	—	—		—	—	—	
		0.0	—	—	0.0			—	
	(10)	1.7	2.7	0.3		—	—	—	
		0.0	—	—	0.0			—	
	(11)	-0.0	1.6	-0.0		—	—	—	
		0.0	—	—	0.0			—	
	(20)	-0.0	0.0	-0.0		—	—	—	
		0.0	—	—	0.0			—	
	(41)	11.0	8.6	7.7		0.46	< 0.1	101.5	
		16.0	2.3	13.7	12.9	$^{+0.52}_{-0.43}$		89	
	(72)	-0.0	1.5	-0.0		—	—	—	
		0.0	—	—	0.0			—	
18	AX J1740.2−3102		−2.404	−0.114					GRS1737−31
	(26)	0.0	-0.0	0.9		—	—	—	
		0.0	—	—	0.0			—	

(Continuing to the next page.)

Table 5.1: Source list (Continued from the previous page.)

No	Name		$l_{\rm II}$	$b_{\rm II}$					ID
	(Obs-ID)	$\sigma^{0.7-10}$	$\sigma^{0.7-3}$	σ^{3-10}		Γ	$N_{\rm H}$	χ^2	(refs.)
		$F_{\rm X}^{0.7-10}$	$F_{\rm X}^{0.7-3}$	$F_{\rm X}^{3-10}$	$L_{\rm X}^{2-10}$	Error	Error	d.o.f.	
	(42)	>50	>50	>50		1.53	6.2	131.4	
		1313.4	85.5	1227.9	1622.1	$^{+0.06}_{-0.06}$	$^{+0.3}_{-0.2}$	136	
19	AX J1743.9−2945		−0.885	−0.109					1E1740.7−2942
	(1)	>50	>50	>50		1.36	13.1	142.8	[79]
		1799.1	27.8	1771.3	2764.5	$^{+0.07}_{-0.07}$	$^{+0.5}_{-0.5}$	128	
	(10)	>50	38.4	>50		1.51	13.6	90.38	
		1363.3	21.7	1341.6	2205.9	$^{+0.11}_{-0.11}$	$^{+0.8}_{-0.8}$	80	
	(11)	>50	31.1	>50		1.41	13.3	70.18	
		1287.4	19.8	1267.6	2016.8	$^{+0.12}_{-0.12}$	$^{+0.9}_{-0.8}$	67	
	(20)	>50	12.0	>50		—	—	—	
		0.0	—	—	0.0			—	
	(41)	>50	>50	>50		1.13	12.2	202.3	
		2078.0	30.0	2048.0	2963.2	$^{+0.06}_{-0.06}$	$^{+0.4}_{-0.4}$	163	
20	AX J1744.9−2921		−0.439	−0.073					KS1741−293
	(7)	4.2	1.6	4.0		—	—	—	
		0.0	—	—	0.0			—	
	(8)	0.7	0.3	0.6		—	—	—	
		0.0	—	—	0.0			—	
	(72)	>50	16.9	>50		2.12	20.3	87.46	
		768.4	6.8	761.6	1840.8	$^{+0.20}_{-0.19}$	$^{+1.7}_{-1.6}$	78	
21	AX J1746.4−2844		0.257	−0.034					1E1743.1−2843
	(2)	>50	9.1	>50		2.11	19.5	70.32	
		909.0	8.9	900.0	2116.7	$^{+0.22}_{-0.21}$	$^{+1.9}_{-1.7}$	64	
	(3)	>50	15.5	>50		1.9	19.1	105.4	
		1006.3	8.9	997.4	2155.8	$^{+0.21}_{-0.20}$	$^{+1.9}_{-1.8}$	79	
	(4)	>50	14.7	>50		1.77	17.6	63.74	
		1021.1	10.2	1010.9	2006.3	$^{+0.19}_{-0.19}$	$^{+1.6}_{-1.5}$	77	
	(5)	>50	17.7	>50		1.42	16.7	119.8	
		1305.8	11.3	1294.5	2257.0	$^{+0.18}_{-0.17}$	$^{+1.5}_{-1.4}$	102	
	(12)	>50	36.9	>50		1.83	18.2	244.0	
		1117.1	10.8	1106.3	2270.2	$^{+0.08}_{-0.08}$	$^{+0.7}_{-0.7}$	180	
	(13)	>50	26.3	>50		1.76	17.4	138.2	
		976.5	10.1	966.4	1900.0	$^{+0.13}_{-0.12}$	$^{+1.1}_{-1}$	94	
	(14)	>50	14.1	>50		1.71	18.9	39.17	
		1298.4	10.0	1288.4	2600.8	$^{+0.19}_{-0.19}$	$^{+1.7}_{-1.6}$	38	
	(21)	>50	35.3	>50		2.12	18.6	208.4	
		599.3	7.0	592.3	1362.3	$^{+0.09}_{-0.09}$	$^{+0.8}_{-0.8}$	190	
	(39)	>50	2.1	>50		1.65	20.6	69.77	
		764.9	4.3	760.6	1571.0	$^{+0.35}_{-0.33}$	$^{+3.3}_{-3}$	61	
22	AX J1745.5−2901		−0.094	−0.015					
	(2)	20.5	8.3	19.0		0.7	3.6	40.02	
		61.1	3.4	57.8	61.5	$^{+0.48}_{-0.54}$	$^{+2.3}_{-1.9}$	45	
	(7)	14.8	4.9	14.5		0.73	4.3	34.18	
		74.5	3.6	70.9	77.2	$^{+1.15}_{-0.76}$	$^{+11}_{-3.1}$	36	
	(9)	7.9	1.1	8.9		2.4	17.7	23.48	
		61.9	1.0	60.9	152.8	$^{+4.51}_{-2.16}$	$^{+37.4}_{-13.6}$	22	
	(12)	>50	16.7	>50		1.69	10.4	255.8	
		124.0	4.0	119.9	188.8	$^{+0.24}_{-0.22}$	$^{+1.7}_{-1.5}$	214	
	(31)	4.1	-0.0	6.9		—	—	—	

(Continuing to the next page.)

Table 5.1: Source list (Continued from the previous page.)

No	Name		$l_{\rm II}$	$b_{\rm II}$					ID
	(Obs-ID)	$\sigma^{0.7-10}$	$\sigma^{0.7-3}$	σ^{3-10}		Γ	$N_{\rm H}$	χ^2	(refs.)
		$F_{\rm X}^{0.7-10}$	$F_{\rm X}^{0.7-3}$	$F_{\rm X}^{3-10}$	$L_{\rm X}^{2-10}$	Error	Error	d.o.f.	
		0.0	—	—	0.0			—	
	(39)	27.2	6.7	27.8		1.27	7.7	110.6	
		82.7	3.2	79.5	104.3	$^{+0.57}_{-0.38}$	$^{+3.9}_{-2.1}$	80	
23	AX J1749.2−2725		1.702	0.114					AXJ1749.2−2725
	(19)	20.9	-0.0	28.8		0.76	15.4	42.75	
		244.4	1.4	243.0	352.9	$^{+0.91}_{-0.50}$	$^{+9.6}_{-4.5}$	31	
	(23)	24.0	5.6	29.2		0.1	4.5	9.307	
		148.4	3.7	144.7	148.4	$^{+1.00}_{-1.02}$	$^{+8.1}_{-<4.5}$	5	
	(24)	6.1	-0.0	10.3		0.89	19.4	1.862	
		134.3	0.5	133.9	218.8	$^{+5.03}_{-<3}$	$^{+41.9?}_{-<19.4?}$	3	
	(33)	2.2	0.9	2.3		—	—	—	
		0.0	—	—	0.0			—	
	(34)	1.0	-0.0	2.0		—	—	—	
		0.0	—	—	0.0			—	
	(43)	1.8	-0.0	4.5		—	—	—	
		0.0	—	—	0.0			—	
	(46)	29.4	1.9	36.2		0.51	10.4	4.079	
		85.7	1.0	84.7	105.0	$^{+0.73}_{-0.64}$	$^{+7}_{-5.2}$	6	
24	AX J1745.0−2855		−0.052	0.123					GRS1741.9−2853
	(2)	1.9	-0.0	2.9		8.77	961	36.77	
		8.3	0.0	8.3	0.0	$^{+0.00x}_{-0.00x}$	$^{+>100}_{-<100}$	52	
	(3)	—	—	—		—	—	—	
		0.0	—	—	0.0			—	
	(7)	-0.0	0.6	-0.0		—	—	—	
		0.0	—	—	0.0			—	
	(9)	1.4	-0.0	2.7		—	—	—	
		0.0	—	—	0.0			—	
	(12)	10.3	1.1	12.0		1.75	11.9	68.34	
		15.4	0.4	15.0	25.0	$^{+2.40}_{-1.32}$	$^{+14.2?}_{-7.5?}$	76	
	(31)	>50	31.2	>50		2.36	11.4	89.13	
		851.9	40.1	811.8	1624.5	$^{+0.16}_{-0.16}$	$^{+0.9}_{-0.8}$	91	
	(39)	-0.0	-0.0	-0.0		—	—	—	
		0.0	—	—	0.0			—	
25	AX J1740.5−3014		−1.698	0.265					
	(22)	5.1	0.2	7.7		3.05	11.7	—	
		23.0	1.7	21.3	56.4	$^{+0.00x}_{-0.00x}$	$^{+>100}_{-<100}$	0	
	(76)	4.5	1.3	4.9		—	—	—	
		0.0	—	—	0.0			—	
26	AX J1744.5−2845		0.040	0.305					GROJ1744−28
	(2)	-0.0	-0.0	0.6		—	—	—	
		0.0	—	—	0.0			—	
	(3)	-0.0	-0.0	0.2		—	—	—	
		0.0	—	—	0.0			—	
	(9)	0.4	-0.0	1.4		—	—	—	
		0.0	—	—	0.0			—	
	(12)	—	—	—		—	—	—	
		0.0	—	—	0.0			—	
	(27)	>50	>50	>50		1.14	5.5	1724.	
		90689.5	4791.5	85898.0	103134.9	$^{+0.01}_{-0.01}$	$^{+0}_{-0}$	754	

(Continuing to the next page.)

Table 5.1: Source list (Continued from the previous page.)

No	Name		$l_{\rm II}$	$b_{\rm II}$					ID
	(Obs-ID)	$\sigma^{0.7-10}$	$\sigma^{0.7-3}$	σ^{3-10}		Γ	$N_{\rm H}$	χ^2	(refs.)
		$F_{\rm X}^{0.7-10}$	$F_{\rm X}^{0.7-3}$	$F_{\rm X}^{3-10}$	$L_{\rm X}^{2-10}$	Error	Error	d.o.f.	
	(31)	>50	>50	>50		—	—	—	
		0.0	—	—	0.0			—	
	(39)	>50	>50	>50		0.87	4.7	1453.	
		34903.8	1736.8	33167.0	37238.8	$^{+0.01}_{-0.01}$	$^{+0}_{-0}$	650	
	(55)	0.6	-0.0	1.7		—	—	—	
		0.0	—	—	0.0			—	
	(56)	-0.0	-0.0	1.2		—	—	—	
		0.0	—	—	0.0			—	
27	AX J1748.8−2709		1.888	0.333					
	(34)	-0.0	-0.0	-0.0		—	—	—	
		0.0	—	—	0.0			—	
	(46)	8.6	1.7	11.8		1.46	7.3	3.111	
		46.0	2.2	43.8	59.1	$^{+4.85}_{-<3}$	$^{+18.9}_{-<7.3}$	2	
28	AX J1743.9−2847		−0.065	0.403					
	(9)	13.3	13.2	5.2		2.64	0.7	18.06	
		8.7	4.7	4.0	5.5	$^{+1.71}_{-1.01}$	$^{+1.2}_{-<0.7}$	15	
	(27)	-0.0	5.7	-0.0		2.64	8.7	—	
		0.0	0.0	0.0	0.0	$^{+1.71}_{-1.01}$	$^{+3.4}_{-1.1}$	—	
	(31)	16.7	7.1	15.7		—	—	—	
		0.0	—	—	0.0			—	
	(39)	-0.0	23.2	-0.0		—	—	—	
		0.0	—	—	0.0			—	
	(55)	0.7	2.9	-0.0		—	—	—	
		0.0	—	—	0.0			—	
	(56)	3.9	1.9	3.5		—	—	—	
		0.0	—	—	0.0			—	
29	AX J1739.1−3020		−1.934	0.456					XTE J1739−302
	(76)	>50	>50	>50		0.85	3.2	92.17	[185]
		921.5	63.1	858.4	919.4	$^{+0.10}_{-0.10}$	$^{+0.3}_{-0.3}$	82	
30	AX J1749.2−2639		2.359	0.505					GROJ1750−27
	(25)	>50	>50	>50		0.46	3.2	140.3	
		6185.2	299.7	5885.5	6017.5	$^{+0.08}_{-0.07}$	$^{+0.3}_{-0.2}$	111	
31	AX J1742.6−2901		−0.418	0.513					
	(54)	2.5	2.8	0.7		—	—	—	
		0.0	—	—	0.0			—	
	(55)	7.1	9.2	0.8		$\gtrsim 10$	10.1	3.167	
		5.5	4.5	1.0	59.6		$^{+2.2}_{-5.4}$	5	
32	AX J1740.5−2938		−1.175	0.581					
	(77)	5.8	7.6	0.0		4.55	< 2.3	6.130	
		6.6	6.4	0.2	0.4	$^{+>5}_{-1.39}$		5	
33	AX J1742.5−2845		−0.205	0.682					
	(9)	3.6	5.3	-0.0		—	—	—	
		0.0	—	—	0.0			—	
	(29)	1.0	0.7	0.8		—	—	—	
		0.0	—	—	0.0			—	
	(31)	—	—	—		—	—	—	
		0.0	—	—	0.0			—	
	(55)	11.6	13.4	1.5		4.92	0.5	1.621	
		10.7	10.1	0.5	1.6	$^{+>5}_{-2.08}$	$^{+2}_{-<0.5}$	4	

(Continuing to the next page.)

Table 5.1: Source list (Continued from the previous page.)

No	Name		l_{II}	b_{II}					ID
	(Obs-ID)	$\sigma^{0.7-10}$	$\sigma^{0.7-3}$	σ^{3-10}		Γ	N_{H}	χ^2	(refs.)
		$F_{\mathrm{X}}^{0.7-10}$	$F_{\mathrm{X}}^{0.7-3}$	F_{X}^{3-10}	L_{X}^{2-10}	Error	Error	d.o.f.	
	(88)	8.7	12.0	0.1		6.43	3	—	
		13.6	12.0	1.6	10.6	$^{+>4}_{-5.31}$	$^{+4.8}_{-<3}$	0	
34	AX J1747.8−2633		2.285	0.824					GX 3+1
	(90)	>50	>50	>50		1.76	2.2	244.0	
		47314.1	9291.1	38023.0	45647.1	$^{+0.04}_{-0.04}$	$^{+0.1}_{-0.1}$	197	
35	AX J1739.3−2924		−1.116	0.927					
	(44)	11.2	4.5	12.0		0.98	1.8	6.910	
		15.7	1.8	13.9	14.5	$^{+1.61}_{-1.18}$	$^{+6}_{-<1.8}$	7	
36	AX J1740.3−2904		−0.726	0.931					
	(44)	17.4	11.2	13.6		0.62	0.1	8.148	
		41.3	6.3	35.0	33.3	$^{+0.64}_{-0.40}$	$^{+1.2}_{-<0.1}$	9	
	(58)	9.1	4.0	9.5		-0.39	< 44.6	6.856	
		45.1	2.5	42.7	38.1	$^{+5.05}_{-1.08}$		5	
37	AX J1740.4−2857		−0.612	0.972					
	(58)	8.5	9.2	1.9		2.66	< 0.5	16.36	
		6.1	4.6	1.6	2.1	$^{+1.27}_{-0.68}$		8	
38	AX J1739.5−2910		−0.900	1.013					
	(44)	6.5	8.2	0.1		3.93	0.2	8.422	
		3.1	2.9	0.3	0.5	$^{+>6}_{-1.34}$	$^{+1.8}_{-<0.2}$	12	
39	AX J1740.2−2848		−0.509	1.091					
	(58)	19.0	6.5	21.7		0.55	2.6	6.061	
		34.1	2.1	32.0	32.6	$^{+0.66}_{-0.74}$	$^{+3.2}_{-2.3}$	8	
40	AX J1740.7−2818		−0.028	1.255					SLX1737−282
	(29)	>50	>50	>50		2.1	1.9	103.5	
		531.7	144.9	386.8	493.5	$^{+0.11}_{-0.11}$	$^{+0.2}_{-0.2}$	94	
	(30)	>50	>50	>50		2.17	2	92.48	
		425.8	119.5	306.4	399.6	$^{+0.16}_{-0.15}$	$^{+0.2}_{-0.2}$	75	
	(60)	>50	>50	>50		2.34	2.2	31.75	
		546.5	160.9	385.6	528.9	$^{+0.21}_{-0.19}$	$^{+0.3}_{-0.3}$	35	
	(61)	>50	>50	>50		2.36	2	22.39	
		545.6	171.8	373.8	511.0	$^{+0.31}_{-0.29}$	$^{+0.5}_{-0.4}$	18	
	(88)	>50	>50	>50		2.18	1.9	43.53	
		400.9	115.6	285.3	371.0	$^{+0.19}_{-0.18}$	$^{+0.3}_{-0.2}$	36	
41	AX J1738.4−2902		−0.914	1.279					
	(44)	6.4	7.2	1.0		3.6	< 1.1	14.51	
		5.7	5.2	0.5	0.9	$^{+>6}_{-1.34}$		10	
	(59)	2.8	3.0	0.6		—	—	—	
		0.0	—	—	0.0			—	
42	AX J1737.4−2908		−1.111	1.420					GRS1734−292
	(59)	45.1	30.8	33.2		1.41	1.1	4.681	
		360.0	74.5	285.5	309.2	$^{+0.52}_{-0.50}$	$^{+1.1}_{-<1.1}$	6	
	(81)	>50	>50	>50		1.51	1.7	16.08	
		261.4	48.8	212.6	239.1	$^{+0.20}_{-0.19}$	$^{+0.4}_{-0.3}$	24	
43	AX J1735.1−2930		−1.695	1.645					
	(80)	24.9	19.8	15.3		1.8	< 0.9	6.897	
		41.4	19.8	21.6	23.9	$^{+0.73}_{-0.29}$		4	
44	AX J1734.6−2916		−1.562	1.868					
	(83)	6.7	7.4	1.4		$\gtrsim 10$	11	6.265	
		2.4	1.9	0.5	35.3		$^{+3.6}_{-<11}$	3	

(Continuing to the next page.)

Table 5.1: Source list (Continued from the previous page.)

No	Name		$l_{\rm II}$	$b_{\rm II}$					ID
	(Obs-ID)	$\sigma^{0.7-10}$	$\sigma^{0.7-3}$	σ^{3-10}		Γ	$N_{\rm H}$	χ^2	(refs.)
		$F_{\rm X}^{0.7-10}$	$F_{\rm X}^{0.7-3}$	$F_{\rm X}^{3-10}$	$L_{\rm X}^{2-10}$	Error	Error	d.o.f.	
45	AX J1739.6−2730		0.515	1.888					
	(70)	10.9	6.0	10.4		1.07	0.9	5.406	
		12.6	2.1	10.6	10.8	$^{+0.98}_{-0.97}$	$^{+2.1}_{-<0.9}$	6	
46	AX J1738.3−2659		0.797	2.408					SLX1735−269
	(15)	>50	>50	>50		2.18	1.6	321.4	
		1495.3	469.7	1025.7	1315.5	$^{+0.03}_{-0.03}$	$^{+0}_{-0}$	274	

No: Sequence number.

Name: Target name designated here.

(**Obs-ID**): Observation ID in Table 4.1.

($l_{\rm II}$, $b_{\rm II}$): Source (galactic) coordinates (deg.).

$\sigma^{0.7-10}$, $\sigma^{0.7-3}$, σ^{3-10}: Significance in 0.7–10 keV, 0.7–3 keV, 3–10 keV, respectively.

$F_X^{0.7-10}$, $F_X^{0.7-3}$, F_X^{3-10}: Observed flux in 0.7–10 keV, 0.7–3 keV, 3–10 keV, respectively (10^{-13}erg cm^{-2} s^{-1}).

$L_{\rm X}^{2-10}$: (Absorption-corrected) luminosity in 2–10 keV for the assumed distance of 8.5 kpc (10^{33}erg s^{-1}).

Γ: Photon index.

$N_{\rm H}$: Hydrogen equivalent column density in unit of 10^{22} H cm^{-2}.

Error: Statistical uncertainties with 90% confidence for one interesting parameter.

χ^2/d.o.f.: χ^2 and degree of freedom in each fitting.

ID (refs.): (X-ray) identification & references (the number is referred from Bibliography list at the end).

Table 5.2: Identification of the detected X-ray sources in the Galactic Center region

ASCA-Name (Coord.)	Radio (Coord.(offset))	IR/Optical (Coord.(offset))	X-ray (Coord.(offset))
AX J1755.2−3017 (359.912, −2.484)			
AX J1758.0−2818 (1.939, −2.020)		HD 316682 (1.928, −2.037 (73))	
AX J1754.5−2928 (0.544, −1.937)			
AX J1754.0−2930 (0.463, −1.858)			
AX J1755.7−2818 (1.681, −1.584)			
AX J1754.2−2755 (1.849, −1.100)			
AX J1748.5−2957 (359.455, −1.068)		HD 316341 (359.461, −1.083 (58))	
AX J1750.4−2900 (0.484, −0.934)			1RXP J175029.8−285957 (0.497, −0.945 (63))
AX J1747.4−3003 (359.251, −0.914)		IRAS 17442−3001 (359.272, −0.919 (74))	SLX 1744−300 (359.260, −0.911 (31))
AX J1753.6−2745 (1.914, −0.890)		IRAS 17503−2744 (1.902, −0.880 (58))	
AX J1747.4−3000 (359.293, −0.885)			SLX 1744−299 (359.299, −0.886 (22)) EQ 1744.2−2959 (359.292, −0.884 (6))
AX J1748.3−2854 (0.329, −0.475)			
AX J1751.1−2749 (1.585, −0.453)		HD 162237 (1.577, −0.473 (80))	
AX J1746.1−2931 (359.556, −0.391)			H 1742−294 (359.557, −0.387 (16)) 2E 1742.9−2929 (359.558, −0.393 (8))
AX J1748.1−2829 (0.670, −0.220)	NAME VLA J1748−2828 (0.676, −0.222 (20))		XTE J1748−288 (0.676, −0.234 (54))
AX J1742.7−3022 (358.438, −0.203)	GPSR 358.440−0.210 (358.440, −0.210 (26))	[RHI84] 10− 414 (358.454, −0.212 (65))	
AX J1744.3−2941 (359.216, −0.146)		IRAS 17410−2940 (359.198, −0.150 (65))	AX J1744.3−2940 (359.225, −0.137 (46)) [HPG94] 4 (359.219, −0.130 (57))
AX J1740.2−3102 (357.596, −0.114)			Granat 1737−31 (357.588, −0.099 (59))
AX J1743.9−2945 (359.115, −0.109)	EQ 174042−294305 (359.120, −0.101 (32))		
AX J1744.9−2921 (359.561, −0.073)	GPSR5 359.558−0.077 (359.558, −0.077 (19))	IRAS 17417−2919 (359.563, −0.082 (34)) [OF84] 5 (359.550, −0.070 (42))	KS 1741−293 (359.554, −0.067 (33))

(Continuing to the next page.)

Table 5.2: Identification table (Continued from the previous page.)

ASCA-Name (Coord.)	Radio (Coord.(offset))	IR/Optical (Coord.(offset))	X-ray (Coord.(offset))
AX J1746.4−2844 (0.257, −0.034)	[CCE98b] 000.26−0.01 (0.265, −0.013 (80))	[RHI84] 10− 568 (0.249, −0.041 (37))	2E 1743.1−2842 (0.259, −0.029 (18))
AX J1745.5−2901 (359.906, −0.015)	GRS 359.91 +00.01 (359.910, 0.000 (57))	GCIRS 27 (359.924, −0.028 (80)) [MRR94] 42 (359.903, −0.007 (32))	
AX J1749.2−2725 (1.702, 0.114)			AX J1749.2−2725 (1.701, 0.115 (6))
AX J1745.0−2855 (359.948, 0.123)	[HJB85] Sgr A−H (359.960, 0.135 (59))	[OF84] 21 (359.927, 0.115 (80))	Granat 1741−288 (359.964, 0.124 (59))
AX J1740.5−3014 (358.302, 0.265)	GPSR5 358.310+0.272 (358.310, 0.272 (35))		SAX J1740.5−3013 (358.319, 0.275 (68))
AX J1744.5−2845 (0.040, 0.305)			
AX J1748.8−2709 (1.888, 0.333)	GPSR5 1.874+0.333 (1.874, 0.333 (51)) PMN J1748−2709 (1.876, 0.322 (58)) GPSR5 1.878+0.320 (1.878, 0.320 (60)) GPSR 1.879+0.322 (1.879, 0.322 (52)) GPSR5 1.897+0.334 (1.897, 0.334 (33))		
AX J1743.9−2847 (359.935, 0.403)			
AX J1739.1−3020 (358.066, 0.456)			
AX J1749.2−2639 (2.359, 0.505)			
AX J1742.6−2901 (359.582, 0.513)			
AX J1740.5−2938 (358.825, 0.581)			1RXS J174034.3−293749 (358.831, 0.571 (42))
AX J1742.5−2845 (359.795, 0.682)		V* V2384 Oph (359.802, 0.679 (28)) GSC 06839−00253 (359.815, 0.683 (72))	
AX J1747.8−2633 (2.285, 0.824)			
AX J1739.3−2924 (358.884, 0.927)			
AX J1740.3−2904 (359.274, 0.931)			
AX J1740.4−2857 (359.388, 0.972)			1RXS J174024.6−285706 (359.388, 0.961 (40))
AX J1739.5−2910 (359.100, 1.013)	SNR 359.1+00.9 (359.100, 0.990 (80))	HD 316072 (359.104, 1.013 (11))	
AX J1740.2−2848			

(Continuing to the next page.)

Table 5.2: Identification table (Continued from the previous page.)

ASCA-Name (Coord.)	Radio (Coord.(offset))	IR/Optical (Coord.(offset))	X-ray (Coord.(offset))
(359.491, 1.091)			
AX J1740.7−2818 (359.972, 1.255)			1E 1737.5−2817 (359.960, 1.244 (57)) RX J1740.7−2818 (359.975, 1.250 (21))
AX J1738.4−2902 (359.086, 1.279)			RX J1738.4−2901 (359.091, 1.285 (28))
AX J1737.4−2908 (358.889, 1.420)		HD 316076 (358.886, 1.409 (42))	1RXS J173728.0−290759 (358.891, 1.409 (41)) 1WGA J1737.4−2907 (358.897, 1.430 (45))
AX J1735.1−2930 (358.305, 1.645)			
AX J1734.6−2916 (358.438, 1.868)			
AX J1739.6−2730 (0.515, 1.888)		Terz V 2982 (0.529, 1.888 (48))	
AX J1738.3−2659 (0.797, 2.408)		IRAS 17351−2656 (0.807, 2.422 (61))	SLX 1735−269 (0.785, 2.398 (58)) 1ES 1735−26.9 (0.799, 2.403 (20))

NOTE: — see SIMBAD database for the name of each source.

ASCA-**Name**: see Table 5.1.

Radio|**IR/Optical**|**X-ray**: SIMBAD identification with each band.

(**Coord.**): the galactic coordinates ($l_{\rm II}$, $b_{\rm II}$).

(**offset**): position offset between the catalogued value and the *ASCA* measurement in unit of arcsecond.

Chapter 6

Results II. — Nature of Bright Sources

We here report the timing and spectral results on about 10 of bright X-ray sources in the Galactic Center region. Although several sources are persistent, many of them are transient. Other than point-like sources, the results on several extended sources are also presented.

Since past hard X-ray satellites have had no direct imaging capability, their data quality of the sources in the Galactic Center region, where many sources are densely distributed, was not good. We can first resolve the sources with imaging by *ASCA*. It means that the signal to noise ratio of the data for timing or spectral analysis is definitely much better than that with past satellites except for the brightest sources. In addition, the spectral resolution of *ASCA* is much better than that of past satellites. Thus, it is expected that we can give stronger constraint for the emission mechanism, and can study the nature of each source the best.

6.1 Persistent point sources

We here define the persistent point source as the source which satisfies each of the following criteria: (1) if *ASCA* observed the source position more than twice, the case that *ASCA* always detected the source whenever *ASCA* observed the source position, (2) if *ASCA* observed the source position only once, the case that the source had been already reported with some other satellites, and that *ASCA* also detected it. In other words, for the sources which *ASCA* discovered for the first time, and of which the position was observed with *ASCA* only once, they are regarded as transient sources in this thesis, and discussed in the next section.

In consequence, the persistent point sources with 2–10 keV flux of larger than $\sim 10^{-11}$erg cm^{-2} s^{-1} in this region are 1E 1740.7−2942, A 1742−294, 1E 1743.1−2843, SLX 1737−282, GRS 1734−292, AX J1749.2−2725, SLX 1744−299, SLX 1744−300, GX 3+1, AX J1745.6−2901, and SLX 1735−269.

6.1.1 1E 1740.7−2942

1E 1740.7−2942 is one of the most unusual sources in the Galactic Center region. Detailed review can be found in Section 2.2.2. The main part of the results were published in Sakano *et al.* (1997, 1998b, 1999a).

One of the important problems for this source is the possibility that this source is directly powered from a molecular cloud (Section 2.2.2). X-ray spectrum and time variability would be keys for the study. In particular, the equivalent width of fluorescent iron line as a function of absorption column provides direct evidence whether the source is really in a dense cloud or not. Churazov, Gilfanov, & Sunyaev (1996) and Sheth *et al.* (1996) have examined the X-ray spectra of this source with the Performance Verification (PV) and AO-2 phases of the early *ASCA* operations. Their derived $N_{\rm H}$ values, hence the conclusions, are not fully consistent with each other. This is partly due to the fact that they fitted the spectra with different energy range. More serious problem for the detailed spectral study of this source, particularly on the iron line, iron K-edge and low energy absorption structures, is possible contamination of the thin thermal Galactic plasma emission which includes strong emission lines (Koyama *et al.* 1996). Thus we have made further observations after the PV and the AO-2 phases, and tried to give further constraints on the emission mechanism of this source.

Observations & Data screening

ASCA observed this source five times: the observation IDs of 1, 10, 11, 20 and 41 in Table 4.1. For this source, good SIS data in the observations with IDs of 1, 10 and 11 were obtained, hence we also analyzed the SIS data. To increase the statistics, we converted the SIS Faint data to the Bright data format and treated both modes of the data uniformly. Table 6.1 summarizes the observation log and the data screening criteria for the SIS data.

Table 6.1: Observational log with data mode, data selection etc. for SISs

Obs-ID	Phase	Bit-Rate	Data Mode	SIS Exposure[1]
1	PV	High	4CCD Faint	24
		Medium	1CCD Bright	12
7[2]	PV	High	4CCD Faint	6
		Medium	4CCD Bright	14
8[2]	PV	High	4CCD Faint	12
		Medium	4CCD Bright	3
10	AO-2	High	2CCD Faint	12
		Medium	1CCD Faint	5
11	AO-2	High	2CCD Faint	9
		Medium	1CCD Faint	4
20	AO-3	— Out of SIS FOV —		
41	AO-5	— Out of SIS FOV —		

[1] : unit of kilo-second.

[2] : These pointings do not include 1E 1740.7−2942 in their field of views (FOVs). They are used for background estimation.

Parameter	Description
SIS_RBMF=0	Only use data when RBM monitor count was below the threshold
BR_EARTH>10	Elevation from the bright earth rim
T_SAA<128	Time after SAA passage
T_DY_NT<128	Time after day-night transition
Sn_Pixlm<800	Number of SIS events above threshold

Results and Analysis

Light curves Since the X-rays from 1E 1740.7−2942 are limited to above about 2 keV (see next section or X-ray images in Fig. 5.2), we made light curve for each observation, accumulating 2–10 keV photons in the circular region within 3′ radius from the source. To increase statistics, we summed the data of SIS 0 and 1, or GIS 2 and 3 with a time bin of 256 sec. Fig. 6.1(a)–(h) show the light curves with 2–10 keV band. Constant flux assumption for the light curve of each observation is rejected by χ^2-tests with more than 90% confidence. Thus the X-ray flux was found to be variable although the variability amplitude is not large.

We also examined FFT analysis for the GIS 2+3 data of high-bit rate with 1/16 sec time resolution, and found no periodic variation in the time scale of 1/8 – 1000 second from any of the five separate observations (see Fig. 6.2 for an example).

As for the long term variability, we found the averaged flux in PV phase decreased to about 75% and 50% in AO-2 and AO-3 phases, respectively, and then increased in AO-5 phase to about the same flux as in PV phase (see Fig. 6.4 and Table 6.2).

Spectral Analysis The diffuse Galactic Center hot plasma, which is distributed near 1E 1740.7−2942, emits diffuse X-rays including strong iron lines, with significant flux variations from position to position (Koyama *et al.* 1996). Therefore the spectrum of 1E 1740.7−2942 may be contaminated by the diffuse X-rays, especially in the low energy band and in the iron line feature.

To minimize possible effect to the spectrum due to the background variation for the detailed study of the iron line of this source, we accumulated the source X-ray photons in a small circle of $2'$ radius and extracted the background taken from the annulus of $2'$–$4'$ radius. We thus made the background subtracted spectra with GIS2+3 and SIS0+1 for each observation phase. For two data sets in AO-2 phase (Obs-ID=10 & 11), we summed the data and treated them as one data set since the satellite attitudes in both the observations were nearly the same, and since we found no significant spectral differences in both the data. For the AO-3 data, we excluded the region closely near to the detector edge or the calibration isotope from the background region.

We fitted each spectrum with an absorbed power-law, using the photo-electronic cross-sections by Bałucińska-Church & McCammon (1992). The abundances for the absorbing matters were fixed to the solar values (Anders & Grevesse 1989), but that of iron was allowed to be varied, because the 7.1-keV edge structure carries unique information of the iron column. The spectrum in each observation with the best-fit model is given in Fig. 6.3(a)–(f) and the best-fit parameters for all the observations are listed in Table 6.2.

We then fitted the GIS and the SIS data for each phase simultaneously with a power-law model. The results with the best statistics are also given in Table 6.2. The best-fit photon index is in the range of 0.9–1.3, the hydrogen column density is $(8\text{–}11)\times10^{22}$ H cm^{-2}, and the iron abundance is found to be about 2 solar.

Although we found no clear emission line in each spectrum, we included a 6.4 keV line for the further fitting, because the emission line from neutral iron at

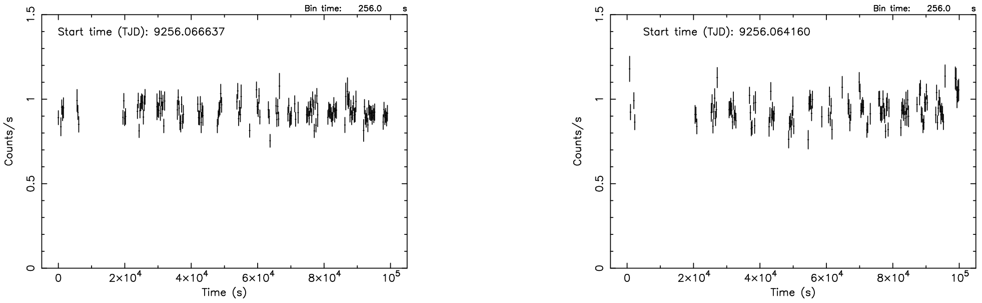

(a) GIS2+3 data of PV (Obs-ID=1) (b) SIS0+1 data of PV (Obs-ID=1)

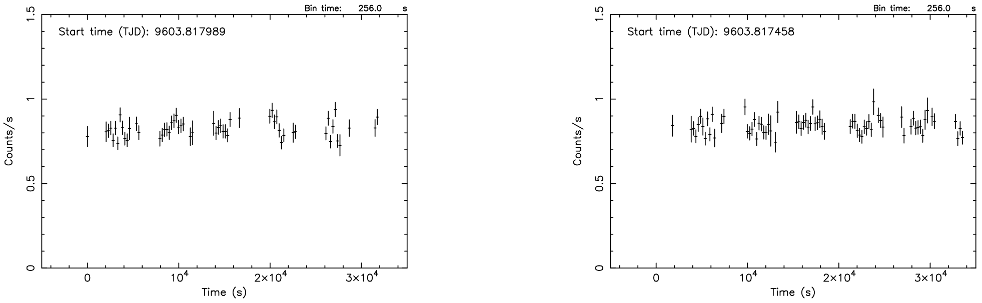

(c) GIS2+3 data of AO-2 (Obs-ID=10) (d) SIS0+1 data of AO-2 (Obs-ID=10)

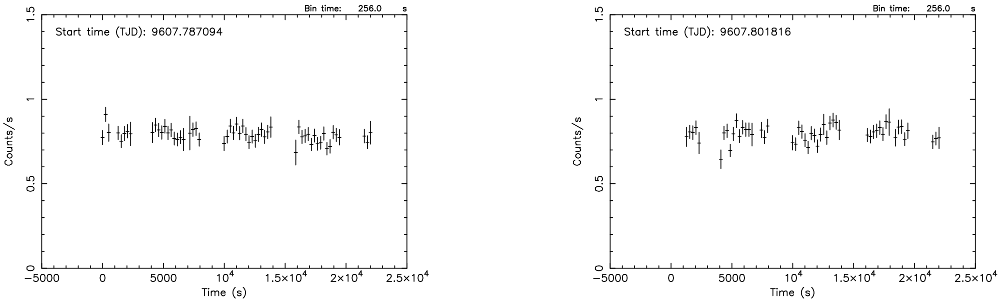

(e) GIS2+3 data of AO-2 (Obs-ID=11) (f) SIS0+1 data of AO-2 (Obs-ID=11)

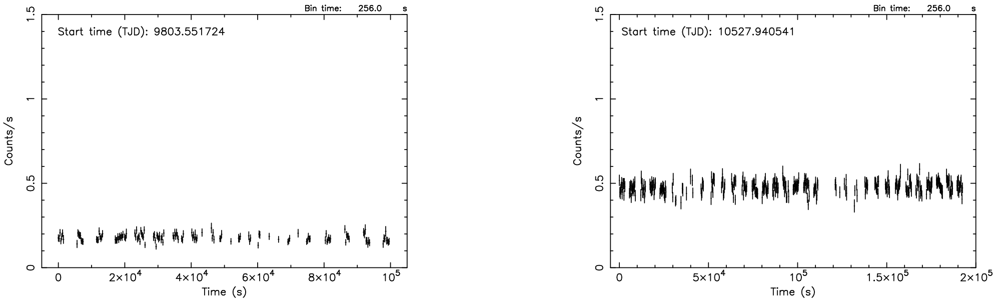

(g) GIS2+3 data of AO-3 (Obs-ID=20) (h) GIS2+3 data of AO-5 (Obs-ID=41)

Figure 6.1: (1E 1740.7−2942) The 2–10 keV light curves with 256 second bin taken with GIS 2+3 or SIS 0+1. Unit of the start and the end time is TJD.

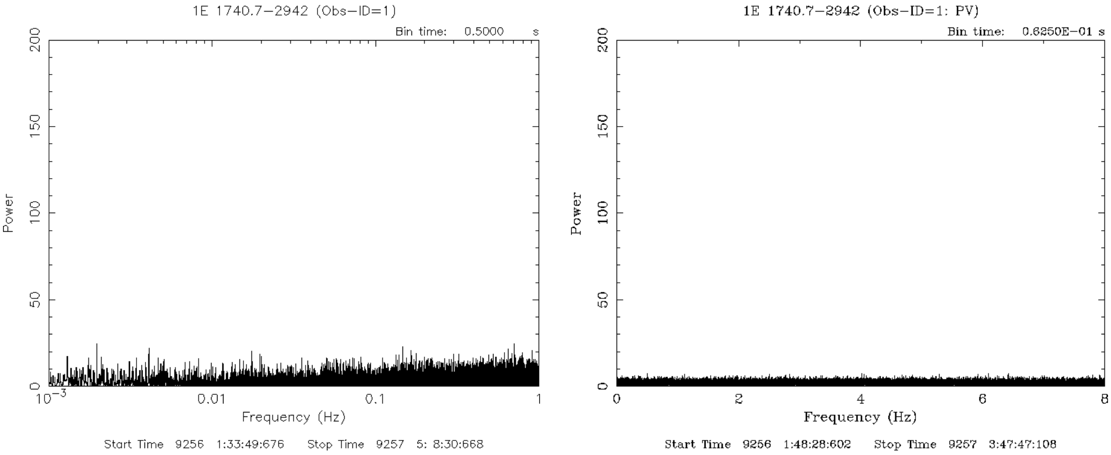

Figure 6.2: (1E 1740.7−2942) The GIS2+3 power spectrum density for the 2–10 keV band data of Obs-ID=1. (left) High and medium-bit data were used. (right) Only high-bit data were used.

6.4 keV gives direct information around the cold gas near 1E 1740.7−2942. In this fitting we fixed the line energy and the intrinsic width to be 6.4 keV and 0 keV, respectively. The resultant parameters are listed in Table 6.2 together with the 2–10 keV flux (absorption included).

In Fig. 6.4, we summarize the long term spectral behavior. No significant difference, except for the flux change, is found from observation to observation in a time span of 3.5 years. In addition, the spectral slope is rather flat. Thus we can conclude that 1E 1740.7−2942 has been in the hard sate of the galactic black hole spectrum.

Since the galactic black hole candidates often have a soft component with temperature of less than 1.0 keV (e.g., Tanaka & Lewin 1995; van Paradijs 1998), we examined whether the 1E 1740.7−2942 spectrum requires a soft component or not. We tried to fit the data with a power-law model adding a soft black body component, and found no significant improvement by this procedure, hence the spectrum requires no soft component. However it is not clear whether this is real or merely due to large absorption in the low energy band.

The Galactic diffuse emission includes strong iron K-shell lines from neutral (at 6.4 keV) and highly ionized irons (at 6.7 keV and 6.97 keV) (Koyama *et al.* 1996; Maeda 1998). Since the K-shell line of a neutral iron (6.4 keV) plays a key role for the nature of 1E 1740.7−2942, we estimated the fluctuation of the diffuse K-shell lines (the 6.4 keV-lines) in the source extraction region, using the SIS data. We made spectra from a circular region with a radius of $4'$ near the center of each SIS chip in the mapping observations of the Galactic Center region. We then fitted each

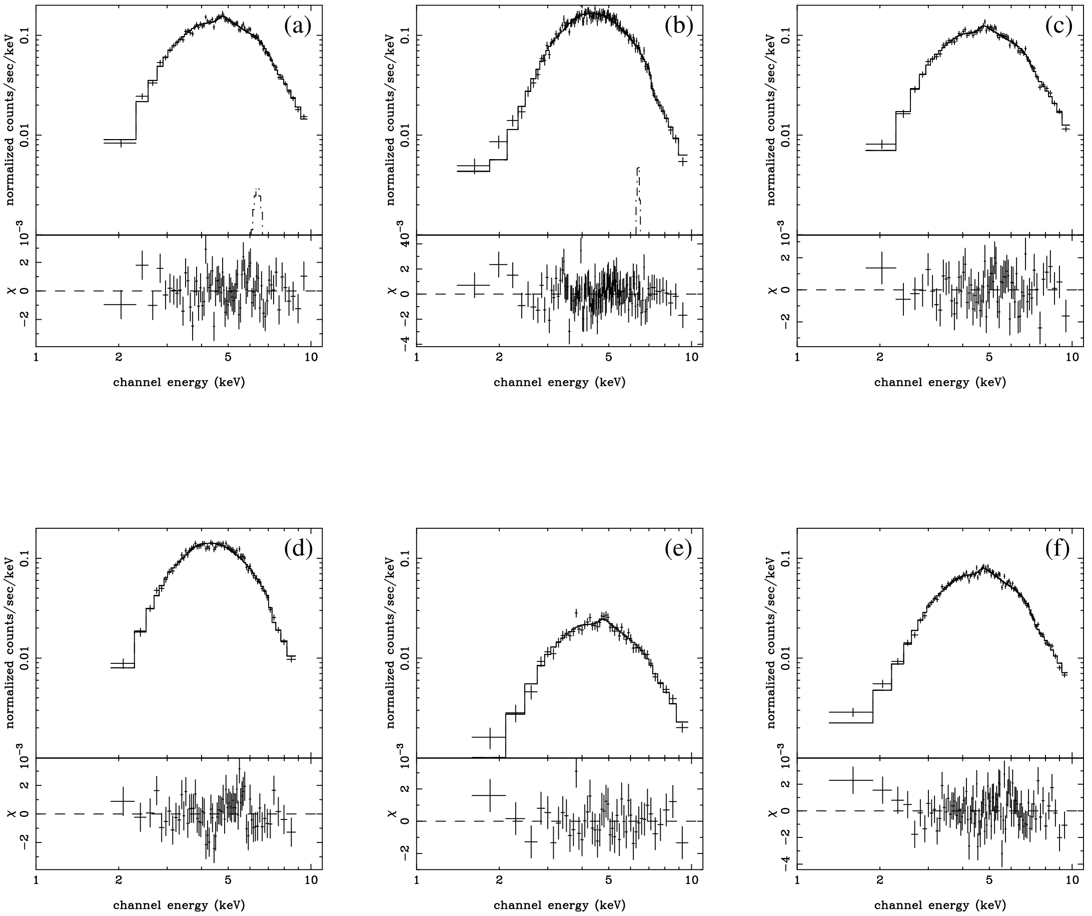

Figure 6.3: (1E 1740.7−2942) GIS2+3 or SIS0+1 spectra with the best-fit model; (a) PV (Obs-ID=1; GIS 2+3), (b) PV (Obs-ID=1; SIS 0+1), (c) AO-2 (Obs-ID=10+11; GIS 2+3), (d) AO-2 (Obs-ID=10+11; SIS 0+1), (e) AO-3 (Obs-ID=20; GIS 2+3), (f) AO-5 (Obs-ID=41; GIS 2+3). Note that the data for the two observations in AO-2 phase (Obs-ID=10 & 11) are summed and treated as one data set.

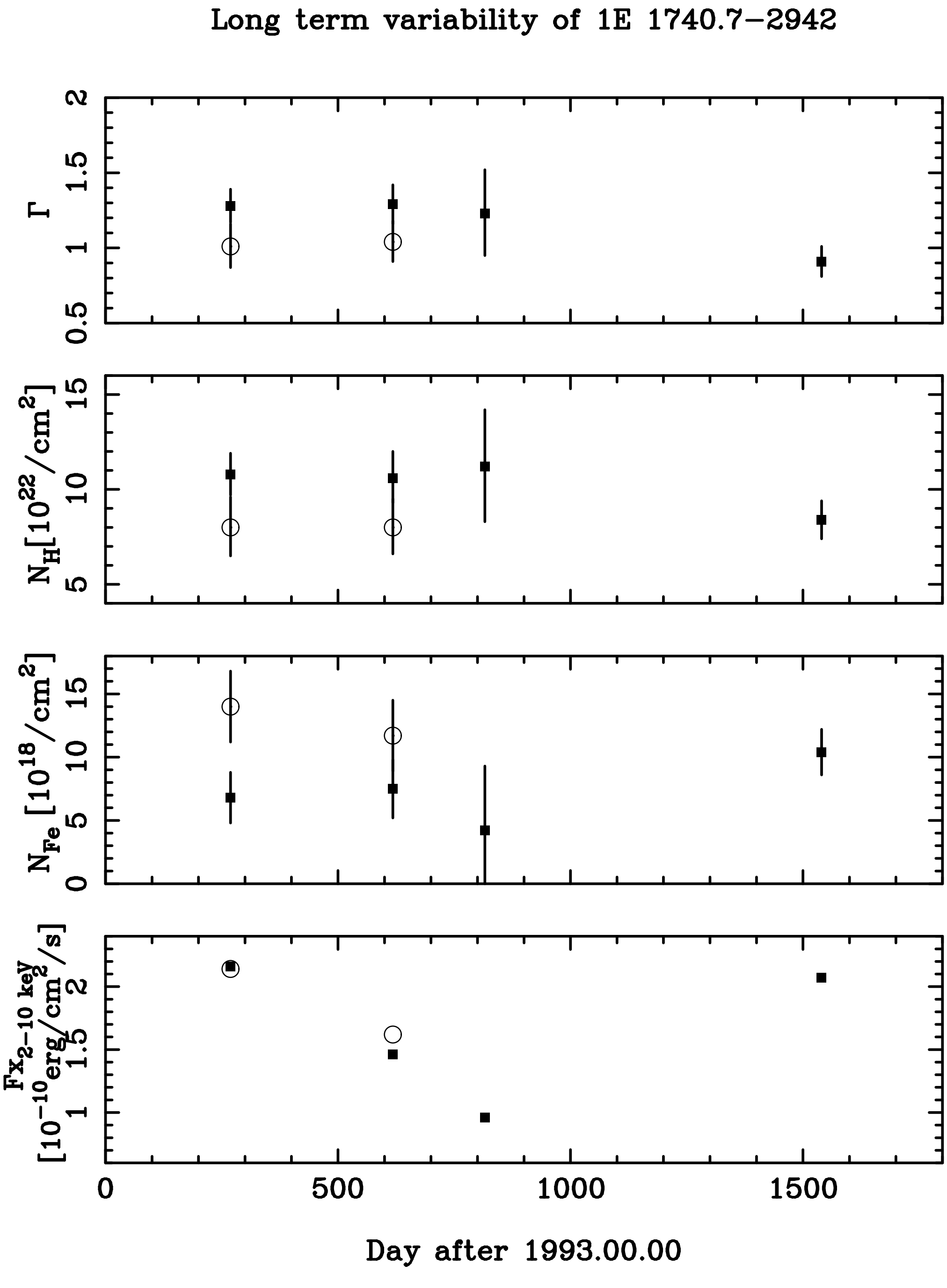

Figure 6.4: (1E 1740.7−2942) Long term variability of a power-law photon index Γ, hydrogen column density N_{H} in unit of 10^{22} H cm^{-2}, iron column density N_{Fe} in unit of 10^{18} Fe cm^{-2} and the observed X-ray flux in the 2–10 keV band F_{X} in unit of 10^{-10} erg cm^{-2} s^{-1}. Close boxes and open circles represent the data taken with GIS and SIS, respectively.

Table 6.2: (1E 1740.7−2942) Best-fit parameters in the fitting with a power-law function

		Absorbed Power-law Model						6.4 keV-line Inclusive	
Phase		$\Gamma^{\dagger}$	$I_{1\mathrm{keV}}{}^{\ddagger}$	$N_{\mathrm{H}}{}^{\P}$	$N_{\mathrm{Fe}}{}^{\S}$	χ^2/d.o.f.	$F_{\mathrm{X}}{}^{\%}$	$L_{6.4\mathrm{keV}}{}^{\#}$	$EW_{6.4\mathrm{keV}}{}^{\$}$
PV	GIS	1.28 ± 0.11	$4.8^{+1.1}_{-0.9}$	10.8 ± 1.1	6.7 ± 2.0	89.2/69	2.16	6 ± 8	17 ± 22
	SIS	$1.01^{+0.15}_{-0.14}$	$3.0^{+1.0}_{-0.7}$	$8.0^{+1.6}_{-1.5}$	14.0 ± 2.8	136.4/115	2.14	5 ± 7	13 ± 18
	GIS+SIS	1.18 ± 0.09	$4.0^{+0.7}_{-0.6}$	9.8 ± 0.9	9.3 ± 1.6	256.0/188	2.15	5 ± 5	13 ± 14
AO-2	GIS	1.29 ± 0.13	$3.3^{+1.0}_{-0.7}$	$10.6^{+1.4}_{-1.3}$	7.5 ± 2.3	73.4/63	1.46	< 6.3	< 25
	SIS	$1.04^{+0.14}_{-0.13}$	$2.3^{+0.7}_{-0.5}$	$8.0^{+1.5}_{-1.4}$	11.7 ± 2.8	75.4/63	1.62	< 4.8	< 17
	GIS+SIS	1.24 ± 0.09	$3.2^{+0.6}_{-0.5}$	9.8 ± 1.0	$9.1^{+1.8}_{-1.7}$	238.9/130	1.51	< 4.3	< 15
AO-3	GIS	$1.23^{+0.29}_{-0.28}$	$2.0^{+1.4}_{-0.8}$	$11.2^{+3.0}_{-2.9}$	4 ± 5	46.6/44	0.96	< 9	< 56
AO-5	GIS	0.91 ± 0.10	$2.3^{+0.5}_{-0.4}$	8.4 ± 1.0	10.4 ± 1.8	131.6/89	2.07	0.7 ± 7	2 ± 20

[†]: Photon index.

[‡]: Intensity of continuum at 1keV [10^{-2}photon keV^{-1} cm^{-2} s^{-1}] (absorption corrected).

[¶]: Hydrogen column density [10^{22} H cm^{-2}].

[§]: Iron column density [10^{18} Fe cm^{-2}].

[%]: Observed flux with 2–10 keV [10^{-10} erg cm^{-2} s^{-1}].

[#]: Luminosity of 6.4keV-line [10^{-5}Photon cm^{-2} s^{-1}] (absorption corrected).

[$]: Equivalent width of 6.4 keV-line [eV].

spectrum in the 4.5–10 keV band with a continuum plus three Gaussian lines fixing the center energies to be 6.4, 6.7 and 6.97 keV. The intensity ratio of the 6.7 keV to 6.97 keV lines was kept to be constant from place to place, because Maeda (1998) and Koyama *et al.* (1996) found no significant variation of the flux ratio. Fig. 6.5 shows the 6.4 keV-line fluxes along positions, where the flux is converted to the value in a $2'$ radius, the same radius of the source region. From Fig. 6.5, we can safely conclude that uncertainty of the iron line flux in 1E 1740.7−2942 due to the background fluctuation is less than 0.6×10^{-5} photon sec^{-1} cm^{-2}/($2'$-circle). This value is, at most, 15% of that from 1E 1740.7−2942, hence can be ignored in the following discussion.

Discussion

Absorption and Iron Abundance The *ASCA* results of 1E 1740.7−2942 have been already reported by Churazov *et al.* (1996) and Sheth *et al.* (1996). Although they used essentially the same data sets, their results are not fully consistent with each other. The major difference is found in the N_{H} values.

With a single power-law fitting and absorption gas of solar abundance, Churazov *et al.* (1996) gave N_{H} to be 1.7×10^{23} H cm^{-2} of the *ASCA* spectrum in the range of the 4–10 keV band, but found 1×10^{23} H cm^{-2} when the full energy range of 0.4–10 keV was used. Sheth *et al.* (1996) estimated N_{H} to be 0.8×10^{23} H cm^{-2}

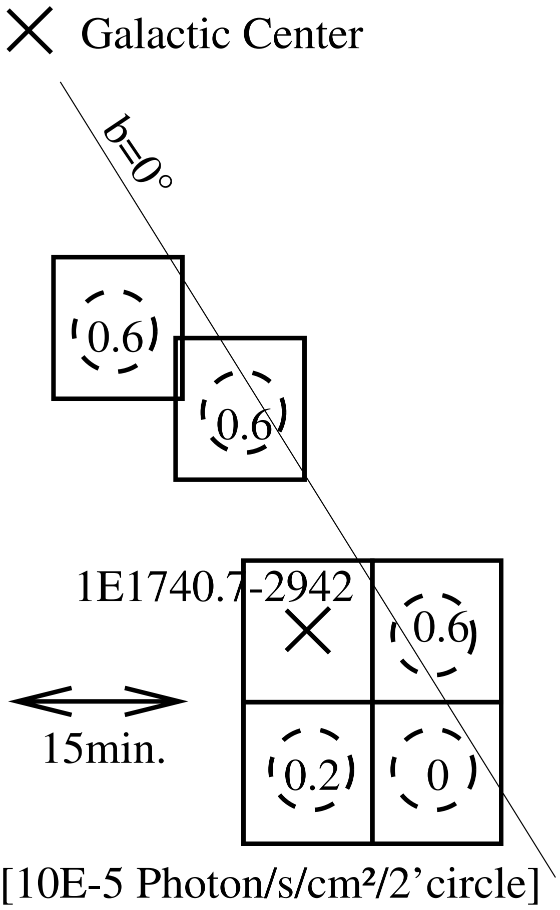
Galactic Center
b=0°
0.6
0.6
1E1740.7-2942
0.6
15min.
0.2
0
[10E-5 Photon/s/cm²/2'circle]

Figure 6.5: (1E 1740.7−2942) Diffuse 6.4-keV line distribution near 1E 1740.7−2942 estimated by a spectral analysis in a 4′ radius circle of each SIS chip for the data taken in 1993 (Obs-ID=7 & 8; see Table 6.1). The best-fit flux of the neutral iron 6.4 keV line is normalized to the value in a 2′ radius region with an assumption of the uniform distribution of diffuse 6.4 keV line in the circle. These are given in the circles on the figure with the unit of 10^{-5} photon s^{-1} cm^{-2}/(2′-radius circle).

by the same model fitting but in the 0.5–12 keV range. We found that the apparent inconsistency can be solved if iron is overabundant relative to the other elements. In fact, we have shown that the spectra of 1E 1740.7−2942 are well presented with a single-power model absorbed by the gas column of 1×10^{23} H cm^{-2}, in which iron abundance is 2 solar.

Murakami *et al.* (1999a, 2000a, 2000b) analyzed the reflected X-ray by the giant molecular cloud Sgr B2, which is located in nearly the same (angular) distance but in the opposite direction from the Galactic Center, and found that iron is overabundant relative to the other elements. On the other hand, Sellgren, Carr, & Balachandran (1997), Ramírez *et al.* (1998), and Carr *et al.* (1999) with the infrared observations of the atmosphere on the giant stars near the Galactic Center, estimated that the iron abundance relative to hydrogen is consistent with the solar value. Thus further deep observations of K-edge absorption feature of X-ray sources near the Galactic Center are required.

No change of $N_{\rm H}$ during the *ASCA* long term observations implies that the absorption region should have a size larger than a few light-yrs, excluding a possibility of an accretion disk or stellar corona. Thus 1E 1740.7−2942 is very likely to be located near at the Galactic Center.

The radio observations of the large molecular cloud toward 1E 1740.7−2942, on the other hand, gave the total hydrogen column density to be $N_{\rm H} \sim 6 \times 10^{23}$ H cm^{-2} (Bally *et al.* 1991; Vilhu *et al.* 1997). One may argue, however, that the conversion factor from the CO line intensity to the hydrogen column density may have large uncertainty. Oka *et al.* (1998), for example, pointed out that the usual conversion factor is not appropriate for the clouds in the Galactic Center region, and that the derived mass in the ordinary manner should be reduced by several factors. Taking this possible uncertainty into account, we still suspect that the molecular cloud is located behind 1E 1740.7−2942.

6.4-keV iron line We found no significant line emission from a neutral iron (6.4 keV-line). The upper-limits of the equivalent width are estimated to be a few ten eV, depending on the observation period and detector. The most stringent limit is found to be 15 eV in the combined (GIS and SIS) analysis of AO-2. These results of small equivalent width further confirm the result by Churazov *et al.* (1996) with larger data sets.

The equivalent width <15 eV implies that the mean iron column density around 1E 1740.7−2942 is less than $N_{\rm Fe} < 5 \times 10^{17}$ Fe cm^{-2} (Inoue 1985; Awaki 1991). This value is smaller than 1/10 of the total column density estimated from the 7.1 keV edge depth. Hence 1E 1740.7−2942 cannot be in a local dense cloud as suggested by Bally & Leventhal (1991) and Mirabel *et al.* (1991).

Bally & Leventhal (1991) estimated the required local density of the interstellar matter around 1E 1740.7−2942 for the observed luminosity of 1E 1740.7−2942 when it is powered directly by the interstellar matter in the case of Bondi-Hoyle accretion (Bondi & Hoyle 1944). The calculated luminosity is,

$$L = 2.3 \times 10^{36}\ \eta \left[\frac{M}{M_{\odot}}\right]^{2} \left[\frac{v}{10\ \mathrm{km\ s^{-1}}}\right]^{-3} \left[\frac{n_{\mathrm{H}}}{10^{4}\ \mathrm{cm^{-3}}}\right] \quad (\mathrm{erg\ s^{-1}}), \tag{6.1}$$

where η is the fraction of the released energy with emission from the rest mass energy, M is the mass of the central compact object, v is the relative velocity of the compact object against the cloud, and n_{H} is the hydrogen density of the cloud. The highest luminosity of 1E 1740.7−2942 in the *ASCA* observations is estimated to be 3×10^{36} erg s^{-1}, from the X-ray flux of 2×10^{-10} erg cm^{-2} s^{-1} in the 2–10 keV band and the source distance of 8.5 kpc. Since the spectrum is extracted within $2'$-radius (5 pc-radius), the observed upper-limit of the iron equivalent width is converted to the local density of

$$n_{\mathrm{H}} = 7 \times 10^{2}\ (Z_{\mathrm{Fe}})^{-1} \quad (\mathrm{H\ cm^{-3}}), \tag{6.2}$$

where Z_{Fe} is iron abundance relative to solar.

Then, assuming $\eta = 0.1$, we can set possible ranges of M and v for the Bondi-Hoyle accretion scenario as is given in Fig. 6.6 with solid lines, while the dashed line shows the most probable case of $Z_{\mathrm{Fe}} = 2$ in equation (2). Thus we find that the velocity of 1E 1740.7−2942 must be less than 10 km s^{-1} even in the case of the large mass of 20M$_{\odot}$ under the Bondi-Hoyle accretion scenario.

The velocity of black holes would be larger than that of normal stars due to additional kick velocity by supernova explosions. Since no data of the velocity dispersion of black holes are found, the best alternative way to estimate the velocity of 1E 1740.7−2942 is to use the velocity dispersion of neutron stars, which are also produced by supernova explosions. Thus we refer the velocity dispersion of the radio pulsars (neutron stars) (Lorimer *et al.* 1997; Hansen & Phinney 1997) and find that the velocity of 1E 1740.7−2942 would be larger than 10 km s^{-1} with more than 99% probability. We therefore conclude that the Bondi-Hoyle scenario that 1E 1740.7−2942 is powered directly from a molecular cloud is unlikely.

Long term variability Pavlinsky *et al.* (1994) reported the long term variability of 1E 1740.7−2942 measured with ART-P on board *Granat*. According to

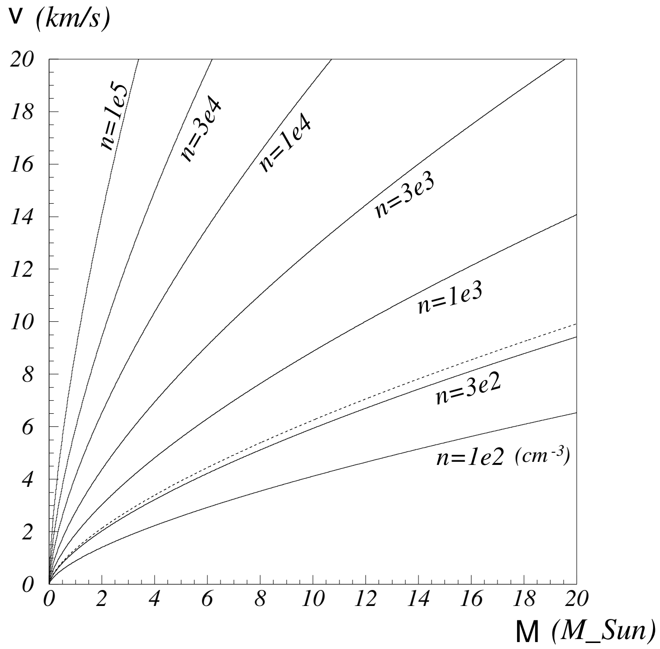

Figure 6.6: The relation between the mass (M) and the velocity (v) of the central source for certain cloud density (n) to explain the observed luminosity of 1E 1740.7−2942 in the Bondi-Hoyle scenario (solid lines). The dashed line shows the case of the estimated upper limit of the density (eq. [2] with $Z_{\mathrm{Fe}} = 2$).

their results, 1E 1740.7−2942 was usually in a medium or high state since 1990 with occasional exceptions of low state. Since the spectral shape during the *ASCA* observations showed no significant change except for the variability of the total flux, we safely assume that the spectra in the *Granat* observations has the same photon index ($\Gamma \sim 1.2$) as those of the *ASCA* spectra. Then we found that the *ASCA* fluxes of (1–2)$\times10^{-10}$ erg cm^{-2} s^{-1} in the 2–10 keV band corresponds to (2.5–5)$\times10^{-10}$ erg cm^{-2} s^{-1} in the 8–20 keV band, the middle to high-state fluxes of *Granat.* The *ASCA* flux is also in agreement with the BATSE light curve for the same period (Zhang *et al.* 1997). The similarity between the *ASCA* and BASTE light curves is another indication of the spectral invariance over larger energy range.

Summary

Using all the *ASCA* data of 1E 1740.7−2942, available at the time of this writing, we conclude as follows:

1. We found that 1E 1740.7−2942 was in the middle to high flux state, showing long term variation of the factor of two in a span of 3.5 years, while the photon index and column density have been nearly constant.

2. The wide band spectrum in the 1–10 keV band is well fitted with an absorbed power-law, where the iron abundance is twice as the others in a unit of solar value. The power-law slope is particularly flat with $\Gamma = 0.9$–1.3, which implies that 1E 1740.7−2942 was in the hard state. The large hydrogen column density of $N_{\rm H} \sim 1 \times 10^{23}$ H cm^{-2} supports the location of 1E 1740.7−2942 to be near the Galactic Center.

3. From the iron-edge structure we estimated the iron column density to be $N_{\rm Fe} \sim 1 \times 10^{19}$ Fe cm^{-2}.

4. The iron equivalent width has been very small with the upper-limit of 15 eV. This indicates that the iron column near around 1E 1740.7−2942 is less than $N_{\rm Fe} < 5 \times 10^{17}$ Fe cm^{-2}.

5. Our results favor the geometry that 1E 1740.7−2942 is not in the radio molecular cloud. The cloud would be, by chance, in the line of sight to, or possibly behind 1E 1740.7−2942. This indicates that the X-ray emission does not originate by the direct accretion from the molecular cloud. 1E 1740.7−2942 is probably a normal black hole binary.

6.1.2 A 1742−294

A 1742−294 is the brightest persistent source in the Galactic Center $2° \times 2°$ degree. The preliminary results with *ASCA* were published in Maeda *et al.* (1994) and Sakano *et al.* (1998b).

Observations

ASCA observed this source four times: the observation IDs of 6, 7, 41, and 51 in Table 4.1. Note that we did not use GIS3 data for the observation ID=7 because A 1742−294 is located very close to the calibration isotope of GIS3. In fact, A 1742−294 is located out of the GIS good mask (see the second subsection in Section 5.1.1 and Fig. 5.1 for the good mask).

Time variabilities

Fig. 6.7(a)–(e) show the GIS2+3 light curve in each observation. We clearly detected 11 bursts with the duration of about 10–20 seconds. Fig. 6.8 shows a burst profile with hardness ratio of a typical burst, where the hardness ratio is defined as Count(1–3keV)/Count(3–10keV). Most of the bursts were found to show spectral

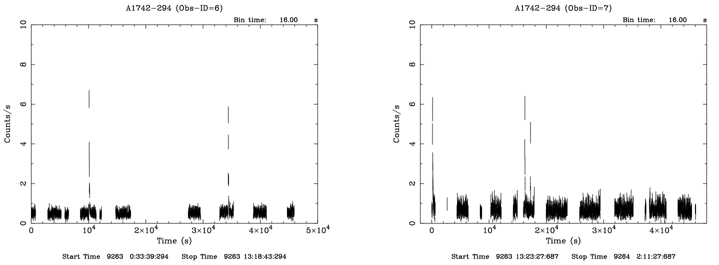

(a) Obs-ID=6 (b) Obs-ID=7

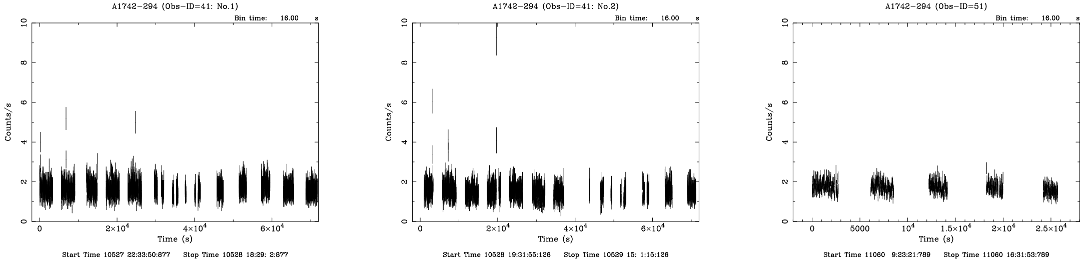

(c) Obs-ID=41 (1st half) (d) Obs-ID=41 (2nd half) (e) Obs-ID=51

Figure 6.7: (A 1742−294) The GIS2+3 light curves with 16 sec bin for 2–10 keV band. Eleven bursts were detected. Unit of the start and the end time is TJD.

softening in the burst decay phase, which implies that those bursts are the type-I bursts, whereas a few bursts show not so clear type-I features possibly due to lack of statistics. In consequence, we confirmed that this source is a low mass X-ray binary (LMXB) of a neutron star.

The peak flux in the largest burst was derived to be about 1×10^{-8} erg cm^{-2} s^{-1}. If we assume that this burst reaches the Eddington limit for a neutron star with the mass and the radius of 1.4 $M_\odot$ and 10 km, respectively, the distance to A 1742−294 is estimated at about 11 kpc.

We also found the significant variability for $\sim 10^4$ seconds (Fig. 6.9) with amplitude of about 20%, as well as the long term variability for years by a factor of 2.5. Although we tried the pulse search with FFT analysis, no significant periodicity was found (see Fig. 6.10 for an example).

Spectral analysis

We fitted the spectrum of A 1742−294 with a power-law function with absorption by solar-abundance material. For the data of Obs-ID=41, which has the best statistics, the fitting result was found to be rejected, although for the data of Obs-ID=7 and 51, the result was sufficiently good probably due to lack of statistics. The fitting results are given in Table 6.3 and in Fig. 6.11.

The most significant residual of the fitting is seen above iron K-edge (Fig. 6.11).

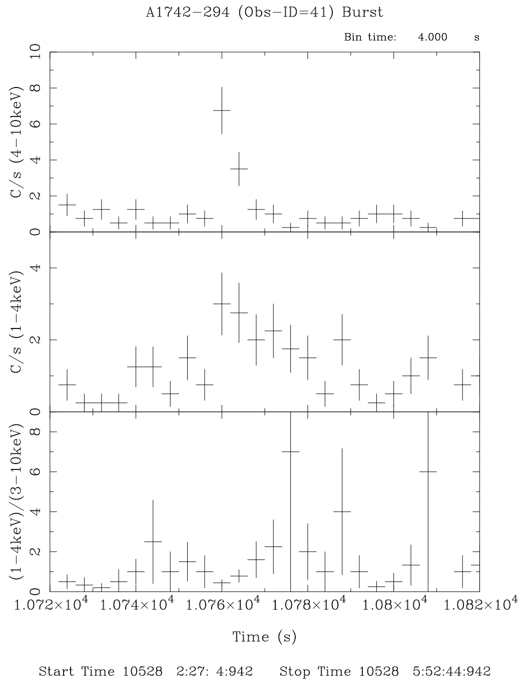

Figure 6.8: (A 1742−294) Typical burst profile with hardness ratio, taken with GIS2+3. Each bin width is 4 sec. The upper, middle and lower panels show the profiles of 4–10 keV band, 1–4 keV band, and hardness ratio defined as (Count rate of 1–4 keV)/(Count rate of 4–10 keV), respectively.

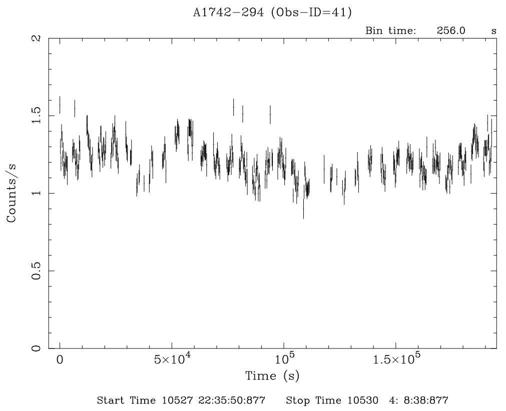

Figure 6.9: (A 1742−294) The GIS2+3 light curves with 256 sec bin for Obs-ID=41 with 2–10 keV. Significant time variability for 10^4 sec was detected. Unit of the start and the end time is TJD.

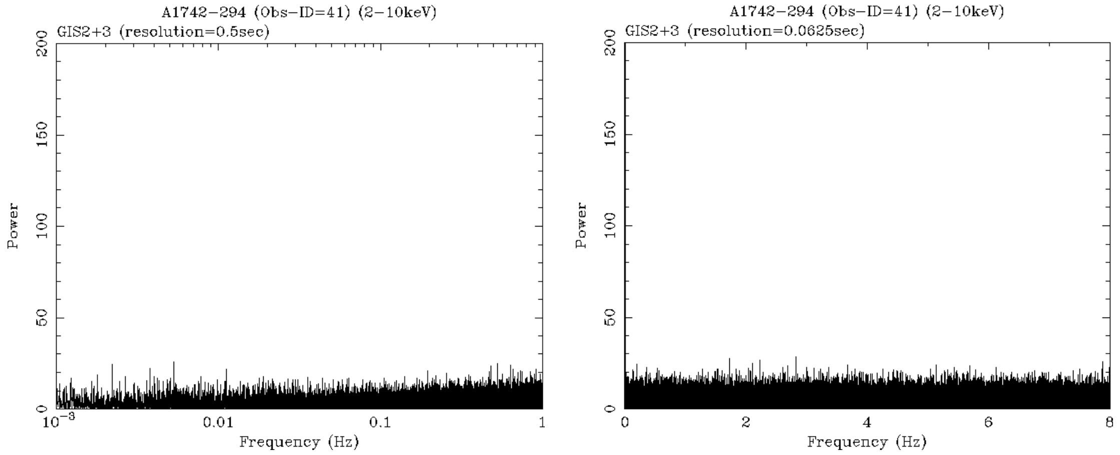

Figure 6.10: (A 1742−294) The GIS2+3 power spectrum density for the 2–10 keV band data of Obs-ID=41. (left) High and medium-bit data were used. (right) Only high-bit data were used.

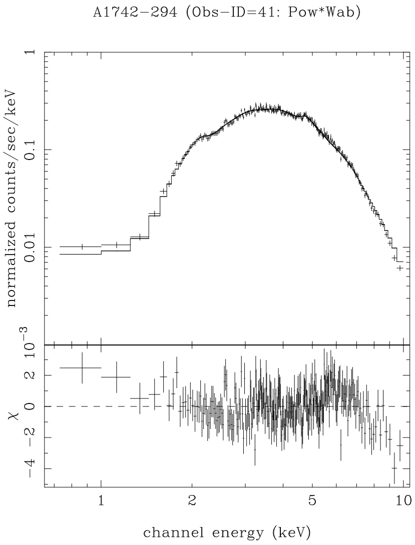

Figure 6.11: (A 1742−294) The GIS2+3 spectra in observation ID=41 and the model when we applied a power-law function with absorption with the ISM of solar abundance material.

It suggests that the iron abundance of the absorbing matter may be larger than the solar value, which we first assumed. Then we allowed the iron (and heavier atoms than iron) abundance of the absorbing matter to be varied, and fitted the spectra with the absorbed power-law model. Table 6.3 and Fig. 6.12 show the best-fit parameters with 90% confidence uncertainties and the best-fit models with the data spectra, respectively. The fitting results are accepted within 90% confidence also for the data of Obs-ID=41[1]. Consequently the best-fit photon index, the hydrogen (equivalent) column density and iron abundance for the absorbing matter were found to be 1.7, 3.5×10^{22}H cm^{-2} and 4 (solar), respectively.

Discussion

The fact that A 1742−294 shows type-I X-ray bursts strongly suggests that this source is a LMXB. The spectral shape (power-law function with photon index of 1.7) is also typical of LMXBs. In addition, long term variability by a few factors is also the usual nature of LMXBs. Thus we confirmed that A 1742−294 is a LMXB.

---

[1] For the data of Obs-ID=6, the fitting result is still bad. The residual is largely scattered. The most distinct residual is at between 5 and 6 keV. It may be the artifact, possibly due to the incomplete background subtraction or calibration uncertainty. In fact, the detected position in the data were near to the detector edge, where the background is high.

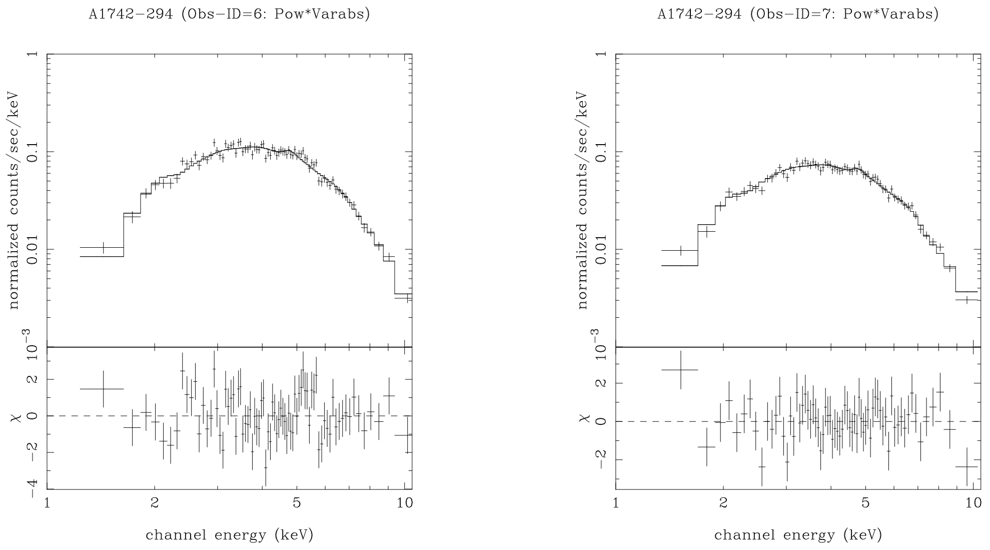

(a) Obs-ID=6

(b) Obs-ID=7

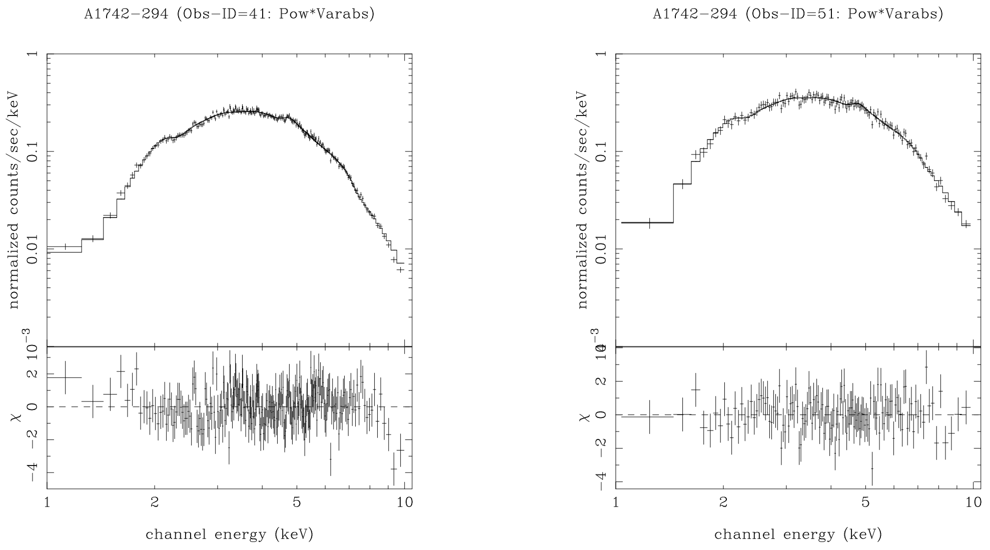

(c) Obs-ID=41

(d) Obs-ID=51

Figure 6.12: (A 1742−294) The GIS2+3 spectra with the best-fit model. The fitting model is a power-law function with absorption by ISM of which the abundances are fixed to be solar, but allowed to be free for only iron.

Table 6.3: (A 1742−294) Best-fit parameters in the fitting with a power-law function.

Obs-ID	$\Gamma^{\dagger}$	$I_{1\mathrm{keV}}{}^{\ddagger}$	$N_{\mathrm{H}}{}^{\P}$	$N_{\mathrm{Fe}}{}^{\S}$	$F_{\mathrm{X}}{}^{\%}$	χ^2/d.o.f.
(In the case of the absorbing matter with solar abundances)						
6	$1.40^{+0.10}_{-0.10}$	$5.6^{+1.0}_{-1.0}$	$5.9^{+0.4}_{-0.4}$	(linked)$^{\#}$	2.64	104.3/75
7	$1.64^{+0.10}_{-0.10}$	$7.5^{+1.4}_{-1.2}$	$6.5^{+0.4}_{-0.4}$	(linked)$^{\#}$	2.25	67.31/66
41	$1.84^{+0.03}_{-0.03}$	$24.8^{+1.3}_{-1.3}$	$6.6^{+0.1}_{-0.1}$	(linked)$^{\#}$	5.27	292.4/228
51	$1.82^{+0.07}_{-0.06}$	$9.4^{+1.1}_{-1.0}$	$5.8^{+0.3}_{-0.2}$	(linked)$^{\#}$	2.12	125.6/128
(In the case of the absorbing matter with iron abundance anomaly)						
6	$1.36^{+0.14}_{-0.14}$	$5.2^{+1.4}_{-1.1}$	$4.4^{+1.8}_{-1.9}$	4^{+4}_{-4}	2.62	103.3/74
7	$1.46^{+0.15}_{-0.15}$	$5.6^{+1.6}_{-1.2}$	$3.0^{+2.0}_{-2.0}$	8^{+4}_{-4}	2.23	63.52/65
41	$1.69^{+0.05}_{-0.05}$	$19.3^{+1.6}_{-1.4}$	$3.5^{+0.6}_{-0.6}$	$7.4^{+1.4}_{-1.4}$	5.23	253.8/227
51	$1.73^{+0.10}_{-0.10}$	$8.1^{+1.5}_{-1.3}$	$3.9^{+1.3}_{-1.3}$	5^{+3}_{-3}	2.12	122.6/127

†: Photon index.

‡: Intensity of continuum at 1keV [10^{-2}photon keV^{-1} cm^{-2} s^{-1}] (absorption corrected).

$\P$: Hydrogen column density [10^{22} H cm^{-2}].

§: Iron column density [10^{18} Fe cm^{-2}].

$^{\%}$: Observed flux with 2–10 keV [10^{-10} erg cm^{-2} s^{-1}].

$^{\#}$: Iron column density is simultaneously varied with hydrogen column density with solar abundance ratio.

Lewin *et al.* (1976) found type-I bursts of which the peak luminosity is 10^{39}erg s^{-1} or larger on the assumption of the distance to be 10 kpc. It implies that this source is probably located in front of the Galactic Center; the distance may be about 5 kpc. However, since then, no burst with such high luminosity has been reported in spite of the intensive observations of the Galactic Center region with many satellites; the reported maximum burst luminosity after SAS-3 observations by Lewin *et al.* (1976) was 1×10^{38}erg s^{-1} (for a distance of 8.5 kpc) with *Granat*/ART-P observation by Pavlinsky *et al.* (1994), which is consistent with our results. SAS-3 results might have some systematic uncertainty because the detector was not an imaging one, and the luminosity of nearby other sources were unknown. On the other hand, our estimated peak luminosity is much more reliable, because we could clearly resolve the source, although we are not confident whether the burst really reached the Eddington limit or not. Consequently, the distance to A 1742−294 is probably about the same as that to the Galactic Center or a little further, although the possibility that the distance is 5 kpc or nearer cannot be excluded.

Summary

- We have detected A 1742−294 four times with *ASCA*. We detected 11 bursts, and found most of them to be type-I bursts. Hence we confirmed this source to be a persistent bright LMXB. The distance to the source estimated from the burst peak flux suggests that the source distance is about the same as that of the Galactic Center.
- We found the time variability from 10^4 sec to years by a factor of 2.
- The spectrum was found to be well represented with an absorbed power-law function, but require that the absorbing matter is iron-overabundant of about four times as the solar ratio.

6.1.3 1E 1743.1−2843

Although 1E 1743.1−2843 is a relatively bright persistent source, the nature has been not well studied. The preliminary results with *ASCA* were published in Maeda *et al.* (1994) and Sakano *et al.* (1998b), Cremonesi *et al.* (1999).

Observations

ASCA observed this source 10 times: the observation IDs of 2, 3, 4, 5, 12, 13, 14, 21, 27 and 39 in Table 4.1. Note that we did not use the data of the observation ID=27 because (1) the statistics was bad due to the quite bright transient pulsar GRO J1744−28 (see Nishiuchi *et al.* 1998), (2) 1E 1743.1−2843 was detected at near the detector edge where NXB rate is high, whereas we have no rise-time information to reject NXB in this observation (see Table 4.2). The total exposure time is about 340 ksec[2].

Analysis & Results

First we searched time variability for 1E 1743.1−2843. Fig. 6.13(a)–(i) show the light curves with 2–10 keV band of this source taken with GIS2+3. We found time

---

[2] In fact, we had another 38 ksec observation with medium bit-rate in Obs-ID=39, although they are not included in Table 4.1. In the observation, GRO J1744−28 was so bright that the telemetry saturation occurred in the medium bit-rate data. Therefore, we do not use the medium bit-rate data of Obs-ID=39 in principle, according to the criterion for the telemetry saturation, described in Section 4.2.2. However, we used also those data in searching for the burst-like activity. In that case, the total exposure time is about 380 ksec.

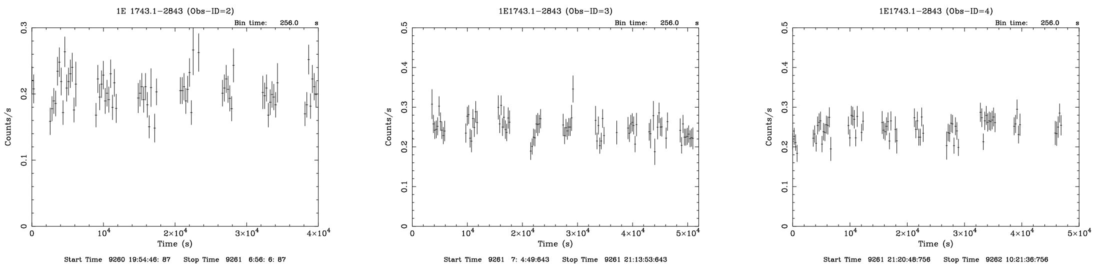

(a) Obs-ID=2 (b) Obs-ID=3 (c) Obs-ID=4

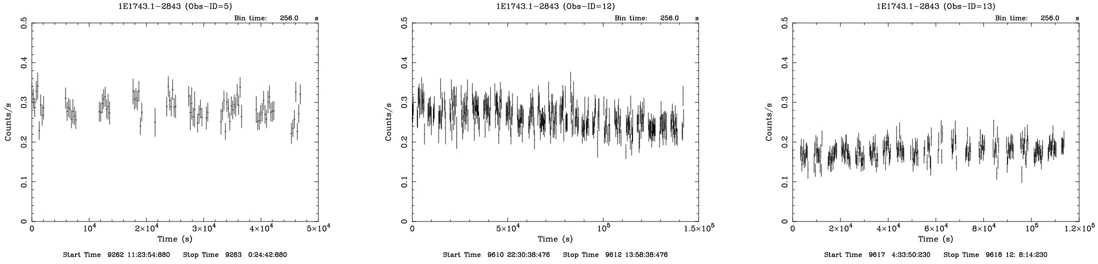

(d) Obs-ID=5 (e) Obs-ID=12 (f) Obs-ID=13

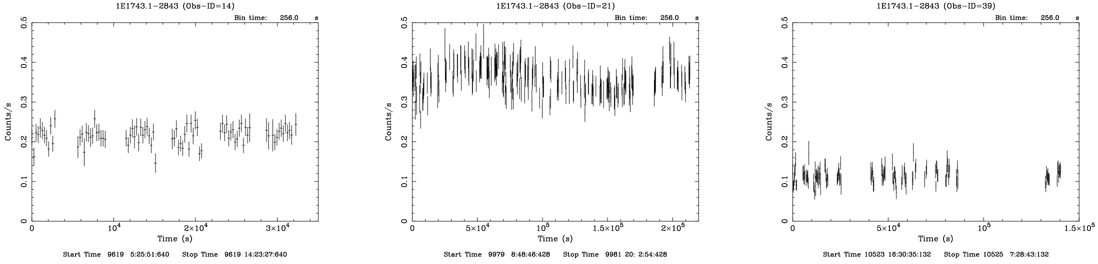

(g) Obs-ID=14 (h) Obs-ID=21 (i) Obs-ID=39

Figure 6.13: (1E 1743.1−2843) The GIS2+3 light curves with 256 sec bin for 2–10 keV bands. Unit of the start and the end time is TJD.

variability with various scale of 10^3–10^5 sec with amplitude of $\lesssim 20\%$. On the other hand we found neither significant burst-like activity like type-I bursts nor pulsation from this source (see the FFT results for the Obs-ID=21 (Fig. 6.14), of which the data have the best statistics).

The spectrum in each period is found to be almost well represented with an absorbed power-law function. Table 6.4 and Fig. 6.15 show the best-fit parameters with 90% confidence uncertainties and the best-fit models with the data spectra, respectively. The spectral shape had been nearly constant through 4 years observations with photon index of $\Gamma \sim 1.9$ and hydrogen (equivalent) column density of $N_{\mathrm{H}} \sim 1.9 \times 10^{22}$H cm^{-2}, although we found the flux variability by a factor of 2 for years.

Then we investigated the long term variability since 1979, using references (see Section 2.2.4 and Table 2.1). For past observation results by other satellites, we assume the spectral shape to be the same as our *ASCA* result, and converted their

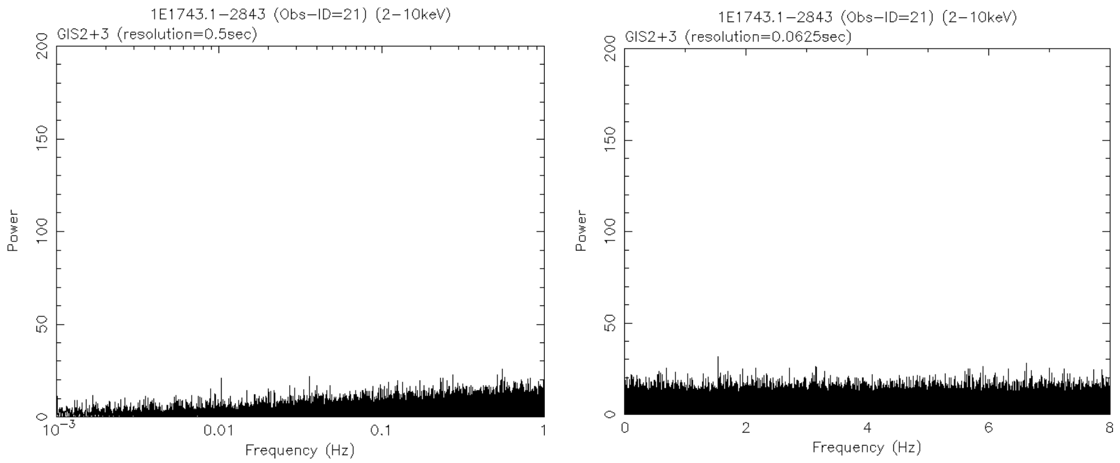

Figure 6.14: (1E 1743.1−2843) The GIS2+3 power spectrum density for the 2–10 keV band data of Obs-ID=21. (left) High and medium-bit data were used. (right) Only high-bit data were used.

count rate to the luminosity. We assume the distance to the source to be the same as that of the Galactic Center, 8.5 kpc. Fig 6.16 shows the result. Significant variability by a factor of larger than 2 is seen.

Discussion

We found that the column density to 1E 1743.1−2843 is rather large, $N_{\rm H}\sim 2\times 10^{23}$H cm^{-2}, which seems larger than column densities of many other sources of this region. This source position is quite near to the Galactic plane, $b_{\rm II}\sim -0.03^\circ$, which corresponds to the angular distance from "true" Galactic plane that goes through Sgr A* is only about 0.02°. Therefore, the large column density of this source could be due to the small distance from the plane, where dense molecular clouds are intensively distributed. Anyway, this large column density implies that 1E 1743.1−2843 is located in the Galactic Center region or further.

Then we consider the category of this source. The large absorption may suggest that 1E 1743.1−2843 is a background object behind our galaxy, such as an extragalactic AGN. No significant flux above the 35 keV band with past observations (e.g., Goldwurm *et al.* 1994), which indicates spectral turn-off near the energy 10–30 keV, probably rules out the AGN or galactic black hole possibility. In addition, if this source was an AGN, it should be the AGN with the brightest persistent X-ray flux.

On the other hand, the large absorption may suggest the proto star origin. However, if this source was a proto star, the distance should be less than several tens parsec, calculated from the averaged X-ray luminosity of proto stars, $\sim 10^{31}$erg s^{-1}

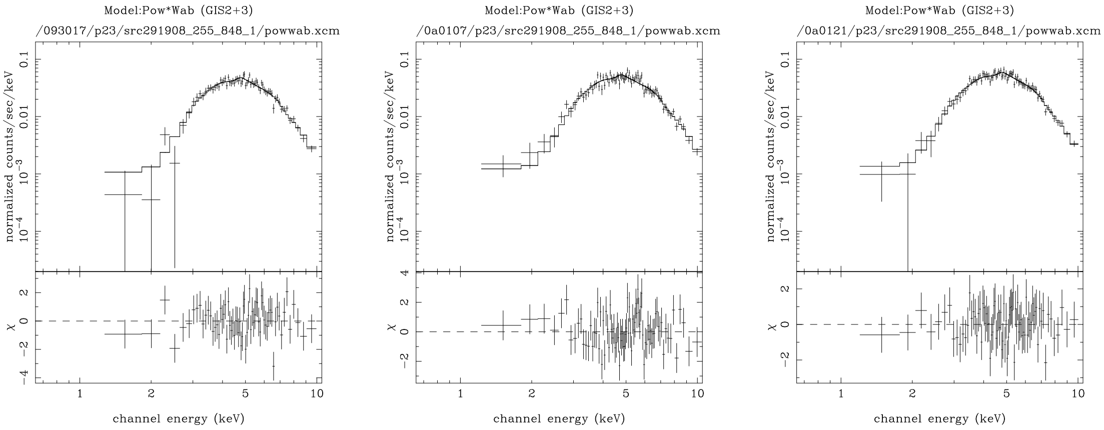

(a) Obs-ID=2 (b) Obs-ID=3 (c) Obs-ID=4

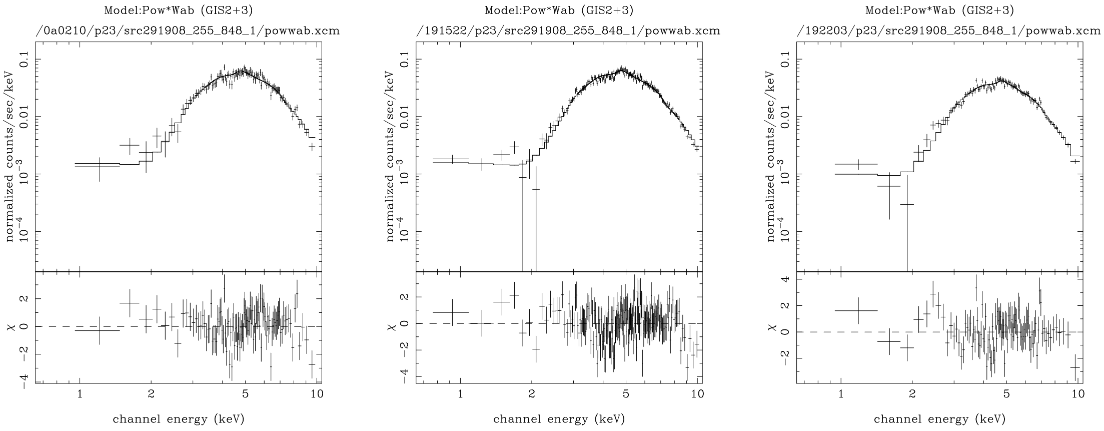

(d) Obs-ID=5 (e) Obs-ID=12 (f) Obs-ID=13

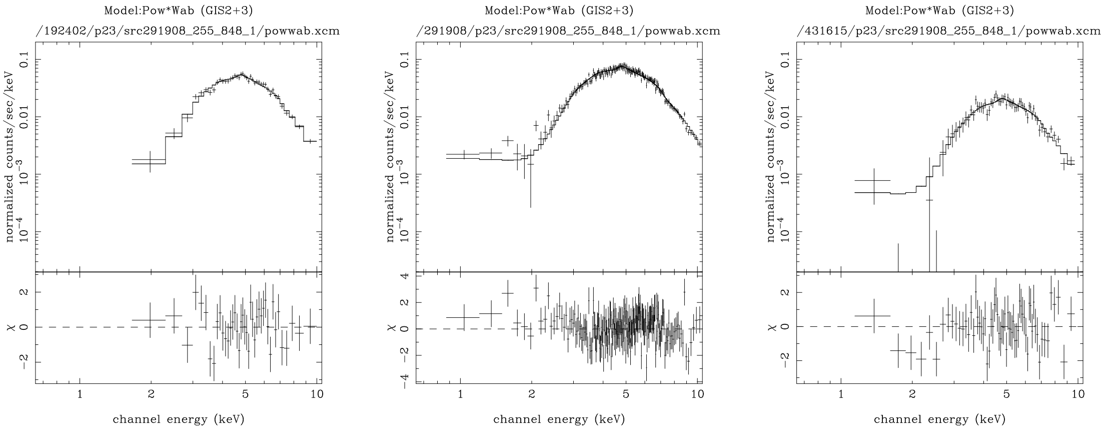

(g) Obs-ID=14 (h) Obs-ID=21 (i) Obs-ID=39

Figure 6.15: (1E 1743.1−2843) The GIS2+3 spectra when an absorbed power-law function is applied.

Table 6.4: (1E 1743.1−2843) Best-fit parameters in the fitting with a power-law function.

Obs-ID	$\Gamma^{\dagger}$	$I_{\rm 1keV}{}^{\ddagger}$	$N_{\rm H}{}^{\P}$	$F_{\rm X}{}^{\%}$	χ^2/d.o.f.
2	$2.11^{+0.22}_{-0.21}$	$11.1^{+6.0}_{-3.7}$	$19.5^{+1.9}_{-1.7}$	0.9	70.32/64
3	$1.90^{+0.21}_{-0.20}$	$8.4^{+4.4}_{-2.8}$	$19.1^{+1.9}_{-1.8}$	1.0	105.4/79
4	$1.77^{+0.19}_{-0.19}$	$6.4^{+2.9}_{-1.9}$	$17.6^{+1.6}_{-1.5}$	1.0	63.74/77
5	$1.42^{+0.18}_{-0.17}$	$4.1^{+1.7}_{-1.2}$	$16.7^{+1.5}_{-1.4}$	1.3	119.8/102
12	$1.83^{+0.08}_{-0.08}$	$7.9^{+1.4}_{-1.1}$	$18.2^{+0.7}_{-0.7}$	1.1	244.0/180
13	$1.76^{+0.13}_{-0.12}$	$5.9^{+1.7}_{-1.3}$	$17.4^{+1.1}_{-1.0}$	1.0	138.2/94
14	$1.71^{+0.19}_{-0.19}$	$7.6^{+3.6}_{-2.3}$	$18.9^{+1.7}_{-1.6}$	1.3	39.17/38
21	$2.12^{+0.09}_{-0.09}$	$7.3^{+1.5}_{-1.2}$	$18.6^{+0.8}_{-0.8}$	0.60	208.4/190
39	$1.65^{+0.35}_{-0.33}$	$4.2^{+4.2}_{-2.0}$	$20.6^{+3.3}_{-3.0}$	0.76	69.77/61

†: Photon index.

‡: Intensity of continuum at 1keV [10^{-2}photon keV^{-1} cm^{-2} s^{-1}] (absorption corrected).

$\P$: Hydrogen column density [10^{22} H cm^{-2}].

§: Iron column density [10^{18} Fe cm^{-2}].

$^{\%}$: Observed flux with 2–10 keV [10^{-10} erg cm^{-2} s^{-1}].

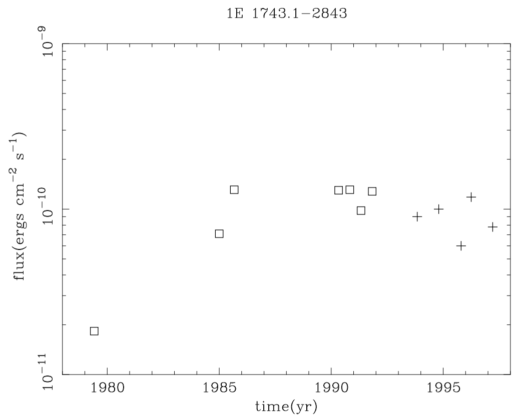

Figure 6.16: (1E 1743.1−2843) Long term variability including other satellites results. Crosses are for the *ASCA* data, whereas open rectangles are for the other satellite data.

(Tsuboi 1999). In such a case, infrared or radio observations should have already found this region as a proto star region, whereas no evidence for that has been reported.

From the spectral shape of power-law spectrum with photon index of 1.8, the flux and the time variability, in consequence, a LMXB near the Galactic Center is the most probable candidate. Thus X-ray luminosity for the distance to 8.5 kpc is estimated to be 2×10^{36}erg s^{-1}, a luminosity in which type-I bursts are expected. However, no burst has been detected through long term observations not only with *ASCA* but also with other previous instruments, with perhaps more than 1200 ksec exposure in total.

Summary

- We have detected 1E 1743.1−2843 ten times, always in the observations with *ASCA*. We found the time variability from 10^3 sec to years by a factor of 2.
- The spectrum was found to be well represented with an absorbed power-law function with photon index of 1.9 and $N_{\rm H}$ of $\sim 1.9 \times 10^{23}$H cm^{-2}.
- The most likely candidate for the class of this source is a LMXB. However, firm evidence, such as, type-I burst or discovery of the companion star, has not been found, yet.

6.1.4 SLX 1737−282

Observations

ASCA observed this source 5 times: the observation IDs of 29, 30, 60, 61 and 88 in Table 4.1. Note that we did not use the the GIS3 data for the observation IDs of 60 and 61 because the source is located out of the GIS good mask (see the second subsection in Section 5.1.1 and Fig. 5.1 for the good mask).

Analysis & Results

The detailed nature on SLX 1737−282 has been unknown, including the information whether this source is a persistent source or not (see Section 2.2.5). Therefore, we first made an identification of this source. Skinner *et al.* (1987) reported the coordinates of SLX 1737−282 to be ($l_{\rm II}$, $b_{\rm II}$)=(359.°994, 1.°202) with error radius of 3′ by *Spacelab*-2 measurement or to be ($l_{\rm II}$, $b_{\rm II}$)=(359.°981, 1.°242) with error radius of 1′ by *Einstein* measurement. Our detected position of AX J1747.0−2818

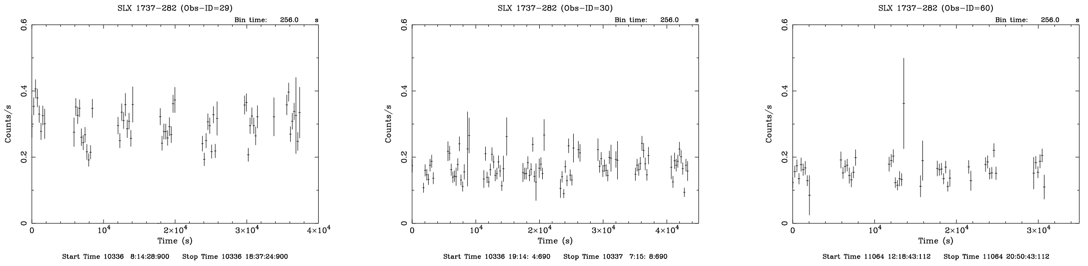

(a) Obs-ID=29 (b) Obs-ID=30 (c) Obs-ID=60

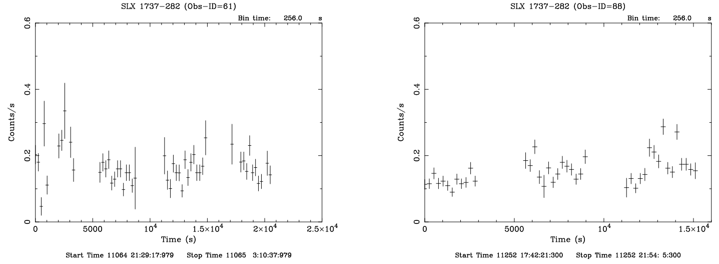

(d) Obs-ID=61 (e) Obs-ID=88

Figure 6.17: (SLX 1737−282) The GIS2+3 light curves with 256 sec bin for 2–10 keV bands. Unit of the start and the end time is TJD.

is ($l_{\rm II}$, $b_{\rm II}$)=(359.°972, 1.°255) with error radius of 1′ (Table 5.1). Thus, the offsets of the *ASCA* position from the the *Spacelab*-2 and the *Einstein* measurements are 3.′42 and 0.′96, respectively. From the positional coincidence and the hard X-ray emission, we identified AX J1747.0−2818 in Table 5.1 as SLX 1737−282.

We searched time variability for SLX 1737−282. Fig. 6.17(a)–(e) show the light curves with 2–10 keV band of this source taken with GIS2+3. We found time variability with various scale of 10^3–10^4 sec with amplitude of 100% at maximum. On the other hand we found neither significant burst-like activity like type-I bursts nor pulsation from this source (see the FFT results for the Obs-ID=30 (Fig. 6.18), of which the data have the best statistics).

The spectrum in each period is found to be almost well represented with an absorbed power-law function. Table 6.5 and Fig. 6.19 show the best-fit parameters with 90% confidence uncertainties and the best-fit models with the data spectra, respectively. The spectral shape had been nearly constant through 2.5 years observations with photon index of Γ = 2.1–2.4 and hydrogen (equivalent) column density of $N_{\rm H}$= (1.8–2.2)$\times 10^{22}$H cm^{-2}, although we found the long term flux variability with small amplitude of less than 30%.

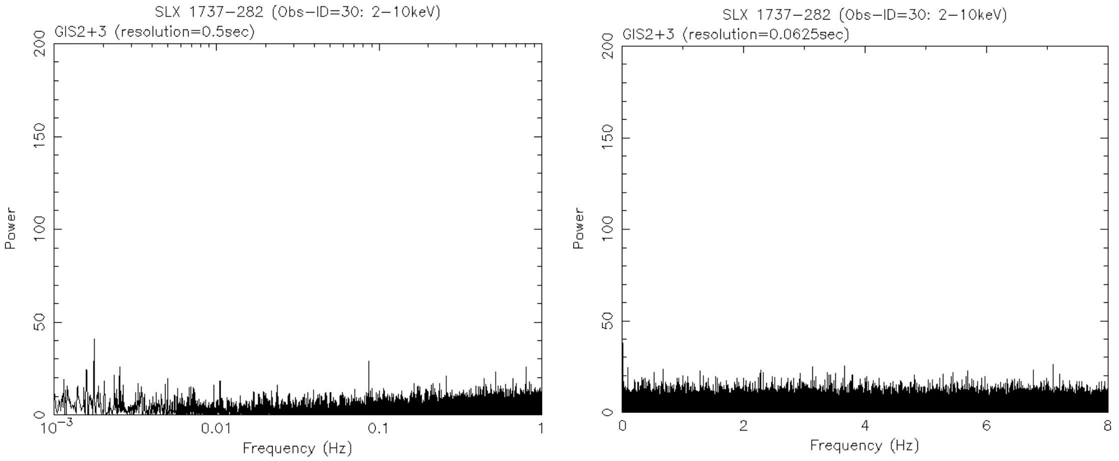

Figure 6.18: (SLX 1737−282) The GIS2+3 power spectrum density for the 2–10 keV band data of Obs-ID=30. (left) High and medium-bit data were used. (right) Only high-bit data were used.

Table 6.5: (SLX 1737−282) Best-fit parameters in the fitting with a power-law function.

Obs-ID	$\Gamma^{\dagger}$	$I_{\rm 1keV}{}^{\ddagger}$	$N_{\rm H}{}^{\P}$	$F_{\rm X}{}^{\%}$	χ^2/d.o.f.
29	$2.10^{+0.11}_{-0.11}$	$2.6^{+0.5}_{-0.4}$	$1.86^{+0.17}_{-0.16}$	4.8	103.5/94
30	$2.17^{+0.16}_{-0.15}$	$2.3^{+0.6}_{-0.5}$	$1.95^{+0.25}_{-0.23}$	3.8	92.48/75
60	$2.34^{+0.21}_{-0.19}$	$3.9^{+1.4}_{-1.0}$	$2.17^{+0.33}_{-0.30}$	4.9	31.75/35
61	$2.36^{+0.31}_{-0.29}$	$3.9^{+2.1}_{-1.3}$	$1.97^{+0.48}_{-0.44}$	4.8	22.39/18
88	$2.18^{+0.19}_{-0.18}$	$2.2^{+0.7}_{-0.5}$	$1.86^{+0.27}_{-0.25}$	3.6	43.53/36

†: Photon index.

‡: Intensity of continuum at 1keV [10^{-2}photon keV^{-1} cm^{-2} s^{-1}] (absorption corrected).

¶: Hydrogen column density [10^{22} H cm^{-2}].

§: Iron column density [10^{18} Fe cm^{-2}].

$^{\%}$: Observed flux with 2–10 keV [10^{-11} erg cm^{-2} s^{-1}].

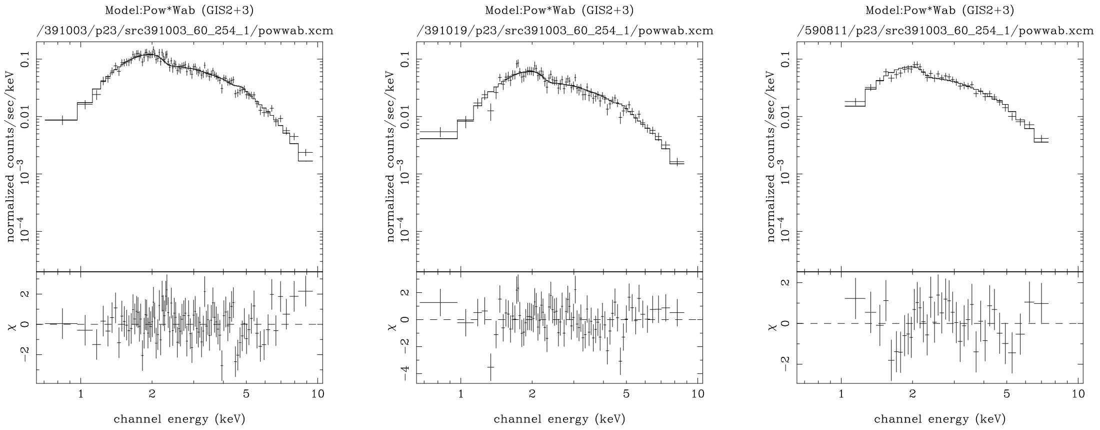

(a) Obs-ID=29 (b) Obs-ID=30 (c) Obs-ID=60

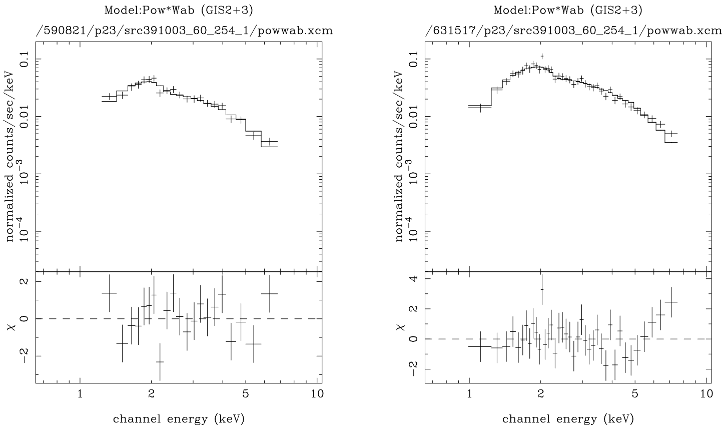

(d) Obs-ID=61 (e) Obs-ID=88

Figure 6.19: (SLX 1737−282) The GIS2+3 spectra when an absorbed power-law function is applied.

Discussion

We found that the column density to SLX 1737−282 is not small, $N_{\rm H}\sim 2\times 10^{22}$H cm^{-2}, which suggests that it is not located near the sun, but located in the distance of kpc order or farther. If we assume the distance to be the same as the Galactic Center, the absorption-corrected luminosity for 2–10 keV band is 6×10^{35} erg s^{-1}, which is, in fact, consistent with the upper limit derived with *Granat*/ART-P by Pavlinsky *et al.* (1994).

The featureless spectrum is a typical nature for LMXBs. The photon index of about 2.2 is within the nominal range of that of LMXBs. On the other hand, the spectrum is much steeper than that of X-ray pulsars with high mass companion. No significant flux above the 35 keV band with past observations (e.g., Goldwurm *et al.* 1994), which indicates spectral turn-off near the energy 10–30 keV, probably rules out the AGN or galactic black hole possibility. The violent variability of this source might suggest the cataclysmic variable (CV) origin. However, CVs generally have strong iron K-line (e.g, Ezuka & Ishida 1999), while this source does not show such a nature.

Summary

- We have detected SLX 1737−282 five occasions from 1996 to 1999 with the 2–10 keV observed flux of (3.5–5.0)$\times10^{-11}$ erg cm^{-2} s^{-1}. It suggests that this source is a persistent source.

- We found that the spectral shape had been nearly constant through 2.5 years observations and was well represented with an absorbed power law function with photon index of Γ = 2.1–2.4 and hydrogen (equivalent) column density of $N_{\rm H}$= (1.8–2.2)$\times10^{22}$H cm^{-2}.

- This column density value implies that the distance of this source may be several kpc or farther. The absorption-corrected luminosity for 2–10 keV band is 6×10^{35} erg s^{-1} for the assumed distance of 8.5 kpc.

- We also found the intensity variability of 10^3–10^4 seconds with amplitude of 100%, whereas we found no significant pulsation or burst-like activity.

- The category of SLX 1737−282 is still unknown, although a LMXB is the most likely candidate.

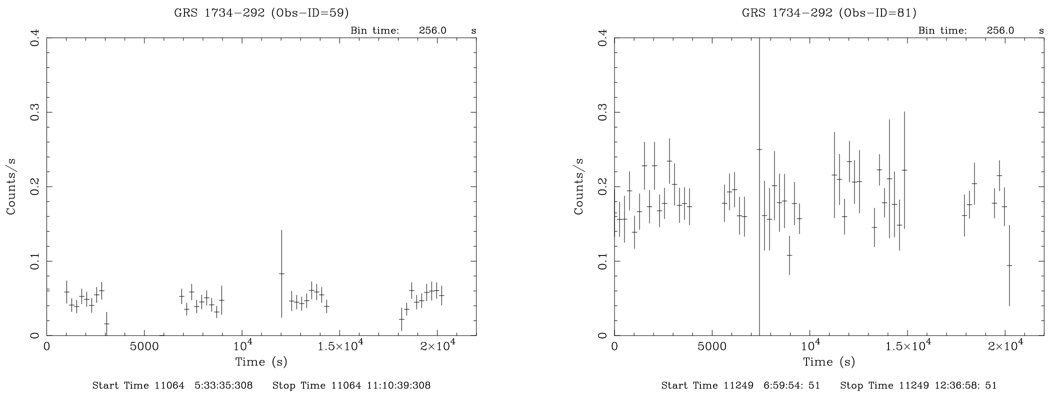

Figure 6.20: (GRS 1734−292) The GIS2+3 light curves with 256 sec bin for 2–10 keV bands. Unit of the start and the end time is TJD. (left) Obs-ID=59 (right) Obs-ID=81.

6.1.5 GRS 1734−292

Observations

ASCA observed this source twice: the observation IDs of 59 and 81 in Table 4.1. The exposure time for both of the observations are short, less than 10 ksec. Hence the statistics were not good, although this is a relatively bright source.

Analysis & Results

Fig. 6.20 show the light curves with 2–10 keV band of this source taken with GIS2+3. Constant flux assumption for the light curves of each observation is accepted. Thus, we found no significant variability in each observation period.

The spectrum in each period is found to be well represented with an absorbed power-law function. Table 6.6 and Fig. 6.21 show the best-fit parameters with 90% confidence uncertainties and the best-fit models with the data spectra, respectively. The spectral shape in each observation is consistent with each other with photon index of Γ = 1.3–1.7 and hydrogen (equivalent) column density of N_{H}= (1.3–2.0)$\times10^{22}$H cm^{-2}.

Discussion

The X-ray emission has been always detected with *ASCA* whenever we observed this source. In fact, other than the analyzed data taken in 1998 and 1999, we detected this source at the edge of *ASCA* GIS field of view in 1997 (Obs-ID=44)[3].

---

[3] The detected position is too farther from the detector center; the calibration uncertainty is quite large there. That is why we did not use the data for spectral analysis.

Table 6.6: (GRS 1734−292) Best-fit parameters in the fitting with a power-law function.

Obs-ID	$\Gamma^\dagger$	$I_{1\mathrm{keV}}{}^\ddagger$	$N_\mathrm{H}{}^\P$	$F_\mathrm{X}{}^\%$	χ^2/d.o.f.
59	$1.41^{+0.52}_{-0.5}$	$0.56^{+0.69}_{-0.31}$	$1.11^{+1.08}_{-1.02}$	3.3	4.681/6
81	$1.51^{+0.2}_{-0.19}$	$0.51^{+0.19}_{-0.13}$	$1.67^{+0.38}_{-0.35}$	2.5	16.08/24

†: Photon index.

‡: Intensity of continuum at 1keV [10^{-2}photon keV^{-1} cm^{-2} s^{-1}] (absorption corrected).

¶: Hydrogen column density [10^{22} H cm^{-2}].

§: Iron column density [10^{18} Fe cm^{-2}].

%: Observed flux with 2–10 keV [10^{-11} erg cm^{-2} s^{-1}].

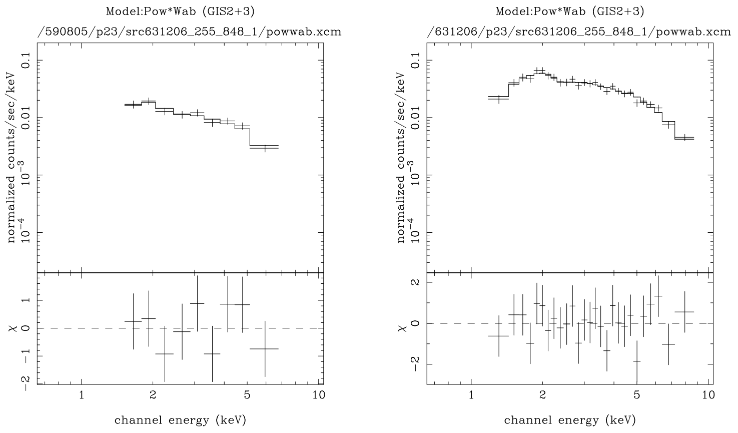

(a) Obs-ID=29 (b) Obs-ID=30

Figure 6.21: (GRS 1734−292) The GIS2+3 spectra when an absorbed power-law function is applied.

Thus GRS 1734−292 is probably a persistent X-ray source.

We found the spectrum to be well represented with a power law function within the statistics. The derived photon index of 1.3–1.7 is within the nominal range of that of Seyfert 1s. Thus our result is consistent with the identification of GRS 1734−292 is a Seyfert 1 galaxy by Martí *et al.* (1998).

Our derived hydrogen column density is $N_{\rm H}$= (1.3–2.0)$\times 10^{22}$ H cm^{-2}. This column is significantly smaller than that derived Pavlinsky *et al.* (1994) with *Granat*/ART-P. Whereas ART-P is a coded-mask detector, *ASCA* can directly resolve the target with imaging. Adding to this, *ASCA*/GIS energy resolution is much better than ART-P. Hence our derived value is presumably much more reliable than that with ART-P. In fact, our derived column density is close to the optical extinction or the H I absorption measured by Martí *et al.* (1998), $N_{\rm H}$=$(1.0 \pm 0.2) \times 10^{22}$ H cm^{-2} (see Section 2.2.6). Thus, our measurement of column density further supports the identification by Martí *et al.* (1998).

6.1.6 AX J1749.2−2725

AX J1749.2−2725 is a source that we newly discovered with *ASCA*. We already published the initial results with the *ASCA* data until 1997 (Torii *et al.* 1998). Thus we briefly summarize the published results, and then mention the result with the observation in 1998 (Obs-ID=46).

Observations

ASCA observed this source six times: the observation IDs of 19, 23, 24, 33, 43 and 46 in Table 4.1. Since observations of IDs of 23 and 24 are continuous observations in 1995 September and since the exposures of both of the observations are rather small ($\lesssim$ 5 ksec), we summed those data, and treated them uniformly.

This source is located in the strong stray light structure from GX 3+1. However, this source is apparent in the hard energy band above 3 keV, especially above 7 keV (see Fig. 5.2). It suggests that the intrinsic hardness of this source, or quite strong absorption.

Analysis & Results

Results with the data until 1997 First we analyzed the data of Obs-ID=19, which have by far the longest exposure time in all the observations for this source. Fig. 6.22 shows the power spectrum density obtained with FFT for the data from

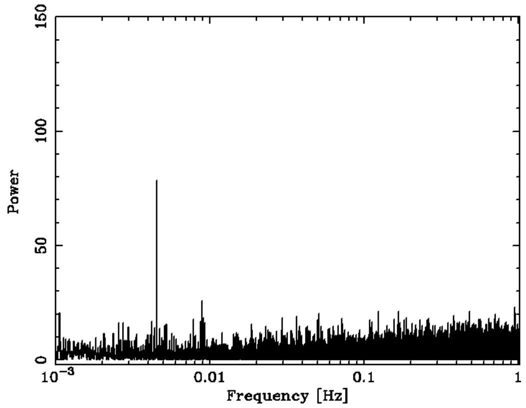

Figure 6.22: (AX J1749.2−2725) The GIS2+3 power spectrum density for the 0.7–10 keV band data of Obs-ID=19. The power is normalized so that the value for random fluctuation is 2.

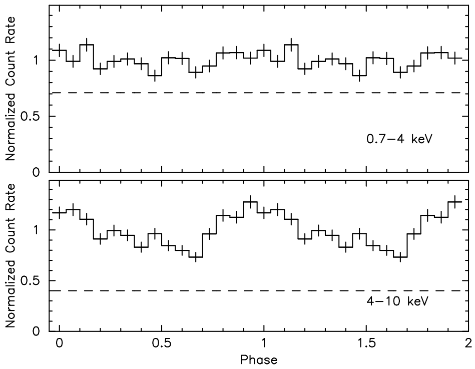

Figure 6.23: (AX J1749.2−2725) Folded light curves with the folding epoch of MJD 49802.0. (top) 0.7–4 keV (bottom) 4–10 keV. Two complete cycles have been plotted. The estimated background levels are shown by the dashed line in each panel.

the source region of radius 4′. It displays a significant pulsation around 220 second. In fact, the background, or the origin of stray light, GX 3+1, shows no such periodicity. Hence the periodicity is definitely originated from AX J1749.2−2725 itself.

With an epoch-folding search, we determined the period to be $P = 220.38 \pm 0.20$ sec for the assumed null-period derivative. In fact, we found the period derivative to be small, $|\dot{P}| < 2.2 \times 10^{-5}$s s^{-1}, by trying epoch-folding searches for four split data sets in the observation. Fig. 6.23 shows the folded light curve in the energy bands of 0.7–4 keV and 4–10 keV. Pulsation was found to be not significant in the energy band below 4 keV, where the background dominates.

We detected the pulsation with $P = 220.44 \pm 0.80$ also in the observations of Obs-ID=23 and 24 in 1995 September, whereas we could not detect significant pulsation in the observations of Obs-IDs=33 or 43. In fact, the source was faint in the observations of Obs-IDs=33 or 43. The significance of the source detection was only 3σ and 8σ for each observation, respectively.

The spectrum is described with an absorbed power-law function with photon index of Γ =0.7–1.3 and hydrogen column density of $N_{\rm H}$=(7–13)$\times 10^{22}$ H cm^{-2}, although the fitting result was not so good, possibly due to large systematic error with strong stray light. The spectral parameter did not change significantly from the observation of Obs-ID=19 to that of Obs-ID=23, 24.

Table 6.7: (AX J1749.2−2725) Best-fit parameters in the fitting with a power-law function.

Obs-ID	$\Gamma^{\dagger}$	${I_{1\mathrm{keV}}}^{\ddagger}$	${N_{\mathrm{H}}}^{\P}$	${F_{\mathrm{X}}}^{\%}$	χ^2/d.o.f.
19§	$1.0^{+0.3}_{-0.3}$	4^{+4}_{-2}	10^{+3}_{-3}	30	481.3/364
23&24§	$0.9^{+0.6}_{-0.5}$	$2.4^{+6.0}_{-1.5}$	9^{+6}_{-4}	25	116.1/110
33$^{\#}$	—	—	—	1.9$^{\#}$	—
43$^{\#}$	—	—	—	3.4$^{\#}$	—
46	$0.5^{+0.7}_{-0.6}$	$0.4^{+1.4}_{-0.3}$	10^{+7}_{-5}	8.6	4.079/6

†: Photon index.

‡: Intensity of continuum at 1keV [10^{-3}photon keV^{-1} cm^{-2} s^{-1}] (absorption corrected).

¶: Hydrogen column density [10^{22} H cm^{-2}].

%: Observed flux with 2–10 keV [10^{-12} erg cm^{-2} s^{-1}].

§: Simultaneous fitting for the data with each sensor (Torii *et al.* 1998).

#: Flux is determined on the assumption of the same spectral shape as that in Obs-ID=19.

Results with the data in 1998 We detected the pulsation with $P = 219.9 \pm 1.0$ also in the observation of Obs-ID=46 in 1998. This uncertainty is too large to derive a significant $\dot{P}$ from the previous observations.

The spectral parameter is found to be consistent with those derived with the data before 1998, except for the flux. The flux was smaller by a few factors than that in 1995 March and September (Obs-IDs of 19 and 23&24), but larger by a few factors that in 1996 September and 1997 September (Obs-IDs of 43 and 46, respectively). Table 6.7 and Fig. 6.24 show the best-fit parameters with 90% confidence uncertainties and the best-fit models with the data spectra,

Discussion

The observed period of $P \simeq 220$ seconds should be a spin period of a degenerate star. If it is a white dwarf, AX J1749.2−2725 should be classified as a DQ Her-type system, which has a relatively short period for a white dwarf (e.g., Patterson 1994). In that case, the distance of AX J1749.2−2725 should be less than $\lesssim 1.3(L_{\mathrm{X}}/10^{34}\mathrm{erg\ s^{-1}})^{1/2}$ kpc, since the X-ray luminosity of a white dwarf system is less than 10^{34} erg s^{-1}. Then, a large fraction of the heavy absorption of $N_{\mathrm{H}} \sim 10^{23}$ H cm^{-2} should be due to the circumstellar material.

Although we cannot exclude the possibility for a white dwarf binary scenario, all the observational facts of the hard spectrum, the absorption, the apparent location near the Galactic Center and the apparent large flux suggests that AX J1749.2−2725 is more likely to be a neutron star system. In this case, the large

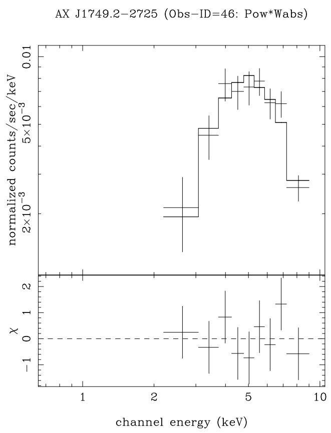

Figure 6.24: (AX J1749.2−2725) The GIS2+3 spectrum for the observation of Obs-ID=46 with the best-fit model in the fitting with an absorbed power law function.

absorption may be able to be explained with the large interstellar column density to the Galactic Center region. The 2–10 keV luminosity then is calculated to be $L_{\rm X}$= (2–40)×10^{34} erg s^{-1} for the 3 years *ASCA* data, on the assumption of the distance of 8.5 kpc.

6.1.7 SLX 1744−299/300

SLX 1744−299 and SLX 1744−300 are two bright sources closely located by an apparent offset of about 3′.

Observations

ASCA observed these sources three times: the observation IDs of 47, 48 and 71 in Table 4.1. All three observations were made in 1998 September.

Analysis & Results

Fig. 6.25 shows the *ASCA* image of the SLX 1744−299/300 complex. Two peaks are clearly seen. We determined the position of each peak to be ($l_{\rm II}$, $b_{\rm II}$) = (359.°293, −0.°885) and (359.°251, −0.°914), applying the peak finding method described in Section 5.2 for the data of Obs-ID=71, which had the best statistics. Since the statistical positional uncertainty was negligible, we adopt the nominal systematic error of *ASCA* for the positional error radius in this case: 40″ for the absolute positions and less than a few arcsec for the relative positions. Hence the former peak corresponds to SLX 1744−299, whereas the latter, to SLX 1744−300. During our

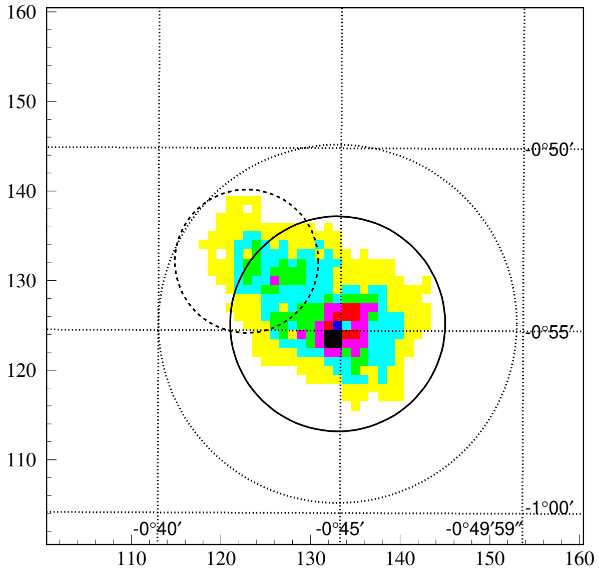

Figure 6.25: (SLX 1744−299/300) The 3–10 keV image with the photon extracting region for SLX 1744−300. The brightest spot is SLX 1744−300. The coordinates are galactic, whereas the unit of X and Y-axes is GIS channel (1 channel$\simeq 0'.25$). The source spectrum/light-curve for SLX 1744−300 is accumulated within the $3'$-radius circle indicated with solid line. The background events are collected from $r = 3'$–$5'$ annular region, which is located between solid line and dotted line in the figure. The photons in $2'$ radius region around SLX 1744−299 (indicated with scattered line) are not used for both of the source and the background events.

observation periods, SLX 1744−300 was apparently brighter than SLX 1744−299.

For timing and spectral analyses, we chose the photon collecting regions with the same method described in Section 5.2. Circles in Fig. 6.25 shows the accumulated area of the source photons (and the background photons for the spectral analysis), for example. Fig. 6.26(a)–(i) show the light curves of SLX 1744−299 and SLX 1744−300 with 2–10 keV band taken with GIS2+3, where the background events are not subtracted.

We clearly detected seven bursts with the duration of about 10–20 seconds from SLX 1742−300. At least two bursts were type-I because the spectral softning in the burst decay phase was apparent, whereas others did not show the clear type-I feature. Fig. 6.27 shows a observed type-I burst profile with hardness ratio, where the hardness ratio is defined as Count(1–4keV)/Count(4–10keV). Hence, we confirmed that SLX 1744−300 is a (type-I) burster, *i.e.*, definitely a low mass X-ray binary (LMXB) of a neutron star. On the other hand, we found no burst from

SLX 1744−299.

The peak flux of the largest burst from SLX 1744−300 was about 4×10^{-9} erg cm^{-2} s^{-1} below 10 keV. Therefore absorption-corrected peak luminosity is calculated to be $L_{\rm X}\sim 6\times10^{37}{d_{8.5{\rm kpc}}}^2$ erg s^{-1}, where d is the source distance normalized to 8.5 kpc. This value is smaller by a factor of 3 than that detected with Spacelab-2 by Skinner *et al.* (1990).

Then we made the spectra of the both sources according to the method described above. The derived spectra are shown in Fig. 6.28 and Fig. 6.29, for SLX 1744−299 and SLX 1744−300, respectively.

We tried fitting of each spectrum with a power-law and a bremsstrahlung model. For the SLX 1744−300 spectrum of the observation, Obs-ID=71, a power-law function fitting gives the best-fit values of photon index of $\Gamma \sim 2.14$, $N_{\rm H}\sim 5.9 \times 10^{22}$ H cm^{-2} and χ^2/d.o.f=412.9/198 (see Fig. 6.29), whereas a bremsstrahlung model fitting gives the best-fit values of temperature $kT \sim 7.1$, $N_{\rm H}\sim 5.1 \times 10^{22}$ H cm^{-2} and χ^2/d.o.f=253.3/198 (Fig. 6.31(c)). Thus, the bremsstrahlung model is much better for the spectral model than a power-law function. On the other hand, we found the SLX 1744−299 spectrum to be well represented with both of a power-law function (Fig. 6.30) and a bremsstrahlung model (Fig. 6.28, for example).

Table 6.8 shows the best-fit parameters with 90% confidence uncertainties, whereas Fig. 6.30 and Fig. 6.31 show the best-fit models with the data spectra of SLX 1744−299 and SLX 1744−300, respectively.

Discussion

We found that SLX 1744−300 was significantly brighter than SLX 1744−300. It is against the past results with other satellites (see Section 2.2.7). Thus, the fluxes of the both sources are probably highly variable.

Our derived column density for SLX 1744−300, $N_{\rm H}$=4.6–5.1, is significantly larger than the value estimated with *ROSAT* by Predehl & Kulkarni (1995), but is consistent with *SAX* result by Sidoli *et al.* (1999). This is possibly because *ROSAT* measurement of such high column density may have large systematic error.

Summary

- We detected both of SLX 1744−299 and SLX 1744−300 in 1998 September observations. SLX 1744−299 was apparently brighter by a factor of more than 2 than SLX 1744−300 through the observations.

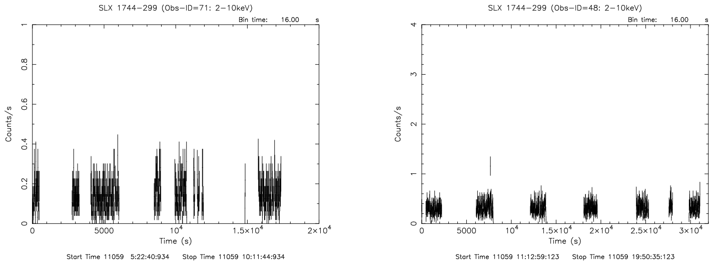

(a) SLX 1744−299 Obs-ID=47

(b) SLX 1744−299 Obs-ID=48

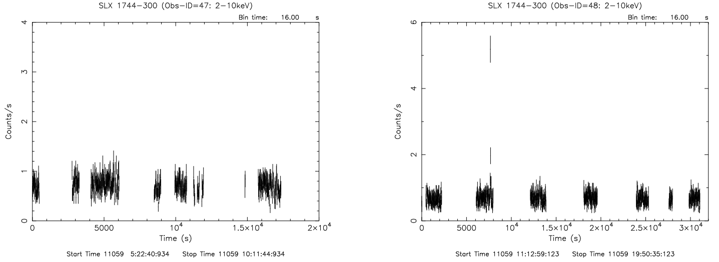

(c) SLX 1744−300 Obs-ID=47

(d) SLX 1744−300 Obs-ID=48

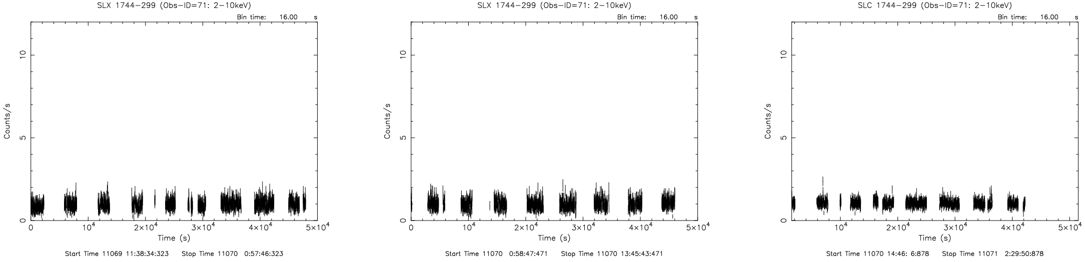

(e) SLX 1744−299 Obs-ID=71 (No.1)

(f) SLX 1744−299 Obs-ID=71 (No.2)

(g) SLX 1744−299 Obs-ID=71 (No.3)

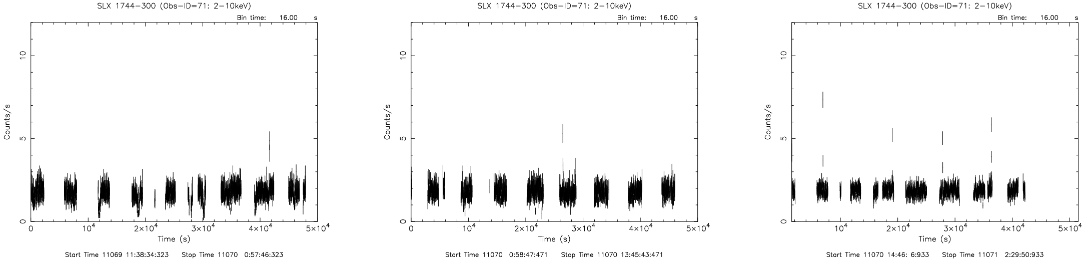

(h) SLX 1744−300 Obs-ID=71 (No.1)

(i) SLX 1744−300 Obs-ID=71 (No.2)

(j) SLX 1744−300 Obs-ID=71 (No.3)

Figure 6.26: (SLX 1744−299/300) The GIS2+3 light curves with 16 sec bin for 2–10 keV bands. Unit of the start and the end time is TJD. Seven bursts were detected from SLX 1744−300.

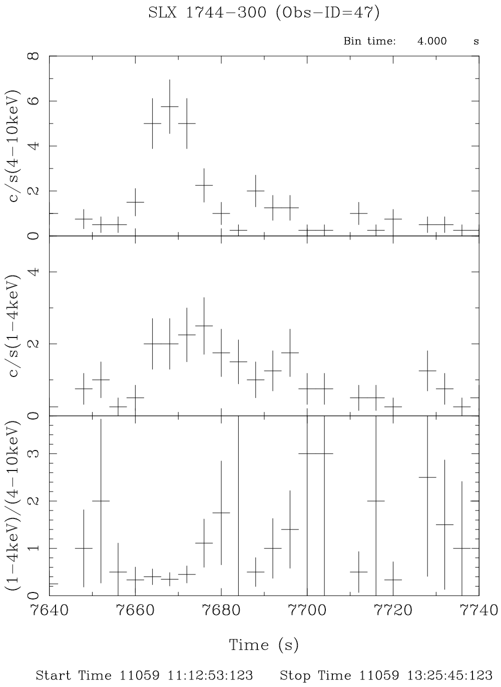

Figure 6.27: (SLX 1744−300) A burst profile with hardness ratio, taken with GIS2+3. Each bin width is 4 sec. The upper, middle and lower panels show the profiles of 4–10 keV band, 1–4 keV band, and hardness ratio defined as (Count rate of 1–4 keV)/(Count rate of 4–10 keV), respectively.

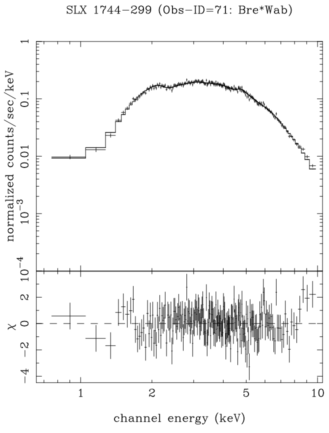

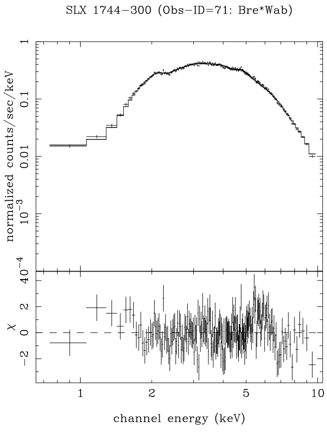

Figure 6.28: (SLX 1744−299) The GIS2+3 spectrum with the best-fit model in the fitting with a bremsstrahlung model.

Figure 6.29: (SLX 1744−300) The GIS2+3 spectrum with the best-fit model in the fitting with a power law function.

Table 6.8: (SLX 1744−299/300) Best-fit parameters in the fitting with a power-law function or a bremsstrahlung model.

SLX 1744−299 (Model: Power law)					
Obs-ID	$\Gamma^{\dagger}$	$I_{1\mathrm{keV}}{}^{\ddagger}$	$N_{\mathrm{H}}{}^{\P}$	$F_{\mathrm{X}}{}^{\%}$	χ^2/d.o.f.
47	$2.33^{+0.94}_{-0.76}$	$1.6^{+5.4}_{-3.3}$	$3.16^{+2.07}_{-1.57}$	0.2	23.90/24
48	$1.79^{+0.17}_{-0.16}$	$3.2^{+1.0}_{-0.7}$	$3.68^{+0.40}_{-0.37}$	0.9	49.76/61
71	$1.86^{+0.03}_{-0.03}$	$6.1^{+0.4}_{-0.3}$	$4.26^{+0.09}_{-0.09}$	1.4	180.1/183

SLX 1744−300 (Model: Bremsstrahlung)					
Obs-ID	kT	$I_{1\mathrm{keV}}{}^{\ddagger}$	$N_{\mathrm{H}}{}^{\P}$	$F_{\mathrm{X}}{}^{\%}$	χ^2/d.o.f.
47	$7.26^{+1.50}_{-1.09}$	$9.0^{+0.9}_{-0.8}$	$4.66^{+0.29}_{-0.27}$	2.0	85.77/82
48	$9.05^{+1.62}_{-1.24}$	$9.6^{+0.7}_{-0.6}$	$4.79^{+0.22}_{-0.21}$	2.3	82.58/62
71	$7.12^{+0.21}_{-0.20}$	$13.5^{+0.2}_{-0.2}$	$5.08^{+0.06}_{-0.06}$	2.8	253.3/198

†: Photon index.

‡: Intensity of continuum at 1keV [10^{-2} photon keV^{-1} cm^{-2} s^{-1}] (absorption corrected).

¶: Hydrogen column density [10^{22} H cm^{-2}].

$^{\%}$: Observed flux with 2–10 keV [10^{-10} erg cm^{-2} s^{-1}].

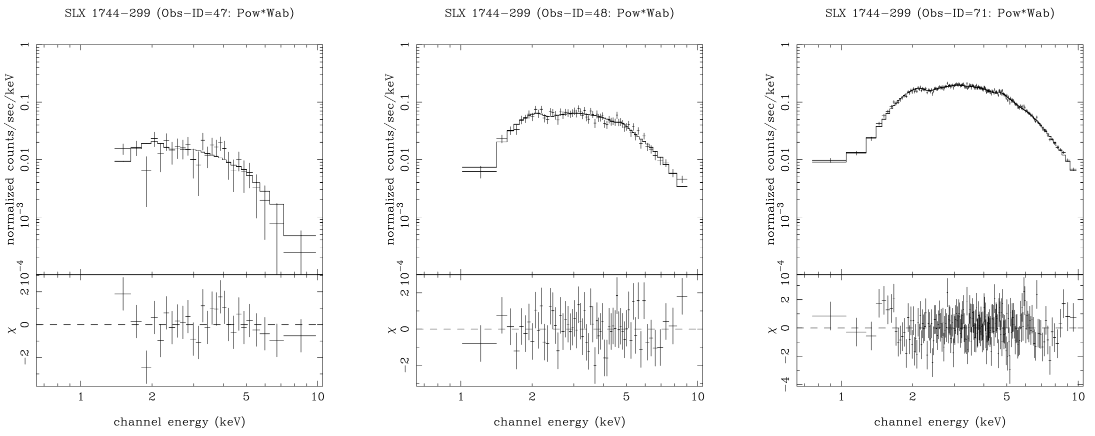

(a) Obs-ID=47 (b) Obs-ID=48 (c) Obs-ID=71

Figure 6.30: (SLX 1744−299) The GIS2+3 spectra with the best-fit model in the fitting with a power law function.

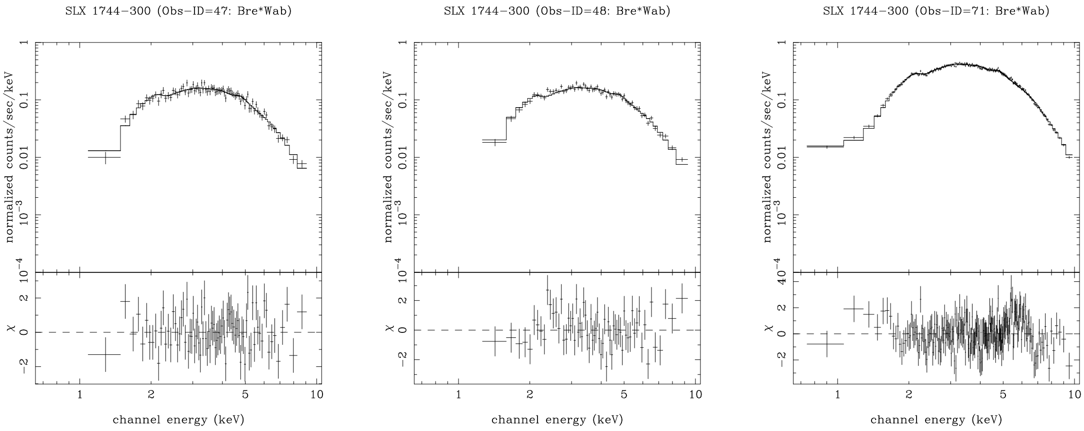

(a) Obs-ID=47 (b) Obs-ID=48 (c) Obs-ID=71

Figure 6.31: (SLX 1744−300) The GIS2+3 spectra with the best-fit model in the fitting with a bremsstrahlung model.

- We detected seven bursts from SLX 1744−300. At least two bursts were type-I bursts, hence we confirmed that this source is a LMXB. The peak luminosity of the largest burst was $L_{\rm X}\sim 6 \times 10^{37} {d_{8.5{\rm kpc}}}^2$ erg s^{-1}.

- We found the spectrum of SLX 1744−300 to be represented with the bremsstrahlung model with $kT \sim 7.1$keV, however the power law model is rejected. On the other hand, the spectrum of SLX 1744−299 was well represented with a power law function or the bremsstrahlung. The spectral parameters for both of the sources had not changed except for the flux in the observations in 1998 September with the separation of about 10 days.

6.1.8 GX 3+1

GX 3+1 is the brightest source in this region, and has been well studied with other satellites. Since this source is quite bright, timing analysis with *ASCA* is not so good as other satellites with large effective area. Only the strong point with *ASCA* is the wide spectral range from 0.7 to 10 keV and the energy resolution. Hence we concentrate on determining the spectral parameter for this source, especially, absorption column density.

Observations

GX 3+1 was observed only once with *ASCA*: the observation ID of 90 in Table 4.1. We used only GIS3 data because the source is located out of the GIS2 good mask

Table 6.9: (GX 3+1) Best-fit parameters in the fitting with a power-law function and bremsstrahlung.

(Model: Power law)				
$\Gamma^{\dagger}$	${I_{1\mathrm{keV}}}^{\ddagger}$	${N_{\mathrm{H}}}^{\P}$	${F_{\mathrm{X}}}^{\%}$	χ^2/d.o.f.
$1.76^{+0.04}_{-0.04}$	$1.43^{+0.09}_{-0.08}$	$2.16^{+0.07}_{-0.07}$	4.46	244.0/197

(Model: Bremsstrahlung)				
kT	${I_{1\mathrm{keV}}}^{\ddagger}$	${N_{\mathrm{H}}}^{\P}$	${F_{\mathrm{X}}}^{\%}$	χ^2/d.o.f.
$11.40^{+0.10}_{-0.09}$	$1.38^{+0.03}_{-0.03}$	$1.87^{+0.05}_{-0.05}$	4.39	246.5/197

†: Photon index.

‡: Intensity of continuum at 1keV [photon keV^{-1} cm^{-2} s^{-1}] (absorption corrected).

¶: Hydrogen column density [10^{22} H cm^{-2}].

$^{\%}$: Observed flux with 2–10 keV [10^{-9} erg cm^{-2} s^{-1}].

(see the second subsection in Section 5.1.1 and Fig. 5.1 for the good mask).

Analysis & Results

We tried to fit the spectrum with two models: power law and bremsstrahlung, both with absorption. Table 6.9 and Fig. 6.32 show the best-fit parameters with 90% uncertainty and the spectra with the best-fit models, respectively. The fitting results are quite similar to the both models. The derived column density is N_{H}=1.8–2.2.

6.1.9 Other sources

Other persistent bright point sources in this region are AX J1745.6−2901 and SLX 1735−269. Since their *ASCA* data were already analyzed in detail (Maeda *et al.* 1996; David *et al.* 1997), we did not reanalyze the data, but referred to their results. We review the results in Section 2.2.1 & 2.2.9.

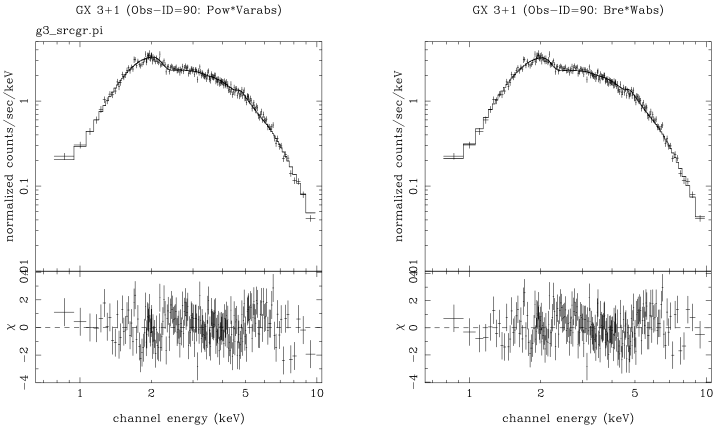

Figure 6.32: (GX 3+1) The GIS3 spectra with the best-fit model. Applied models are (left) power law function (right) bremsstrahlung model.

6.2 Transient point sources

The transient point sources mentioned in this section are GRS 1737−31, KS 1741−293, GRS 1741.9−2853, and XTE J1739−302.

For GRO J1744−28, XTE J1748−288, GRO J1750−27, which were observed and detected with *ASCA*, Nishiuchi *et al.* (1999), Kotani *et al.* (2000) and Dotani *et al.* (1997) already reported the *ASCA* results about them, respectively. Therefore, we briefly summarize the reported *ASCA* results about them in Section 2.2.14 and 2.2.15, respectively, and do not execute the detailed analysis.

6.2.1 GRS 1737−31

GRS 1737−31 was the transient source discovered with *Granat*/SIGMA on 1997 March 14 (Sunyaev *et al.* 1997). Detailed review is found in Section 2.2.10.

Observations

ASCA observed the region around GRS 1737−31 twice: the observation IDs of 26 and 42 in Table 4.1. The latter observation was TOO (see Table 4.2), 19 days after the report of flaring of this source. The *ASCA* initial result with the TOO observation was reported by Ueda *et al.* (1997) in IAU Circular.

Analysis & results

In the first observation of Obs-ID=26, GRS 1737−31 was not significantly detected. We estimated the 2σ flux upper limit to be 2.2×10^{-13} erg cm^{-2} s^{-1} in 2–10 keV band, assuming the same spectral shape in the TOO observation of Obs-ID=42, described later in this sub-section.

Then we concentrate on the analysis of the data in the TOO observation, Obs-ID=42. The light curve with 2–10 keV band (Fig. 6.33) show the significant variability on time scales of 10^3–10^4 seconds, although the variation amplitude is not so large, $\lesssim$20%. On the other hand we found neither significant burst-like activity like type-I bursts nor pulsation from this source (see the FFT results (Fig. 6.34)).

The spectrum is found to be well represented with an absorbed power-law function with photon index $\Gamma = 1.53 \pm 0.06$ and hydrogen column density $N_{\rm H}$= $(6.16 \pm 0.25) \times 10^{22}$ H cm^{-2}. The X-ray flux with 2–10 keV was 1.3×10^{-10} erg cm^{-2} s^{-1}. This 2–10 keV flux corresponds to 10% of that of 2–200 keV, measured with *XTE* at the same time (Cui *et al.* 1997). Fig. 6.35 shows the best-fit

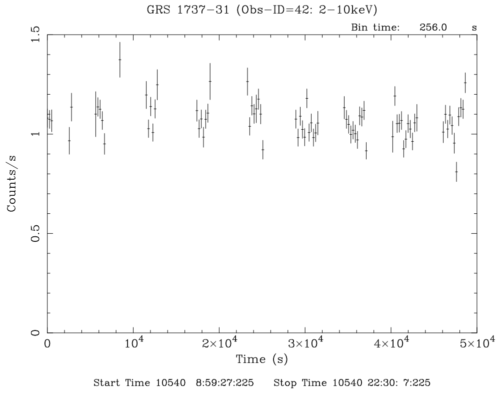

Figure 6.33: (GRS 1737−31) The GIS2+3 light curves with 256 sec bin for 2–10 keV bands. Unit of the start and the end time is TJD.

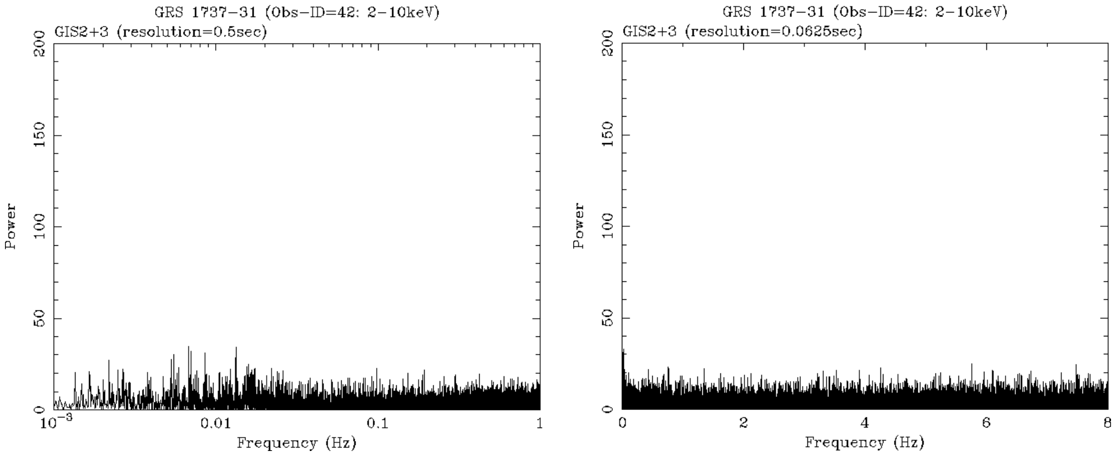

Figure 6.34: (GRS 1737−31) The GIS2+3 power spectrum density for the 2–10 keV band data of Obs-ID=42. (left) High and medium-bit data were used. (right) Only high-bit data were used.

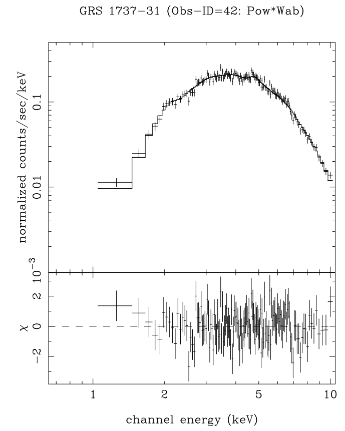

Figure 6.35: (GRS 1737−31) The GIS2+3 spectrum with the best-fit model when an absorbed power-law function is applied.

model with the data spectrum.

Discussion

We found that the column density to GRS 1737−31 is large, $N_{\rm H}\sim 6\times10^{22}$H cm^{-2}. This column density may suggest that the source distance is several kpc or larger, or probably in the Galactic Center region. Then we calculated the luminosity in 2–10 keV band to be 1.6×10^{36} erg s^{-1} for the assumed distance of 8.5 kpc.

The spectral shape of power law with photon index $\Gamma\sim1.5$, time variability and transient nature are consistent with that this source may be the black hole candidate, although a LMXB is also possible. We thus confirm the suggestion of this source as a black hole candidate by Cui *et al.* (1997).

Summary

- We detected GRS 1737−31 with *ASCA* in the observation on 1999 April 2, but detected no significant emission in 1995 September with the 2σ upper limit of the 2–10 keV flux of 2.2×10^{-13} erg cm^{-2} s^{-1}. It also showed the short time variability with 10^3–10^4 sec in 1999 April.

- The spectrum was found to be well represented with an absorbed power-law function with photon index of 1.53 and $N_{\rm H}$ of $\sim 6.2\times10^{22}$H cm^{-2} for 1–10 keV band.

- Our result is consistent with the suggestion of this source as a black hole candidate.

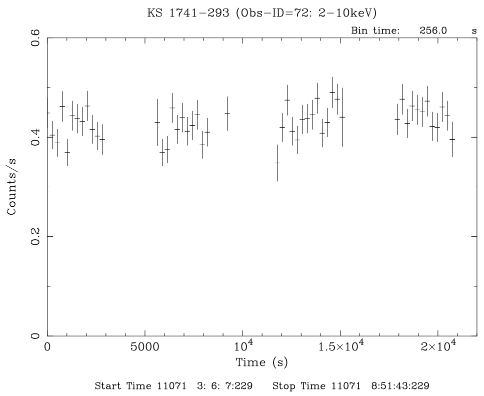

Figure 6.36: (KS 1741−293) The GIS2+3 light curve with 256 sec bin for the 2–10 keV band. Unit of the start and the end time is TJD.

6.2.2 KS 1741−293

KS 1741−293 was a transient burster discovered with *Mir/Kvant* in 1989 (in't Zand *et al.* 1991). Detailed review is found in Section 2.2.11.

Observations

ASCA observed the region around KS 1741−293 three times: the observation IDs of 7, 8 and 72 in Table 4.1. The first two observations were made on 1993 October 3 and 4, whereas the last one, on 1998 September 15.

Analysis & results

In the first two observations of Obs-ID=7 and 8, KS 1741−293 was not significantly detected. We estimated the 2σ flux upper limit to be 1.4×10^{-12} and 1.3×10^{-12} erg cm^{-2} s^{-1} in 2–10 keV band, respectively, assuming the same spectral shape in the observation Obs-ID=72, described later in this sub-section.

Then we concentrate on the analysis of the data Obs-ID=72. Fig. 6.36 shows the light curve with the 2–10 keV band. Constant flux assumption for the light curve is accepted. We thus found no significant variability in each observation period. We found no significant pulsation from this source, either (see the FFT results (Fig. 6.37)).

The spectrum is found to be well represented with an absorbed power-law function with photon index $\Gamma = 2.1 \pm 0.2$ and hydrogen column density $N_{\rm H}$= $20.3^{+1.7}_{-1.6} \times 10^{22}$ H cm^{-2}. The observed X-ray flux with 2–10 keV is 7.7×10^{-11} erg cm^{-2} s^{-1}. The χ^2/d.o.f. of the fitting is 87.46/78. Fig. 6.38 shows the best-fit model with the data spectrum.

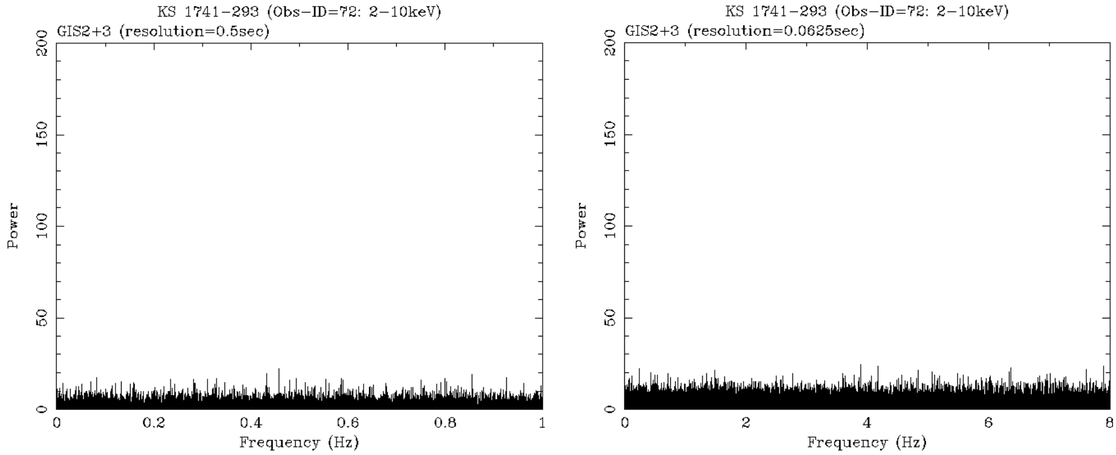

Figure 6.37: (KS 1741−293) The GIS2+3 power spectrum density for the 2–10 keV band data of Obs-ID=72. (left) High and medium-bit data were used. (right) Only high-bit data were used.

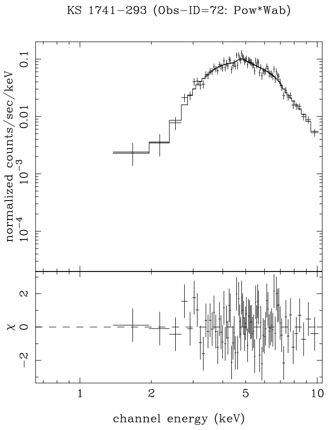

Figure 6.38: (KS 1741−293) The GIS2+3 spectrum with the best-fit model when an absorbed power-law function is applied.

Discussion

We found that the column density to KS 1741−293 is rather large, $N_{\rm H}\sim 2\times10^{23}$ H cm^{-2}, which seems larger than column densities of many other sources of this region. However, this source position is quite near to the Galactic plane, $b_{\rm II}\sim -0.03^\circ$. Therefore, the large column density of this source could be due to the small distance from the plane, where many molecular clouds are densely distributed. In fact, this galactic latitude is almost the same as that of 1E 1743.1−2843, which has also the large column density of $\sim 2\times10^{23}$ H cm^{-2} (see Section 6.1.3). Hence, this high column density supports that the location of KS 1741−293 is actually near the Galactic Center. Then we calculated the luminosity in 2–10 keV band to be 1.8×10^{36} erg s^{-1} for the assumed distance of 8.5 kpc.

The featureless spectrum is a typical nature for LMXBs. The photon index of about 2.1 is within the nominal range of that of LMXBs. Transient nature is, in fact, sometimes seen for LMXBs. On the other hand, the spectrum is much steeper than that of X-ray pulsars with high mass companion, and somewhat steeper than that of galactic black hole candidates. Combining the positional coincidence and the above discussed natures similar to those of LMXBs, we thus conclude that this *ASCA* source is certainly identical with the past transient KS 1741−293.

Summary

- We detected KS 1741−293 with *ASCA* in the observation on 1999 September 15, but detected no significant emission in 1993 September with the upper limit of the 2–10 keV flux of 1.4×10^{-13} erg cm^{-2} s^{-1}. In the observation of 1999 September, no significant time variability was found.

- The spectrum was found to be well represented with an absorbed power-law function with photon index of ∼2.1 and $N_{\rm H}$ of $\sim 20\times10^{22}$H cm^{-2}.

- From the spectral nature and long term variability, the nature of KS 1741−293 is consistent with a LMXB.

6.2.3 GRS 1741.9−2853

GRS 1741.9−2853 was the transient source discovered with *Granat*/ART-P in 1990 spring (Sunyaev *et al.* 1991b). Detailed review is found in Section 2.2.12.

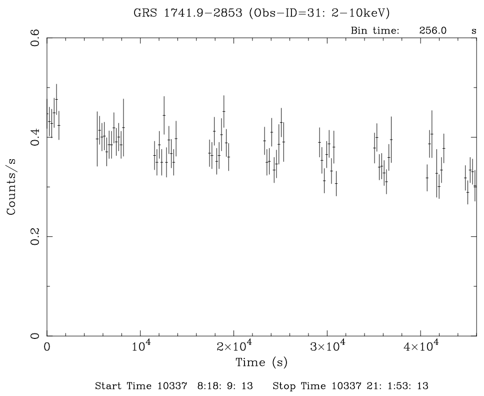

Figure 6.39: (GRS 1741.9−2853) The GIS2+3 light curves with 256 sec bin for 2–10 keV bands. Unit of the start and the end time is TJD. Background is not subtracted except for non-X-ray background which is cut with rise-time discrimination.

Observations

ASCA observed the region around GRS 1741.9−2853 eight times: the observation IDs of 2, 3, 7, 9, 12, 27, 31 and 39 in Table 4.1.

Analysis & results

In the observation Obs-ID=31, GRS 1741.9−2853 were the most clearly detected at the position of ($l_{\rm II}$, $b_{\rm II}$)=(359.948, 0.123) with the nominal error circle of 40″. GRS 1741.9−2853 was also detected in the observation Obs-ID=27, which was TOO observation for a bright transient source, GRO J1744−28. However, in the observation, GRS 1741.9−2853 was embedded in the tail of the PSF of GRO J1744−28 because GRO J1744−28 was too bright; the data quality was rather bad. Therefore we did not use the data in this section.

On the other hand, we found no significant X-ray emission from GRS 1741.9−2853 in the other six observations. We estimated the 2σ flux upper limit to be 8.1, 24, 3.6, 14, 14, 4.2 $\times 10^{-13}$ erg cm^{-2} s^{-1} in 2–10 keV band, for the data in Obs-ID=2, 3, 7, 9, 12 and 39, respectively, assuming the same spectral shape in the observation Obs-ID=31, described later in this sub-section.

Thus we concentrate on the analysis of the data, Obs-ID=31. Fig. 6.39 shows the light curve with 2–10 keV band. No burst was detected, although this observation was made in the same season (1996 September) when Cocchi *et al.* (1999b) detected type-I bursts from this source. We found no pulsation from this source, either.

The spectrum was found to be well represented with an absorbed power-law

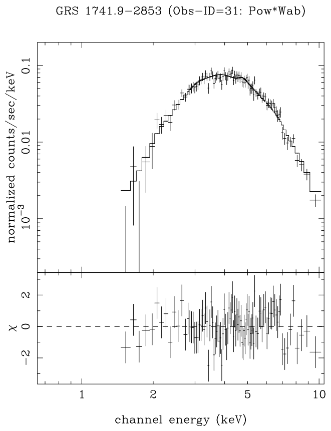

Figure 6.40: (GRS 1741.9−2853) The GIS2+3 spectrum with the best-fit model when an absorbed power-law function is applied.

function with photon index $\Gamma = 2.36 \pm 0.16$ and hydrogen column density $N_{\rm H}=$ $11.4^{+0.9}_{-0.8} \times 10^{22}$ H cm^{-2}. The observed X-ray flux with 2–10 keV was 8.5×10^{-11} erg cm^{-2} s^{-1}. The χ^2/d.o.f. of the fitting is 89.13/91. Fig. 6.40 shows the best-fit model with the data spectrum.

Discussion

We detected significant persistent X-ray emission from GRS 1741.9−2853 in 1996 September and February, but found no significant emission in other times, in fall in 1993, 1994, and in 1997 spring. GRS 1741.9−2853 may be in high state during our observation phase in 1996, whereas the emission in quiescent state was pretty faint. The mechanism which causes such violent flux variability is unknown.

We found that the time-averaged column density to GRS 1741.9−2853 is about $N_{\rm H}\sim 11 \times 10^{22}$ H cm^{-2}. It is consistent with *SAX*/WFC measurement in the first and the third bursts (Cocchi *et al.* 1999b, or see 2.2.12). Thus we further confirmed their results with much smaller uncertainty. However, we did not find any evidence for larger column density above 20×10^{22} H cm^{-2}, as detected with *SAX*/WFC (Cocchi *et al.* 1999b). The light curve was rather stable during our observation in 1996 September.

Summary

- We detected GRS 1741.9−2853 with *ASCA* in the observation on 1999 September and February, but detected no significant emission in several observations from 1993 to 1997.

- The spectrum was found to be well represented with an absorbed power-law function with photon index of ∼2.4 and $N_{\rm H}$ of $\sim 11 \times 10^{22}$H cm^{-2}.

6.2.4 XTE J1739−302

XTE J1739−302 was the transient source discovered with *XTE* on 1997 August 12 (Smith *et al.* 1998a). Detailed review is found in Section 2.2.13. No report for detection of this source has been presented, other than the *XTE* detection on 1997 August 12; we have detected this source, and found the unusual nature.

Observations

ASCA observed the region around XTE J1739−302 only once on 1999 March 11: the observation ID of 76 in Table 4.1.

Analysis & results

The left panel of Fig. 6.41 shows the light curve with 2–10 keV band. Unusual flare, which started at about MJD 51248.319, was clearly detected. The light curve showed a quite violent and complicated profile; it reached the peak with 200–250 sec, then suddenly dropped off to almost 0 flux level with the almost same time scale as that of the flare-up, and again showed the flaring with the almost same time scale, but with about a half peak flux of the first flare. No significant difference between the light curves with the 4–10 keV and the 1–4 keV bands was found (see the right panel of Fig. 6.41).

We showed the X-ray images before and during the flare in Fig. 6.42. In fact, we found no significant X-ray emission before the flare, with the 2σ flux upper limit of 6.9 $\times 10^{-13}$ erg cm^{-2} s^{-1} in 2–10 keV band, assuming the same spectral shape during the flare, described later in this sub-section. Since the first flare peak flux was about 2×10^{-9} erg cm^{-2} s^{-1}, it means that the flare showed the variability by more than three orders in a few hundred seconds.

We also tried pulsation search for time scale of 1–100 seconds with FFT analysis, but failed (Fig. 6.43). In fact, the short effective observation duration may make it difficult to let us find significant periodicity, even if the object has some periodicity.

We accumulated the spectrum only during the flare. The spectrum is found to be well represented with an absorbed power-law function with photon index $\Gamma = 0.80^{+0.10}_{-0.11}$ and hydrogen column density $N_{\rm H}$= $3.17^{+0.33}_{-0.31} \times 10^{22}$ H cm^{-2}. The

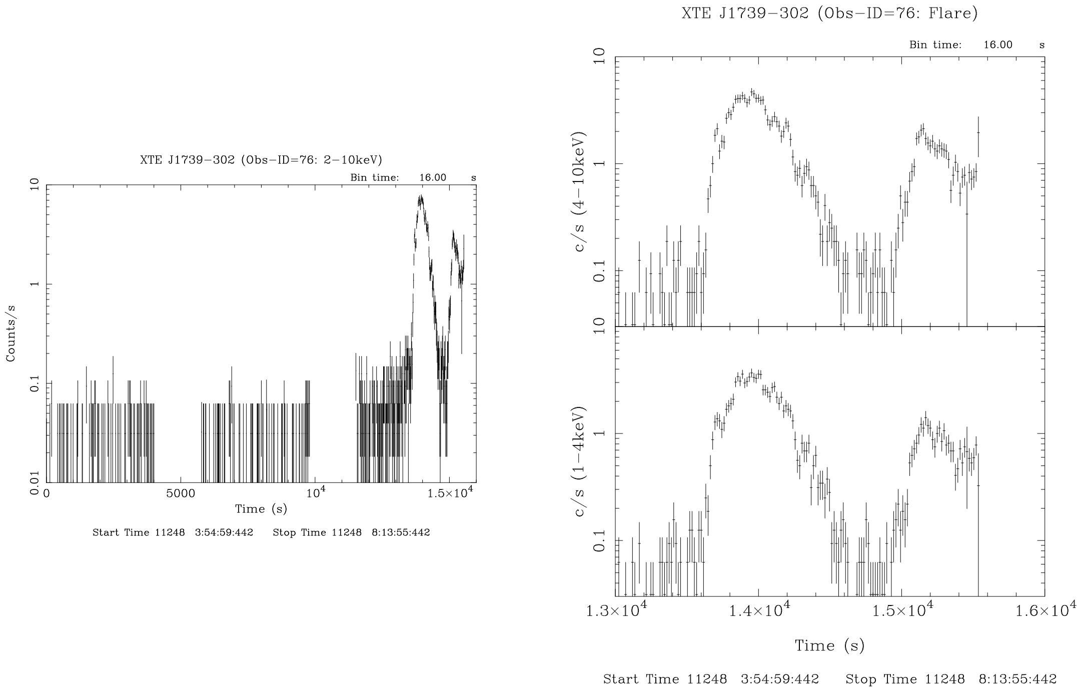

Figure 6.41: (XTE J1739−302) The GIS2+3 light curves with 16 sec bin. Unit of the start and the end time is TJD. Background is not subtracted except for non-X-ray background which is cut with rise-time discrimination. Vertical axis scale is logarithmic. (left) the 2–10 keV light curve for whole observation, (right) the light curve around the flare with the 4–10 keV (top) and the 1–4 keV (bottom).

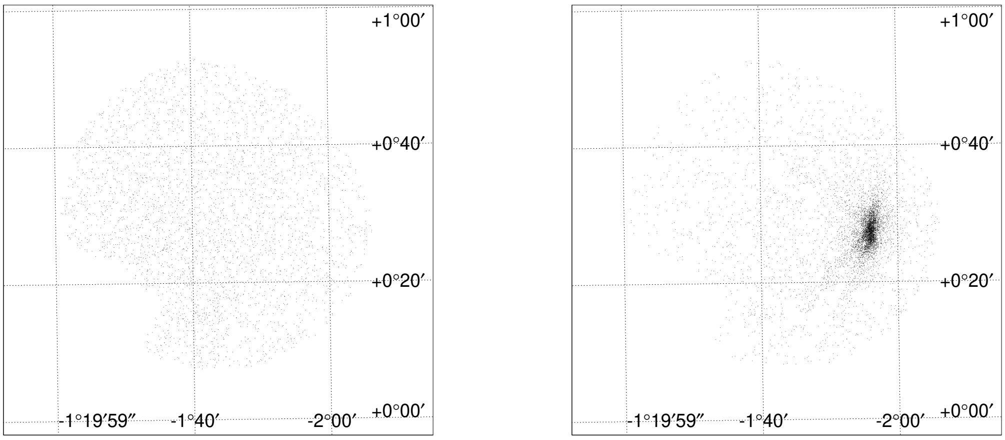

Figure 6.42: (XTE J1739−302) The GIS2 image for the 2–10 keV band data with the galactic coordinates (Obs-ID=76) (left) before the flare (right) during the flare.

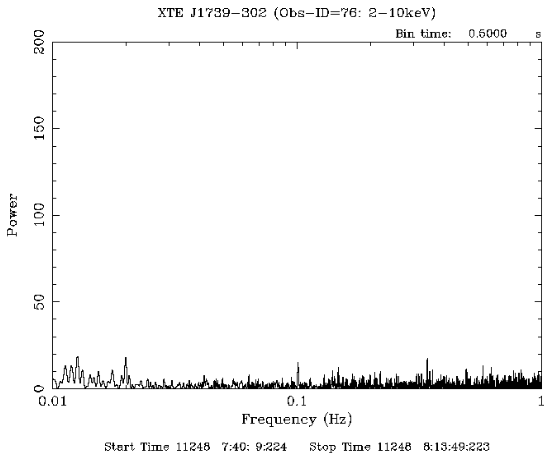

Figure 6.43: (XTE J1739−302) The GIS2+3 power spectrum density for the 2–10 keV band data of Obs-ID=76. High and medium-bit data were used. Note that we do not present the result with only high-bit data because the source is not detected in the observation with high-bit data.

χ^2/d.o.f. of the fitting is 91.41/77. Fig. 6.44 shows the best-fit model with the data spectrum.

On the other hand, we found that a bremsstrahlung model with $kT < 200$ keV is rejected. It is consistent with the quite flat index for a power law. However, this result is inconsistent with the *XTE* result by Smith *et al.* (1998a). They remarked that the *XTE* spectrum from 2 to 25 keV in the high state was well described with a bremsstrahlung model of $kT \sim 12.4 \pm 0.3$ keV (see Section 2.2.13).

Discussion

We found that the time-averaged column density to XTE J1739−302 is about $N_{\rm H}\sim 3\times10^{22}$ H cm^{-2}. It is inconsistent with *XTE*/PCA measurement by Smith *et al.* (1998a) in 1998 August, which gives (5–6)$\times10^{22}$ H cm^{-2}. Their measured temperature was 12 keV, whereas our measurement is more than 200 keV. Temperature and absorption are often coupled with each other in the model fitting. However, Smith *et al.* (1998a) found that a power law is rejected, whereas we found that a bremsstrahlung is rejected, but a power law is accepted. In fact, the best-fit values are well determined in both of the analyses by Smith *et al.* (1998a) and by us. Therefore, the differences of the absorption and the continuum are probably real; the spectral shape may be changed in the period between the *XTE* and the *ASCA* observations. Since this source has shown highly variable flux, the change of the spectral shape may be also possible.

We detected a giant flare from XTE J1739−302, of which the flux was larger

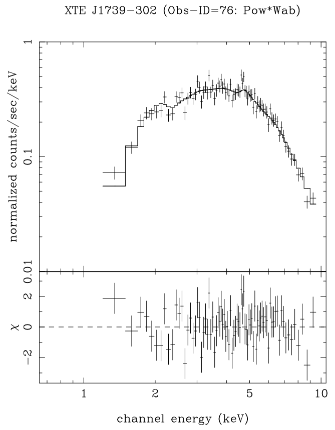

Figure 6.44: (XTE J1739−302) The GIS2+3 spectrum with the best-fit model when an absorbed power-law function is applied.

by more than three orders than that in the preceding quiescent state. The quite short rise time of a few hundred seconds as well as a large flux ratio of in flare to in quiescent makes it quite unusual one.

Be-star/neutron star (Be/NS) binaries often show the transient nature, although such a flare observed in XTE J1739−302 is rare. In addition, the quite flat spectrum of the photon index of ∼0.8 is a common nature for Be/NS binaries, but is rarely observed for other class of sources. Variable absorption is also the nature often reported for Be/NS binaries. Thus, this source is likely to be a Be/NS binary. However, we could not detect any pulsation with *ASCA* in 1999 March observation, the same as Smith *et al.* (1998a), with *XTE* in 1997 August observation. Consequently, the category of this source is still unknown.

Summary

- We detected XTE J1739−302 with *ASCA* in the observation on 1999 March 14. It was not detected in the beginning of the observation; then it showed a giant flare and the following second flare. The flux ratio between the quiescent state and the flare peak was found to be more than three orders, while the rise time was about a few hundred seconds.

- We found that the spectrum was well represented with an absorbed power-law function with photon index of ∼0.8 and $N_{\rm H}$ of $\sim 3 \times 10^{22}$H cm^{-2}. Combining the past result by Smith *et al.* (1998a) with *XTE*, we suspect that this source also showed the spectral change.

- The class of XTE J1739−302 is still unknown. However, a Be/NS binary is a likely candidate.

6.3 Extended sources

In this section, we report the results on discrete extended structures in the Galactic Center region. First we mention the results on radio supernova remnants (SNRs) cataloged (Green 1998). Then we present the results on other extended structures, including newly discovered X-ray structures.

6.3.1 Radio supernova remnants

Nine radio SNRs are cataloged in the Galactic Center 5° × 5° region: G359.0−0.9, G359.1−0.5, G359.1+0.9, Sgr A East (G0.0+0.0), G0.3+0.0, G0.9+0.1, Sgr D SNR (G1.0−0.1), G1.4−0.1, and G1.9+0.3 (Green 1998).

We already published the *ASCA* results on G359.0−0.9 and G359.1−0.5 (Yokogawa *et al.* 1999; Bamba *et al.* 2000; see the review in Sections 2.2.18 and 2.2.19). Thus we here report the new results other than the two SNRs.

G359.1+0.9

Fig. 6.45 shows the GIS image around G359.1+0.9. We detected X-ray emission from the position of G359.1+0.9 with the significance of 9.8σ in 0.7–3 keV band (AX J1739.6−2911 in Fig. 6.45, whereas the significance in 3–10 keV band is 2.1σ.

Faint extended emission around AX J1739.6−2911 also can be seen in the 0.7–3 keV band image. We made the radial profile with the center at the peak of AX J1739.6−2911 and fitted it with the model of the point spread function (PSF) and the background (NXB+CXB(cosmic X-ray background)) where the normalizations of the PSF and the background were allowed to be free. The model is found to be rejected with the confidence of 97.4%, *i.e.*, the slightly extended emission with the radius of $4' \sim 5'$ was marginally detected with the significance of 2.2σ (Fig. 6.46). The size is nearly consistent with or slightly lower than the radius of the radio shell, $r \sim 5'$ (Gray 1994).

The spectrum of the central region of AX J1739.6−2911 was found to be well fitted with the thin thermal plasma model with kT ~0.7 keV (χ^2/d.o.f.=2.67/5) and $N_{\rm H}\sim 0$, although the statistics was not good. This small or 0 column density implies that this source is a foreground source, located in front of the Galactic Center region. The flux is 3×10^{-13} erg cm^{-2} s^{-1} in total X-ray energy band. We can calculate the luminosity of 2×10^{33} erg s^{-1} for the assumed distance of 8.5 kpc. Since the distance is much smaller than 8.5 kpc, the true luminosity is less

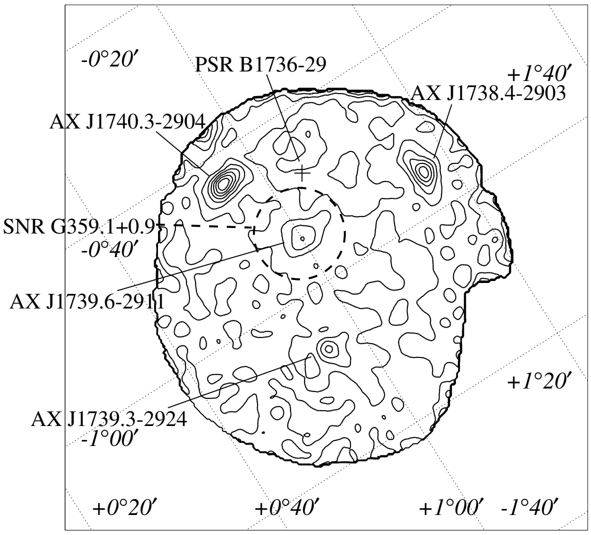

Figure 6.45: GIS2+3 contour map around G359.1+0.9 with 0.7–3.0 keV band. The image is convoluted according to the method in Section 5.1. Contour levels are linearly spaced. The coordinates are in galactic ($l_{\rm II}$, $b_{\rm II}$), and the north is up. The positions of the detected X-ray sources (AX J1738.4−2903, AX J1739.3−2924, AX J1739.6−2911, AX J1740.3−2904), the radio shell of G359.1+0.9, and the radio pulsar PSR B1736−29 are indicated.

than this value by several factors or more. Fig. 6.47 shows the spectrum with the best-fit model.

The extended emission with positional coincidence with the radio structure strongly supports that it is an X-ray counter part of the SNR G359.1+0.9, if the detection of the extended emission is true. The soft spectrum also supports it.

The luminosity, $\lesssim 10^{33}$ erg s^{-1}, may be rather low for an SNR. However, Yamauchi *et al.* (1998a, 1998b) have failed to detect many radio SNRs with *ASCA* Galactic plane survey, suggesting their quite dim X-ray luminosities. Therefore, the low X-ray luminosity of this source may be acceptable for an SNR.

On the other hand, we found in fact a catalogued star, HD 316072, only $11'$ offset from the *ASCA* detected position (Table 5.2), whereas the error radius with *ASCA* is about $1'$. *ASCA* might detect the X-ray emission from this star; the soft spectrum is typical of stars. If the main part of the detected emission comes from this star, the extension of the diffuse emission might be larger, although the statistical significance for the detection is small. Future observations with high sensitivity in soft X-ray band will be encouraged.

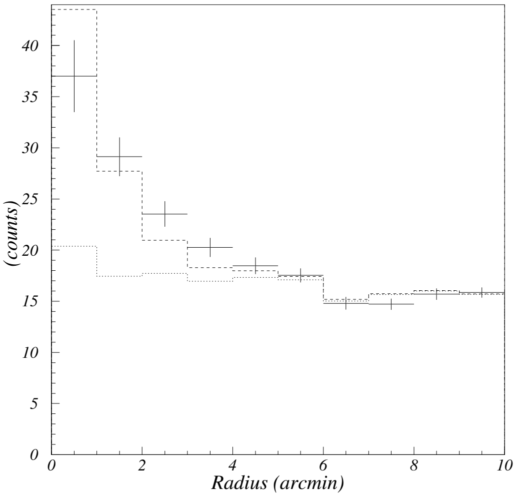

Figure 6.46: The radial profile with the center at the peak of AX J1739.6−2911 (possible counter part of G359.1+0.9). The profile is fitted with the point spread function (see text). The best-fit model is given with the dashed line, whereas the dotted line shows only the background component in the best-fit model.

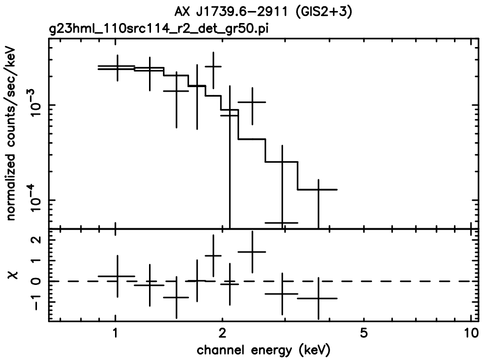

Figure 6.47: The GIS2+3 spectrum of AX J1739.6−2911 (possible counter part of G359.1+0.9) with the best-fit model.

G0.9+0.1

Fig. 6.48 shows the GIS image of G0.9+0.1 with 3–10 keV band. We detected significant X-ray emission from this source in this hard energy band, whereas no significant X-ray is detected in the softer energy band.

The X-ray emitting region is compact and not resolved with *ASCA* GIS. The radio size of the source is 2′ in diameter (Helfand & Becker 1987), hence it is still consistent with the X-ray image.

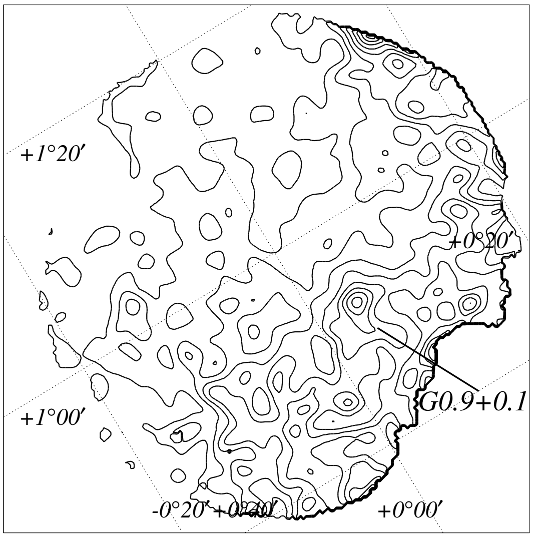

Figure 6.48: GIS2+GIS3 contour map of G0.9+0.1 with 3–10 keV band. The image is convoluted according to the method in Section 5.1. Contour levels are linearly spaced. The coordinates are in galactic ($l_{\rm II}$, $b_{\rm II}$), and the north is up.

The spectrum (Fig. 6.49) was found to be hard; kT >2 keV (the best-fit of 40 keV) in thermal model or $\Gamma \sim$1.5 in power-law model, with heavy absorption of $N_{\rm H}\sim 10^{23}$H cm^{-2}, although the statistics is not good. This hardness may imply the emission to be non-thermal origin. The flux is 2×10^{-12} erg cm^{-2} s^{-1} in 2–10 keV band. It is consistent with the upper limit by *Einstein* (Helfand & Becker 1987), and with the measurement with *SAX* (Mereghetti *et al.* 1998).

The other cataloged SNRs

For the other cataloged SNRs (Sgr A East (G0.0+0.0), G0.3+0.0, Sgr D SNR (G1.0−0.1), G1.4−0.1, and G1.9+0.3), we detected no significant X-ray emission associated with the SNRs. It might be possibly because no strong X-ray is actually emitted. However we should be conservative for no X-ray emission from

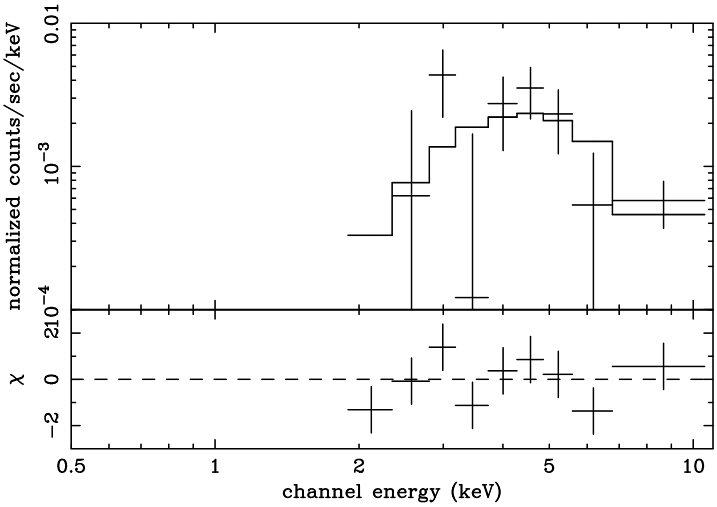

Figure 6.49: The GIS spectrum of G0.9+0.1 with the best-fit model where an absorbed power law function is applied.

those sources because the detected positions of those SNRs are heavily contaminated from nearby strong X-ray sources; Sgr A and AX J1745.6−2901 near Sgr A East, 1E 1743.1−2843 near G0.3+0.0, and GX3+1 near G1.0−0.1, G1.4−0.1, and G1.9+0.3.

6.3.2 Other extended sources

G0.0−1.3 (AX J1751−29.6)

Fig. 6.50 shows the GIS image of "G0.0−1.3" (AX J1751−29.6) in 0.7–3 keV band[4]. We discovered the clearly extended emission with the scale of about 40′ × 10′.

The spectrum is found to have the emission lines from highly ionized ions, hence is the thermal origin (Fig. 6.51). In fact, the spectrum is well fitted with a thin thermal plasma model with $kT = 0.50 \pm 0.08$ keV and $N_{\rm H}$= $(1.3 \pm 0.2) \times 10^{22}$ H cm^{-2}. The X-ray flux is $\sim 10^{-11}$ erg cm^{-2} s^{-1} in 0.5–3 keV band.

The column density suggests that this source may be in front of the Galactic Center region according to Sakano *et al.* (1999b), and be located at the distance of about 4 kpc if we assume the mean interstellar density of 1 H cm^{-3}. Then, the obtained flux is converted to the luminosity of 3×10^{35} erg s^{-1} under the assumption of the distance of 4 kpc. Even in the case of the quite small distance of 1 kpc, the

---

[4] The names are what we name.

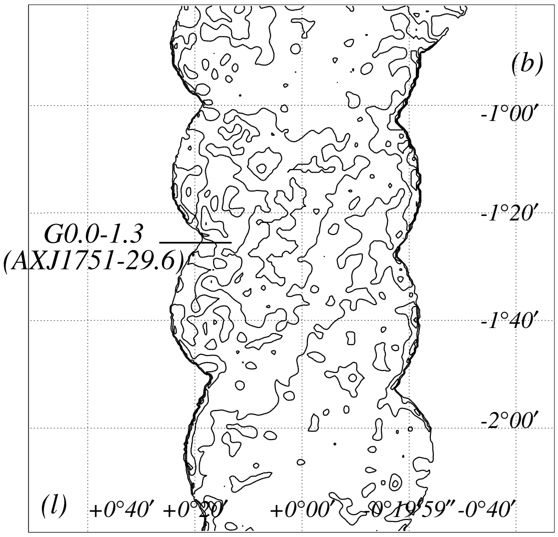
(b)
-1°00′
-1°20′
-1°40′
-2°00′
G0.0-1.3
(AXJ1751-29.6)
(l)
+0°40′
+0°20′
+0°00′
-0°19′59″
-0°40′

Figure 6.50: GIS2+3 contour map of G0.0−1.3 (AX J1751−29.6) with 0.7–3 keV band. The image is convoluted according to the method in Section 5.1. Contour levels are linearly spaced. The coordinates are in galactic ($l_{\rm II}$, $b_{\rm II}$).

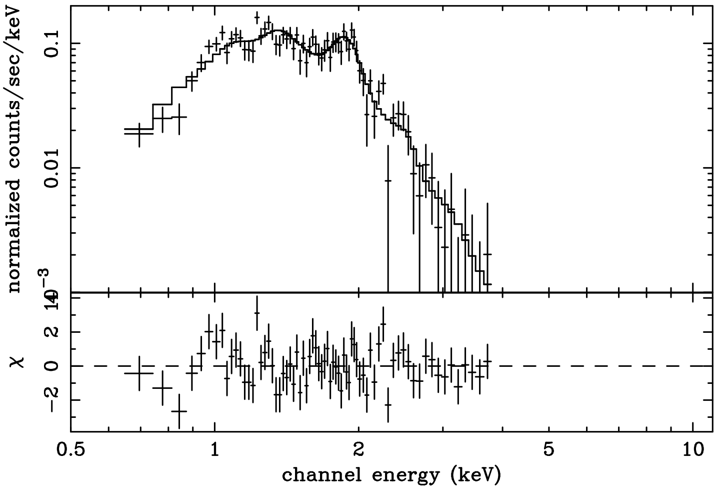

Figure 6.51: The GIS spectrum of G0.0−1.3 (AX J1751−29.6) with the best-fit model where an absorbed power law function is applied.

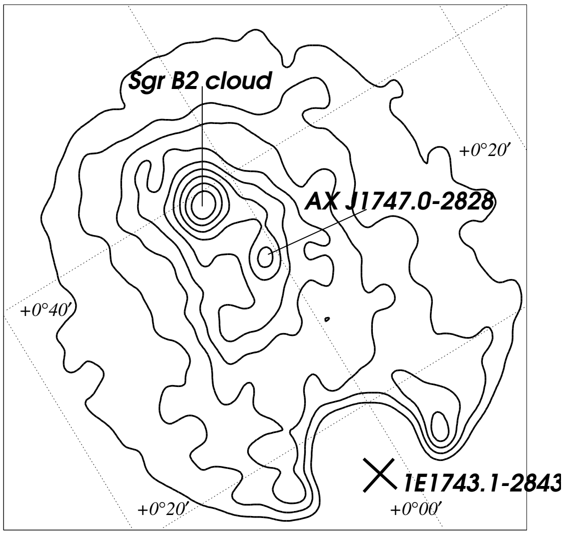

Figure 6.52: GIS2+3 contour map of G0.56−0.01 (AX J1747.0−2828) with 6.0–7.0 keV band, which is dominated by iron Kα line. Contour levels are linearly spaced. The coordinates are in galactic ($l_{\rm II}$, $b_{\rm II}$), and the north is up. Note that this image was corrected only for exposure, NXB was not subtracted, and the region around a bright source 1E 1743.1−2843 was excluded before the smoothing in order to reduce the contamination from 1E 1743.1−2843. The positions of the X-ray reflection nebula Sgr B2 cloud (e.g., Murakami *et al.* 2000a) and 1E 1743.1−2843 are also indicated.

luminosity is larger than 10^{34} erg s^{-1}.

We now consider the classification of the source. The clearly extended emission of the thin thermal plasma with kT ~0.5 keV implies that this source is an SNR or a star forming region. The luminosity is also within the typical range of SNRs but much higher than that of a star forming region. Therefore, AX J1751−29.6 is a strong candidate for a new SNR.

G0.56−0.01 (AX J1747.0−2828)

Fig. 6.52 shows the GIS image of "G0.56−0.01" (AX J1747.0−2828) in 6–7 keV band[5], where this source can be seen the most significantly. The X-ray emitting region is compact and not resolved with GIS.

The background subtracted spectrum is given in Fig. 6.53. We accumulated the source X-ray photons from the 3′-radius circular region around AX J1747.0−2828, and the background photons, from an elliptical region with the major axis parallel

---

[5] The names are what we name

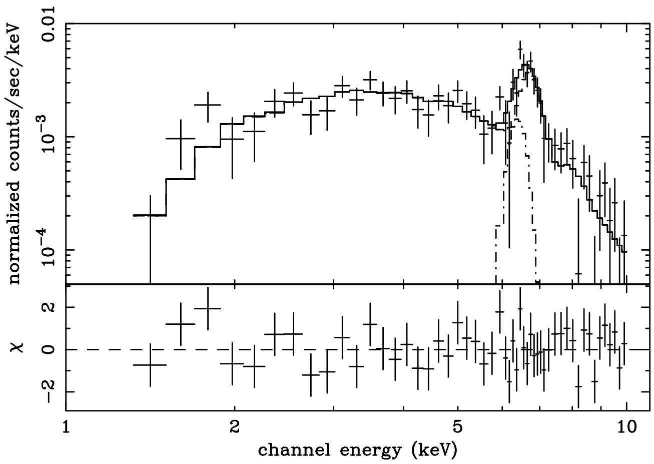

Figure 6.53: The GIS spectrum of G0.56−0.01 (AX J1747.0−2828) with the best-fit models. The fitting model is a thin thermal plasma model with absorption.

to the Galactic plane, excluding the 3′-radius circular regions around AX J1747.0−2828 itself and Sgr B2 (see Murakami *et al.* (2000a)).

The spectrum is found to be characterized with a quite strong line at between 6–7 keV, which is also implied from the X-ray image. We tried to fit the spectrum with the thermal bremsstrahlung and a Gaussian line. Then we found the equivalent width of the line to be quite large, ~2 keV, and the center energy of the Gaussian to be 6.63±0.06 keV, being consistent with Kα line from helium-like iron. Hence, the spectrum is definitely a thin thermal origin with high temperature of several keV or higher.

We then fitted the spectrum with a thin thermal plasma model. The model well represents the total spectral shape. The best-fit temperature is $kT = 6.0^{+1.9}_{-1.5}$ keV, the averaged abundance, $Z > 2$ solar, and the hydrogen column density, $N_{\rm H}$= $(6.1^{+1.6}_{-1.1})\,10^{22}$ H cm^{-2}. The flux is 1.6×10^{-12} erg cm^{-2} s^{-1} in 0.7–10 keV band.

The large column density suggests this source to be located at near the Galactic Center. Thus, the absorption corrected X-ray luminosity is estimated at $\sim 3.6 \times 10^{34}$ erg s^{-1} on the assumption of the distance of 8.5 kpc.

This high temperature and the overabundance suggest AX J1747.0−2828 to be a possible new candidate of a young SNR. The luminosity is also within the range of that of a typical SNR. Although the supernova remnant is the most probable source, the other possibility, for example, a nearby cataclysmic variable, still cannot be absolutely excluded (e.g., Terada *et al.* 1999). In any case, it is a new class object in the Galactic Center region, and accordingly such a class of object is a candidate for the origin of the Galactic Center hot plasma.

6.4 Population of bright sources

In this section, we summarize the results on bright sources in the Galactic Center region and study their population.

6.4.1 Summary of bright sources

Table 6.10 shows the summary of the *ASCA* results on bright X-ray sources in the Galactic Center region. For 14 in total 18 point sources, their likely categories have been identified; seven are (type-I) bursters (definitely LMXBs), three are black hole candidates (BHCs), two are pulsars (probably HMXBs), and the other two are an AGN and the special source, the bursting pulsar.

6.4.2 Population of bright sources in the Galactic Center region

We show the relationship between flux and photon index Γ for each category of sources in Fig. 6.54. It shows the clear difference between bursters and pulsars; the photon indexes of pulsars (or the bursting pulsar) are smaller than 1.3, whereas those of bursters are larger than 1.6. Therefore we can probably distinguish unidentified sources to be pulsar or burster candidates, using this relation. For example, the two unidentified persistent sources, 1E 1743.1−2843 and SLX 1737−282 are strong candidates for bursters according to their photon indexes, whereas XTE J1739−302 may be a pulsar. In fact, transient nature of XTE J1739−302 suggests a Be/NS binary origin, although the observed variability is unusual even for a Be/NS binary (Section 6.2.4).

We have often observed transient sources in TOO observations. This is a strong observational bias for the study on the X-ray population of the Galactic Center region. In fact, most of transients are known to be BHCs and Be-NS binaries. Therefore if we use all the data sets available here, which include transient sources, the sample may have larger BHCs and Be-NS binaries than expected from an unbiased survey observation. Then we limit the sample to only the persistent sources, and find that 9 of 11 sources are identified: 6 bursters (LMXBs), 1 BHC, 1 pulsar (HMXB?) and 1 AGN. It suggests that most part of the X-ray sources in the Galactic Center region are LMXBs. In addition, if we categorize 1743.1−2843 and SLX 1737−282 as LMXBs according to the above mentioned criterion, 8 of 11 sources in the Galactic Center region are regarded as LMXBs. Then we conclude

Table 6.10: Summary of *ASCA* results on bright sources

Name		——— *ASCA* results ———				General remarks	Category
	$\Gamma^\dagger$	$kT^\ddagger$	$N_{\rm H}$¶	Flux%	Remarks		
			(Persistent point sources)				
1E 1740.7−2942	0.9–1.3	—	8–10	10∼22	Short term var. $N_{\rm Fe} \rightarrow Z_{\rm Fe} \sim$ 2solar	Jet, 511 keV? >100keV emission	BHC
A 1742−294	1.6–1.9	—	3–4.5	21∼52	Type-I bursts $N_{\rm Fe} \rightarrow Z_{\rm Fe} \sim$ 4solar(?)	Type-I bursts $d \lesssim$ 8.5kpc?	LMXB
1E 1743.1−2843	1.7–2.1	—	18–20	6∼11	Flux variability No spectral change	No burst	
SLX 1737−282	2.1–2.4	—	1.8–2.2	3.6∼4.9	Persistent Short term var.		
GRS 1734−292	1.3–1.7	—	1.3–2.0	2.5∼3.3	No short term var.	Radio jet opt/IR (z = 0.0214)	AGN (Sey 1)
AX J1749.2−2725	0.7–1.3	—	7–13	0.2∼3	Pulsation(P=220s) Long term flux var.	Nothing	HMXB(?)
SLX 1744−299	1.7–2.0	—	3.3–4.3	9∼14	Long term flux var.	Type-I burst $d \sim$ 8.5kpc	LMXB
SLX 1744−300	(∼2.1)	6.9–7.4	4.7–5.2	46—51	Type-I bursts Bremss. is better	Type-I bursts $d \sim$ 8.5kpc?	LMXB
GX 3+1	1.7–1.8	11.3–11.5	1.8–2.2	∼440		Type-I bursts Long term flux var.	LMXB (Atoll)
AX J1745.6−2901	1.8∼2.2 (*ASCA* results: Maeda *et al.* 1996)	∼ 7	23–31	0.8∼4	Type-I burst, eclipse Long term flux var.		LMXB
SLX 1735−269	2.1–2.2 (*ASCA* results: David *et al.* 1997)	—	1.4–1.55	∼12		Burst Emission up to 100 keV	LMXB
			(Transient point sources)				
GRS 1737−31	1.5–1.6	—	5.9–6.4	< 0.02 ∼ 13	Short term var.	Emission above 100 keV	BHC
KS 1741−293	1.9–2.1	—	19–22	< 0.13 ∼ 8		Type-I bursts $d \sim$ 8.5kpc?	LMXB
GRS 1741.9−2853	2.1–2.5	—	11–12	< 0.04 ∼ 9		Type-I bursts $d \sim$ 8kpc	LMXB
XTE J1739−302	0.7–0.9	—	2.9–3.5	< 0.07 ∼ 200	Unusual giant flare Bremss. is rejected.	Flare state $kT \sim$ 12 keV bremss	
GRO J1744−28	1.0∼1.2 (*ASCA* results: Nishiuchi *et al.* 1999)	—	5–6	< 0.1 ∼ 500	Broad iron-line Type-II bursts & pulsation		Bursting-pulsar
XTE J1748−288	2.6∼2.7 (*ASCA* results: Kotani *et al.* 2000)	—	5–10	< 0.1 ∼ 5	Lines(?) Exponential decay of flux	Jet with 0.93c	BHC
GRO J1750−27	0.4–0.55 (*ASCA* results: Dotani *et al.* 1995)	—	3–3.5	∼ 60	Pulsation	Pulsation	HMXB(?)
			(Extended sources (SNRs & SNR candidates))				
G 359.0−0.9	—	0.3–0.5	1.1–2.0	0.24	Thermal(Shell)	Shell-like SNR	SNR
G 359.1−0.5	—	0.2 & 4	∼8	0.1	Thermal(Center-filled)	Shell-like SNR	SNR
G 359.1+0.9	—	∼0.7	∼0	0.03	Soft X-rays (extended?)	Composite SNR	SNR
G 0.9+0.1	∼1.5	∼2	∼10	0.2	Compact	Composite SNR	SNR
G 0.0−1.3	—	0.4–0.6	1.1–1.5	1.0	Thermal; Extended	no counter part	
G 0.56−0.01	—	4–8	5–7	0.16	Strong iron-K (Z > 2)	no counter part	

†: Photon index.

‡: Temperature [keV] where we use Bremsstrahlung (for point sources) or thin thermal plasma model (for SNRs).

¶: Hydrogen column density [10^{22} H cm^{-2}].

%: Observed flux with 2–10 keV [10^{-11} erg cm^{-2} s^{-1}].

Notes —

Here, "var.", "opt", "Bremss" mean variation, optical, Bremsstrahlung, respectively.)

$Z_{\rm Fe}$ and d are used for iron abundance and distance to the source.)

For other abbreviations, see Appendix B.

For almost all of point sources, flux variation for years was found.

The significant change of the spectral parameters was not observed.

SLX 1744−300: Power law model is rejected.

AX J1745.6−2901: Photon index may be varied.

G 359.1−0.5: Two component for thermal emission is required.

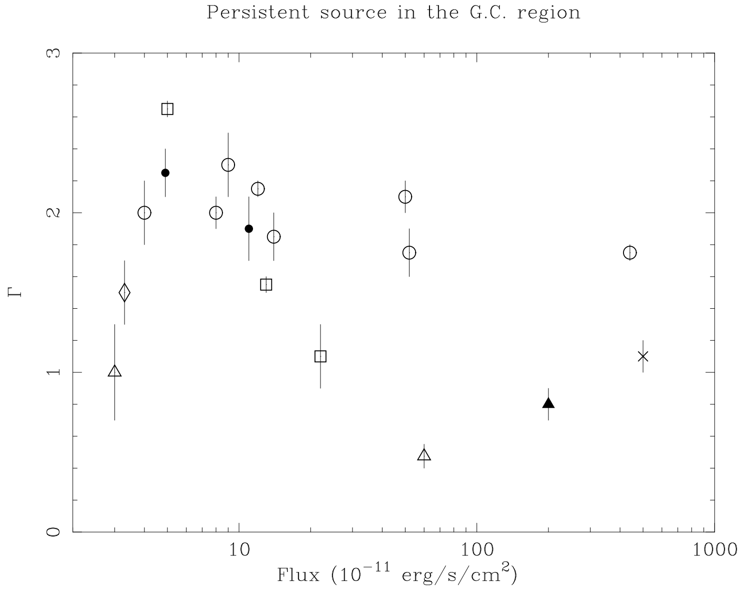

Figure 6.54: Flux-Γ relation for bright sources in the Galactic Center region. Open circles are for bursters; open rectangles, for BHCs; open triangles, for pulsars; open diamond, for an AGN; a cross, for the bursting pulsar GRO J1744−28; closed circles, for unidentified persistent sources; and a closed triangle, for an unidentified transient source.

that the major population of persistent bright X-ray sources in the Galactic Center region is low mass X-ray binary. It follows that the age of these sources are rather old. We discuss this problem in more detail in Chapter 9.

Note that the sources in this sample are sufficiently bright that they are able to be detected whenever *ASCA* observes them with usual exposure. It means that our samples are unbiased.

Chapter 7

Results III. — Column Density Distribution

We here mention the analyses of the column density distribution of the bright sources in the Galactic Center region. Through this chapter, we use the column density values obtained in the fitting where the solar abundances for the absorbing matter were assumed, because the abundances of the absorbing matter were not well determined in most cases. We discuss the systematic uncertainty due to the assumed abundance in Section 7.2.3.

The preliminary results were already published in Sakano *et al.* (1998a, 1999b, 1999d).

7.1 What determines the source column densities?

7.1.1 The most dominant factor for the column density

Fig. 7.1 shows the relation between photon index Γ and column density $N_{\rm H}$ for bright sources. We found no significant correlation between them. Since the source category well correlates with the photon index, it means that the dominant factor to determine the column density to the source is some other thing, such as, source position or distance.

Then we plot the relation of source column densities with $|l_{\rm II}|$ and $|b'|$ in Fig. 7.2 and in Fig. 7.3, respectively, where we define $|b'|$ as the angular distance from the true Galactic plane, which goes through Sgr A* at $(l_{\rm II},\ b_{\rm II})=(359\overset{\circ}{.}944,\ -0\overset{\circ}{.}046)$;

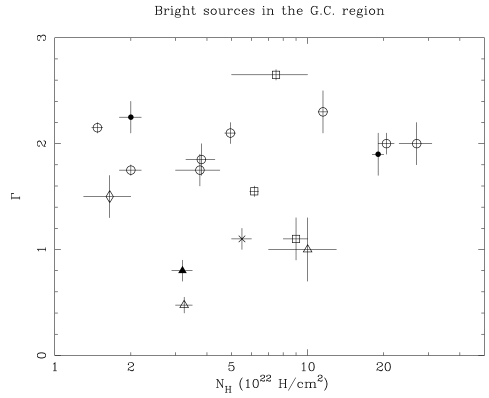

Figure 7.1: N_{H}-Γ relation for bright sources in the Galactic Center region. The meaning of the symbols are the same as in Fig. 6.54 in the previous section.

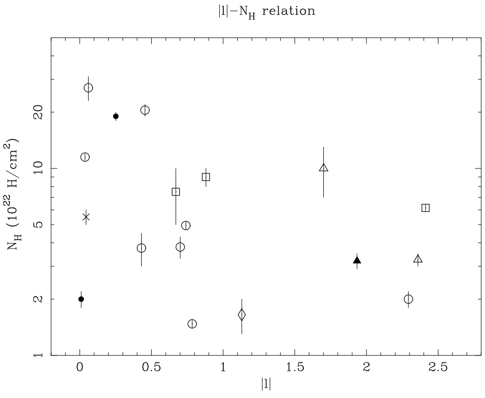

Figure 7.2: $|l_{\mathrm{II}}|$(deg)-N_{H} relation for bright sources. The meaning of the symbols are the same as in Fig. 6.54 in the previous section.

accordingly, $b' \equiv b_{\mathrm{II}} + 0.^{\circ}046$ (see footnote[1]). The source column densities were found to have clear correlation with $|b'|$, *i.e.*, the sources located at smaller $|b'|$ have larger column densities. On the other hand, the correlation between the source column densities and $|l_{\mathrm{II}}|$ is weak, if it exists; although some sources with small $|l_{\mathrm{II}}|$ of $< 1^{\circ}$ have large column densities, some sources with similar $|l_{\mathrm{II}}|$ have only small columns.

Some of the sources might have intrinsic absorption close to the source. However, intrinsic absorption definitely has no correlation with the apparent galactic latitude. Therefore, the contribution of the intrinsic absorption is small in the observed total column density with each source, at least for the sources with column densities of larger than a few times 10^{22}H cm^{-2} in this region.

The source column densities might be possibly related with the distance; the sources with larger distances may have larger column densities. However, the source distances have probably no correlation with the galactic latitude. Therefore the apparent correlation between the column densities and the latitude implies that the dominant factor to determine the source column density is *not* the source distance.

One may argue that there are observational biases to give us such correlation for the selected sources. However, the selected sources are so bright that they should be significantly detected whatever the distances are, if they are located in the Galaxy; this fact supports that there are little observational biases.

---

[1] The center of the galactic coordinates (l_{II}, b_{II}) is shifted from the true Galactic Center, as indicated here. However, the Galactic plane is known to be still parallel to the line of $b_{\mathrm{II}} = 0$. Hence the notation of "$|b'|$-direction" used through this chapter is identical with "$|b_{\mathrm{II}}|$-direction".

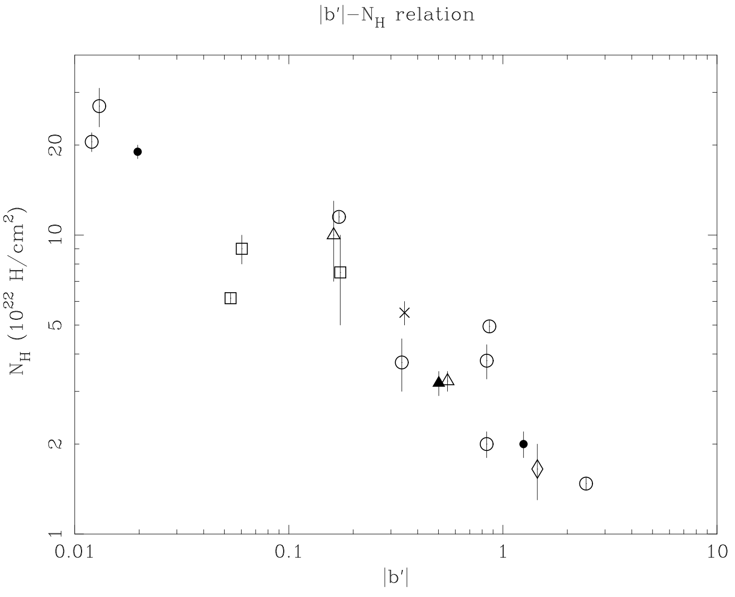

Figure 7.3: $|b'|$(deg)-$N_{\rm H}$ relation for bright sources, where $b' \equiv b_{\rm II} + 0.^\circ 046$. The meaning of the symbols are the same as in Fig. 6.54 in the previous section.

Thus we conclude that the dominant factor to determine the column densities of the bright sources in the Galactic Center region is neither the source category nor the distance.

Then we consider the source distances again. For a source located near the sun, the column density should be quite small. In fact, if we adopt the average interstellar density of 1 H $\rm cm^{-3}$, the column density to the source with the distance of 1 kpc is $\sim 3 \times 10^{21}$ H $\rm cm^{-2}$, which is much smaller than the observed value. Therefore, the distances for the sources are several kpc or farther.

We can check this implication for the distance, using the known source distances. The distances to SLX 1744−299 (Pavlinsky *et al.* 1994), A 1742−294 (Lewin *et al.* 1976) and GRS 1741.9−2853 (Cocchi *et al.* 1999b) are estimated to be nearly the same as 8.5 kpc from the burst peak flux, whereas GRS 1734−292 is identified as an extragalactic object (Martí *et al.* 1998), as reviewed in Section 2.2. No evidence for nearer distance for other sources has been reported, except for GX 3+1, where marginal evidence for slightly nearer distance was reported[2] (see Section 2.2.8). In fact, no optical counter part for other sources has been reported, which is consistent with the observed large column densities with *ASCA*, and with the suggestion for the distances to the sources of kpc or farther.

The interstellar matter (ISM) scale height of ∼100 pc for vertical direction to the Galactic plane corresponds to $0.^\circ7$ for the distance of 8.5 kpc. It means that the sources with latitude larger than $0.^\circ7$ is located not in the disk with thick ISM, but in the bulge with thin ISM, or farther than the bulge, unless the source distance is much smaller than 8.5 kpc. For such sources with high galactic latitude ($\gtrsim 0.^\circ7$), we can give no constraint for the upper limit of the distance from the column density because the ISM density in the bulge is known to be quite small. The galactic latitude of GRS 1734$-$292, which is identified to be an extragalactic object, is $1.^\circ4$, much larger than the above threshold of $0.^\circ7$. Therefore, this identification is not unusual even from the viewpoint of the galactic column density.

---

[2] Note that even if the distance to GX 3+1 is slightly smaller than 8.5 kpc, it does not cause a serious problem according to the reason as discussed in the following paragraph.

We can naturally derive the following suggestion from the above discussed fact; for the sources with the (galactic) latitude of less than $0.^\circ7$, the column density should be generally the increasing function of the distance, other than of the galactic latitude. This effect should be represented on the $N_{\rm H}$-$|b'|$ plot (Fig. 7.3) as the scatter of the data points from the general tendency. For example, we expect the column density of the source at the opposite side of the Galaxy to be about twice as that of the source at the Galactic Center distance. Or the column density of the source with the distance of 4 kpc is less than half of that of the source at the Galactic Center. However, Fig. 7.3 shows no such large scatter. Hence we conclude that the distances to the sources with the galactic latitude of less than $0.^\circ7$, or conservatively less than $0.^\circ3$, are similar to those to each other, and are probably equal to the distance to the Galactic Center, 8.5 kpc, the same as for the case of the three sources of which the distances are determined from the burst peak fluxes.

We summarize the conclusion of this section;

1. The dominant factor that determines the column density of the bright sources is the galactic latitude.

2. The source distances are near that of the Galactic Center, 8.5 kpc, for the sources with $|b_{\rm II}| \lesssim 0.^\circ3$, whereas for the sources with $|b_{\rm II}| > 0.^\circ3$, the distances are several kpc or larger.

7.1.2 The observational formulation to express the column density (1)

We tried to make an observational formula to reproduce the source column densities as a function of $|b'|$ ($\equiv |b_{\rm II} + 0.046^\circ|$). In this procedure, we assumed all the data uncertainties to be the same, because much larger scatter of the data than that by those statistical uncertainties clearly indicate that the systematic error for the model is much larger than the statistical uncertainties for the data. Regardless of the large scatter of the data, to build an observational formula is nevertheless important to find the overall structure of the column density distribution, and to further consider the factors to determine the column density distribution.

We fitted the profile in Fig. 7.3 with (i) power-law, (ii) exponential and (iii) Gaussian functions. Fig. 7.4 and Table. 7.1 show the best-fit model functions with the data points and the best-fit parameters, respectively. Power-law model is clearly the best model, whereas exponential and Gaussian models are not appropriate. Although power law function implies no typical scale for the column density distribution to $|b'|$ direction, our small samples cannot give so strong constraint. Thus, this result simply suggests that the column density distribution probably consists of multi components.

Table 7.1: Best-fit parameters in the fitting of the N_{H}-$|b'|$ profile.

			Power-law	Exponential	Gaussian
N_{H}	$[10^{22}\mathrm{H\ cm^{-2}}]$	$=$	$(I \times \lvert b'\rvert^{\alpha})$	$(I \times e^{-\frac{\lvert b'\rvert}{\alpha}})$	$(I \times e^{-\frac{1}{2}\left(\frac{\lvert b'\rvert}{\alpha}\right)^2})$
α			-0.49	0.24	0.20
I	$[10^{22}\mathrm{H\ cm^{-2}}]$		3.13	20.2	16.9

NOTE — The unit of $|b'|(\equiv |b_{\mathrm{II}} + 0.^{\circ}046|)$ is degree.

7.1.3 The observational formulation to express the column density (2)

We then investigated the more detailed nature of the column density distribution for the bright sources. Fig. 7.5 show the 2-dimensional plot of the source column densities on the galactic coordinates. General tendency of decreasing column densities to increasing (galactic) latitude is again seen. In addition, we can see the similar but much weaker tendency for (galactic) longitude (l) direction; the sources with larger galactic longitudes seem to have generally larger column densities than those with smaller longitudes in the same galactic latitudes.

We fitted this 2-dimensional distribution of the column density as a function of ($|l'|$, $|b'|$), which are defined as the angular distances from Sgr A* (($|l'|$, $|b'|$) $\equiv$ ($|l_{\mathrm{II}} + 0.^{\circ}056|$, $|b_{\mathrm{II}} + 0.^{\circ}046|$); see Section 7.1.1), with (i) power-law(l'-direction) & power-law(b'-direction), (ii) Gaussian(l'-direction) & power-law(b'-direction), (iii) power-law(l'-direction) & Gaussian(b'-direction), (iv) Gaussian(l'-direction) & Gaussian(b'-

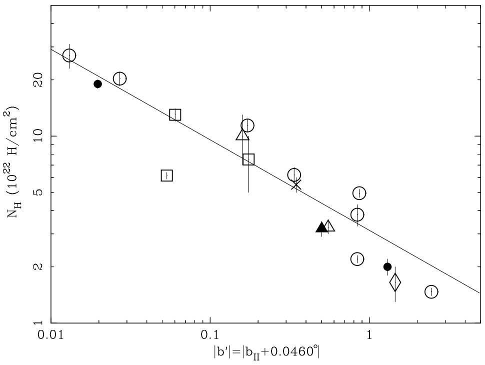

(i) Power-law

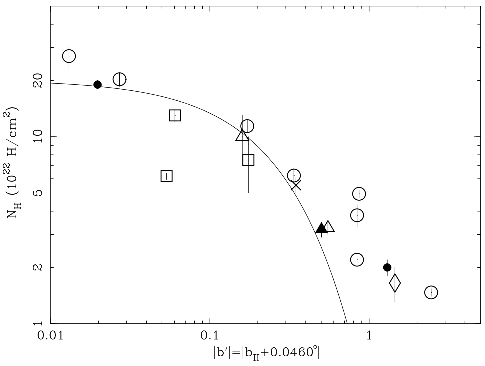

(ii) Exponential

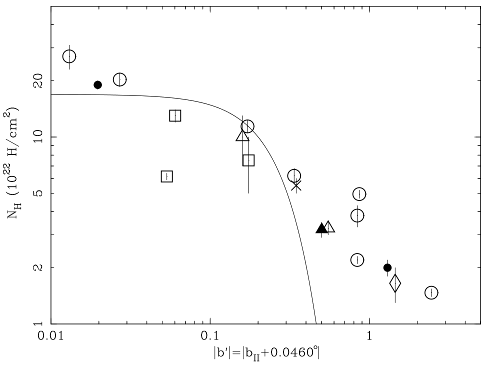

(iii) Gaussian

Figure 7.4: The best-fit $N_{\rm H}$-$|b'|$ ($\equiv |b_{\rm II} + 0.^{\circ}046|$) profiles with the data where three different models are applied. The fitting were made with unweighted method for error with each point. The meaning of the symbols are the same as in Fig. 6.54.

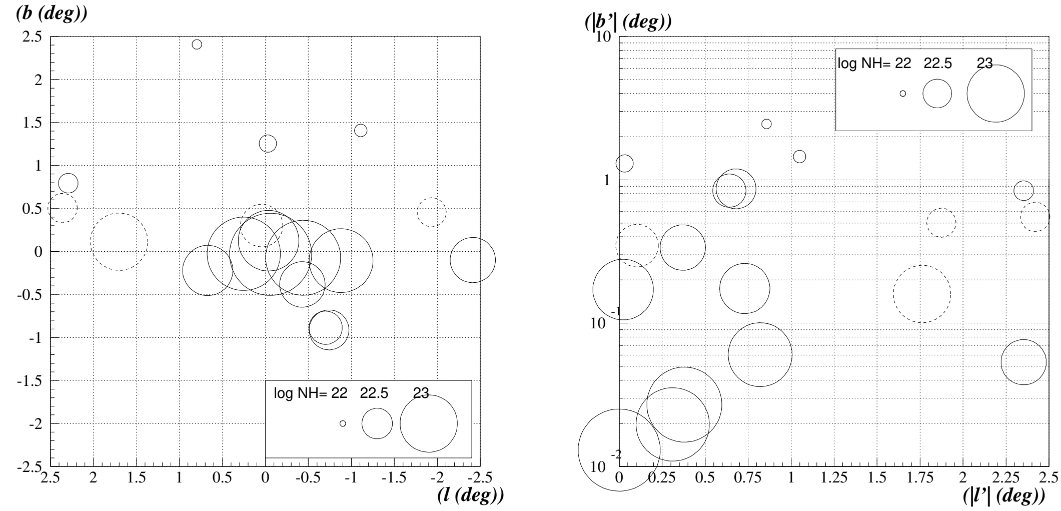

Figure 7.5: $N_{\rm H}$-$l_{\rm II}$-$b_{\rm II}$ relation for bright sources in the Galactic Center region. The positions and the sizes of circles represent the location and the column density for each source, respectively. The radii of circles are logarithmically scaled, as indicated in the small boxes in the figures (the unit of column density $N_{\rm H}$ is (H cm^{-2})). Dashed lines are for pulsars and a pulsar candidate (GRO J1744−28, AX J1749.2−2725, GRO J1750−27, and XTE J1739−302), whereas solid lines are for other class of objects. (Left) the coordinates are galactic, ($l_{\rm II}$, $b_{\rm II}$). (Right) the axes of ($|l'|$, $|b'|$) mean the angular distances from Sgr A*; accordingly, ($|l'|$, $|b'|$) $\equiv$ ($|l_{\rm II} + 0.^\circ056|$, $|b_{\rm II} + 0.^\circ046|$).

direction) models. Table 7.2 shows the best-fit parameters, whereas Fig. 7.6 shows the comparison between the best-fit model and the data points. To visualize the fitting results, we plot the 1-dimension profiles of the data and the best-fit model (Model (ii)) for $|l'|$- and $|b'|$-directions in Fig. 7.7, where we normalize the data and the models to represent those at a certain $|b'|$ and $|l'|$, respectively, using the best-fit function with Model (ii).

The best-fit results show that the parameters for $|b'|$-direction are almost not affected by the difference of the models for $|l'|$-direction. It is natural because the dominant factor that determines the column density of the bright sources is the galactic latitude, as studied in Section 7.1.1.

With this 2-dimensional fitting, we again found that power law model is rather good for the observational column density distribution model for $|b'|$-direction except for three data points with $|b'| > 1\overset{\circ}{.}0$, whereas Gaussian model cannot reproduce the data with $|b'| \gtrsim 0\overset{\circ}{.}4$ at all. The slope of power law for $|b'|$-direction is a little flatter than that with simple 1-dimensional fitting (see Section. 7.1.2: Table 7.1). The small change suggests the influence by $|l'|$-dependence of the column density distribution. The detailed model for $|l'|$-direction however cannot be well restricted (power law or Gaussian). Thus, we here adopt the Gaussian model for $|l'|$-direction because power law model diverges at $|l'| = 0$.

We consequently give the best observational formula for the column density of X-ray sources in the Galactic Center region as,

$$N_{\mathrm{H}} = 4.1 \times e^{-\frac{1}{2}\left(\frac{|l'|}{2.1}\right)^{2}} \times |b'|^{-0.43} \quad (10^{22}\mathrm{H\ cm^{-2}}), \tag{7.1}$$

where the units of $|l'|(\equiv |l_{\mathrm{II}} + 0\overset{\circ}{.}056|)$ and $|b'|(\equiv |b_{\mathrm{II}} + 0\overset{\circ}{.}046|)$ are degree.

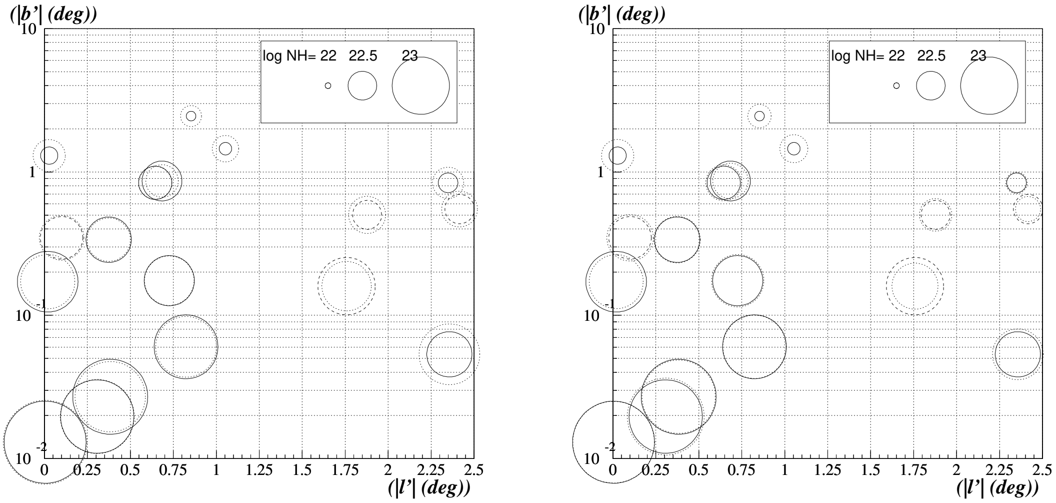

(i) (l:Power, b:Power) (ii) (l:Gauss, b:Power)

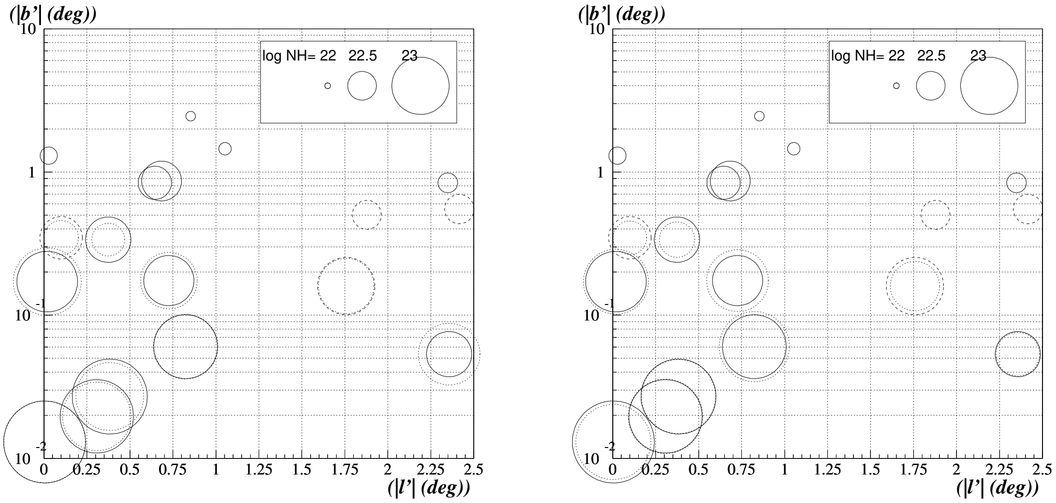

(iii) (l:Power, b:Gauss) (iv) (l:Gauss, b:Gauss)

Figure 7.6: Fitting results for $N_{\rm H}$-$l_{\rm II}$-$b_{\rm II}$ relation for bright sources in the Galactic Center region $((|l'|,\ |b'|) \equiv (|l_{\rm II} + 0.^{\circ}056|,\ |b_{\rm II} + 0.^{\circ}046|))$. The positions and the sizes of circles represent the location and the column density for each source, respectively, the same as in Fig. 7.5 right panel. Dashed lines are the data for pulsars and a pulsar candidate, whereas solid lines are the data for the sources except pulsars. Dotted lines represent the best-fit model, where each model is indicated in bottom of each panel; the notation means (l:"l-direction (fitting) function", b:"b-direction function"). In panels (iii) and (iv), the best-fit model values for several sources are too small ($N_{\rm H} < 1 \times 10^{22}$ H cm^{-2}) to plot; for such data, no corresponding dotted line circle is shown in the panels.

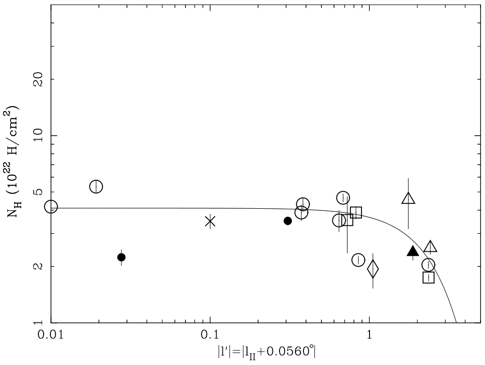

(a) N_{H}-$|l'|$ relation corrected for b-direction with $|b'| = 1.0°$

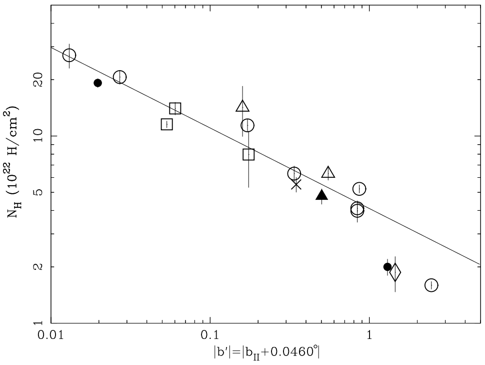

(b) N_{H}-$|b'|$ relation corrected for l-direction with $|l'| = 0.0°$

Figure 7.7: The best-fit (a) N_{H}-$|l'|$ ($\equiv |l_{\mathrm{II}} + 0.^\circ056|$) profile where Gaussian function is applied, (b) N_{H}-$|b'|$ ($\equiv |b_{\mathrm{II}} + 0.^\circ046|$) profile where power-law function is applied, and both with the data. Data and models are normalized so that (a) they represent the points at $|b'| = 1.^\circ0$ after correction for $|b'|$-direction with the best-fit power-law function, and so that (b) they represent the points at $|l'| = 0.^\circ0$ after correction for $|l'|$-direction with the best-fit Gaussian function. The meaning of the symbols are the same as in Fig. 6.54. The fitting were made with unweighted method for error with each point. The point at $|l'| = 0.^\circ01$ in panel (a), with AX J1745.6−2901, is in fact located at $|l'| = 0.^\circ004$ for the best obtained position with *ASCA*. Since the positional uncertainty for the point is large, about $0.^\circ006$, we here plot the point at $|l'| = 0.^\circ01$. Note that we used the best position of $|l'| = 0.^\circ004$ for the point in the fitting,

Table 7.2: Best-fit parameters in the fitting of the $N_{\rm H}$-$|l'|$-$|b'|$ relation

	Power($\|l'\|$)	Gauss($\|l'\|$)
Power($\|b'\|$)	$\alpha_l = -0.05$ $\alpha_b = -0.43$ $I = 3.4$	$\sigma_l = 2.1$ $\alpha_b = -0.43$ $I = 4.1$
Gauss($\|b'\|$)	$\alpha_l = -0.12$ $\sigma_b = 0.20$ $I = 13.7$	$\sigma_l = 1.5$ $\sigma_b = 0.19$ $I = 20.5$

NOTE —

$N_{\rm H}$=$I \times g(|l'|) \times h(|b'|)$ [10^{22}H cm^{-2}]

Power: $f(x) \equiv x^{\alpha}$

Gauss: $f(x) \equiv e^{-\frac{1}{2}\left(\frac{x}{\sigma}\right)^2}$

The units of $|l'|(\equiv |l_{\rm II} + 0\overset{\circ}{.}056|)$ and $|b'|(\equiv |b_{\rm II} + 0\overset{\circ}{.}046|)$ are degree.

7.2 The Galactic Center cold interstellar matter distribution

7.2.1 Fitting of the $N_{\rm H}$ profile with the Galactic Center ISM model

To consider the cold interstellar matter (ISM) distribution in the Galactic Center region, we have to subtract the contribution of the ISM distributed on the disk. We constructed the model for the Galactic disk ISM distribution, combining the results by Olling & Merrifield (1998), Malhotra (1994, 1995), Merrifield (1992) and Dame *et al.* (1987). The detailed formulation is given in Appendix A. Using eq. A.5 and A.6, we can calculate the total column density to the Galactic Center region due to the disk ISM as a function of $|l'|$, $|b'|$ and the distance.

We assumed a 3-dimensional Gaussian density distribution as the model for the cold ISM located truly in the Galactic Center region: axially symmetric Gaussian function for the radial direction from the Galactic Center (Sgr A*) along the Galactic plane, and with an independent width to the perpendicular direction to the plane; namely,

$$n_{\rm H} = I \times e^{-\frac{1}{2}\left(\frac{R}{\sigma_R}\right)^2} \times e^{-\frac{1}{2}\left(\frac{|z|}{\sigma_z}\right)^2}, \tag{7.2}$$

where $n_{\rm H}$ is the ISM density, I is the normalization, R is the Galactocentric radius along the Galactic plane, $|z|$ is the distance from the plane, and σ_R and σ_z are the widths (σ) of the Gaussian functions for the radial (R) and perpendicular (z) directions.

We tried to fit this cold ISM model to the observed column density ($N_{\rm H}$) profile. The accurate source distances are unknown except for GRS 1734−292. Thus we assumed that all the sources are located on the plane which is perpendicular to both of the Galactic plane and the line of sight to the Galactic Center. In this case, the distance to all the sources are nearly 8.5 kpc. We then fitted the observed column density distribution with the free parameters of σ_R, σ_z and normalization (eq. 7.2).

Table 7.3 shows the best-fit parameters, whereas Fig. 7.8 shows the comparison between the best-fit model and the data points. To visualize the fitting results, we plot the 1-dimension profile of the data and the best-fit model for $|b'|$-direction in Fig. 7.9(a), where we normalize the data and the models to represent those at $|l'| = 0\overset{\circ}{.}0$, using the best-fit function.

Table 7.3: Best-fit parameters for $N_{\rm H}$-$|l'|$-$|b'|$ profile where the Galactic Center and Galactic disk ISM mass distribution model (eq. 7.2, A.5 and A.6) is applied.

Normalization (I) [H cm^{-3}]	σ_R [pc]	σ_z [pc]
280	20	170

NOTE — See eq. 7.2, for notation.

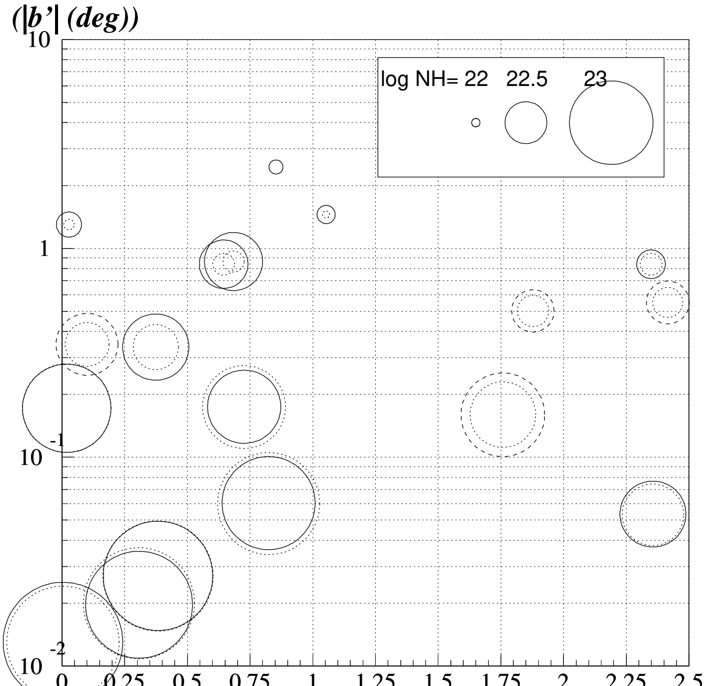

Figure 7.8: Fitting results for $N_{\rm H}$-$l_{\rm II}$-$b_{\rm II}$ relation for bright sources in the Galactic Center region where the Galactic Center and Galactic disk ISM mass distribution model is applied $((|l'|, |b'|) \equiv (|l_{\rm II} + 0.^\circ056|, |b_{\rm II} + 0.^\circ046|))$. The positions and the sizes of circles represent the location and the column density for each source, respectively, the same as in Fig. 7.5 right panel. Dashed lines are the data for pulsars and a pulsar candidate, whereas solid lines are the data for the sources except pulsars. Dotted lines represent the best-fit model.

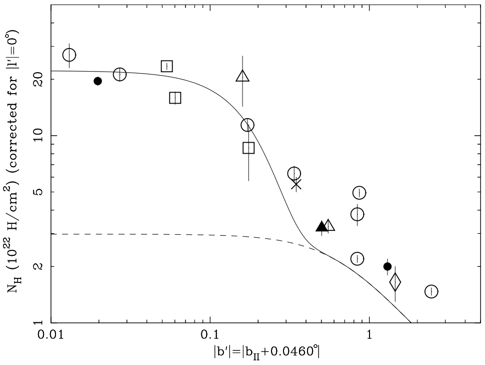

(a) $N_{\rm H}$-$|b'|$ relation, where $N_{\rm H}$ is corrected for l-direction with $|l'| = 0.^\circ 0$

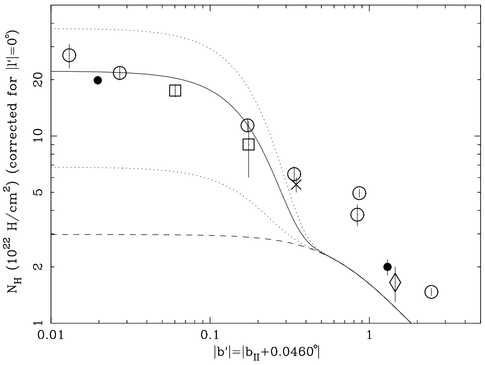

(b) the same as (a), but with only the sources $|l'| < 1.^\circ 25$

Figure 7.9: The best-fit $N_{\rm H}$-$|b'|$ ($\equiv |b_{\rm II} + 0.^\circ 046|$) profiles where the Galactic Center ISM model is applied (see text), with the data of (a) all the bright sources, (b) the bright sources with $|l'| < 1.^\circ 25$ ($|l'| \equiv |l_{\rm II} + 0.^\circ 056|$). Data and models are normalized so that they represent the points at $|l'| = 0.^\circ 0$, corrected for $|l'|$-direction with the best-fit Gaussian function. Solid and dashed lines are the model of the total column density and of the column density due to the Galactic disk formulated in Appendix A, respectively. Dotted lines are the threshold for the expected data scatter (see text (Section 7.2.2)). The meaning of the symbols are the same as Fig. 6.54. The fitting were made with unweighted method for error with each point. Note that the best-fit model line (solid and dashed lines) in panel (b) are identical with those in panel (a); we did not fit the data only shown in panel (b).

7.2.2 The ISM distribution in the Galactic Center region

From Fig. 7.9, we found that the column densities of the sources with $|b'| \gtrsim 0.^{\circ}4$ are well explained only with the Galactic disk components except for a few sources. It is natural because such sources with larger $|b'|$ are probably located in the bulge (or farther), where the ISM is quite thin, as already discussed in Section 7.1.1.

Using this result, we can discuss the ISM distribution truly in the Galactic Center region, separating it from the ISM in the disk. Because of the disk component, the Galactic Center ISM distribution needs steeper function for $|b'|$-direction than in the simple fitting made in the previous section. In addition, this time, Gaussian function for $|b'|$-direction is not a bad model. It is definitely because about zero column densities for the sources with large $|b'|$ require steep cut off in the profile. We found that the scale lengths for radial (σ_R) direction (or $|l'|$-direction) along the Galactic plane and for vertical (σ_z) direction (or $|b'|$-direction) are 170 pc and 20 pc, respectively (see Table 7.3). Hence, regardless of the fitting model, the scale length for the vertical direction is much smaller than that for the parallel direction.

The observed column density ($N_{\rm H}$) profile (Fig. 7.9) again shows only a little scatter. However, if the sources are distributed isotropically for radial direction along the Galactic plane, the distances to each source are reflected by the scatter of the data in the column density ($N_{\rm H}$) profile because farther sources should have larger column densities than nearer sources. To evaluate this effect quantitatively, we need to know the spatial distribution of bright X-ray sources in the Galactic Center region. Then we consider the source distribution from our sample, since this work is almost the first detailed study for that.

We can see that 5 in 18 sources, *i.e.*, 30% of the sources, in the list are distributed at $|l_{\rm II}|(\cong |l'|) > 1.^{\circ}25$ (= half of $2.^{\circ}5$ region) (Fig. 5.2 or Fig. 7.5). It means that 30% of the 13 sources at $|l_{\rm II}|(\cong |l'|) < 1.^{\circ}25$ are distributed with the Galactocentric distance R of larger than 190 pc, if the X-ray source distribution is axially symmetric. From the best-fit model of Gaussian distribution for radial direction at $|l'| = 0$, we calculated the column density originated in the Galactic Center ISM of the sources with $R > 190$ pc to be smaller than 20% or larger than 180% of that of the source with the Galactic Center distance, according to the source locations in front of or behind the Galactic Center, respectively.

On the other hand, the observed scatter from the best-fit function is $\lesssim 30\%$ for the sources with $|l'| < 1.^{\circ}25$ and $|b'| < 0.^{\circ}3$, [3] as shown in Fig. 7.9(b). According to the above discussed source spatial distribution, about 2 of 6 sources with $|b'| < 0.^\circ 3$ should show much smaller (< 20%) or much larger (>180%) column densities than other sources.

---

[3] Four sources with $|b'| > 0.^{\circ}3$ show much larger column densities than the model. For the positions of those four sources, the Galactic Center ISM contribution for the total column is

The observed column density profile with little scatter may mean that the column densities of the sources with $|l'| < 1.^\circ 25$ and $|b'| < 0.^\circ 3$ are independent of the source distance[4]. A possible explanation for this fact is that the ISM distribution in the Galactic Center region is not center-filled function like Gaussian, but is a "wall"-like (or more probably, ring-like) distribution; the wall or the ring is sufficiently dense to account for most of the total column density due to the Galactic Center ISM. Another possible reason for the little scatter of the data is that X-ray sources are intensively distributed along some distinct structure like the arm in the Galactic Center region. Note that this suggestion is almost independent of the detailed shape of the function first assumed, for example, Gaussian or exponential, because this suggestion is principally based on the fact that the column density profile shows little scatter.

However, our sample of only 6 sources is still small to discuss detailed nature of the Galactic Center ISM distribution or the X-ray source distribution. Future X-ray observations with higher sensitivity would give us much larger samples, and accordingly give a good constraint for this problem.

7.2.3 Total mass of the Galactic Center cold ISM

We tried to estimate the total mass of the cold interstellar matter in the Galactic Center region. Although we derived the possibility that the distribution of the Galactic Center cold ISM may be not Gaussian-like for radial direction along the Galactic plane, the model instead of Gaussian is not proposed due to small sample. Therefore we here adopt the simple model for the ISM density distribution that we used: 3-dimensional Gaussian function (eq. 7.2). Then we calculated the total mass of the cold ISM in the Galactic Center region to be 6.4×10^7 $M_\odot$, integrating eq. 7.2 with the best-fit result in Table 7.3.

In all the analyses in this chapter, we have assumed the abundance to be solar. The hydrogen column density determined with the X-ray absorption is inversely

---

probably small. Therefore, the discrepancy between the model and the data is presumably due to uncertainty of the Galactic disk mass model. Since our interest here is about the Galactic Center ISM distribution, we do not discuss on those sources.

[4] We gave the general discussion on the relation between the data scatter in the column density profile and the source distance in Section 7.1.1.

proportional to the abundance; accordingly the derived total mass is also inversely proportional to the abundance. The abundance in the Galactic Center region is still debatable, but is not smaller than solar: consistent with solar (Sellgren, Carr, & Balachandran 1997, Ramírez *et al.* 1998, and Carr *et al.* 1999), or even larger (e.g., Murakami *et al.* 2000a). In fact, we found that larger iron abundance[5] than the solar value to explain the deep iron edge in the X-ray spectrum is required for two cases: 1E 1740.7−2942 (Section 6.1.1) and A 1742−294 (Section 6.1.2). Since we assumed the abundances to be solar in this chapter, our estimated total mass should be regarded as an upper limit; it may be reduced by some factors.

7.3 Comparison with other wavelengths results

7.3.1 Scale lengths of the Galactic Center ISM distribution

Our derived scale lengths (σ of Gaussian) of the cold ISM in the Galactic Center region for the radial and the vertical direction are 170 pc and 20 pc (Table 7.3), respectively, which corresponds to the angles of $70'$ for l-direction and $8'$ for b-direction at 8.5 kpc distance. Tsuboi *et al.* (1999b) derived this vertical scale length (σ_z) to be about 11 pc from the Galactic Center survey with CS molecular line ($J = 1 - 0$). Hence, our derived value is slightly larger than that with CS line, but near. This vertical scale length σ_z is much smaller than that near the sun, $\sigma_z = 74$ pc (with CO line; Dame *et al.* 1987). When we extrapolate the function on the vertical scale length of eq. A.4 to the Galactic Center, we obtain 27 pc. Since the formulation of eq. A.4 has large uncertainty for radial variation of σ_z (see the original papers referred in Appendix A), this value is still consistent with our derived σ_z. Therefore, the vertical scale length σ_z of the cold ISM in the Galactic Center region may be consistent with the overall tendency seen in the Galaxy.

For radial direction, since the radio molecular structure for l-direction is quite complicated (e.g., Tsuboi *et al.* 1999b), it is a little difficult to compare the representative value. However, the most distinct radio molecular structures are seen in $|l_{\rm II}| \lesssim 1^\circ$ along the simply increasing function of velocity along line of sight in the longitude-velocity map. Thus, our derived scale length for radial direction is also consistent with the radio result.

---

[5] Note that our derived iron abundance is the relative abundance to lighter elements, mostly oxygen.

7.3.2 Total mass of the Galactic Center cold ISM

We discuss the total mass of the cold interstellar matter in the Galactic Center region. This problem has been discussed since 1980's, because the observations have given inconsistent results with each other (see the review by Morris & Serabyn (1996)).

Blitz *et al.* (1985) estimated the upper limit of the total interstellar mass in the Galactic Center region (within 500 pc radius) to be about $6 \times 10^7 M_\odot$ from the γ-ray observations[6]. The far-infrared observations by Cox & Laureijs (1989) gave a consistent value. However, the radio molecular observations have given larger values of more than a few $10^8 M_\odot$ (e.g., Bania 1986). A plausible explanation for this inconsistency is that the conversion factor of CO line intensity to H_2 column has radial gradient (Sodoroski *et al.* 1995). Recently, from the radio CO observations, Oka *et al.* (1998) or Dahmen *et al.* (1998) suggested that the molecular clouds in the Galactic Center region should be in pressure equilibrium, rather than in self-gravitational equilibrium. Their results gave a smaller conversion factor, hence gave a smaller value of the total cold mass to be $(2\text{–}5)\times 10^7 M_\odot$ within 500 pc radius. The CS (J=1−0) result by Tsuboi *et al.* (1999b) also supports it; they derived it to be $(3\text{–}8)\times 10^7 M_\odot$.

Our estimation for the cold mass is based on a new and independent technique. Although the observations are limited within less than 380 pc, the derived total mass of 6.4×10^7 $M_\odot$ is the mass of all the Galactic Center ISM since the integration is made from 0 to infinite radius (Section 7.2.3). Note that this is an upper limit and may be reduced by some factors when we take the abundance into account (see Section 7.2.3). Thus our result is consistent with the γ-ray, far-infrared results, and recent radio results by Oka *et al.* (1998). Therefore, we favor that the molecular clouds in the Galactic Center region are in pressure equilibrium with the external large pressure probably due to strong magnetic fields (Morris & Serabyn 1996) and/or high pressure plasma found with the X-ray observations (e.g., Koyama *et al.* 1996).

---

[6] Since diffuse γ-ray in the Galaxy is mainly produced with interaction of cosmic ray and matter, one can estimate the mass from the flux of γ-ray, assuming the uniformity of the flux of cosmic ray.

Chapter 8

Results IV.
— Nature of Faint Sources

8.1 Application of the relation between column density and source position to the faint sources

We tried to compare the derived column density and source position relation (N_H-$|l'|$-$|b'|$ relation) with those of faint sources in the Galactic Center region of which the column densities are determined with sufficiently small uncertainties.

First, we compared the the data points with simple $|b'|$-N_H relation in Fig. 7.4(i) and Table 7.1. The results are given in Fig. 8.1(a). Many of the faint sources were found to show significantly smaller column densities than the derived relation for bright sources in the Galactic Center region. They are probably foreground sources, like stars.

Then, we compared the data with faint sources with the combined model of the Galactic Center and the Galactic plane ISM distribution, which is used in Section 7.2.1. Fig. 8.1(b), (c), (d) show the results. Note that the Galactic plane ISM model is almost invariant for any longitude if $|l'| < 2°$, which is the range that we used. In addition, the points with galactic latitude $|b'| \gtrsim 0.^\circ5$ are known to show almost no ISM component in the Galactic Center region (see Section 7.2.1, in particular, Fig. 7.9). Many of the sources again show significantly smaller column densities than the disk mass model. Only four sources, AX J1742.6$-$2901, AX J1740.2$-$2848, AX J1754.5$-$2928 and AX J1754.2$-$2755 in ascending order of $|b'|$, are left as the candidates for those located at the bulge[1]. We investigate and discuss on the natures of these four sources in following sections.

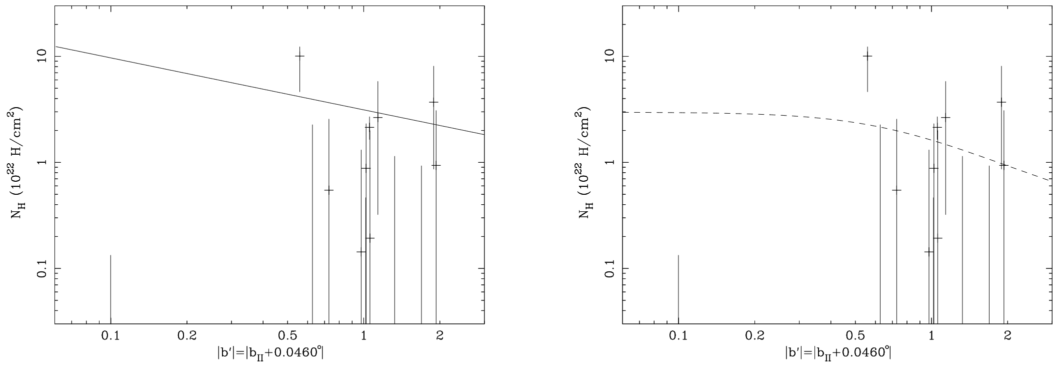

(a) Simple power law (b) The disk ISM model

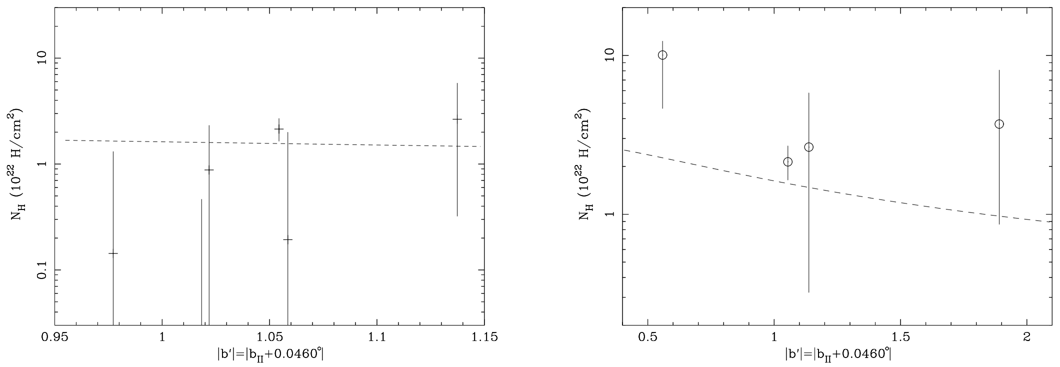

(c) The disk ISM model (zoomed up) (d) The disk ISM model (with selected sources)

Figure 8.1: Application of the N_{H}-$|b'|$ relation (solid or dashed line) obtained in the previous chapter to faint sources (the data), where $|b'| \equiv |b_{\mathrm{II}} + 0.^{\circ}046|$; (a) simple power law function derived in Fig. 7.4(i) and Table 7.1 is applied, (b) the Galactic disk mass model (see Section 7.2.1) is applied, (c) the same as panel (b), but with the different scale, (d) the data only for the selected sources, which are candidates for *not* foreground sources, are plotted.

---

[1] Among these sources, AX J1754.5−2928 may possibly be a foreground source with the distance of $\gtrsim$1kpc, when the lower limit of the column density is the actual value.

8.2 Nature of faint X-ray sources located probably near the Galactic Center

In the previous section (Section 8.1), we obtained another four sources which are probable candidates of the sources located in the Galactic Center region. Table 8.1 shows the relation between the observed flux and photon index for the four sources, which is a subset of Table 5.1.

Table 8.1: Flux-Γ relation of newly selected four sources

Name	$l_{\rm II}$¶	$b_{\rm II}$¶	$F_{\rm X}^{0.7-10{\rm keV}\dagger}$	$F_{\rm X}^{3-10{\rm keV}\dagger}$	$L_{\rm X}^{2-10{\rm keV}\ddagger}$	$\Gamma^{\S}$
AX J1754.5−2928	0.544	−1.937	2.2	0.2	2.0	$7.6^{+>2}_{-3.8}$
AX J1754.2−2755	1.849	−1.100	90	60	85	$2.5^{+0.4}_{-0.3}$
AX J1742.6−2901	−0.418	0.513	5.5	1.0	60	> 4
AX J1740.2−2848	−0.509	1.091	34	32	33	$0.6^{+0.6}_{-0.8}$

¶: Galactic coordinates in unit of degree.

†: Observed flux in unit of [10^{-13}erg cm^{-2} s^{-1}]; absorption is not corrected.

‡: (Absorption-corrected) luminosity in unit of [10^{33}erg s^{-1}].

§: Photon index.

We then discuss the nature of each source. Since no counter part with other wavelengths is listed for all the four sources in the database (Table 5.2), the discussion is based on only our results.

8.2.1 AX J1754.5−2928

The large photon index Γ of $\sim$ 8, or at least $\sim$4, suggests that the spectral model is in fact not a power law but is probably a thin thermal plasma (or possibly a blackbody). Then we fitted the spectrum with thin thermal plasma model with solar abundance materials, and found the temperature and column density to be $0.4^{+0.8}_{-0.3}$ keV and $2.5^{+5.9}_{-1.8} \times 10^{22}$ H cm^{-2}, respectively with χ^2/d.o.f=1.813/5. This low temperature is typical for stars. The possible small column density of $\gtrsim 0.7 \times 10^{22}$ H cm^{-2} may suggest the small distance. Consequently this source is likely to be a foreground star, although other possibility, for example, a faint compact source with low temperature and high luminosity, which is located at the bulge, is not excluded.

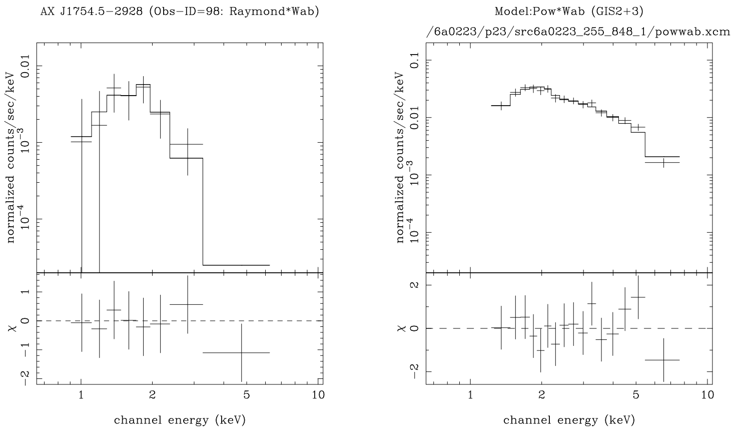

(a) AX J1754.5−2928 (b) AX J1754.2−2755

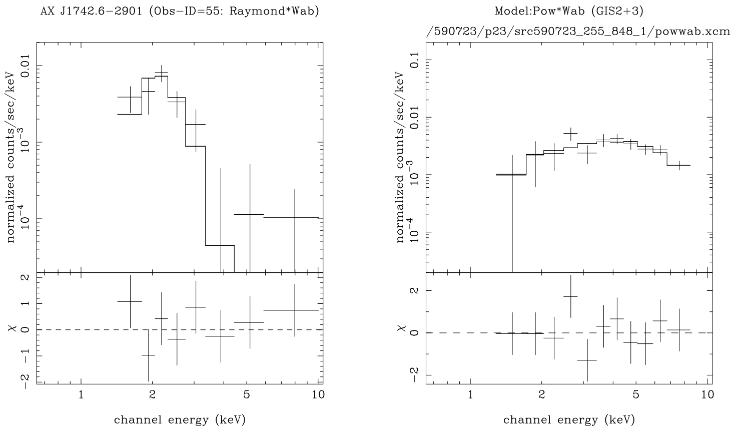

(c) AX J1742.6−2901 (d) AX J1740.2−2848

Figure 8.2: The spectra of the faint sources with best-fit models located probably near the Galactic Center. The applied fitting models are (a) thin thermal plasma model with absorption, (b) a power law with absorption, (c) thin thermal plasma model with absorption, (d) a power law with absorption.

8.2.2 AX J1754.2−2755

This source is rather bright, with the 3–10 keV observed flux of about 6×10^{-12} erg cm^{-2} s^{-1}. Thus the photon index is well determined with small uncertainty, and is in good agreement with those of bursters (see Fig. 6.54). Hence this source is also likely to be a low mass X-ray binary although no significant burst was detected during the observations.

8.2.3 AX J1742.6−2901

The large photon index Γ of larger than 4 is similar to AX J1754.5−2928, possibly a star. The spectral model is in fact not a power law but is probably a thin thermal plasma (or possibly a blackbody), the same as the case of AX J1754.5−2928. Then we fitted the spectrum with thin thermal plasma model with solar abundance materials, and found the temperature and column density to be $0.14^{+0.44}_{-0.04}$ keV and $16^{+6}_{-11} \times 10^{22}$ H cm^{-2}, respectively, with χ^2/d.o.f=3.863/5.

This unusual best-fit spectral parameters may be due to incomplete background subtraction. However better statistics is essential to estimate the accurate background, hence further observations are encouraged.

8.2.4 AX J1740.2−2848

The spectrum of this source (Fig. 8.2(d)) is found to be quite hard; the photon index of ~ 0.6. The fact that this source is more distinct in the hardest image with 7.1–10.0 keV (Fig. 5.2(c)) apparently indicates the hardness of this source.

This flat index suggests this source to be possibly a X-ray pulsar. Thus, using the 2–10 keV band data, we tried the pulse search with the FFT analysis (Fig. 8.3), then the epoch folding search (Fig. 8.4), and found the significant pulsation with the period of 725 ± 12 seconds for the assumed null-period derivative. Fig. 8.5(a) shows the folded light curve, which consists of one large peak for half of the period and constant flux for the other half. Although a following second peak may seem to exist, it is not significant statistically. The pulse fraction with 2–10 keV band was found to be about 50% (55%±15% with statistical uncertainty). Note that this apparent pulsation must not be due to the background, because the flux of the pulse component is large, and is comparable with that of the whole background intensity, and because the background shows no such pulsation (Fig. 8.5(b)). Since the observation of this source was made only once, and since the statistics is not good, we could not constrain the derivative of pulse period. We designated this newly discovered source as AX J1740.2−2848, as usual manner.

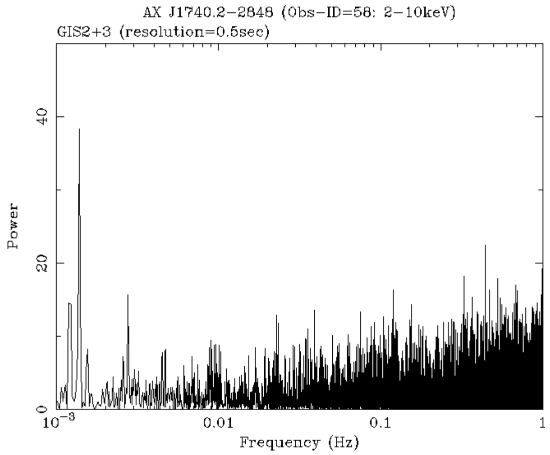

Figure 8.3: (AX J1740.2−2848) GIS2+3 FFT results with 2–10 keV band.

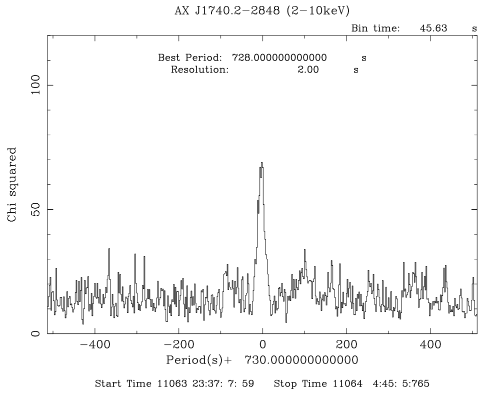

Figure 8.4: (AX J1740.2−2848) Result of the GIS2+3 Epoch folding search with 2–10 keV band.

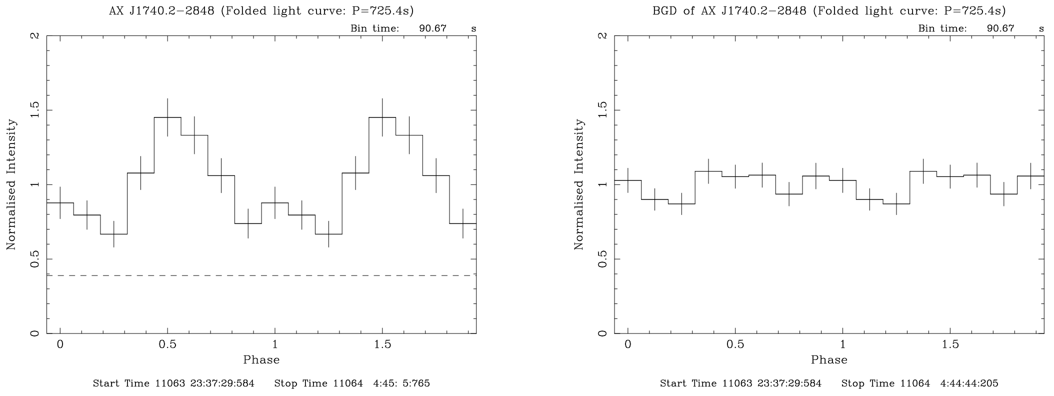

(a) Source region (b) Background region

Figure 8.5: (AX J1740.2−2848) GIS2+3 folded light curves with P =725.4 seconds in the 2–10 keV band. Two complete cycles are plotted. (a) For the source region with radius of $3'$. The estimated background level is shown by the dashed line. (b) For the annular background region with radius of 4’–8’, centered at the source position.

The column density of this source, $N_{\rm H}\sim 2.6^{+3.2}_{-2.3}$, is probably large, but is not well determined. If the source distance is 8.5 kpc, the 2–10 keV luminosity is about 3×10^{34} erg s^{-1}.

Then we consider the category of this source. (1) The observed pulsation period of 725 seconds is rather large for a neutron star system, but still within the accepted range (Bildsten *et al.* 1997). If it is a white dwarf system, it should be a DQ Her-type system, which has a relatively short period for a white dwarf (e.g., Patterson 1994). (2) The spectral shape of power law with photon index of ~0.6 strongly suggests that this source is an accretion-powered neutron pulsar. The DQ Her-type white dwarf system also has a hard spectrum. However it usually shows strong Kα line from highly ionized iron. On the other hand, this source has no strong iron Kα line, although statistics is not so good. (3) The source luminosity is within the nominal range of accretion-powered X-ray pulsars, but probably higher than that of white dwarf binaries ($\lesssim 10^{32}$ erg s^{-1}). The location near the Galactic Center may suggest the distance is near 8.5 kpc.

All these facts strongly imply that this source, AX J1740.2−2848, is an accretion-powered neutron star system. However, the possibility that this source is a nearby DQ Her-type white dwarf binary is not excluded. Future observation to search for the companion star is highly encouraged.

8.3 Population of faint X-ray sources in the direction for the Galactic Center

Table 8.2 summarizes the population of faint X-ray sources discussed in this section. One or two of all the four candidate sources in the Galactic Center region are merely a foreground star, one of them is a possible LMXB, whereas the other one is identified as a pulsar, probably a HMXB.

Table 8.2: Summary of population of faint X-ray sources

Name	Likely category
AX J1754.5−2928	foreground star (?)
AX J1754.2−2755	LMXB (?)
AX J1742.6−2901	?? (star ?)
AX J1740.2−2848	Pulsar (HMXB?)

Chapter 9

Discussion

We already obtained the most complete and the largest sample of the X-ray sources seen in the direction toward the Galactic Center (Chapter 5). Among those, we performed the intensive analyses on the selected bright sources, and understood the natures in detail (Chapter 6). In addition, we developed the method to estimate the distance to the sources and thus discern whether each source is actually located in the Galactic Center region or nearer (Chapter 7). It means that we obtained the source sample which contains only the sources located actually in the Galactic Center region[1], separating them from foreground sources. Then, we picked up the candidate sources which are actually located in the Galactic Center region according to the column density criterion, and studied the nature of each source (Chapter 8).

Our sample of X-ray sources is almost complete for the $5{\times}5$ degree^2 Galactic Center region, although it contains some observation biases that are discussed in the following section. Hard X-ray above 3 keV is nearly transparent to the Galactic Center. Therefore our sample provides us a good opportunity to discuss the source distribution in the Galactic Center region. In this chapter, we discuss the X-ray population in the Galactic Center region, and further discuss on the implication to the past starburst activity in the Galactic Center region.

---

[1] For the sources with $|b_{\rm II}| > 0.^{\circ}3$, we cannot restrict the upper limit of the source distance; such sources are located in the bulge or farther.

9.1 Number and density of the Galactic Center bright sources

9.1.1 Observation biases

First, we consider the observation bias in selecting the sources. We basically use the source data with only bright sources to minimize the observation bias unless otherwise mentioned. Two (or three) sources in the Galactic Center region studied in the previous chapter are too faint; their spectra are not enough well determined if they are located on the Galactic plane due to high background. In fact, it is rather difficult and complex to estimate the position dependent flux threshold to well determine the spectral parameters.

Flux variability (Transient activity)

There are some transient sources in the bright source list (Table 6.10). Some of the transient sources are observed with TOO observations after the report on the transient activity with other satellites; it causes the observational bias for the unified study.

However, it is difficult to discern whether a source is transient or really persistent because long term monitoring is essential to discern it. Then we adopted the simple criterion described in the beginning of Section 6.1. We adopted the persistent sources based on this criterion as at least the unbiased sample.

In the Galactic Center region, some transient sources may be always seen. It means that if we adopt only persistent sources, it may cause another observation bias. Thus we checked the first pointings in which the position of each transient source was (unbiasedly) observed, and found that no transient source in the list, except for XTE J1739−302, was significantly detected in the first unbiased observation.

On the other hand, we excluded SLX 1735−269 from the list, although it is probably a persistent source. It is because the position of SLX 1735−269 is too far from the Galactic Center and would have not been observed in the (unbiased) Galactic Center survey if we had not known the source.

Most of sources show flux variability for a long term, or even during one observation period. We thus define the flux of each source as the mean flux in the first observation of the source to avoid the observation bias.

Stray light effect

The pointings near GX 3+1 are heavily contaminated with the stray light from GX 3+1. It causes the observation threshold to much increase effectively; the fluxes of some of sources listed in the bright source list might be below the detection threshold if the source location was near GX 3+1. Hence, we do not use the data with the region of $l_{\rm II} > 1^\circ\!.0$ and $b_{\rm II} > 0^\circ\!.0$. It means that three sources, GRO J1750−27, AX J1749.2−2725 and GX 3+1 itself, are excluded in the list that we use here. Then, the effective observation area is calculated to be ~ 16 deg^2.

9.1.2 Comparison with the population on the Galactic plane

Table 9.1 shows the summary of positions and fluxes of the bright sources. We directly made the source number to flux relation (Log$N$-Log$S$ $(N > S)$ relation) with 2–10 keV band for the Galactic Center bright sources and show it in Fig 9.1, superposing it on the Log$N$-Log$S$ $(N > S)$ relation for the sources on the Galactic plane obtained from the results with *ASCA* Galactic plane survey (Sugizaki 1999). In the Log$N$-Log$S$ $(N > S)$ relation, we exclude GRS 1734−292, which is already identified as an extragalactic AGN (Martí *et al.* 1998; see review in Section 2.2.6).

The distances to the detected sources in the Galactic Center region with $|b_{\rm II}| > 0^\circ\!.3$ are unknown, hence some of them may be located out of our Galaxy, just as GRS 1734−292. Ueda *et al.* (1998a, 1999) derived the Log$N$-Log$S$ $(N > S)$ relation for the sources in blank sky regions from the results with *ASCA* Large Sky Survey (LSS) and *ASCA* Medium Sensitive Survey (MSS). We estimated the expected number of extragalactic objects with the 2–10 keV flux of 10^{-12} erg cm^{-2} s^{-1} in the observed Galactic Center region from the Log$N$-Log$S$ $(N > S)$ relation to be ∼0.3 even if the source spectrum is assumed to be not absorbed in the Galaxy. Since the X-rays from extragalactic sources toward this region must be absorbed with hydrogen column density of larger than 10^{22} H cm^{-2}, this expected number of 0.3 is an upper limit. Consequently, we can safely assume that there is no more extragalactic object, other then GRS 1734−292.

Whereas our data contain only the sources actually located near the Galactic Center, the on-plane data contain all the sources in the line of sight. Therefore, we can conclude that the density of X-ray point sources in the Galactic Center region is much larger than that on the Galactic plane. The difference of the density may follow the matter concentration in the Galactic Center region.

Table 9.1: Summary of positions & fluxes of bright sources

Name	$l_{\rm II}$	$b_{\rm II}$	$R^{\S}$	$F_{\rm X}{}^{\dagger}$	$L_{\rm X}{}^{\ddagger}$	Category¶	Bias$^{\#}$
(Persistent point sources)							
1E 1740.7−2942	359.12	−0.11	124	220	280	BHC	
A 1742−294	359.57	−0.38	75	260	290	LMXB	
1E 1743.1−2843	0.25	−0.03	46	91	210	LMXB(?)	
SLX 1737−282	359.97	1.26	196	48	49	LMXB(?)	
GRS 1734−292	358.87	1.40	217	33	31	AGN	
SLX 1744−299	359.30	−0.89	159	19	23	LMXB	
SLX 1744−300	359.26	−0.91	165	200	260	LMXB	
AX J1745.6−2901	359.94	−0.03	2	60	180	LMXB	
SLX 1735−269	0.78	2.40	388	160	160	LMXB	Yes
(Transient point sources)							
GRS 1737−31	357.59	−0.10	353	< 1	< 3	BHC	Yes
KS 1741−293	359.55	−0.03	59	< 1	< 3	LMXB	Yes
GRS 1741.9−2853	359.96	0.13	27	< 1	< 3	LMXB	Yes
XTE J1739−302	358.07	0.46	292	91	92	HMXB(?)	
GRO J1744−28	0.04	0.30	54	< 1	< 3	special*	Yes
XTE J1748−288	0.67	−0.24	112	< 1	< 3	BHC	Yes
GRO J1750−27	2.36	0.50	372	< 1	< 3	HMXB	Yes
(In the region contaminated by GX 3+1 stray light)							
GX 3+1	2.29	0.79	374	4500	4400	LMXB	Yes
AX J1749.2−2725	1.70	0.12	265	30	39	HMXB	Yes
(Fainter point sources)							
AX J1754.2−2755	1.85	−1.10	327	8	8	LMXB(?)	Yes
AX J1740.2−2848	359.49	1.091	171	3	3	HMXB	Yes

§: The (linear) distance from Sgr A* in unit of [pc], where the distance to Sgr A* of 8.5 kpc is assumed.

†: Observed flux with 2–10 keV in unit of [10^{-12} erg cm^{-2} s^{-1}] in the first unbiased observation.

‡: Luminosity with 2–10 keV in unit of [10^{34} erg s^{-1}] (absorption corrected).

¶: We regard bursters (except GRO J1744−28) as LMXBs, whereas we here regard pulsars as HMXBs because most of pulsars are HMXBs (Bildsten *et al.* 1997).

#: Whether the data have some observational bias or not.

*: GRO J1744−28 is a special source, the bursting pulsar, which is possibly accompanied with a low mass companion (see Section 2.2.14).

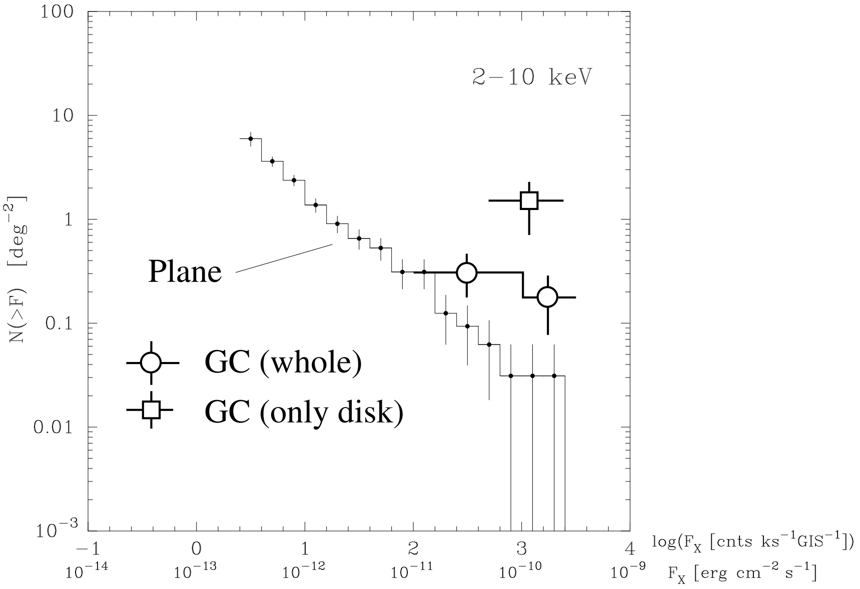

Figure 9.1: The 2–10 keV Log$N$-Log$S$ ($N > S$) relation of the Galactic Center sources. Open circles show the data with the Galactic Center bright sources in the whole region (see text), whereas a open box shows the same data but only on-plane data with $|b_{\rm II}| < 0.^\circ 3$. Note that an AGN, GRS 1734−292, is excluded from the data. Small closed circles show the on-plane data ($|b_{\rm II}| < 0.^\circ 3$, $|l_{\rm II}| < 40^\circ$) with the *ASCA* Galactic plane survey, derived by Sugizaki (1999). Note that on-plane data include the contribution from extragalactic sources.

9.1.3 Comparison with star distribution

Grebenev *et al.* (1996) derived X-ray population in the Galactic Center region with ART-P/*Granat*, and compared it with the galactic star population model (Bahcall & Soneira model; see Bahcall (1986) and references therein). We compared our result with them in Fig. 9.2. Then our result was found to be consistent with the ART-P result, and supports the implication that although the X-ray source number is larger than that in the Galactic plane, it still follows the distribution of stars, *i.e.*, the star to X-ray (point) source ratios in the Galactic Center region and on the Galactic plane are consistent with each other.

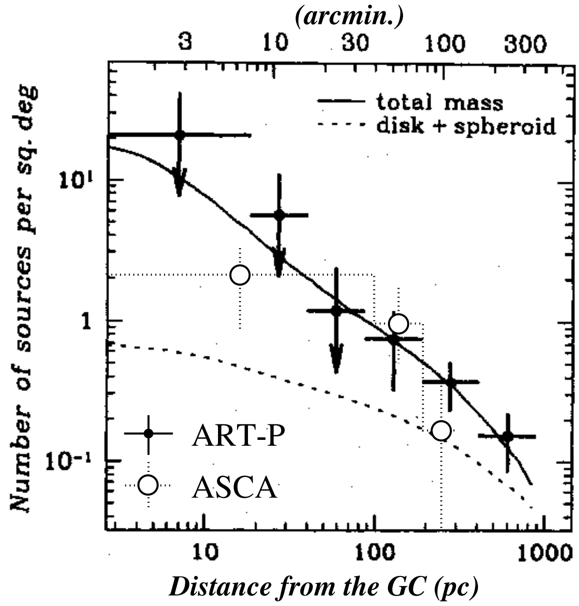

Figure 9.2: The surface density of the Galactic Center X-ray sources detected with *ASCA* (open circles and dotted line) and ART-P/*Granat* (closed circles; Grebenev *et al.* 1996). Solid and dashed lines are what the predicted surface mass density of stars in the Galactic Center direction according to Bahcall & Soneira model (Bahcall 1986) is normalized to the ART-P data (Grebenev *et al.* 1996).

9.2 Population of X-ray sources in the Galactic Center region

9.2.1 X-ray population obtained with *ASCA* in the Galactic Center region

Table 9.2 summarizes the X-ray population obtained with *ASCA*. Then we find the major population, at least 50% of all the sources, in the Galactic Center region is low mass X-ray binaries (LMXBs). On the other hand, there are small number of HMXBs, at most 25% of all the sources.

Table 9.2: X-ray population in the Galactic Center region obtained with *ASCA*

	LMXB	HMXB	BHC	others[†]
whole sample	8 (+3)	3 (+1)	3	1
unbiased sample	4 (+2)	0 (+1)	1	0

NOTE: — This table is based on Table 9.1. An AGN, GRS 1734−292, is excluded from the list.
[†]: Category of “others” includes the bursting pulsar GRO J1744−28, which is probably accompanied with a low mass companion (see Section 2.2.14).

9.2.2 Comments on the nature of black hole candidates

Three black hole candidates (BHCs) observed in the Galactic Center region are probably binary X-ray systems (see Section 6.1.1 for 1E 1740.7−2942, in particular). Since the major population of the Galactic Center region is found to be LMXBs, the companion star for the three BHCs may be also LMXBs.

Most of BHCs show nova feature, whereas only a small number of BHCs showing persistent emission are known: Cyg X-1, LMC X-1, LMC X-3, 1E 1740.7−2942, GRS 1758−258, 4U 1755−338, 4U 1957+11 and GX 339−4 (White & van Paradijs 1996; van Paradijs 1998). In these BHCs with persistent emission, the optical counterparts are identified for only the first three sources; they all are high mass stars. Therefore, BHCs with persistent emission is thought to be the black holes with high mass companion (e.g., van Paradijs 1998; Lasota 1999). In the persistent BHCs, however, 1E 1740.7−2942 and GRS 1758−258 are located in the Galactic Center region or the bulge[2]; therefore they may be low mass X-ray binaries as mentioned above. It may suggest that some of BHCs with low mass companion show persistent emission against the conventional result, although the possibility that these two sources are actually accompanied with high mass companion is not excluded.

---

[2] GRS 1758−258 is located at $(l_{\rm II}, b_{\rm II})$=$(4.^\circ5, -1.^\circ4)$.

9.2.3 Comparison with LMC/SMC population

We compare our results on X-ray population in the Galactic Center region with those in the whole Galaxy, Large Magellanic Cloud (LMC) and Small Magellanic Cloud (SMC).

In the "*Catalogue of X-Ray Binaries*" (van Paradijs 1995), 79 Galactic persistent LMXBs (+BHCs with unidentified companion) and 34 persistent HMXBs are listed; accordingly, the number ratio of (LMXB+BHC) to HMXB is about 40% (Grebenev *et al.* 1996). When we take account of the more recent discoveries with *ASCA*, *SAX* and *XTE*, the ratio becomes about 70/100= 70% (e.g., Yokogawa *et al.* 2000b). On the other hand, the estimated number relation in the Galactic Center sources is ∼20% or less. Thus, the deficit of HMXBs in the Galactic Center region is found to be apparent.

If we compare our results in the Galactic Center region with those in Magellanic Clouds, the difference is more apparent. Yokogawa *et al.* (2000b) performed the detailed study on the X-ray population of the SMC, with *ASCA*. They discovered several new X-ray pulsars; accordingly, the number of detected HMXBs in the SMC is 25 at present (Yokogawa *et al.* 2000b). The total mass of the SMC and the Galactic Center region (radius of ∼350pc) is about the same. Thus we can directly compare the number of HMXBs in the both regions, about 25/4 for SMC/GC regions, *i.e.*, there are much fewer HMXBs in the Galactic Center region than in SMC. In addition, there is no LMXB known in SMC. It indicates the quite large HMXB/LMXB ratio in SMC.

In addition, Schmidtke *et al.* (1999) performed the LMC/SMC survey with *ROSAT* and derived the ratio HMXB/LMXB∼25 in Magellanic Clouds. It is again much larger than that of the Galactic Center region (smaller than 0.4).

In the above comparison, we must consider the possible observation bias. We however found no observation bias that makes the above discussion change according to the following reasons: (1) The detection of high mass X-ray binary is usually based on their hard X-ray nature about above 3 keV, because the pulse fraction is generally larger in harder energy band than in softer energy band. Such hard X-ray energy photons are not so absorbed in the interstellar absorption. Therefore, one can detect pulsating X-rays even if the source is located in the Galactic Center region where thick interstellar matter of $\sim 10^{23}$ H cm^{-2} is distributed. (2) The distance of the SMC, 60 kpc, is about 7 times farther than that of the Galactic Center; accordingly, the apparent flux is about 60 times smaller for the SMC sources than for the Galactic Center sources. It means the much smaller detection efficiency in SMC than in the Galactic Center region. In fact, the luminosity of the faintest pulsar detected in SMC is 2.5×10^{35} erg s^{-1} in 0.7–10 keV band (Yokogawa *et al.* 2000b), whereas the luminosity of AX J1740.2$-$2828, the faintest pulsar in the Galactic Center region, is only 3×10^{34} erg s^{-1} in 2–10 keV band. Therefore, this bias should cause rather higher detection rate of HMXBs in the Galactic Center region. However, the observational result is contrary. (3) Since the distance to the SMC is 7 times farther than to the Galactic Center, SMC is apparently more crowded with X-ray sources than the Galactic Center region. This bias may again cause higher detection rate of HMXBs and pulsation in the Galactic Center region, in particular for non-imaging detectors, and is contrary to the observational result. (4) The area of SMC, about $2^\circ \times 2^\circ$ is smaller than the Galactic Center region ($5^\circ \times 5^\circ$ with our definition). It may cause the higher detection efficiency of the transient sources in SMC because one can observe SMC repeatedly or for longer time than in the Galactic Center region, in a given total observation time. However, the Galactic Center region is the most important target in the space and have been always observed intensively with almost all the satellites. Therefore the Galactic Center region is probably observed with longer time than SMC; at least, there is definitely no large difference to cause the observed difference in the number of HMXBs by a factor of 6. In fact, there is no such strong observation bias between *ASCA* observations of SMC and the Galactic Center region. In addition, since about a half of pulsars and pulsar candidates in SMC was discovered with *ASCA*, this kind of the observational bias in the result is definitely small.

Consequently, we can safely conclude that the number of HMXBs or HMXB/LMXB ratio is much larger in SMC than in the Galactic Center region.

Since the companions of HMXBs are considered to be born $\sim 10^7$ years ago, the number of HMXBs or HMXB/LMXB ratio is a good indicator for the past star formation activity in the observed region. Yokogawa *et al.* (2000b) discussed that the large number of HMXBs implies the past violent starburst activity in SMC. In fact, some other evidence also supports the implication.

On the other hand, the past star formation history in the Galactic Center region is not well understood, although some evidence for the past starburst activity was reported (see the review in Section 2.1). In the above discussion, we found that HMXBs or HMXB/LMXB ratio in the Galactic Center region is smaller than that in the whole Galaxy, and in addition, much smaller than that in SMC. This result accordingly suggests rather quiet star formation history $\sim 10^7$ years ago. Although our sample is still small, it may give an important information for quantitative discussion on the evolution of the Galactic Center region (e.g., Lipunov *et al.* 1996). Future survey with better sensitivity and monitoring observations, for example with XMM, would confirm our result with much better statistics.

Chapter 10

Concluding Remarks

We performed extensive studies on X-ray population as well as the cold matter distribution in the Galactic Center 5×5 degree^2 region, using the *ASCA* data since 1993 until 1999. The principal results are summarized as follows;

1. We obtained the finest image in 3–10 keV with the angular resolution of about $1'$. We clearly resolved the point sources and the diffuse structures.

2. We detected 46 point sources, combining the source search results with 0.7–3 keV and 3–10 keV bands. Among those, we performed the intensive study on the ten bright sources. In particular, we detected X-ray bursts from A 1742$-$294 and SLX 1744$-$300, X-ray pulsation from AX J1749.2$-$2725, or X-ray flare from XTE J1739$-$302. The power law slopes of the spectra for the sources were found to be significantly different according to the class of objects. On the other hand, we analyzed the data of the radio supernova remnants and two newly discovered X-ray structures, designated as AX J1751$-$29.6 and AX J1747.0$-$2828. Significant line emission from both of AX J1751$-$29.6 and AX J1747.0$-$2828 was found.

3. We found the column density of each bright source in the Galactic Center region to be well expressed with a function of the galactic coordinates. In particular, it strongly depends on the galactic latitude. On some reasonable assumptions, we estimated cold gas distribution in the Galactic Center region, and derived the Gaussian widths for parallel and perpendicular directions to the Galactic plane to be $\sim$170 and $\sim$20 pc, respectively, where the distance to the Galactic Center is 8.5 kpc. The upper limit of the total ISM mass in the Galactic Center region is estimated to be $6\times10^7 M_\odot$.

4. Based on the derived function for the column density, we established the method to estimate the distance of the sources in the direction toward the Galactic Center, and applied the method to the faint sources toward this region. From one of the faint sources which was estimated to be actually located in the bulge or farther (AX J1740.2−2848), we discovered a significant pulsation with the period of 725±12 seconds.

5. We found the density of the X-ray sources in the Galactic Center region are larger than that of the sources on the Galactic plane. The distribution of the X-ray point sources in the Galactic Center region is still consistent with that of stars. However, the deficit of high mass X-ray binaries in the Galactic Center region is apparent. It may suggest no violent starburst activity $\sim 10^7$ years ago in the Galactic Center region.

Appendix A

The Galactic Disk Interstellar Mass Distribution Model

We here present the formulation of the model for the distribution of the interstellar hydrogen mass, based on the model by Olling & Merriefield (1998). They constructed a face-on ISM distribution model, as shown in Fig. A.1. We derived a simplified analytical model from their model for the radial direction of the Galaxy,

$$\begin{aligned}
\Sigma_{\mathrm{HI}}(r) \quad [\mathrm{M}_{\odot}\ \mathrm{pc}^{-2}] &= \frac{45}{\mathrm{R}_0}r - 36 && (0.9\mathrm{R}_0 \le r \le \mathrm{R}_0) \\
&= \frac{45}{8\mathrm{R}_0}r - \frac{9}{16} && (0.1\mathrm{R}_0 \le r \le 0.9\mathrm{R}_0) \\
&= 0.0 && (r \le 0.1\mathrm{R}_0) \qquad \text{(A.1)} \\
\Sigma_{\mathrm{H}_2}(r) \quad [\mathrm{M}_{\odot}\ \mathrm{pc}^{-2}] &= -\frac{80}{9\mathrm{R}_0}r + \frac{187}{18} && (0.55\mathrm{R}_0 \le r \le \mathrm{R}_0) \\
&= \frac{110}{9\mathrm{R}_0}r - \frac{11}{9} && (0.1\mathrm{R}_0 \le r \le 0.55\mathrm{R}_0) \\
&= 0.0 && (r \le 0.1\mathrm{R}_0) \qquad \text{(A.2)}
\end{aligned}$$

where Σ_{H} is a face-on (column) density, r is a Galactocentric radius, and R_0 is the distance to the Galactic Center, 8.5 kpc.

For the vertical distiribution (z) to the Galactic plane, we assumed Gaussian distribution (Spitzer 1942) with scale height of $\sigma_z(r)$ as a function of the Galactocentric radius r,

$$\sigma_{z,\mathrm{HI}}(r) \quad [\mathrm{pc}] = \frac{200}{\mathrm{R}_0}r + 20 \tag{A.3}$$

$$\sigma_{z,\mathrm{H}_2}(r) \quad [\mathrm{pc}] = \frac{47}{\mathrm{R}_0}r + 27, \tag{A.4}$$

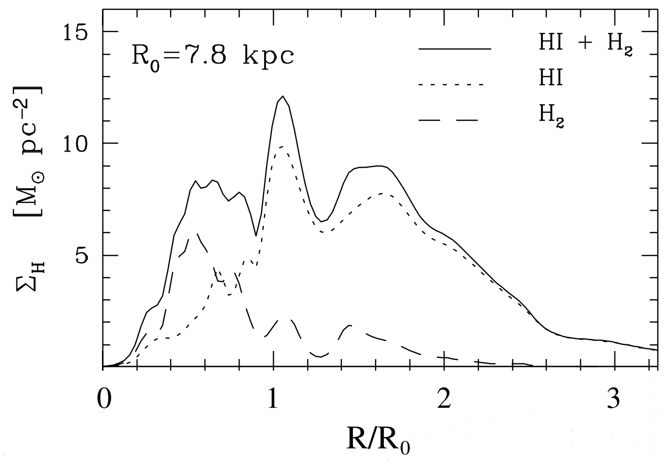

Figure A.1: Face-on surface density distribution of the H_I (dotted line), H_2 (dashed line), and the sum of both (solid line) for the Galaxy. The profile is not affected with the distance to the Galactic Center, R_0, although it is defined as 7.8 kpc in the figure. This figure is identical with the upper panel of Figure 2 in Olling & Merrifield (1999). They used the ISM distribution data with Burton (1988), Malhotra (1995), Wouterloot *et al.* (1990), and Bronfman *et al.* (1988).

accoding to Malhotra (1995) and Merrifield (1992) for H_I, and to Malhotra (1994) and Dame *et al.* (1987) for H_2.

Consequently, the disk interstellar hydrogen densities for HI ($n_{\rm HI}$) and H_2 ($n_{\rm H_2}$) are represented as follows[1];

$$\begin{aligned}
n_{\rm HI}(r,z)\ \ [\mathrm{H\ cm^{-3}}] &= \frac{40.8}{\sqrt{2\pi}}\left(\frac{\frac{45}{\mathrm{R_0}}r-36}{\sigma_{z,\rm HI}(r)}\right)\exp\left\{-\frac{1}{2}\left(\frac{z}{\sigma_{z,\rm HI}(r)}\right)^2\right\} \quad (0.9\mathrm{R_0}\le r\le \mathrm{R_0})\\
&= \frac{40.8}{\sqrt{2\pi}}\left(\frac{\frac{45}{8\mathrm{R_0}}r-\frac{9}{16}}{\sigma_{z,\rm HI}(r)}\right)\exp\left\{-\frac{1}{2}\left(\frac{z}{\sigma_{z,\rm HI}(r)}\right)^2\right\} \quad (0.9\mathrm{R_0}\le r\le \mathrm{R_0})\\
&= 0.0 \qquad (r\le 0.1\mathrm{R_0}) \qquad \text{(A.5)}\\
n_{\rm H_2}(r,z)\ \ [\mathrm{H\ cm^{-3}}] &= \frac{40.8}{\sqrt{2\pi}}\left(\frac{-\frac{80}{9\mathrm{R_0}}r+\frac{187}{18}}{\sigma_{z,\rm H_2(r)}}\right)\exp\left\{-\frac{1}{2}\left(\frac{z}{\sigma_{z,\rm H_2(r)}}\right)^2\right\} \quad (0.55\mathrm{R_0}\le r\le \mathrm{R_0})\\
&= \frac{40.8}{\sqrt{2\pi}}\left(\frac{\frac{110}{9\mathrm{R_0}}r-\frac{11}{9}}{\sigma_{z,\rm H_2(r)}}\right)\exp\left\{-\frac{1}{2}\left(\frac{z}{\sigma_{z,\rm H_2(r)}}\right)^2\right\} \quad (0.55\mathrm{R_0}\le r\le \mathrm{R_0})\\
&= 0.0 \qquad (r\le 0.1\mathrm{R_0}) \qquad \text{(A.6)}
\end{aligned}$$

where $\sigma_{z,\rm HI}(r)$ and $\sigma_{z,\rm H_2}(r)$ are defined in eq. A.3 and eq. A.4, respectively.

---

[1] Note that the unit of $n_{\rm H_2}$ is expressed as [H cm^{-3}] here.

Appendix B

Terminology

AGN Active Galactic Nucleus.

ARF Auxiliary Response Function.

ART-P An instrument on board *Granat*.

ASCA The 4th japanese X-ray astronomical satellite.

ASM All Sky Monitor. It was equipped with *Ginga*, *XTE*, and *SAX*.

BATSE Burst and Transient Source Experiment on board *CGRO*.

BH(C) Black Hole (Candidate).

BSAX Beppo Satellite per Astronomia X, which was launched in 1996 August.

CCD Charge Coupled Device.

CGRO Compton Gamma Ray Observatory.

COR The geomagnetic Cut Off Rigidity (GeV). One of the selection item to cut high background region.

CXB Cosmic X-ray Background.

d.o.f. degree of freedom.

EGRET γ-ray detector on board *CGRO*.

ELV The ELeVation angle from the earth rim. One of the selection item to select good region for an observation.

FFT Fast Fourier Transform.

FOV Filed Of View.

Ginga The third japanese astronomical X-ray satellite.

GIS Gas Imaging Spectrometer on board *ASCA* (see Chapter 3).

GSFC Goddard Space Flight Center; one of departments in NASA.

HMXB High Mass X-ray Binary. It is usually used for a neutron star binary.

IAU International Astronomical Union

IR InfraRed.

ISM InterStellar Matter

LMXB Low Mass X-ray Binary. It is usually used for a neutron star binary.

LMC Large Magellanic Cloud.

MJD Modified Julian Days (= (Julian Days)$-$2400000.5).

NASA National Aeronautics and Space Administration (at U.S.A.).

NIR Near InfraRed.

NS Neutron Star.

NXB Non-X-ray Background.

OSSE Oriented Scintillation Spectrometer Experiment on board *CGRO*.

PCA Proportional Counter Array aboard *XTE*.

PSF Point Spread Function.

PV (phase) Performance Verification phase (in *ASCA* operation).

RBM_CONT The Radiatoin Belt Monitor COuNT rate. One of the selection item to cut high background region.

RDD Residual Dark Distribution (see Chapter 3).

ROSAT RÖntgen SATellit, which was launched in 1990 June.

RXTE The Rossi X-ray Timing Explorer, which was launched in 1995 December.

SAA	The South Atlantic Anomaly. It is the region where the number of high energy particles are extraordinarily large.
SAX	Identical with BSAX.
SIGMA	An instrument on board *Granat*
SIS	Solid-state Imaging Spectrometer on board *ASCA* (see Chapter 3).
SMC	Small Magellanic Cloud.
SNR	SuperNova Remnant.
TJD	Truncated Julian Days (= (Julian Days)$-$2440000.5).
TOO	Target Of Opportunity.
VLBA	Very Long Baseline Array (a radio interferometer).
WFC	Wide Filed Camera aboard *SAX*.
XRT	X-Ray Telescope aboard *ASCA*.
XTE	Identical with RXTE.

Bibliography

[1] E. Anders and N. Grevesse. *Geochimica et Cosmochimica Acta*, 53:197, 1989.

[2] K. Asai, T. Dotani, F. Nagase, K. Mitsuda, S. Kitamoto, K. Makishima, T. Takeshima, and K. Kawabata. Ginga observations of GX 3+1: Long-term variabilities, branches, and X-ray bursts. *PASJ*, 45:801–810, December 1993.

[3] T. Augusteijn and *et al.*. *ApJ*, 486:1013, 1997.

[4] H. Awaki. PhD thesis, Nagoya University, 1991.

[5] J. N. Bahcall. *ARA&A*, 24:577, 1986.

[6] J. Bally and M. Leventhal. Is the Galactic Centre gamma-ray source 1E1740.7−2942 accreting from a molecular cloud? *Nature*, 353:234–237, September 1991.

[7] J. Bally, A. A. Stark, R. W. Wilson, and C. Henkel. *ApJ*, 324:223, 1988.

[8] M. Bałucińska-Church and D. McCammon. *ApJ*, 400:699, 1992.

[9] A. Bamba, J. Yokogawa, M. Sakano, and K. Koyama. Deep X-ray observations of supernova remnants G 359.1−0.5 and G 359.0−0.9 with *ASCA*. *PASJ*, in press, 2000.

[10] T. M. Bania. A latitude survey of carbon monoxide emission near the Galactic center. *ApJ*, 308:868, 1986.

[11] D. Barret and J. E. Grindlay. ROSAT-HRI observations of sigma hard X-ray sources of the Galactic center region. *A&A*, 311:239–244, July 1996.

[12] D. Barret, J. E. McClintock, and J. E. Grindlay. Luminosity differences between black holes and neutron stars. *ApJ*, 473:963+, December 1996.

[13] A. Bazzano, M. Cocchi, L. Natalucci, and *et al.*. In C. D. Dermer, M. S. Strickman, and J. D. Kurfess, editors, *proc. of thr 4th Compton symposium*, page 733. AIP, 1997b.

[14] A. Bazzano, M. Cocchi, P. Ubertini, J. Heise, J. In't Zand, and J. M. Muller. SLX 1735−269. *IAU Circ.*, 6668:2+, May 1997a.

[15] A. Bazzano, C. La Padula, P. Ubertini, and R. K. Sood. Variability of the Galactic Center in the hard X-ray range. *ApJL*, 385:L17–L20, January 1992.

[16] G. F. Bignami, P. A. Caraveo, and S. Mereghetti. Optical observations of high energy sources. *A&AS*, 97:229–234, January 1993.

[17] L. Bildsten and E. F. Brown. Thermonuclear burning on the accreting X-ray pulsar GRO J1744−28. *ApJ*, 477:897+, March 1997.

[18] L. Bildsten, D. Chakrabarty, J. Chiu, M. H. Finger, D. T. Koh, R. W. Nelson, T. A. Prince, B. C. Rubin, D. M. Scott, M. Stollberg, B. A. Vaughan, C. A. Wilson, and R. B. Wilson. Observations of accreting pulsars. *ApJS*, 113:367+, December 1997.

[19] L. Blitz, J. B. G. M. Bloemen, W. Hermsen, and T. M. Bania. The gamma-ray deficit toward the Galactic Center. *A&A*, 143:267, 1985.

[20] J. Bondi and F. Hoyle. *MNRAS*, 104:21, 1944.

[21] L. Bouchet, P. Mandrou, J. P. Roques, G. Vedrenne, B. Cordier, A. Goldwurm, F. Lebrun, J. Paul, R. Sunyaev, E. Churazov, M. Gilfanov, M. Pavlinsky, S. Grebenev, G. Babalyan, I. Dekhanov, and N. Khavenson. Sigma discovery of variable e^+-e^- annihilation radiation from the near Galactic Center variable compact source 1E 1740.7−2942. *ApJL*, 383:L45–L48, December 1991.

[22] H. V. D. Bradt, T. Ohashi, and K. A. Pounds. X-ray astronomy missions. *ARA&A*, 30:391–427, 1992.

[23] G. Branduardi, J. C. Ives, P. W. Sanford, A. C. Brinkman, and L. Maraschi. Observations of the transient X-ray source at the Galactic Centre A 1742−28. *MNRAS*, 175:47P–56P, May 1976.

[24] L. Bronfman, R. S. Cohen, H. Alvarez, J. May, and P. Taddeus. *ApJ*, 324:248, 1988.

[25] B. E. Burke, R. W. Mountain, P. J. Daniels, and V. S. Dolat. *IEEE Trans. Nuc. Sci.*, 41:375, 1994.

[26] B. E. Burke, R. W. Mountain, D. C. Harrison, M. W. Bautz, J. P. Doty, G. R. Ricker, and P. J. Daniels. *IEEE Trans.*, ED-38:1069, 1991.

[27] W. B. Burton. In G. L. Verschuur and K. I. Kellermann, editors, *Galactic and Extragalactic Radio Astronomy (A&A Library)*, page 295. Springer-Verlag, 1988.

[28] John S. Carr, K. Sellgren, and Suchitra C. Balachandran. The first stellar abundance measurements in the Galactic Center: the m supergiant IRS 7. *ApJ*, in press, 1999.

[29] L. X. Cheng, M. Leventhal, D. M. Smith, N. Gehrels, J. Tueller, and G. Fishman. BATSE all-sky search for transient gamma-ray lines between 300 and 550 kev. *ApJ*, 503:809+, August 1998.

[30] A. M. Cherepashchuk, V. P. Goranskij, E. A. Karitskaya, A. E. Nadjip, A. Savage, N. I. Shakura, R. A. Sunyaev, and A. A. Volchkov. The investigation of the error boxes of Kvant and Granat X-ray sources in the region of Galactic Center. *A&A*, 289:419–428, September 1994.

[31] E. Churazov, M. Gilfanov, B. Cordier, and M. C. Schmitz-Fraysse. GRS 1734−292. *IAU Circ.*, 5623:2+, September 1992.

[32] E. Churazov, M. Gilfanov, and R. Sunyaev. Is 1E 1740.7−2942 inside the dense molecular cloud? constraints from ASCA data. *ApJL*, 464:L71–+, June 1996.

[33] E. Churazov, M. Gilfanov, R. Sunyaev, A. Dyachkov, N. Khavenson, V. Kovtunenko, R. Kremnev, K. Sukhanov, M. Niel, L. Bouchet, P. Mandrou, J. P. Roques, B. Cordier, A. Goldwurm, F. Lebrun, and J. P. Leray. Spectral states of 1E1740.7−2942. *A&AS*, 97:173–176, January 1993.

[34] E. Churazov, M. Gilfanov, R. Sunyaev, A. Dyachkov, N. Khavenson, V. Kovtunenko, R. Kremnev, K. Sukhanov, M. Niel, L. Bouchet, P. Mandrou, J. P. Roques, B. Cordier, A. Goldwurm, F. Lebrun, and J. P. Leray. Spectral states of 1E1740.7−2942. *A&AS*, 97:173–176, January 1993c.

[35] E. Churazov, M. Gilfanov, R. Sunyaev, N. Khavenson, B. Novikov, A. Dyachkov, R. Kremnev, K. Sukhanov, B. Cordier, P. Paul, P. L., A. Claret, L. Bouchet, J. P. Roques, P. Mandrou, and G. Vedrenne. Review of Granat/sigma observations of the Galactic Center region. *ApJS*, 92:381–385, June 1994.

[36] E. Churazov, M. Gilfanov, R. Sunyaev, B. Novickov, I. Chulkov, V. Kovtunenko, A. Sheikhet, K. Sukhanov, A. Goldwurm, B. Cordier, J. Paul, P. O. Petrucci, E. Jourdain, J. P. Roques, L. Bouchet, and P. Mandrou. Detection of the A 1742−294 X-ray burster above 35 kev. *ApJ*, 443:341–347, April 1995.

[37] E. Churazov, M. Gilfanov, R. Sunyaev, M. Pavlinsky, S. Grebenev, A. Dyachkov, V. Kovtunenko, R. Kremnev, M. Niel, P. Mandrou, G. Vedrenne, J. P. Roques, B. Cordier, A. Goldwurm, F. Lebrun, and J. Paul. Low-flux hard state of 1E 1740.7−2942. *ApJ*, 407:752–757, April 1993.

[38] M. Cocchi, A. Bazzano, L. Natalucci, P. Ubertini, J. Heise, J. M. Muller, and J. J. M. in't Zand. Discovery of type-I X-ray bursts from GRS 1741.9−2853. *A&A*, 346:L45–L48, June 1999b.

[39] M. Cocchi, J. J. M. in't Zand, A. Bazzano, and *et al.*. *Nucl. Phys. B*, 69/1–3:232, 1999a.

[40] D. Cole and *et al.*. *ApJ*, 480:377, 1997.

[41] F. Combes. Distribution of co in the Milky Way. *ARA&A*, 29:195–237, 1991.

[42] J. J. Condon, W. D. Cotton, E. W. Greisen, Q. F. Yin, R. A. Perley, and J. J. Broderick. *BAAS*, 183:6402C, 1993.

[43] W. R. Cook, J. M. Grunsfeld, W. A. Heindl, D. M. Palmer, T. A. Prince, S. M. Schindler, and E. C. Stone. Coded-aperture imaging of the Galactic Center region at gamma-ray energies. *ApJL*, 372:L75–L78, May 1991.

[44] B. Cordier, J. Paul, J. Ballet, A. Goldwurm, L. Bouchet, J. P. Roques, P. Mandrou, G. Vedrenne, E. Churazov, M. Gilfanov, R. Sunyaev, B. Novikov, I. Chulkov, N. Kuleshova, I. Tserenin, and A. Sheikhet. The soft gamma-ray source 1E 1740.7−2942 revisited - sigma observation of a new transient activity beyond 200-kev. *A&A*, 275:L1–+, August 1993.

[45] B. Cordier, J. Paul, A. Goldwurm, P. Laurent, L. Bouchet, E. Jourdain, J. P. Roques, P. Mandrou, M. Gilfanov, E. Churazov, R. Sunyaev, N. Khavenson, A. Dyachkov, B. Novikov, R. Kremnev, and V. Kovtunenko. Sigma soft gamma-ray observations of 1E 1740.7−2942 in the spring of 1992 - discovery of a sub-luminous state of emission and precise gamma-ray position measurement. *A&A*, 272:277+, May 1993.

[46] P. Cox and R. Laureijs. In *Proceedings of IAU symposium 136: "The Center of the Galaxy"*, page 121, 1989.

[47] D. I. Cremonesi, S. Mereghetti, L. Sidoli, and G. L. Israel. BeppoSAX and ASCA observations of the Galactic bulge source 1E 1743.1−2843. *A&A*, 345:826–830, May 1999.

[48] W. Cui, W. A. Heindl, J. H. Swank, D. M. Smith, E. H. Morgan, R. Remillard, and F. E. Marshall. RXTE observations of a new X-ray transient: GRS 1737−31. *ApJL*, 487:L73–+, September 1997.

[49] G. Dahmen, S. Huttemeister, T. L. Wilson, and R. Mauersberger. Molecular gas in the Galactic Center region. ii. gas mass and $n(h_2)/i(^{12}co)$ conversion based on a $c^{18}o$ ($j = 1 \rightarrow 0$) survey. *A&A*, 331:959, 1998.

[50] P. David, A. Goldwurm, T. Murakami, J. Paul, P. Laurent, and P. Goldoni. ASCA X-ray observations of the Galactic bulge source SLX 1735−269. *A&A*, 322:229–233, June 1997.

[51] C. Day, K. Arnaud, K. Ebisawa, E. Gotthelf, J. Ingham, K. Mukai, and N. White. “the ABC guide to *ASCA* data reduction” version 4. NASA/GSFC, 1995.

[52] S. Djorgovski, D. Thompson, J. Mazzarella, A. Klemola, G. Neugebauer, K. Matthews, and L. Armus. 1E 1740.7−2942. *IAU Circ.*, 5596:2+, August 1992.

[53] T. Dotani. ASCA sis calibration information. *In: “A Catalog of Galactic Supernova Remnants”*, http://www.astro.isas.ac.jp/d̃otani/, 1999.

[54] T. Dotani, R. Fujimoto, F. Nagase, and H. Inoue. GRO J1750−27. *IAU Circ.*, 6241, 1995.

[55] T. Dotani, A. Yamashita, H. Ezuka, K. Takahashi, G. Crew, K. Mukai, and the SIS Team. Recent progress of sis calibration and software. *The ASCA news (Greenbelt: NASA GSFC)*, 5:14, 1997.

[56] A. Eckart and R. Genzel. Observations of stellar proper motions near the Galactic Centre. *Nature*, 383:415–417, 1996.

[57] A. Eckart and R. Genzel. Stellar proper motions in the central 0.1 pc of the galaxy. *MNRAS*, 284:576–598, January 1997.

[58] R. Egger and X. Sun. In D. Breitschwerdt, M. J. Freyberg, and J. Trümper, editors, *proc. of “The Local Bubble and Beyond”, IAU Colloq. 166*, page 417. Springer, 1998.

[59] C. J. Eyles, G. K. Skinner, A. P. Willmore, and F. D. Rosenberg. *Nature*, 261:476, 1976.

[60] H. Ezuka and M. Ishida. Iron line diagnostics of the postshock hot plasma in magnetic cataclysmic variables observed with ASCA. *ApJS*, 120:277–298, February 1999.

[61] H. Falcke, A. Cotera, W. J. Duschl, F. Melia, and M. J. Rieke, editors. *The central parcecs of the Galaxy.* ASP Conf. Ser. 186, June 1999.

[62] R. P. Fender, S. J. B. Burnell, and E. B. Waltman. The radio-jet X-ray binaries. *Vistas in Astronomy*, 41:3–13, 1997.

[63] M. H. Finger, D. T. Koh, R. W. Nelson, T. A. Prince, B. A. Vaughan, and R. B. Wilson. Discovery of hard X-ray pulsations from the transient source GRO J1744−28. *Nature*, 381:291–293, 1996.

[64] G. J. Fishman and *et al.*. *IAU Circ.*, 6272, 1995.

[65] A. M. Ghez, B. L. Klein, M. Morris, and E. E. Becklin. High proper-motion stars in the vicinity of Sagittarius A*: Evidence for a supermassive black hole at the center of our galaxy. *ApJ*, 509:678–686, December 1998.

[66] A. Goldwurm, B. Cordier, J. Paul, J. Ballet, L. Bouchet, J. P. Roques, G. Vedrenne, P. Mandroui, R. Sunyaev, E. Churazov, M. Gilfanov, A. Finogenov, A. Vikhlinin, A. Dyachkov, N. Khavenson, and V. Kovtunenko. Evidence against a massive black-hole at the Galactic Center. *Nature*, 371:589+, October 1994.

[67] A. Goldwurm, M. Vargas, J. Paul, S. Faisse, L. Bouchet, V. Borrel, J. P. Roques, P. Mandrou, R. Sunyaev, E. Churazov, M. Gilfanov, N. Khavenson, A. Dyachkov, A. Sheikhet, R. Kremnev, and V. Kovtunenko. Sigma hard X-ray observations of the Galactic bulge source SLX 1735−269. *A&A*, 310:857–860, June 1996.

[68] E. Gotthelf. *The ASCA news (Greenbelt: NASA GSFC)*, 4:31, 1996.

[69] A. D. Gray. The most Galactic Center survey - part two - new results on published supernova remnants and G 2.4+1.4. *MNRAS*, 270:835–846, October 1994.

[70] S. A. Grebenev, M. N. Pavlinsky, and R. Sunyaev. Population of X-ray sources near the Galactic Center according to ART-P/Granat. In *Roentgenstrahlung from the Universe*, pages 141–142, February 1996.

[71] D. A. Green. *In: "A Catalog of Galactic Supernova Remnants"*, http://www.mrao.cam.ac.uk/surveys/snrs/, 1998.

[72] Ariel 5 GROup. *IAU Circ.* 2934, 1976.

[73] B. A. Harmon, M. L. McCollough, C. A. Wilson, S. N. Zhang, and W. S. Paciesas. XTE J1748−288. *IAU Circ.*, 6933:3+, June 1998.

[74] M. J. Harris, G. H. Share, and M. D. Leising. *ApJ*, 420:649, 1994a.

[75] M. J. Harris, G. H. Share, and M. D. Leising. SMM observations of gamma-ray transients. 3: A search for a broadened, redshifted positron annihilation line from the direction of the Galactic Center. *ApJ*, 433:87–95, September 1994b.

[76] T. Hasegawa, T. Oka, F. Sato, M. Tsuboi, and A. Miyazaki. The structure and kinematics of molecular gas in the Galactic Center. In V. O. S. Aachen, editor, *Proc. of "The Physics and Chemistry of the Interstellar Medium", Abstract Book of the 3rd Cologne-Zermatt Symposium, held in Zermatt, September 22-25, 1998*, pages E25–+, 1998.

[77] N. Hayashida, K. Honda, N. Inoue, K. Kadota, F. Kakimoto, K. Kamata, S. Kawaguchi, Y. Kawasaki, N. Kawasumi, H. Kitamura, E. Kusano, Y. Matsubara, K. Murakami, M. Nagano, D. Nishikawa, H. Ohoka, N. Sakaki, K. M. Sasaki, Shinozaki, N. Souma, M. Takeda, M. Teshima, R. Torii, I. Tsushima, Y. Uchihori, T. Yamamoto, S. Yoshida, and H. Yoshii. The anisotropy of cosmic ray arrival directions around 10^{18}ev. *Astropart. Phys.*, 10:303–311, 1999.

[78] W. A. Heindl, W. R. Cook, J. M. Grunsfeld, D. M. Palmer, T. A. Prince, S. M. Schindler, and E. C. Stone. An observation of the Galactic Center hard X-ray source, 1e 1740.7−2942, with the caltech coded-aperture telescope. *ApJ*, 408:507–513, May 1993.

[79] W. A. Heindl, T. A. Prince, and J. M. Grunsfeld. Observations of 1E 1740.7−2942 with ROSAT and the VLA. *ApJ*, 430:829–833, August 1994.

[80] J. Heise. SAX J1750.8−2900 and GRS 1737−31. *IAU Circ.*, 6606:1+, March 1997.

[81] D. J. Helfand and R. H. Becker. *ApJ*, 314:203, 1987.

[82] P. Hertz and J. E. Grindlay. The einstein Galactic plane survey - statistical analysis of the complete X-ray sample. *ApJ*, 278:137–149, March 1984.

[83] R. M. Hjellming, M. P. Rupen, A. J. Mioduszewski, D. A. Smith, and *et al.*. *A&A*, 193:in press, 1998.

[84] K. Hurley, C. Kouveliotou, T. Cline, D. Cole, M. C. Miller, A. Harmon, G. Fishman, M. Briggs, J. van Paradijs, J. Kommers, and W. Lewin. Precise interplanetary network localization of the bursting pulsar GRO J1744−28. *ApJ*, submitted (astro-ph/9912506), 2000.

[85] Y. Ihisaki, Y. Ueda, H. Kubo, Y. Ikebe, K. Makishima, and the GIS Team. Reproducibility of the GIS non X-ray background. *The ASCA news (Greenbelt: NASA GSFC)*, 5:26, 1997.

[86] H Inoue. *Space Science Reviews*, 40:317, 1985.

[87] J. In't Zand. PhD thesis, Utrecht University, 1992.

[88] J. in't Zand, J. Heise, M. Smith, J. M. Muller, P. Ubertini, and A. Bazzano. SAX J1818.6−1703 and KS 1741−293. *IAU Circ.*, 6840:2+, March 1998.

[89] J. J. M. In't Zand, J. Heise, A. C. Brinkman, R. Jager, G. K. Skinner, T. G. Patterson, H. C. Pan, M. R. Nottingham, A. P. Willmore, and O. Al-Emam. Two new X-ray transients near the Galactic Center. *Advances in Space Research*, 11:187–190, 1991.

[90] Y. Ishisaki. *Spectra and Large-scale Isotropy of the Cosmic X-ray Background from ASCA Observations*. PhD thesis, University of Tokyo, 1996.

[91] J. G. Jernigan, H. V. Bradt, R. E. Doxsey, R. G. Dower, J. E. McClintock, and K. M. V. Apparao. Positions of Galactic X-ray sources with $l_{\rm ii}$ between -20 deg and $+6$ deg. *Nature*, 272:701–704, April 1978.

[92] G. V. Jung, D. J. Kurfess, W. N. Johnson, R. L. Kinzer, J. E. Grove, M. S. Strickman, W. R. Purcell, D. A. Grabelsky, and M. P. Ulmer. OSSE observations of 1E 1740.7$-$2942 in 1992 september. *A&A*, 295:L23–L26, March 1995.

[93] N. Kawai, E. E. Fenimore, J. Middleditch, R. G. Cruddace, G. G. Fritz, W. A. Snyder, and M. P. Ulmer. X-ray observations of the Galactic Center by spartan 1. *ApJ*, 330:130–141, July 1988.

[94] G. H. Kellogg, S. Murray, H. Tananbaum, and R. Giacconi. *ApJL*, 169:L99, 1971.

[95] J. A. Kennea and G. K. Skinner. No eclipses in A1742$-$289 archival data. *PASJ*, 48:L117–L117, December 1996.

[96] F. K. Knight, III Johnson, W. N., J. D. Kurfess, and M. S. Strickman. High-energy X-ray observations of the Galactic Center region. *ApJ*, 290:557–567, March 1985.

[97] T. Kotani, N. Kawai, F. Nagase, M. Namiki, M. Sakano, T. Takeshima, Y. Ueda, and M. Matsuoka. *Astrophysical Letters and Communications*, submitted, 2000.

[98] C. Kouveliotou, J. Van Paradijs, G. J. Fishman, M. S. Briggs, J. Kommers, B. A. Harmon, C. A. Meegan, and W. H. G. Lewin. A new type of transient high-energy source in the direction of the Galactic Centre. *Nature*, 379:799+, 1996.

[99] K. Koyama, H. Awaki, H. Kunieda, S. Takano, Y. Tawara, S. Yamauchi, I. Hatsukade, and F. Nagase. Intense 6.7-keV iron line emission from the Galactic Centre. *Nature*, 339:603–605, 1989.

[100] K. Koyama, Y. Maeda, T. Sonobe, T. Takeshima, Y. Tanaka, and S. Yamauchi. ASCA view of our Galactic Center: Remains of past activities in X-rays? *PASJ*, 48:249–255, April 1996.

[101] K. Koyama, K. Makishima, and Y. Tanaka. Thermal X-ray emission with intense 6.7-keV iron line from the Galactic ridge. *PASJ*, 38:121–131, 1986.

[102] H. Kunieda, A. Furuzawa, M. Watanabe, and the *ASCA* XRT Team. *The ASCA news (Greenbelt: NASA GSFC)*, 3:3, 1995.

[103] S. Kuznetsov, M. Gilfanov, E. Churazov, R. Sunyaev, I. Korel, N. Khavenson, A. Dyachkov, I. Chulkov, J. Ballet, P. Laurent, S. Kuznetsov, M. Gilfanov, and E. Churazov. Properties of the hard X-ray radiation from Cygnus X-1 and 1E1740.7−2942. *MNRAS*, 292:651+, December 1997.

[104] J. Lasota. Why do black-hole X-ray binaries tend to be transient? In *Proceedings of the ESO Workshop on "Black Holes in Binaries and Galactic Nuclei: Diagnostics, Demography and Formation"*, in press, 1999.

[105] D. A. Leahy. *A&A*, 216:193L, 1989.

[106] M. Leventhal. Recent balloon observation of the Galactic Center 511 kev annihilation line. *Advances in Space Research*, 11:157–164, 1991.

[107] W. H. G. Lewin, J. A. Hoffman, J. Doty, D. R. Hearn, G. W. Clark, J. G. Jernigan, F. K. Li, J. E. McClintock, and J. Richardson. Discovery of X-ray bursts from several sources near the Galactic centre. *MNRAS*, 177:83P–92P, December 1976.

[108] W. H. G. Lewin, R. E. Rutledge, J. M. Kommers, J. Van Paradijs, and C. Kouveliotou. A comparison between the rapid burster and GRO J1744−28. *ApJL*, 462:L39–+, May 1996.

[109] W. H. G. Lewin, J. Van Paradijs, G. Hasinger, W. H. Penninx, A. Langmeier, M. Van Der Klis, F. Jansen, E. M. Basinska, M. Sztajno, and J. Trümper. Quasi-periodic oscillations in the X-ray flux of GX3+1 (4u 1744−26). *MNRAS*, 226:383–394, May 1987.

[110] V. M. Lipunov, L. M. Ozernoy, S. B. Popov, K. A. Postnov, and M. E. Prokhorov. Population synthesis of X-ray sources at the Galactic Center. *ApJ*, 466:234+, July 1996.

[111] D. C. Lis and P. F. Goldsmith. *ApJ*, 337:704, 1989.

[112] D. R. Lorimer, M. Bailes, and P. A. Harrison. *MNRAS*, 289:592, 1997.

[113] F. J. Lu, T. P. Li, X. J. Sun, M. Wu, and C. G. Page. X-ray map from the exosat Galactic plane survey and a direct demodulation technique. *A&AS*, 115:395+, February 1996.

[114] Y. Maeda. PhD thesis, Kyoto University, 1998.

[115] Y. Maeda and K. Koyama. ASCA observations of the Galactic Center. In R. Gredel, editor, *Proc. of the 4th ASP international meeting jointly organized by the Inter-American Observatory (CTIO), held March 10-15, 1996 in La Serena, Chile, "The*

Galactic Center", Astronomical Society of the Pacific Conference Series, Volume 102, pages 423+. (San Francisco): Astronomical Society of the Pacific (ASP), 1996.

[116] Y. Maeda, K. Koyama, and ASCA team. X-ray binary sources near the Galactic Center with ASCA. In *New horizon of X-ray astronomy — first results from ASCA —*, pages 497–498. Universal Academy Press, Inc., 1994.

[117] Y. Maeda, K. Koyama, and M. Sakano. *PASJ*, submitted, 2000.

[118] Y. Maeda, K. Koyama, M. Sakano, T. Takeshima, and S. Yamauchi. A new eclipsing X-ray burster near the Galactic Center: A quiescent state of the old transient A 1742−289. *PASJ*, 48:417–423, June 1996.

[119] S. R. Majewski. *ARA&A*, 31:575–638, 1993.

[120] K. Makishima, M. Ishida, T. Ohashi, T. Dotani, H. Inoue, K. Mitsuda, Y. Tanaka, M. J. L. Turner, and R. Hoshi. X-ray spectra of varying X-ray emission components in the low-mass X-ray binary GX 3+1. *PASJ*, 41:531–555, 1989.

[121] K. Makishima, K. Mitsuda, H. Inoue, K. Koyama, M. Matsuoka, T. Murakami, M. Oda, Y. Ogawara, T. Ohashi, N. Shibazaki, Y. Tanaka, J. Marshall, F., S. Hayakawa, H. Kunieda, F. Makino, F. Nagase, Y. Tawara, S. Miyamoto, H. Tsunemi, K. Tsuno, K. Yamashita, and I. Kondo. Discovery of X-ray bursts from GX 3+1 /4U 1744−26/. *ApJ*, 267:310–314, April 1983.

[122] K. Makishima, M. Tashiro, K. Ebisawa, H. Ezawa, Y. Fukazawa, S. Gunji, M. Hirayama, E. Idesawa, Y. Ikebe, M. Ishida, Y. Ishisaki, N. Iyomoto, T. Kamae, H. Kaneda, K. 'I. Kikuchi, Y. Kohmura, H. Kubo, K. Matsushita, K. Matsuzaki, T. Mihara, K. 'I. Nakagawa, T. Ohashi, Y. Saito, Y. Sekimoto, T. Takahashi, T. Tamura, T. Tsuru, Y. Ueda, and N. Y. Yamasaki. In-orbit performance of the gas imaging spectrometer onboard ASCA. *PASJ*, 48:171–189, April 1996.

[123] I. Malet, J. P. Roques, L. Bouchet, G. Vedrenne, J. Paul, B. Cordier, J. Ballet, F. Lebrun, R. Sunyaev, E. Churazov, M. Gilfanov, N. Khavenson, A. Dyachkov, N. Kuleshova, A. Sheikhet, and I. Tzerenin. Sigma observations of the Galactic Center at 511 kev. *ApJ*, 444:222–225, May 1995.

[124] S. Malhotra. The vertical equilibrium of molecular gas in the Galactic disk. *ApJ*, 433:687–704, October 1994.

[125] S. Malhotra. The vertical distribution and kinematics of hi and mass models of the Galactic disk. *ApJ*, 448:138+, July 1995.

[126] P. Mandrou. *IAU Circ.*, 5032:1+, 1990.

[127] F. E. Marshall and D. M. Smith. *IAU Circ.*, 6603, 1997.

[128] J. Martí, I. F. Mirabel, S. Chaty, and L. F. Rodríguez. The hard X-ray source (deg) s: a seyfert 1 galaxy behind the Galactic center. *A&A*, 330:72–78, February 1998.

[129] H. A. Mayer-Hasselwander and *et al.*. *A&A*, 335:161, 1998.

[130] S. Mereghetti, P. Caraveo, G. F. Bignami, and T. Belloni. Optical imaging of the fields of the two hard X-ray sources in the Galactic Center region - 1E 1740.7−2942 and GRS 1758−258. *A&A*, 259:205–208, June 1992.

[131] S. Mereghetti, L. Sidoli, and G. L. Israel. Discovery of X-rays from the composite supernova remnant G0.9+0.1 with the BeppoSAX satellite. *A&A*, 331:L77–L79, March 1998.

[132] M. R. Merrifield. The rotation curve of the Milky Way to 2.5 r_0 from the thickness of the h_i layer. *AJ*, 103:1552–1563, May 1992.

[133] P. G. Mezger, W. J. Duschl, and R. Zylka. The Galactic Center: a laboratory for AGN? *A&A Review*, 7:289–388, 1996.

[134] P. G. Mezger, V. Pankonin, J. Schmid-Burgk, C. Thum, and J. Wink. Radio determination of oxygen abundance variation in the galaxy. *A&A*, 80:L3–L5, November 1979.

[135] I. F. Mirabel, J. Paul, B. Cordier, M. Morris, and J. Wink. 1E 1740.7−2942 - a black hole in a molecular cloud? *A&A*, 251:L43–L46, November 1991.

[136] I. F. Mirabel, L. F. Rodriguez, B. Cordier, J. Paul, and F. Lebrun. A double-sided radio jet from the compact Galactic Centre annihilator 1E 1740.7−2942. *Nature*, 358:215–217, July 1992.

[137] I. F. Mirabel, L. F. Rodriguez, B. Cordier, J. Paul, and F. Lebrun. VLA observations of the hard X-ray sources 1E1740.7−2942 and GRS1758−258. *A&AS*, 97:193–197, January 1993.

[138] K. Mitsuda, H. Inoue, N. Nakamura, and Y. Tanaka. *PASJ*, 41:97, 1989.

[139] M. Morris. Magnetic phenomena. In R. Genzel and A. I. Harris, editors, *"The nuclei of Normal Galaxies"*, pages 185–198. Kluwer Academic Publishers, 1994.

[140] M. Morris. What are the radio filaments near the Galactic Center? In L. Blitz and P. Teuben, editors, *"Unsolved Problems of the Milky Way"*, pages 247–261. IAU, 1996.

[141] M. Morris and E. Serabyn. The Galactic Center environment. *ARA&A*, 34:645–702, 1996.

[142] H. Murakami, K. Koyama, Y. Maeda, and M. Sakano. An X-ray reflection nebula Sgr B2 – a new category of X-ray astronomy. *AN*, 320:325, 1999.

[143] H. Murakami, K. Koyama, Y. Maeda, M. Sakano, M. Nishiuchi, and M. Tsujimoto. Observation of fe-line emission from Sagittarius B2 – evidence for past activities of our galaxy. *Advances in Space Research*, 25(3/4):575–578, 2000b.

[144] H. Murakami, K. Koyama, M. Sakano, M. Tsujimoto, and Y. Maeda. ASCA observations of the Sgr B2 cloud: An X-ray reflection nebula. *ApJ*, in press, 2000a.

[145] J. E. Naya, S. D. Barthelmy, L. M. Bartlett, N. Gehrels, M. Leventhal, A. Parsons, B. J. Teegarden, and J. Tueller. Detection of high-velocity ^{26}Al towards the Galactic Centre. *Nature*, 384:44–46, 1996.

[146] M. Nishiuchi, K. Koyama, Y. Maeda, K. Asai, T. Dotani, H. Inoue, K. Mitsuda, F. Nagase, Y. Ueda, and C. Kouveliotou. ASCA observations of GRO J1744−28. *ApJ*, 517:436–448, May 1999.

[147] T. Ohashi, K. Ebisawa, Y. Fukazawa, K. Hiyoshi, M. Horii, Y. Ikebe, H. Ikeda, H. Inoue, M. Ishida, Y. Ishisaki, T. Ishizuka, S. Kamijo, H. Kaneda, Y. Kohmura, K. Makishima, T. Mihara, M. Tashiro, T. Murakami, R. Shoumura, Y. Tanaka, Y. Ueda, K. Taguchi, T. Tsuru, and T. Takeshima. The gas imaging spectrometer on board ASCA. *PASJ*, 48:157–170, April 1996.

[148] T. Oka, T. Hasegawa, M. Hayashi, T. Handa, and S. Sakamoto. Co (j = 2−1) line observations of the Galactic Center molecular cloud complex. ii. dynamical structure and physical conditions. *ApJ*, 493:730+, January 1998.

[149] R. P. Olling and M. R. Merrifield. Refining the oort and Galactic constants. *MNRAS*, 297:943–952, July 1998.

[150] W. S. Paciesas, B. A. Harmon, G. N. Pendleton, M. H. Finger, G. J. Fishman, C. A. Meegan, B. C. Rubin, and R. B. Wilson. Studies of hard X-ray source variability using BATSE. *A&AS*, 97:253–255, January 1993.

[151] J. Patterson. *PASP*, 106:209, 1994.

[152] M. N. Pavlinsky, S. A. Grebenev, and R. A. Sunyaev. ART-P X-ray map of the Galactic Center region. *Sov. Astron. Lett.*, 18(2):116–120, April 1992.

[153] M. N. Pavlinsky, S. A. Grebenev, and R. A. Sunyaev. X-ray images of the Galactic Center obtained with ART-P/Granat: Discovery of new sources, variability of

persistent sources, and localization of X-ray bursters. *ApJ*, 425:110–121, April 1994.

[154] N. Prantzos. Galactic 1.8 MeV emission from ^{26}al. In *IAU Symp. 188: The Hot Universe*, volume 188, pages 31+, 1998.

[155] P. Predehl and S. R. Kulkarni. G359.23−0.92, the mouse, a pulsar powered bow shock? *A&A*, 294:L29–L31, February 1995.

[156] P. Predehl and J. Trümper. ROSAT observation of the Sgr A region. *A&A*, 290:L29–L32, October 1994.

[157] T. Prince, G. Skinner, S. Kulkarni, K. Matthews, and G. Neugebauer. Galactic center. *IAU Circ.*, 5252:1+, April 1991.

[158] R. J. Proctor, G. K. Skinner, and A. P. Wilmore. X-ray emission from the region of the Galactic Centre. *MNRAS*, 185:745–754, 1978.

[159] W. R. Purcell, L. X. Cheng, D. D. Dixon, R. L. Kinzer, J. D. Kurfess, M. Leventhal, M. A. Saunders, J. G. Skibo, D. M. Smith, and J. Tueller. OSSE mapping of Galactic 511 keV positron annihilation line emission. *ApJ*, 491:725+, December 1997.

[160] S. V. Ramírez, K. Sellgren, J. Carr, S. Balachandran, R. D. Blum, and D. Terndrup. Stellar abundances at the Galactic Center. In *The Central Parsecs, Galactic Center Workshop 1998, Tucson, Sep. 7-11, 1998, Eds. H. Falcke, A. Cotera, W. Huschl, F. Melia, and M. Rieke; To be published in the ASP Conf. Ser.*, pages pp.373–378, September 1998.

[161] M. J. Reid, A. C. S. Readhead, R. C. Vermeulen, and R. N. Treuhaft. The proper motion of Sagittarius A*. i. first vlba results. *ApJ*, 524:816–823, October 1999.

[162] M. Sakano, K. Imanishi, M. Tsujimoto, K. Koyama, and Y. Maeda. Further studies of 1E 1740.7−2942 with ASCA. *ApJ*, 520:316–323, July 1999a.

[163] M. Sakano, K. Koyama, and Y. Maeda. ASCA observations of the great annihilator near the Galactic Center. In F. Makino and K. Mitsuda, editors, *X-ray Imaging and Spectroscopy of Cosmic Hot Plasmas*, pages 489–490. Universal Academy Press, Inc., 1997.

[164] M. Sakano, K. Koyama, M. Nishiuchi, J. Yokogawa, and Y. Maeda. Mass estimation of cold matters in the Galactic Center region using bright hard X-ray sources. *Advances in Space Research*, 23(5/6):969–972, 1999b.

[165] M. Sakano, K. Koyama, M. Nishiuchi, J. Yokogawa, and Y. Maeda. The X-ray global view of the Galactic Center region with the ASCA survey. *AN*, 320:330, 1999c.

[166] M. Sakano, M. Nishiuchi, K. Koyama, J. Yokogawa, and Y. Maeda. Cold matter in the Galactic Center region measured with the X-ray satellite ASCA. In H. Falcke, A. Cotera, W. J. Duschl, F. Melia, and M. J. Rieke, editors, *ASP Conf. Ser. 186: The Central Parsecs of the Galaxy*, pages 569–577. ASP Conf. Ser. 186, June 1999d.

[167] M. Sakano, M. Nishiuchi, Y. Maeda, K. Koyama, and J. Yokogawa. Absorption columns with bright X-ray sources near the Galactic center: — mass estimation in the Galactic Center region. In Y. Sofue, editor, *IAU Symp. 184: The Central Regions of the Galaxy and Galaxies*, volume 184, pages 443–444, 1998a.

[168] M. Sakano, M. Nishiuchi, Y. Maeda, K. Koyama, and J. Yokogawa. Bright X-ray stars near the Galactic Center. In K. Koyama, S. Kitamoto, and M. Itoh, editors, *IAU Symp. 188: The Hot Universe*, volume 188, pages 366–367. Dordrecht: Kluwer Academic, 1998b.

[169] P. C. Schmidtke, A. P. Cowley, J. D. Crane, V. A. Taylor, T. K. McGrath, J. B. Hutchings, and D. Crampton. Magellanic cloud X-ray sources. iii. completion of a *ROSAT* survey. *ApJ*, 117:927–936, feb 1999.

[170] N. S. Schulz, G. Hasinger, and J. Trümper. Spectral classification of low-mass X-ray binary (LMXB) energy spectra with color-color diagrams. *A&A*, 225:48–68, November 1989.

[171] D. M. Scott, M. H. Finger, R. B. Wilson, D. T. Koh, T. A. Prince, B. A. Vaughan, and D. Chakrabarty. Discovery and orbital detemination of the transient X-ray pulsar GRO J1750−27. *ApJ*, 488:831–835, oct 1997.

[172] K. Sellgren, J. S. Carr, and S. Balachandran. First stellar iron abundance measurements in the Galactic Center. In Y. Sofue, editor, *IAU Symposia 184: The Central regions of the Galaxy and Galaxies (London: Kluwer Academic Publishers)*, volume 184, page pp.21, 1997.

[173] P. J. Serlemitsos, L. Jalota, Y. Soong, H. Kunieda, Y. Tawara, Y. Tsusaka, H. Suzuki, Y. Sakima, T. Yamazaki, H. Yoshioka, A. Furuzawa, K. Yamashita, H. Awaki, M. Itoh, Y. Ogasaka, H. Honda, and Y. Uchibori. The X-ray telescope on board ASCA. *PASJ*, 47:105–114, February 1995.

[174] S. Sheth, E. Liang, C. Luo, and T. Murakami. ASCA measurement of the hydrogen column density to 1E 1740.7−2942. *ApJ*, 468:755+, September 1996.

[175] L. Sidoli and S. Mereghetti. The X-ray diffuse emission from the Galactic Center. *A&A*, 349:L49–L52, September 1999.

[176] L. Sidoli, S. Mereghetti, G. L. Israel, L. Chiappetti, A. Treves, and M. Orlandini. The zoo of X-ray sources in the Galactic Center region: Observations with BeppoSAX. *ApJ*, 525:215–227, November 1999.

[177] L. O. Sjouwerman, H. J. Habing, M. Lindqvist, H. J. van Langevelde, and A. Winnberg. Oh/ir stars as signposts for ancient starburst activity in the Galactic Center. In *ASP Conf. Ser. 186: The Central Parsecs of the Galaxy*, pages 379+, June 1999.

[178] G. K. Skinner, A. J. Foster, A. P. Willmore, and C. J. Eyles. Localization of one of the Galactic Centre X-ray burst sources. *MNRAS*, 243:72–77, March 1990.

[179] G. K. Skinner, H. C. Pan, M. Maisack, R. Staubert, K. N. Borozdin, A. C. Brinkman, J. Englhauser, M. R. Gilfanov, A. C. Kaniovsky, W. Pietsch, R. A. Sunyaev, and J. J. M. in't Zand. The spectrum and position of the hard Galactic Centre source 1E1740.7−2942. *A&A*, 252:172–178, December 1991.

[180] G. K. Skinner, A. P. Willmore, C. J. Eyles, D. Bertram, and M. J. Church. Hard X-ray images of the Galactic Centre. *Nature*, 330:544–547, December 1987.

[181] D. A. Smith, A. Levine, and A. Wood. XTE J1748−288. *IAU Circ.*, 6932:1+, June 1998b.

[182] D. M. Smith, W. A. Heindl, J. Swank, M. Leventhal, I. F. Mirabel, and L. F. Rodriguez. X-ray timing in 1E 1740.7−2942 and GRS 1758−258. *ApJL*, 489:L51–+, November 1997a.

[183] D. M. Smith, M. Leventhal, R. Cavallo, N. Gehrels, J. Tueller, and G. Fishman. Limits on reported transient emission events near 0.5 MeV from the Crab and 1E 1740.7−2942. *ApJ*, 458:576+, February 1996.

[184] D. M. Smith, D. Main, F. Marshall, J. Swank, W. Heindl, and M. Leventhal. XTE J1739−302. *IAU Circ.*, 6748:2+, September 1997b.

[185] D. M. Smith, D. Main, F. Marshall, J. Swank, W. A. Heindl, M. Leventhal, J. J. M. in't Zand, and J. Heise. XTE J1739−302: An unusual new X-ray transient. *ApJL*, 501:L181–+, July 1998a.

[186] T. J. Sodoroski, N. Odegard, E. Dwek, M. G. Hauser, Franz B. A., and *et al.*. *ApJ*, 452:262, 1995.

[187] Y. Sofue, T. Handa, N. Nakai, H. Hirabayashi, M. Inoue, and K. Akabane. A 10 GHz radio continuum survey of the Galactic plane region. ii — the Galactice center region 4° × 4° —. *NRO Report*, 33, 1984.

[188] Y. Sofue, W. Reich, and P. Reich. The Galactic Center spur - a jet from the nucleus? *ApJL*, 341:L47–L49, June 1989.

[189] T. Strohmayer, F. E. Marshall, R. M. Hjellming, M. P. Rupen, and A. J. Mioduszewski. XTE J1748−288. *IAU Circ.*, 6934:2+, June 1998.

[190] T. E. Strohmayer, K. Jahoda, A. B. Giles, and U. Lee. Millisecond pulsations from a low-mass X-ray binary in the Galactic center region. *ApJ*, 486:355+, September 1997.

[191] M. Sugizaki. *Faint X-ray sources resolved in the ASCA Galactic plane survey and their contribution to the X-ray ridge emission.* PhD thesis, University of Tokyo, 1999.

[192] R. Sunyaev. Gx 1+4, KS 1731−260, GRS 1741.9−2853, A1524−62. *IAU Circ.*, 5104:1+, September 1990a.

[193] R. Sunyaev. The Galactic Center. *IAU Circ.*, 5123:2+, October 1990b.

[194] R. Sunyaev and E. Churazov. Equivalent width, shape and proper motion of the iron fluorescent line emission from molecular clouds as an indicator of the illuminating source X-ray flux history. *MNRAS*, 297:1279–1291, July 1998.

[195] R. Sunyaev, E. Churazov, M. Gilfanov, M. Pavlinsky, S. Grebenev, G. Babalyan, I. Dekhanov, N. Khavenson, L. Bouchet, P. Mandrou, J. P. Roques, G. Vedrenne, B. Cordier, A. Goldwurm, F. Lebrun, and J. Paul. Three spectral states of 1E 1740.7−2942 — from standard Cygnus X-1 type spectrum to the evidence of electron-positron annihilation feature. *ApJL*, 383:L49–L52, December 1991c.

[196] R. Sunyaev, E. Churazov, M. Gilfanov, M. Pavlinsky, S. Grebenev, G. Babalyan, I. Dekhanov, N. Yamburenko, L. Bouchet, M. Niel, J. P. Roques, P. Mandrou, A. Goldwurm, B. Cordier, P. Laurent, and J. Paul. Two hard X-ray sources in 100 square degrees around the Galactic center. *A&A*, 247:L29–L32, July 1991b.

[197] R. Sunyaev, E. Churazov, M. Revnivtsev, S. Trudolyubov, M. Vargas, J. Paul, J. P. Roques, and E. Jourdain. GRS 1737−31. *IAU Circ.*, 6599:2+, March 1997.

[198] R. Sunyaev, M. Pavlinsky, M. Gilfanov, E. Churazov, and S. *et al.* Grebenev. *Sov. Astron. Lett.*, 17:42–45, 1991a.

[199] R. A. Sunyaev, E. M. Churazov, M. R. Gilfanov, M. Pavlinsky, S. Grebenev, I. Dekhanov, A. V. Kuznetsov, N. S. Iyamburenko, G. K. Skinner, and T. G. Patterson. Imaging of the Galactic Center field by Kvant and Granat. *Advances in Space Research*, 11:177–185, 1991.

[200] Y. Tanaka, H. Inoue, and S. S. Holt. The X-ray astronomy satellite ASCA. *PASJ*, 46:L37–L41, June 1994.

[201] Y. Tanaka and W. H. G. Lewin. In W. H. G. Lewin, J. van Paradijs, and E. P. J. van den Heuvel, editors, *X-ray Binaries*, page 126. New York: Cambridge University Press, 1995.

[202] Y. Terada, H. Kaneda, K. Makishima, M. Ishida, K. Matsuzaki, F. Nagase, and T. Kotani. A peculiar X-ray transient source, AX J1842.8−0423, discovered with ASCA. *PASJ*, 51:39–44, February 1999.

[203] The *XTE*/ASM team. `http://space.mit.edu/XTE/ASM_lc.html`, 1999.

[204] K. Torii, K. Kinugasa, K. Katayama, T. Kohmura, H. Tsunemi, M. Sakano, M. Nishiuchi, K. Koyama, and S. Yamauchi. Discovery of a 220 second X-ray pulsar, AX J1749.2−2725. *ApJ*, 508:854–858, December 1998.

[205] M. Tsuboi, T. Handa, and N. Ukita. Dense molecular clouds in the Galactic Center region. i. observations and data. *ApJS*, 120:1–39, January 1999.

[206] M. Tsuboi and A. Miyazaki. The Galactic Center filled with molecular shells. In *IAU Symp. 184: The Central Regions of the Galaxy and Galaxies*, volume 184, pages E90–+, 1997.

[207] M. Tsuboi, A. Miyazaki, and T. Tsutsumi. Flare of Sgr A* at short millimeter wavelengths. In H. Falcke, A. Cotera, W. J. Duschl, F. Melia, and M. J. Rieke, editors, *The central parcecs of the Galaxy*, pages 105+. ASP Conf. Ser. 186, June 1999a.

[208] Y. Tsuboi. PhD thesis, Kyoto University, 1999.

[209] P. Ubertini, A. Bazzano, M. Cocchi, L. Natalucci, J. Heise, R. Jager, J. In't Zand, J. M. Muller, M. Smith, G. Celidonio, A. Coletta, R. Ricci, P. Giommi, D. Ricci, M. Capalbi, M. T. Menna, and S. Rebecchi. GS 1826−238. *IAU Circ.*, 6611:1+, April 1997.

[210] P. Ubertini, A. Bazzano, M. Cocchi, L. Natalucci, J. Heise, J. M. Muller, and J. J. M. In't Zand. Bursts from GS 1826−238: A clocked thermonuclear flashes generator. *ApJL*, 514:L27–L30, March 1999.

[211] K. I. Uchida, M. Morris, and F. Yusef-Zadeh. *AJ*, 104:1533, 1992.

[212] Y. Ueda. *ASCA studies of faint X-ray sources and the relation to the cosmic X-ray background.* PhD thesis, University of Tokyo, 1996.

[213] Y. Ueda, T. Dotani, S. Uno, H. Inoue, F. Nagase, Y. Maeda, M. Sakano, P. Durouchoux, and J. H. Swank. GRS 1737−31. *IAU Circ.*, 6627:2+, April 1997.

[214] Y. Ueda, T. Takahashi, H. Inoue, T. Tsuru, M. Sakano, Y. Ishisaki, Y. Ogasaka, K. Makishima, T. Yamada, M. Akiyama, and K. Ohta. Log n-log s relations and spectral properties of sources from the ASCA large sky survey: Their implications for the origin of the cosmic X-ray background (cxb). *ApJ*, 518:656–671, June 1999.

[215] Y. Ueda, T. Takahashi, H. Inoue, T. Tsuru, M. Sakano, Y. Ishisaki, Y. Ogasaka, K. Makishima, T. Yamada, and K. Ohta. A population of faint galaxies that contribute to the cosmic X-ray background. *Nature*, 391:866+, February 1998a.

[216] Y. Ueda, T. Takahashi, H. Inoue, T. Tsuru, M. Sakano, K. Ohta, Y. Ishisaki, Y. Ogasaka, K. Makishima, and T. Yamada. Sky surveys with ASCA – large sky survey. *Astronomische Nachrichten*, 319:47+, 1998b.

[217] J. van Paradijs. In W. H. G. Lewin, J. van Paradijs, and E. P. J. van den Heuvel, editors, *"X-ray Binaries"*. Cambridge UP, 1995.

[218] J. van Paradijs. Neutron stars and black holes in X-ray binaries. In R. Buccheri, J. van Paradijs, and M. A. Alpar, editors, *The Many Faces of Neutron Stars*, page in press. London: Kluwer Academic Publishers, 1998.

[219] M. Vargas, A. Goldwurm, M. Denis, J. Paul, V. Borrel, J. P. Roques, E. Jourdain, M. Niel, S. Trudolyubov, E. Churazov, M. Gilfanov, R. Sunyaev, A. Dyachkov, N. Khavenson, I. Chulkov, and A. Bogomolov. Sigma survey of the Galactic Center region and discovery of a hard X-ray transient. *A&AS*, 120:C291–+, December 1996.

[220] O. Vilhu, D. Hannikainen, P. Muhli, J. Huovelin, J. Poutanen, Ph. Durouchoux, and P. Wallyn. In C. Winkler, T. J.-L. Courvoisier, and Ph. Durouchoux, editors, *proc. of 2nd INTEGRAL workshop "The Transparent Universe"*, page 221. Noordwijk: ESA : ESA SP-382, 1997.

[221] W. Voges, B. Aschenbach, T. Boller, H. Bräuninger, U. Briel, W. Burkert, K. Dennerl, J. Englhauser, R. Gruber, F. Haberl, G. Hartner, G. Hasinger, M. Kürster, E. Pfeffermann, W. Pietsch, P. Predehl, C. Rosso, J. H. M. M. Schmitt, J. Trümper, and H. U. Zimmermann. The ROSAT all-sky survey bright source catalogue. *A&A*, 349:389–405, September 1999.

[222] M. G. Watson, R. Willingale, P. Hertz, and J. E. Grindlay. An X-ray study of the Galactic Center. *ApJ*, 250:142–154, November 1981.

[223] N. E. White and J. van Paradijs. The Galactic distribution of black hole candidates in low mass X-ray binary systems. *ApJL*, 473:L25–+, December 1996.

[224] R. Wijnands and M. Van Der Klis. The X-ray timing behavior of the X-ray burst source SLX 1735−269. *A&A*, 345:L35–L38, May 1999.

[225] P. M. Woods, C. Kouveliotou, J. Van Paradijs, M. S. Briggs, C. A. Wilson, K. Deal, B. A. Harmon, G. J. Fishman, W. H. G. Lewin, and J. Kommers. Properties of the second outburst of the bursting pulsar (GRO J1744−28) as observed with BATSE. *ApJ*, 517:431–435, May 1999.

[226] J. G. A. Wouterloot, J. Brand, W. B. Burton, and K. K. Kwee. *A&A*, 230:21, 1990.

[227] A. Yamashita. *Study of the Origin of the Cosmic X-ray Background from ASCA Deep Sky Observations.* PhD thesis, University of Tokyo, 1998.

[228] A. Yamashita, T. Dotani, M. Bautz, G. Crew, H. Ezuka, K. Gendreau, T. Kotani, K. Mitsuda, C. Otani, A. Rasmussen, G. Ricker, and H. Tsunemi. *IEEE Trans. Nucl. Sci.*, 44:847, 1997.

[229] S. Yamauchi and ASCA Galactic Plane Survey team. X-ray SNRs found with the *ASCA* Galactic plane survey. In W. Becker and M. Itoh, editors, *proc. of thr Symposium "Japanese-German Workshop on High Energy Astrophysics"*, pages 110–112. MPE Report 270, oct 1998b.

[230] S. Yamauchi, M. Kawada, K. Koyama, H. Kunieda, and Y. Tawara. Optically thin hot plasma near the Galactic Center - mapping observations of the 6.7 keV iron line. *ApJ*, 365:532–538, December 1990.

[231] S. Yamauchi, K. Koyama, K. Kinugasa, K. Torii, M. Nishiuchi, T. Kosuga, and Y. Kamata. Study of X-ray SNRs detected in the ASCA Galactic plane survey project. *Astronomische Nachrichten*, 319:111, 1998a.

[232] J. Yokogawa, K. Imanishi, M. Tsujimoto, M. Nishiuchi, K. Koyama, F. Nagase, and Robin H. D. Corbet. A study of the populations of X-ray sources in the small Magellanic cloud with ASCA. *ApJS*, in press, 2000b.

[233] J. Yokogawa, M. Sakano, K. Koyama, and S. Yamauchi. X-ray detection from shell-like SNR G 359.1−0.5. *Advances in Space Research*, page in press, 1999.

[234] S. N. Zhang, B. A. Harmon, and E. P. Liang. In C. D. Dermer, M. S. Strickman, and J. D. Kurfess, editors, *proc. of the Fourth Compton Symposium*, volume 410, page 873. The American Institute of Physics, 1997.

Comments for abbreviations

A&A	Astronomy & Astrophysics
A&AS	Astronomy & Astrophysics, Supplement
BAAS	Bulletin of the American Astronomical Society
ARA&A	Annual Review of Astronomy and Astrophysics
AJ	The Astronomical Journal
AN	Astronomische Nachrichten
ApJ	The Astrophysical Journal
ApJL	The Astrophysical Journal, Letter
ApJS	The Astrophysical Journal, Supplement
MNRAS	Monthly Notices of the Royal Astronomical Society
PASJ	Publications of the Astronomical Society of Japan
PASP	Publications of the Astronomical Society of the Pacific

Acknowledgments

First of all, I would like to devote my best gratitude to Prof. K. Koyama for his continuous and patient guidance and encouragement throughout five years of my graduate course. I am greatly indebted to Dr. Y. Maeda, who has been always giving me good suggestions and kind helps. I also express my sincere thanks to Dr. S. Yamauchi and all the members of the *ASCA* Galactic Plane/Center survey team, who have performed the survey, of which the data are essential for this thesis.

The analyses of the *ASCA* data of the Galactic Center region were based on the coorperation by many people. In particular, I am deeply grateful to Dr. K. Torii, Mr. J. Yokogawa, Mr. H. Murakami, Ms. M. Nishiuchi, Ms. A. Bamba, Dr. Y. Ueda, Dr. T. Kotani, Dr. M. Sugizaki, Dr. T. Dotani, and Prof. J. P. Hughes. I also thank Dr. T. Takahashi, Dr. Y. Ishisaki and Dr. A. Yamashita for their providing useful softwares and calibration information with *ASCA*.

To accomplish this thesis, many people have given me valuable suggestion and discussion. Among those, I am especially grateful to Drs. H. Awaki, T. Tsuru, H. Sogawa, M. Ozaki, H. Matsumoto, S. Ueno, Y. Tsuboi, H. Tomida, K. Hamaguchi, K. Motohara, T. Oka, T. Hasegawa, M. Tsuboi, S. Inoue, Y. Fujita, H. Kaneda, and Prof. H. Inoue, Prof. Y. Sofue, and Prof. Ph. Durouchoux.

I acknowledge all the *ASCA* team members, whose efforts have produced the wonderful X-ray satellite, *ASCA*. I have been being obliged by all the people in cosmic ray laboratory in Kyoto University through my graduate school days.

This work was financially supported by the Japan Society for the Promotion of Science for Young Scientists. A part of this work was based on the data in the SIMBAD database and on NASA's ADS abstract service. I also acknowledge NASA/GSFC and Dr. L. Wall, who have developed useful software packages.

Finally, I wish to express many thanks to my family and friends, especially around Pukuton-sou. Without their kind supports, I could have never achieved this work.